Computational Analysis of Intensity Ratios in Magneto-Optical and Plasma Spectroscopy

by

Theodora Argyro Stavrakas

Thesis submitted for the degree of Doctor of Philosophy of the University of London.

Spectroscopy Group,
Blackett Laboratory,
Imerial College
London SW7 2BZ

September 1983

To my Parents

Abstract

In a preliminary investigation at the Physikalisches Institute in Bonn, highly plane-polarised synchrotron radiation was passed through an absorption cell within a superconducting solenoid. The resulting magneto-optical patterns are studied theoretically in the present thesis. They arise from a combination of magnetic circular birefringence (Faraday rotation) and magnetic circular dichroism. The magneto-optical vernier method (Connerade 1983[1]) has been extended with an improved theoretical treatment as well as faster and more detailed computational techniques. In these calculations both MCD and MOR are treated simultaneously, thus making it possible to determine relative f-values to a very high accuracy. The method was then applied to the singlet principal series of SrI, MgI and BaI at temperatures arround 700°C, particle densities of about $10^{16}cm^{-3}$ and magnetic field strengths of up to 4.7 Tesla.

Furthermore, experimental instabilities and effects due to finite resolution of the spectrograph were taken into account by convolving the calculated intensity pattern with an adjustable apparatus function. The effect of different functions (Lorentzian, Gaussian and triangular) has also been studied and the method is shown to be fairly insensitive to various choices of profile.

By this method, the determination of the f-values of two very close-lying lines, originating from different species, proved possible under conditions such that the patterns overlap and we were therefore able to investigate what effect the overlap can have on a precise determination of f-values. Further

it was proved that singlet-triplet alkaline earth transitions are amenable to analysis by the MOV method and the effect of including hyperfine structre in the calculations was also studied.

Finally, calculations of f-values of high Rydberg states for the principal series of the alkaline earths are presented and the dependence of f-values on the externally applied magnetic field is calculated by expanding the relevant eigenfunctions in terms of LS eigenfunctions.

In another investigation, also involving detailed calculation of relative intensities but applied this time not to an atomic vapour but to a highly ionised gas, the results of calculations of the steady-state ionisation balance in a Silicon plasma are presented. The effect of collisional de-excitation on the dielectronic satellite ratios is shown to be important for electron densities in the range 10^{19} to $10^{24}cm^{-3}$ and temperatures greater than 100eV. This is the regime of interest for laser produced and laser compressed plasmas and for which the dielectronic satellite ratios have been proposed as a useful density diagnostic.

The sensitivity of the He-like resonance to intercombination line ratio:

$$\alpha = \frac{N(2^1P_1)\ A(2^1P_1;1^1S_0)}{N(2^3P_1)\ A(2^3P_1;1^1S_0)}$$

to the collisional model for "bound-bound" He-like Silicon has been investigated. Large differences in the calculated value of this ratio result from the use of different collisional models and so it may be possible to compare results of different

theoretical predictions with experiment.

1. Connerade J.P. J.Phys.B.,16,399 (1983)

Chapter I

Background Theory

The theory of magneto-optics is central to a large portion of this thesis so it is appropriate that we begin with a very brief history. The first experiments studying magneto-active materials were performed by Faraday and presented in 1845. This was before the electromagnetic theory of radiation had evolved and Faraday's motivation in performing these experiments was an attempt to develop a unified theory of the electric and magnetic forces. In his 1845 article of the Philosophical Magazine, Faraday stated "This is established, I think for the first time, a true direct relation and dependence between light and the magnetic and electric forces..."[18]. Since then, Faraday's work has also been regarded as useful in establishing the transverse nature of electromagnetic radiation. Among his last experiments Faraday investigated the effect of a magnetic field on the line spectrum of radiation. These experiments were inconclusive. Guided by Faraday's belief in a magnetic effect on line spectra and with the advantage of theoretical predictions by Lorentz [19], Zeeman performed a series of experiments with equipment which was far superior to that available to Faraday. In 1896, he presented results which showed a widening of spectral lines associated with the presence of a magnetic field ("When the electromagnet was put on, the absorption lines immmediately widened along their whole length..."[20]). The subsequent importance of this effect, the Zeeman effect, in the development of the role of the angular momentum in the quantum theory of

atomic structure is well known. Later developments in magneto-optical theory (such as Voigt's and then Kuhn's work) are described in the textbook of Mitchell and Zemansky [21].

More recently magneto-optic effects have proved to be a powerful tool in the investigation of the properties of atoms and molecules. The application of Magnetic Circular Dichroism (MCD) to the study of molecules has been described by Buckingham and Stephens [11,12,17]. In work on which much of this thesis is based, Connerade and co-workers [15,22,23] described preliminary investigations of the application of the Magneto-Optical Vernier technique (MOV) to the study of the spectra of high Rydberg states of the principal series of the alkaline earths. The novelty in the latter work is the combined application of the magnetic circular dichroism (MCD) and of the magnetic optical rotation (MOR) in the study of a single spectrum.

Some recent investigations at the Physikalisches Institute in Bonn provided spectra of absorption series of an atomic vapour in a magnetic field. The availability of synchrotron radiation, of superconducting magnets capable of producing rather high fields and of a spectrograph of high dispersion had lead to the experimental study of such spectra. These results prompted us to investigate theoretically combined MCD and MOR phenomena in some very simple atomic transitions.

In this chapter, some aspects of the background theory necessary for the understanding of magneto-optical spectra will be discussed. Sections 1 and 2 will describe the Zeeman effect in emission and absorption respectively. Sections 3 and 4 will provide the quantum mechanical treatment of the Zeeman effect both without and with the inclusion of hyperfine structure.

Section 5 will provide a discussion of dispersion theory necessary for the understanding of the wavelength dependence of the Faraday effect. A brief discussion of transverse electromagnetic waves and of the propagation of plane polarised light in active media will follow in sections 6 and 7 respectively. In section 8 and 9 the effects of MOR and MCD will be described. Finally, in section 10 the well- known absosrption and dispersion relations basic to all our calculations of MCD and MCR spectra for a line with a Voigt profile are obtained. Previous analyses ([15]) had been based on the unrealistic approximation of pure Doppler profiles. It is concluded that a Voigt line shape is the most suitable choice for the calculations of the refractive index and absorption coefficient used in the derived intensity formula for a plane polarised wave transversing an optically active medium.

1.The Zeeman Effect

Late last century, according to Lorentz's predictions, it was found experimentally that when Mg is placed between the poles of a strong magnet, a spectral line is split into two components when observed along the field and into three components when observed at right angles to the field. The first two components are circularly polarised (σ_+, σ_-) and the latter three are plane polarised (σ_+, π , σ_-) [3].

Lorentz assumed that the electrons which revolve in circular or elliptical orbits randomly in space (belonging to the atoms of the vapour) emit light waves and that their motions are affected by the externally applied magnetic field. A random motion of an electron can be considered to consist of a motion

in a straight line parallel to the field (with 1/3 probability) and of two circular motions in orbits perpendicular to the field, one clockwise (with probability 1/3) and one anti-clockwise (with 1/3 probability). When the B-field is applied, the component parallel to the field and its frequency remain unchanged, while the two circular motions have their frequencies altered by $\Delta\nu = +\text{-} eH/4\pi mc$ due to the force $\underline{F} = e\underline{v}_{\wedge}\underline{H}/c$ that the B-field exerts on the circularly orbiting electrons. Therefore when the observer is along the field direction he will observe two circularly polarised components; one with frequency $\nu_o + \Delta\nu$ which is left handed circularly polarised and the other with frequency $\nu_o - \Delta\nu$ which is right handed circularly polarised. This is the longitudinal Zeeman effect. When the observer is at right angles to the field direction he will observe that the linear motion parallel to the field will emit light in the transverse direction with the E-vector parallel to the field and that the circular components will give two plane polarised waves of frequencies $\nu_o + \Delta\nu$ and $\nu_o - \Delta\nu$ with the E-vector perpendicular to the field as the circular components are viewed edge-on. This is the transverse Zeeman effect. Both Zeeman effects are shown in the diagram below and it can be also noticed that in Fig.I1 the intensities of the two circularly polarised components are equal because with no field the light must be unpolarised. In Fig.I2 it can be seen that the light emitted from the linear motion has an intensity equal to the sum of the two plane polarised components and that these two components are of equal intensity. This description only applies to the normal Zeeman effect and is appropriate for the singlet levels. However in general the patterns are more complex

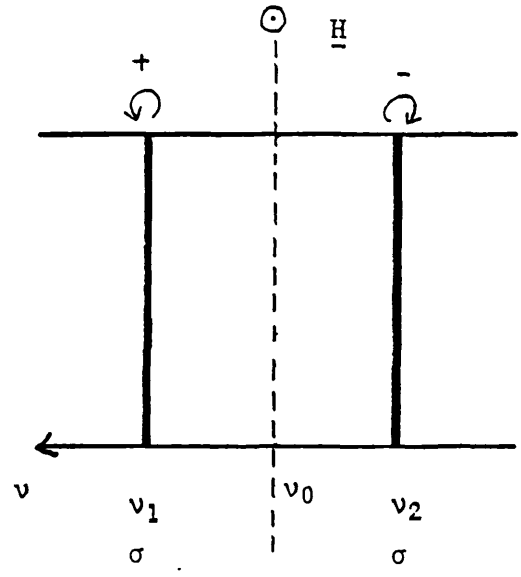

Fig.I1 The longitudinal normal Zeeman effect (showing the polarisations and intensities of the various components discussed in the text).

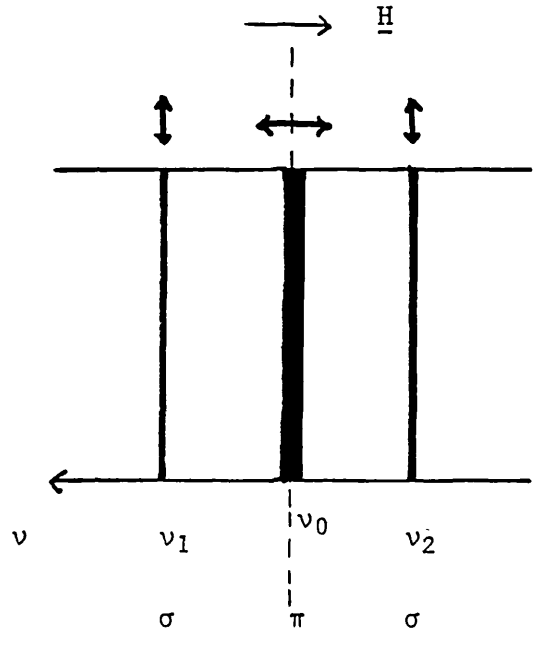

Fig.I2 The transverse normal Zeeman effect (showing the polarisations and the intensities of the various components discussed in the text).

(anomalous Zeeman effect). Singlet to triplet transitions will be further discussed in Chapter V and also in section 3 of the present chapter.

2.The Inverse Zeeman Effect

The inverse Zeeman effect is the Zeeman effect obtained in absorption [3]. In this case white light is sent through an absorbing vapour and this vapour is placed between the poles of a magnet. As unpolarised light is considered to consist of equal amounts of right and left polarised light then the longitudinal inverse Zeeman effect can be explained as follows: ν_o is the natural frequency of the vapour and the left handed circularly polarised light of frequency ν_1 is absorbed by the vapour when the B-field is applied. Therefore the right handed circularly polarised components of frequency ν_1 pass through and are observed. Analogous arguments apply for ν_2. This effect is shown in Fig.I3. In the case of the transverse inverse Zeeman effect, for ν_o, the parallel components of the light are absorbed and so the perpendicular components are transmitted. For ν_1 , the parallel components are all transmitted and half of the perpendicular components are transmitted as the other half have positive rotation at frequency ν_1 are absorbed. The same arguments apply for ν_2. This effect is shown in Fig.I4. The quadratic Zeeman effect and the universal atomic diamagnetism of high Rydberg states will be discussed in Chapter V .

3.The Quantum-Mechanical Description of the Zeeman Effect

The interaction of the atomic electrons with an externally

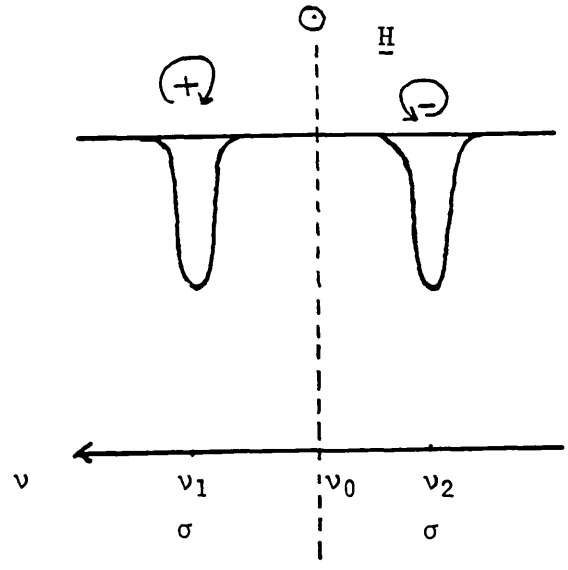

Fig.I3 The longitudinal inverse Zeeman effect (showing the polarisations and the intensities of the various components discussed in the text).

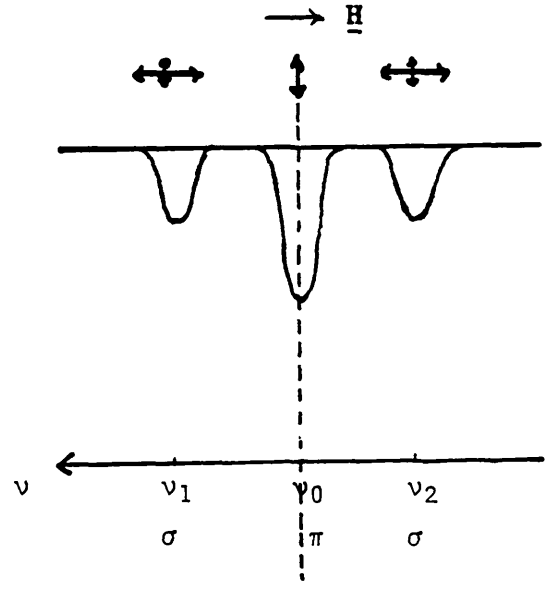

Fig.I4 The transverse inverse Zeeman effect (showing the polarisations and the intensties of the various components discussed in the text).

applied magnetic field B produces the Zeeman effect. The interaction is treated as a small perturbation and has form (for sections 3 and 4 see any standard atomic physics textbook such as [4,5,6,7]):

$$H_{pert} = -\underline{\mu}\cdot\underline{B} \qquad (I1)$$

where $\underline{\mu}$ is the total magnetic moment of the electrons.

The present section will be divided into two parts: the weak field case where it is assumed that the LS coupling holds and the strong field case where that coupling approximation breaks down and L and S precess independently about B with projections M_L and M_S on the z-axis respectively. Equation I1 can be written as:

$$H_{pert} = -(\underline{\mu}_L + \underline{\mu}_S)\cdot\underline{B} = (\mu_B\underline{L} + g_S\mu_B\underline{S})\cdot\underline{B} \qquad (I2)$$

remembering that $\underline{\mu}_L = -g_l\ \mu_B\sum_i \underline{l}_i = -\mu_B\underline{L}$ (since $g_l=1$ for orbital motion) and that $\underline{\mu}_S = -g_s\ \mu_B\sum_i \underline{s}_i = -g_s\ \mu_B\underline{S}$.

In the following results, perturbation theory is applied to cases where the zero-order eigenstates are degenerate. In such cases we must choose a suitable linear combination of wavefunctions to apply perturbation theory to [4].

(a)Weak-Field Case

In this case the LS coupling scheme is valid. The zeroth order Hamiltonian contains the central field

$$\left(\sum_i \frac{-\hbar^2}{2m}\nabla_i^2 + \sum_i U(r_i)\right)$$

and the electrostatic

$$\left(\sum_{i>j}\frac{e^2}{4\pi\varepsilon_0 r_{ij}} - \sum_i \frac{Ze^2}{4\pi\varepsilon_0 r_i} - \sum_i U(r_i)\right)$$

interactions respectively. The electrostatic interaction is considered to be large compared with the spin-orbit interaction ($\sum_i \xi(r_i)\underline{l}_i\underline{s}_i = \zeta(L,S)\underline{L}.\underline{S}$). Further the spin-orbit interaction is large compared to the Zeeman one and so the former is included in the zeroth-order Hamiltonian, so:

$$\mu_B B_{ext} \ll \zeta(LS) \sim \mu_B B \qquad B \ll \zeta(LS)/\mu_B \tag{I3}$$

is the condition to be satisfied for an external field to be considered weak. The basis $/\gamma LSJM_J\rangle$ is appropriate here. This can be seen from the fact that J_z commutes with H_{pert} which implies that $\langle \gamma LSJM_J/H_{pert}/\gamma\ LSJM'_J\rangle = 0$, if $M_J \neq M'_J$. Now,

$$H_{pert} = \mu_B(\underline{L}+g_S\underline{S}).\underline{B} = \mu_B B(L_z+g_S S_z) \tag{I4}$$

and in $/\gamma\ LSJ\rangle$ level notation the energy shift due to the Zeeman effect is given by:

$$\Delta E = \langle \gamma LSJM_J / H_{pert} / \gamma LSJM_J \rangle =$$

$$= \langle \gamma LSJM_J/\mu_B B L_z / \gamma LSJM_J\rangle + \langle \gamma LSJM_J/\mu_B g_S B S_z / \gamma LSJM_J\rangle$$

Since L_z and S_z are the projections of $\underline{L}$ and $\underline{S}$ on the z-axis, it can be shown that:

$$\langle \gamma LSJM_J / L_z \; / \; \gamma LSJM_J \rangle = \langle \gamma LSJM_J / \frac{\underline{L}.\underline{J}}{J(J+1)} J_z \; / \; \gamma LSJM_J \rangle$$

$$\langle \gamma LSJM_J / S_z \; / \; \gamma LSJM_J \rangle = \langle \gamma LSJM_J / \frac{\underline{S}.\underline{J}}{J(J+1)} J_z \; / \; \gamma LSJM_J \rangle$$

Also

$$\underline{L}.\underline{J} = 1/2 \; (\underline{J}^2 + \underline{L}^2 - \underline{S}^2)$$

$$\underline{S}.\underline{J} = 1/2 \; (\underline{J}^2 - \underline{L}^2 + \underline{S}^2)$$

The energy shift thus becomes:

$$\Delta E = \left(\frac{J(J+1)+L(L+1)-S(S+1)}{2J(J+1)} + g_S \frac{J(J+1)-L(L+1)+S(S+1)}{2J(J+1)} \right) \mu_B B M_J \qquad (15)$$

since / $\gamma LSJM$ > is a simultaneous eigenfunction of L^2, S^2, J^2 and J_z. Returning to equation 11, an effective operator for the total magnetic moment $\underline{\mu}_{eff}$ can be defined as:

$$\underline{\mu}_{eff} = -g_J \mu_B \underline{J}$$

and so:

$$H_{pert} = -(-g_J \mu_B \; \underline{J}.\underline{B}) = g_J \mu_B \underline{J}.\underline{B}$$

therefore the energy shift becomes:

$$\Delta E = \langle \gamma LSJM_J | H_{pert} | \gamma LSJM_J \rangle = \langle \gamma LSJM_J | g_J \mu_B B J_z | \gamma LSJM_J \rangle =$$

$$= g_J \mu_B B M_J \qquad \text{(I6)}$$

Comparing equations I5 and I6 we obtain:

$$g_J = \frac{J(J+1)+L(L+1)-S(S+1)}{2J(J+1)} + g_S \frac{J(J+1)-L(L+1)+S(S+1)}{2J(J+1)} \qquad \text{(I7)}$$

where g_J is the Lande g-value.

For singlet levels, S=0 and since $g_S \simeq 2$, $g_J=1$. This means that g_J does not depend on L,S or J and so with no resultant spin, the Zeeman effect is only introduced from the interaction of the orbital magnetic moment of the electrons with the externally applied magnetic field.

A $^1P_1$ level has J=1, therefore $M_J=+1,0,-1$, and by equation I6 the M_J degeneracy is lifted, each level J splits into 2J+1 states labelled by M_J. So for this particular case we get three levels, each differing from the next by an energy shift equal to $\mu_B B$.

The electric dipole selection rules for M_J are:

$$\Delta M_J = 0, +-1 \qquad\qquad M_J = 0 \not\longrightarrow M_J' = 0 \quad \text{if } \Delta J = 0$$

Further, $\Delta M_J=0$ is connected to the π-polarisation where an electric dipole oscillates in the z-direction and $\Delta M_J=+-1$ is connected to the σ-polarisation where the dipole oscillates in

the x-y plane. The π and σ components are plane polarised and perpendicular to each other. When only singlet levels are involved in a transition the Zeeman effect is referred to as normal.

When transitions between multiplets take place, we have the anomalous Zeeman effect and $g_s \neq 1$. The frequency of each of the possible transitions $/\gamma L'S'J'M'_J>$ to $/\gamma LSJM_J>$ can be given by:

$$h\nu_o=(\ E'+\Delta E'\ )-(\ E\ +\Delta E)=\ h\nu_o\ +\mu_B B(g'_J\ M'_J\ -g_J M_J)$$

where $h\nu_o$ is the difference in energy of the unperturbed levels. The components and energy levels of such a transition could be calculated in the same way as for the singlet case but only that the calculations will be more complex.

(b)Strong-Field Case

In this case we have that:

$$\mu_B B(\ L_z+\ g_S S_z) \gg \zeta(LS)\underline{L}.\underline{S}$$

and so as a first approximation we do not include the spin-orbit in the Hamiltonian. The LS coupling scheme now fails and the level notation now becomes $/\gamma LSM_L M_S>$. The energy shift is given by:

$$\Delta E=\langle \gamma LSM_L M_S\ /\mu_B B(L_z+\ g_S S_z)\ /\ \gamma LSM_L M_S\rangle\ \ =(M_L+g_S M_S)\mu_B B$$

Now that M_L and M_S are non-degenerate, the spin-orbit term can be applied as a smaller perturbation:

$$\langle \gamma LSM_L M_S \,/\zeta(LS)L.S\,/\,\gamma LSM_L M_S\rangle = \zeta(LS)M_L M_S$$

So the energy shift, finally becomes:

$$\Delta E = (M_L + g_S M_S)\mu_B B + \zeta(LS)M_L M_S$$

For the strong-field case, the electric dipole selection rules are:

$$\Delta M_S = 0 \qquad \Delta M_L = 0, +-1$$

where $\Delta M_L = 0$ corresponds to the π-polarisation and the $\Delta M_L = +-1$ to the σ-polarisation. The frequency of each possible transition in this case is:

$$h\nu_o = h\nu_o + \mu_B B \Delta M_L + (\zeta(LS)M_L M_S - \zeta(L'S')M'_L M'_S)$$

For even stronger fields the Zeeman effect is known as the Paschen-Back effect. For intermediate fields the appropriate secular equation has to be solved since the Zeeman and the spin-orbit interactions are of comparable size. This is described in greater detail in Chapter VII.

For intermediate fields, J, M_L and M_S cease to be good quantum numbers and now the perturbation is given by:

$$H_{pert} = (L_z+g_S S_z)\mu_B B + \zeta LS$$

This Hamiltonian does not commute with J^2 or L_z and S_z but with $J_z=L_z+S_z$,so $M(=M_J=M_L+M_S)$ becomes a good quantum number. Finally in second order perturbation theory it can be shown that M states begin to depend on B^2 whereas they depended only on B in first order calculations. This quadratic behaviour will be discussed further in Chapter V. States of the same M are found to repel each other and states with the same M never cross.

4.The Zeeman Effect of Hyperfine Structure

In 1924 Pauli attributed to the nucleus a total angular momentum which was labelled by the new quantum number I. This quantum number may have an integral or half integral value, depending on the number of protons and neutrons in the nucleus (both these particles have spin 1/2).

The nucleus has a magnetic moment μ_I and the interaction of this moment

with the electromagnetic field produced at the nucleus by the electrons

gives rise to the hyperfine structure. This small perturbation may be

written as:

$$H_{pert} = -\underline{\mu}_I \cdot \underline{B}_{el}$$

The hyperfine structure is small compared with the fine

structure and therefore we can assume that we are dealing with an isolated level whose energy is labelled by J. Further, I and J are good quantum numbers and the IJ coupling scheme holds. In analogy with the LS coupling, in the IJ coupling the perturbation can be written as:

$$H_{pert} = A\underline{I}.\underline{J}$$

where A is a parameter which is obtained experimentally, $\underline{\mu}_I = g'_I \mu_B \underline{I}$, $g_I \simeq 1$, $g'_I = g_I/1836$ and also $\underline{B}_{el} \propto \underline{J}$.

The zeroth-order wavefunctions are $/ \gamma IJM_I JM_J\rangle$ which are $(2I+1)(2J+1)$-fold degenerate in M_I and M_J. As usual, we can express the new zeroth-order eigenfunctions $/ \gamma IJFM_F\rangle$ as a linear combination of the functions $/ \gamma IM_I JM_J\rangle$ (where F=I+J). The Zeeman effect of hyperfine structure (with the IJ coupling scheme being valid) deals with the interaction of the total magnetic moment $\underline{\mu}_J$ and of the nuclear magnetic moment $\underline{\mu}_I$ with an externally applied magnetic field along the z-axis. The $(2I+1)*(2J+1)$-fold degeneracy is now being lifted.

We will consider the case where the Zeeman and the nuclear magnetic dipole interactions are the perturbations and where the central field and all the internal electrostatic and magnetic interactions are included in the zeroth-order Hamiltonian in the IJ coupling approximation. The pertubation is then:

$$H_{pert} = A\underline{I}.\underline{J} - \underline{\mu}_J \underline{B} - \underline{\mu}_I \underline{B} = A\underline{I}.\underline{J} + g_J \mu_B J_z B - g'_I \mu_B I_z B$$

where $\underline{\mu}_J = -g_J \mu_B \underline{J}$ and $\underline{\mu}_I = g'_I \mu_B \underline{I}$. If $g_J \mu_B B$ is much smaller than A, then we are in the weak field regime (since $g'_I \approx 1/1836.13$) and if $g_J \mu_B B$ is much larger than A we are in the strong field regime. It must be noted that the strong field case is rare in the fine structure problems whereas it is not so in hyperfine structure problems.

(a)Weak-Field Case

For the weak field case ($g_J \mu_B B << A$) the wave function is $/\gamma IJFM_F\rangle$ and AI.J is the first perturbation to be applied. The energy shift is given by:

$$\Delta E = \langle \gamma IJFM_F / \; AI.J \; / \gamma IJFM_F \rangle = 1/2 \; A(F(F+1)-J(J+1)-I(I+1))$$

Applying the same arguments as for the fine structure case, we can say that $/\gamma IJFM_F\rangle$ is a suitable wavefunction for the AI.J and for the $(g_J \mu_B J_z B - g'_I \mu_B I_z B)$ perturbations. In straight analogy with the fine case (equations I5 and I6) the energy shift becomes:

$$\Delta E = g_F \mu_B B M_F$$

where the effective g-value g_F is given by:

$$g_F = g_J \frac{F(F+1)+J(J+1)-I(I+1)}{2F(F+1)} - g'_I \frac{F(F+1)-J(J+1)+I(I+1)}{2F(F+1)}$$

The energy shift for first order is given by:

$$\Delta E_{F,M_F} = Ak/2 + g_F \mu_B \, BM_F$$

where k=F(F+1)-J(J+1)-I(I+1). The selection rules for magnetic dipole radiation are the following:

$\Delta F=0,+-1$ $\quad F=0 \not\rightarrow F=0$ $\quad \Delta M_F=0$ $\quad \sigma$ - polarisation

$\Delta M_F=+-1$ $\quad \pi$ - polarisation

(b)Strong-Field Case

In this case the condition reverses and becomes $A<<g_J \mu_B B$ and also M_J becomes a good quantum number. Therefore the main terms in the equation :

$$H_{pert} = A\underline{I}.\underline{J} - \underline{\mu}_J \underline{B} - \underline{\mu}_I \underline{B}$$

are the second and the third. The energy shift is then given by:

$$\Delta E = \langle IJM_I M_J \, / g_J \mu_B B J_z - g'_I \mu_B B I_z \, / \, IJM_I M_J \rangle = g_J \mu_B B M_J - g'_I \mu_B B M_I$$

The term AI.J contributes to ΔE an amount $AM_I M_J$ and so the total energy splitting is equal to:

$$\Delta E = AM_I M_J + g_J \mu_B B M_J - g'_I \mu_B B M_I$$

Finally it should be noted that in the intermediate field region, the energy splitting is given by the Breit-Rabi formula as follows:

$$\Delta E(F,M) = -\frac{h\Delta\nu}{2(2I+1)} - g_I' \mu_B B M \pm 1/2 h\Delta\nu \,(1+4Mx/(2I+1)+x^2)^{1/2}$$

$$x = \frac{(g_J + g_I')\,\mu_B B}{h\Delta\nu}$$

where $h\Delta\nu$ is the separation between levels F=I+1/2 and F=I-1/2 and also $M = M_F = M_I + M_J$.

5. General and Brief Comments on Dispersion and Absorption Theory

The theory of dispersion tries to relate and explain the variation of the velocity of light in a given material. Since the velocity is equal to c/n (where n= refractive index) the dispersion theory also gives the refractive index as a function of wavelength. The earliest measurements of dispersion were mainly in the visible region and in this wavelength region absorption bands were not observed; therefore this type of dispersion was called normal as opposed to the absorption that includes an absorption band and is called anomalous. Plotting n versus λ the following facts were observed [1,2,3]:

a) Although the refractive index at a certain λ is different for various substances, its variation with wavelength has usually the same form,

b) n and $dn/d\lambda$ decrease in magnitude as λ increases.

c) In general denser substances have larger refractive indices than less dense ones.

Generally it can be said that dispersion curves of different materials cannot be related in a simple way. Thus a general shape of the refractive index as a function of wavelength outside an absorption band can be seen in Fig.I5.

Cauchy attempted to find a mathematical formula for the normal dispersion curves. It had the form:

$$n = A + B/\lambda^2 + C/\lambda^4$$

where A,B and C were constants characteristic of the material involved. However Cauchy's formula could not explain the behaviour of the dispersion curve when an absorption band was included. The anomalous dispersion is shown in Fig.I6.

From Figs.I5 and I6 it can be seen that there is a discontinuity in the absorption band. It was assumed by Sellmeier that the particles in the medium vibrate with a natural frequency ν_o (that is in the absence of an externally applied force). When light passes through the medium it exerts a force on the particles and they vibrate with a frequency ν. As ν approaches ν_o, the amplitude becomes very large. This behaviour can be given by the following formula, which also explains Fig.I6:

$$n^2 = 1 + \sum_i \frac{A_i \lambda^2}{\lambda^2 - \lambda_i^2}$$

where the summation takes into account the possibility of the existence of several (i) absorption bands. Actual experimental

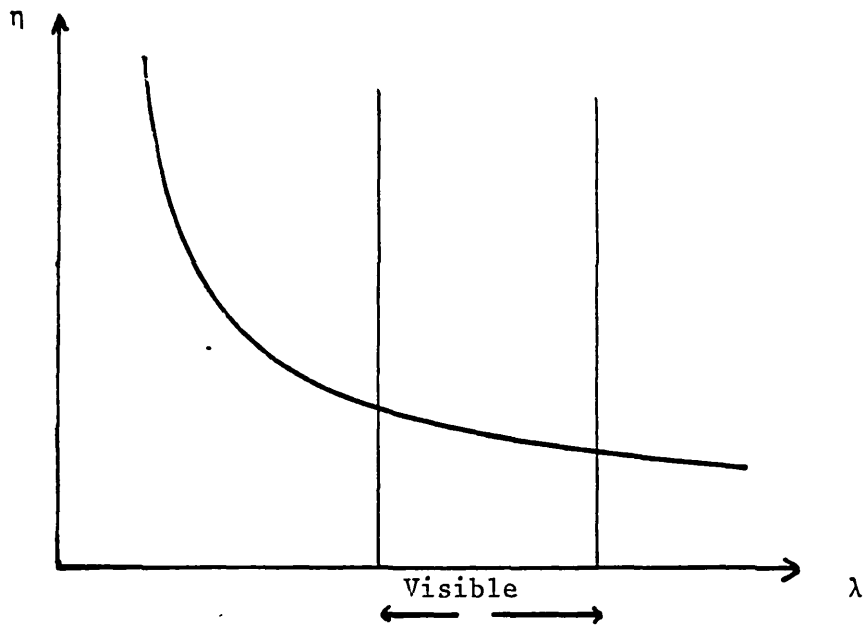

Fig.I5 A typical dispersion curve of a material away from an absorption band.

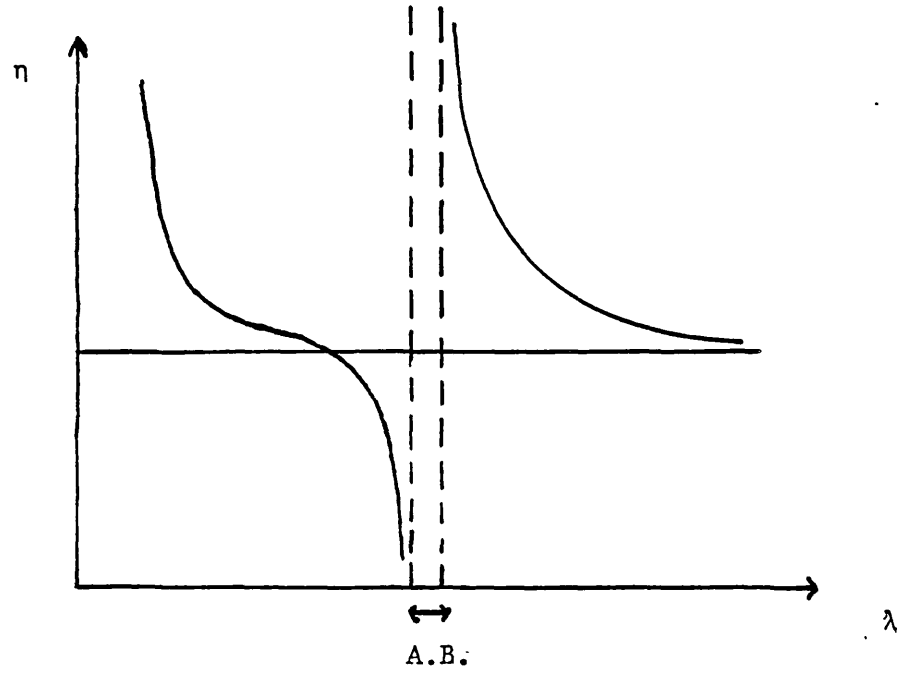

Fig.I6 A typical anomalous dispersion curve of a medium (an absorption band is present).

results (Fig.I7), show that the curve does not go to infinity at either side of each λ_i as would be physically impossible. In order to explain the behaviour of Fig.I7 , Helmholtz assumed that a frictional force proportional to the velocity of the particle was exerted on it and that it absorbs the energy of the wave.

If a is the absorption coefficient then it is useful to define a quantity

$$k = \frac{a\,l}{4\,\pi}$$

where k is a constant and physically represents the fall of the intensity to $1/\exp(4\,\pi k)$ in a distance l along the medium. Therefore, Helmholtz gives the following relations:

$$n^2 - k^2 = 1 + \sum_i \frac{A_i\,\lambda^2}{(\lambda - \lambda_i)^2 + g_i\lambda^2/(\lambda - \lambda_i)^2}$$

$$\text{and} \qquad 2nk = \sum_i \frac{A_i\sqrt{g_i}\,\lambda^3}{(\lambda^2 - \lambda_i^2)^2 + g_i\,\lambda^2}$$

where g_i is a measure of the frictional force. A typical plot of n and k versus λ is shown in Fig.I8. The above equations for $/\lambda/ > /\lambda_o/$ reproduce Sellmeier's equation.

6.The Electromagnetic Theory of Absorption and Dispersion

The fundamental equations in electromagnetic theory are the following four Maxwell equations (for the discussion to follow see any standard text book on Electromagnetism such as [8,9]).

$$\nabla.\underline{D} = \rho \qquad\qquad \nabla \wedge \underline{H} = \underline{J} + \partial\underline{D}/\partial t$$

$$\nabla.\underline{B} = 0 \qquad\qquad \nabla \wedge \underline{E} = -\partial\underline{B}/\partial t$$

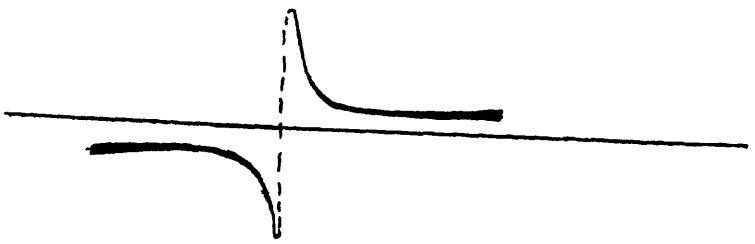

Fig.I7 A typical dispersion curve obtained from experiments in the vicinity of an absorption line.

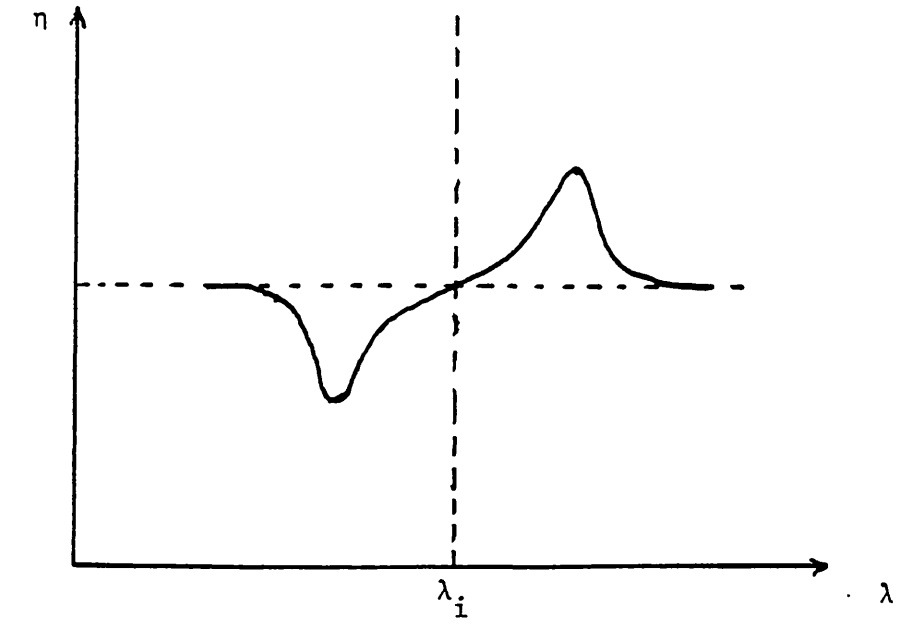

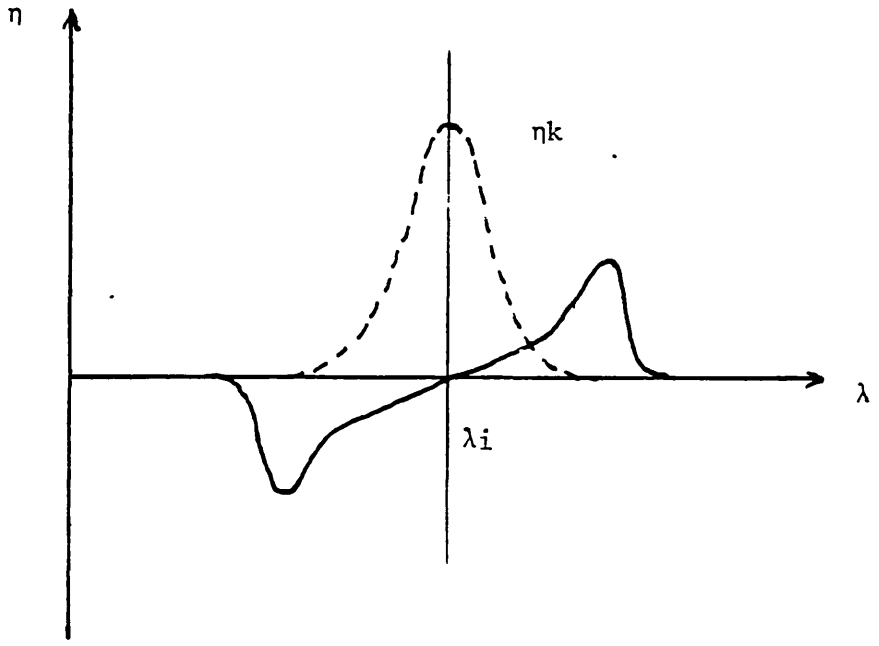

Fig.18 Calculated dispersion (solid line) and absorption coefficient (broken line) curves.

where D is the electric displacement, ρ is the charge density, B is the magnetic induction, E is the electric intensity and J is the current density ($\underline{D}=\varepsilon\underline{E}$ and $\underline{B}=\mu_o\underline{H}$ in the absence of magnetic materials). In vacuo they become:

$$\underline{\nabla}.\underline{E} = 0 \qquad \text{(I8)}$$

$$\underline{\nabla}.\underline{H} = 0 \qquad \text{(I9)}$$

$$\underline{\nabla}\wedge\underline{H} = \varepsilon\partial\underline{E}/\partial t \qquad \text{(I10)}$$

$$\underline{\nabla}\wedge\underline{E} = -\mu_o\partial\underline{H}/\partial t \qquad \text{(I11)}$$

Also,

$$\underline{\nabla}\wedge(\underline{\nabla}\wedge\underline{E}) = \underline{\nabla}(\underline{\nabla}.\underline{E}) - \nabla^2\underline{E}$$

and from above

$$\underline{\nabla}\wedge(\underline{\nabla}\wedge\underline{E}) = -\mu_o\,\underline{\nabla}\wedge(\partial\underline{H}/\partial t) = -\mu_o\partial(\underline{\nabla}\wedge\underline{H})/\partial t$$

Since $\underline{\nabla}.\underline{E}=0$ and $\underline{\nabla}.\underline{B}=0$

$$\text{we get} \quad \nabla^2E = \mu_o\varepsilon\partial^2E/\partial t^2$$

$$\text{And similarly,} \quad \nabla^2H = \mu_o\varepsilon\partial^2H/\partial t^2$$

The last two expressions represent the wave equations for E and H with velosity $v=1/\sqrt{\varepsilon\,\mu_o}$. In a plane wave, E and H have their values constant over a plane (y,z) perpendicular to the direction of propagation x. Therefore $\partial/\partial y$ and $\partial/\partial z$ of E and

B vanish. Maxwell's equations become:

$$\partial E_x / \partial x = 0 \qquad \partial B_x / \partial x = 0$$

$$\partial B_x / \partial t = 0 \qquad \partial E_x / \partial t = 0$$

$$\partial E_z/\partial x = \partial B_y/\partial t \qquad \partial B_z/\partial x = -\mu_o \varepsilon \, \partial E_y/\partial t$$

$$\partial E_y/\partial x = -\partial B_z/\partial t \qquad \partial B_y/\partial x = \mu_o \varepsilon \, \partial E_z/\partial t$$

Let us now suppose that E is in the y direction and H in the z direction. Then E_y can be given as:

(I12)

$$E_y = E_{yo} \, e^{i\omega(t-x/v)}$$

$$v^2 = 1 / \mu_o \varepsilon$$

Using the above equation,

$$\partial B_z/\partial x = (\mu_o \, \partial H_z/\partial x =) - \mu_o \varepsilon \partial E_y/\partial t$$

we obtain that,

$$H_z = \sqrt{\varepsilon_o/\mu_o} \; E_y$$

The velocity v can be written as:

$$v = 1 / \sqrt{\varepsilon \mu_o} = c / \sqrt{\varepsilon/\varepsilon_o} = c/n'$$

where n' is the complex refractive index equal to:

$$n' = n + ik$$

Therefore equation I12 becomes now for the z-direction of propagation [7,6]:

$$E_{z,t} = E_0 \, e^{-kz/c} \, e^{i\omega(t-zn/c)}$$

The intensity of the light is given by:

$$I_z = I_0 \, e^{-2\omega kz/c}$$ and $2\omega k/c = a$ where a is the absorption coefficient

The equation of motion for electrons driven by a force $-eE_{t,z}$ is:

$$\ddot{x} + \gamma\dot{x} + \omega_o^2 x = -e/m \, E_{z,o} \, e^{i\omega t} \quad (\gamma = \text{damping constant})$$

with solution $$x_{z,t} = \frac{-(e/m) \, E_{o,z}}{(\omega_o^2 - \omega^2) + i\omega\gamma} \, e^{i\omega t} = x_{o,z} \, e^{i\omega t}$$

The polarisation is then $P_{t,z} = -\mathcal{N} e x_{o,z} e^{i\omega t}$ if there are $\mathcal{N}$ electrons/ unit volume. Further the susceptibility is $\chi = P/E$, where:

$$\chi = \frac{\mathcal{N} e^2 / m}{(\omega_o^2 - \omega^2) + i\omega\gamma}$$

But since $\varepsilon = \varepsilon_o + \chi$,

$$\varepsilon/\varepsilon_o = 1 + \frac{\mathcal{N} e^2}{2\varepsilon_o m\omega_o} \frac{1}{(\omega_o^2 - \omega^2) + i\gamma/2} \qquad \text{(I13)}$$

But $n' = \sqrt{\varepsilon/\varepsilon_o}$ and therefore:

$$(n')^2 = \varepsilon/\varepsilon_o = 1 + \frac{\mathcal{N} e^2}{2\varepsilon_o m\omega_o} \frac{1}{(\omega_o - \omega) + i\gamma/2}$$

Since $n' = n - ik$ and separating real from imaginary parts the following expressions are obtained assuming $|\omega_o - \omega| \ll \omega_o$ i.e. near an absorption line (using $\mathcal{N} = Nf$ where f is the oscillator strength and N is the number density)

$$n = 1 + \frac{1}{4\pi m\nu_o} \frac{e^2 Nf \quad (\nu - \nu_o)}{(\nu_o - \nu)^2 + (\gamma/4\pi)^2} \qquad \text{(I14)}$$

$$k = \frac{e^2 Nf}{mc} \frac{\gamma/4\pi}{(\nu_o - \nu)^2 + (\gamma/4\pi)^2} \qquad \text{(I15)}$$

These two equations are of great importance and will be used extensively in the sections to come. Going back to equation I13 it can be seen that if $|\omega_o^2 - \omega^2| \gg \omega\gamma$ then a formula of the form of Sellmeier's equation can be obtained:

$$n^2 = 1 + \frac{Ne^2}{\varepsilon_o m} \frac{1}{\omega_o^2 - \omega^2} = 1 + \frac{Ne^2}{\varepsilon_o m} \frac{\lambda^2 \lambda_o^2}{4\pi^2 c^2 (\lambda_o^2 - \lambda^2)} = 1 + \frac{A\lambda^2}{\lambda_o^2 - \lambda^2} \qquad \text{(I16)}$$

where A is a constant and n is real since absorption can be

neglected. This will be called the far-wing approximation equation for future reference.

7.Propagation of Plane Polarised Light in Active Media

Circularly polarised radiation travelling in the z-direction (+ sign for right circular polarisation and - sign for left circular polarisation) is given by the following expression (Buckingham [17])

$$\vec{E}_{+-} = E_0 \exp(i\omega(t-\hat{n}_{+-}z/c)) \ (\hat{i} \pm i\hat{j})$$

where $\hat{i},\hat{j}$ and $\hat{k}$ are the unit vectors of the x,y and z axes. Also the complex refractive index is:

$$\hat{n}_{+-} = n - ik$$

But since $E = E_+ + E_- = E_x i + E_y j$, the ratio E_x/E_y is:

$$E_x / E_y = \frac{\exp(-i(n_+-n_-)z\omega/c) + \exp((-k_+-k_-)z\omega/c)}{\exp(-i(n_+-n_-)z\omega/c) - \exp(+(k_+-k_-)z\omega/c)} =$$

$$\tan (\phi - i\theta) \qquad \text{(I17)}$$

$\Phi = \phi - i\theta$ is the complex magneto-optical angle.

(i) $\phi = \omega z(n_+-n_-)/2c$ represents the Faraday rotation which arises from the fact that the two Zeeman frequencies travel with different velocities in the medium (see section 8 of present chapter) and

(ii) $\theta = \omega z(K_+-K_-)/2c$ represents the ellipticity angle due to the fact that the two Zeeman components have different

absorption (MCD) (see section 9 of this chapter). In a field-free wavelength λ_o of a Lorentz doublet $k_+=k_-$ there is no dichroism, but in general dichroism and birefringence occur together.

The experimental set-up will be extensively discussed in Chapter II of this work but at this point it may be said that the main components of the experiment are a polariser and an analyser which are crossed. Thus, if a wave E_x exits the polariser, after it has crossed the analyser the only transmitted intensity will arise from a rotation to E_y. Therefore the expression (after some algebraic manipulations) is the following:

$$E_y E_y^* =$$

$$E_o^2\{(\exp(-k_+\bar{z}) - \exp(-k_-\bar{z}))^2 + 4\exp(-(k_++k_-)\bar{z})\sin^2((n_+-n_-)\bar{z}/2)\}$$

Relating k to the absorption coefficient a ($2\omega k_+/c=a_+$) and writting $\bar{z}=z\omega/c$ [7] the intensity can be written as:

$$I = \frac{I_o}{4}\{(\exp(-a_+z/2) - \exp(-a_-z/2))^2 + 4\exp(-(a_++a_-)z/2)\sin^2\phi\} \qquad (I18)$$

with expressions for a_+ and n_+ identical to equations I14 and I15 of section 6 of the present chapter. For reasons of clarity and convenience they will be stated again:

$$a_{+-} = \frac{e^2Nf}{mc}\frac{\Gamma_L / 4\pi}{(\nu_o - \nu \pm A)^2 + (\Gamma/4\pi)^2} \qquad (I19)$$

$$n_{+-} = 1 + \frac{e^2Nf}{4\pi m}\frac{1}{(\nu_o \pm \alpha)}\frac{(\nu_o - \nu \pm A)}{(\nu_o - \nu \pm \alpha)^2 + (\Gamma/4\pi)^2} \qquad (I20)$$

where $\alpha = eE/4\pi mc$ is the splitting of the Zeeman components and the B-field is in units of Gauss. Γ_L is the natural line width, $\Gamma_L = \delta\nu_L * 2\pi$ and for typical values of $\delta\lambda_L = 1.60\ 10^{-4}$A [7] and $\lambda_o = 2254$ A, Γ_L is about $4.50\ 10^8$Hz. Both formulae for the absorption coefficient and the refractive index for a line with only natural broadening are therefore given by formulae I19 and I20 in cgs units and shown in Figs.I13.

8.The Faraday Effect (Magnetic Optical Rotation)

Faraday discovered that when plane polarised light transverses a slab of glass in a direction parallel to the applied magnetic field its plane of polarisation is rotated by an angle ϕ given by [3]:

$$\phi = VHl \qquad (I21)$$

where l is the thickness of the slab (cm), V is the Verdet consta nt different for each medium and H is the magnetic field strength .

The Faraday effect is very closely related with the direct and inverse Zeeman effects. As mentioned in section 2 of this chapter when viewed along the field direction, left circularly polarised light with $\nu_o + \Delta\nu = \nu_1$ and right circularly polrised light with $\nu_o - \Delta\nu = \nu_2$ will be observed. For each component ν_1 and ν_2 the corresponding dispersion and absorption curves are shown in Fig.I9. From this figure it can be seen that for λ outside the ν_1 ν_2 region n^- is greater than n^+ and therefore positive rotations can travel faster than negative ones and the plane of polarisation is rotated in the positive direction. Similarly analogous arguments prove that between ν_1 and ν_2 the

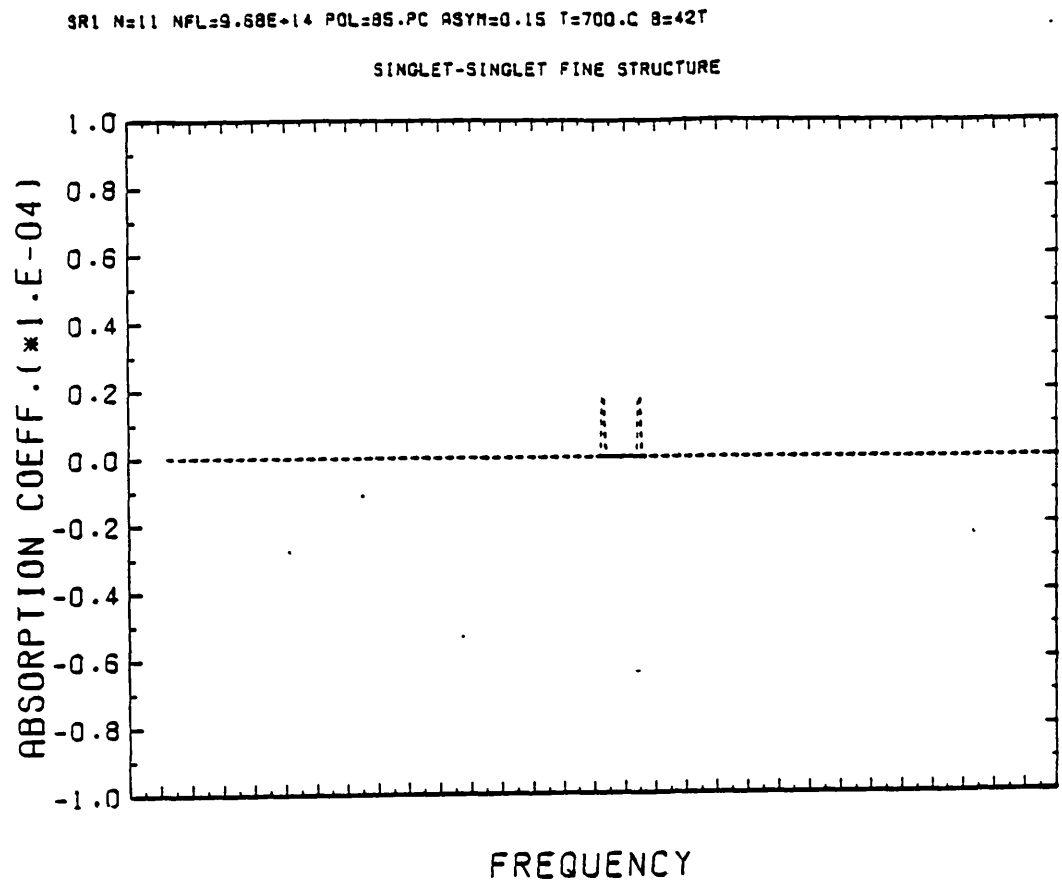

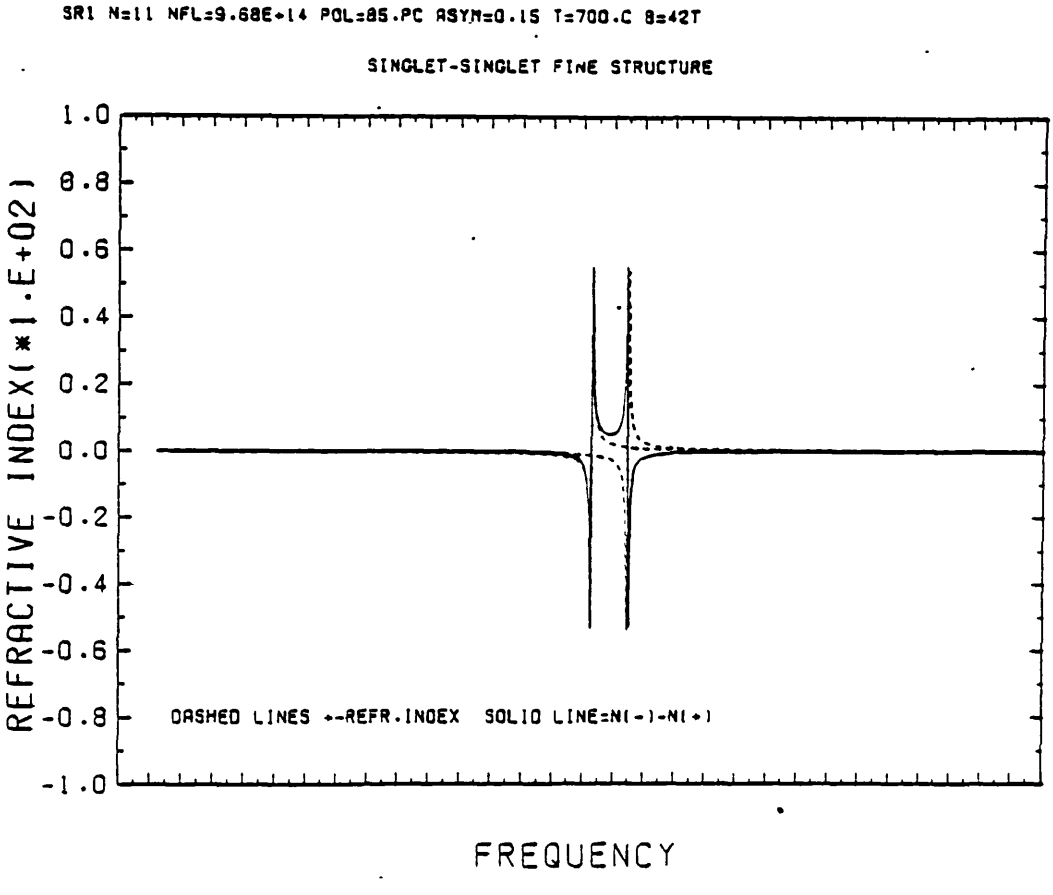

Fig.I13 The computed refractive index and absorption coefficient to be used in the magneto-optical calculations.

plane of polarisation is rotated in the negative direction [3].

9.Magnetic Circular Dichroism (MCD)

Magnetic circular dichroism occurs when the absorption coefficients of right and left circularly polarised light, k_+ and k_- respectively, in an absorption band are different under the influence of an externally applied magnetic field.

The ellipticity angle θ of a wave of circular frequency ω which was initially plane polarised, is defined as:

$$\theta = \omega/2c\ (k_- - k_+) \qquad \text{(I22)}$$

and the rotation angle ϕ (see the previous section of this chapter) is connected to θ and the complex rotation angle as:

$$\hat{\phi} = \phi - i\theta = \omega/2c\ (n_- - n_+) \qquad \text{(I23)}$$

where $\hat{n} = n - ik$ is the complex refractive index and n and k have their usual meanings. Buckingham and Stephens [11] have written a comprehensive review in which they show that MCD and the magnetic optical rotation (MOR) provides basic information about the symmetry of ground and excited states of molecules in the region of an absorption band. The aspects of their arguments which are relevant to atoms will be presented briefly in the rest of this section [11].

The electric displacement and the magnetic induction D and B respectively can be expressed as:

$$\underline{D} = \underline{E} + 4\pi \sum_a N_a \underline{m}_a \qquad \underline{B} = \underline{H}' + 4\pi \sum_a N_a \underline{\mu}_a \qquad \text{(I24)}$$

where $\underline{m}$ and $\underline{\mu}$ are the electric and magnetic moments

respectively and N_a is the number of molecules per unit volume in state a, which in turn can be expressed as:

$$\underline{m} = \alpha_o \underline{E} + \beta_o \underline{H}' + \alpha_1 (\underline{E} \wedge \underline{H}) + \beta_1 (\underline{H}' \wedge \underline{H})$$

$$\underline{\mu} = \gamma_o \underline{E} + \chi_o \underline{H}' + \gamma_1 (\underline{E} \wedge \underline{H}) + \chi_1 (\underline{H}' \wedge \underline{H}) \qquad \text{(I25)}$$

where $\underline{\alpha}$ and $\underline{\chi}$ are the electric and magnetic polarisability tensors and where H is the externally applied magnetic field. Using all the above expressions (equations I24 and I25) and the four Maxwell equations (equations I8 to I11) the complex refractive index of circularly polarised light near an absorption region for two states i and j was found to be equal to [11]:

$$n_{+-}(i \rightarrow j) = \frac{2\pi}{\hbar} N_i \hat{\chi}(\omega, \omega_o) \{\omega_o (|\langle i/m_x/j\rangle|^2 + |\langle i/m_y/j\rangle|^2)$$

$$\pm 2\omega \mathrm{Im}(\langle i/m_x/j\rangle \langle j/m_y/i\rangle)\} \qquad \text{(I27)}$$

$$\hat{\phi} = \omega/2c \sum_{i,j} (\hat{n}_- - \hat{n}_+)(i \rightarrow j) \qquad \text{(I26)}$$

where $\hat{X}(\omega_o, \omega_{oo}) = f(\omega_o, \omega_{oo}) - ig(\omega, \omega_o)$, where ω_o is the $i \longrightarrow j$ transition frequency and where $f(\omega, \omega_o)$ and $g(\omega, \omega_o)$ have the form of Fig.I10.

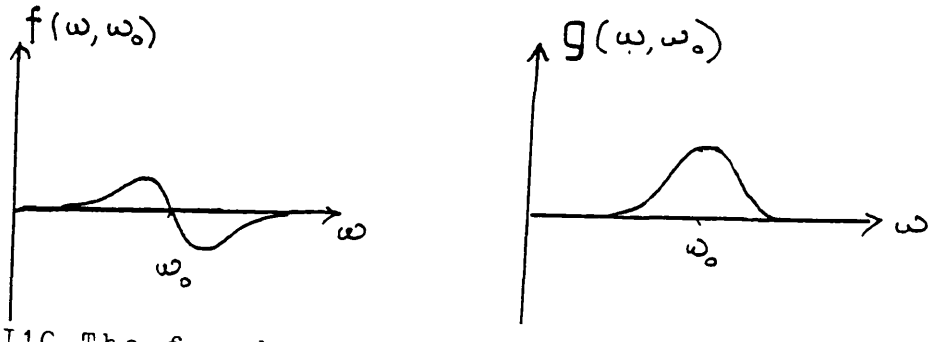

Fig.I1C The f and g quantities' curves [11] (where $\hat{X}(\omega, \omega_o) = f(\omega, \omega_o) - ig(\omega, \omega_o)$).

Then they [11] proceed to a more thorough quantum-mechanical treatment of the problem [13] and also attribute a certain shape to the $i \longrightarrow j$ line in question. They assume a line shape of the type of a damped oscillator ($\hat{X}=1/(\omega_o^2-\omega^2-i\omega\Gamma)$, Γ=FWHM for the $i \longrightarrow j$ line) but state that the exact spectral shape does not actually matter.

Outside an absorption band, the rotation was given by [13] as:

$$\phi(i\rightarrow j) = -\frac{4\pi}{\hbar c} N_a \left(\frac{2\omega_o \omega^2 A(i\rightarrow j)}{\hbar(\omega_o^2-\omega^2)} + \frac{\omega^2}{\omega_o^2-\omega^2}\left\{B(i\rightarrow j) + \frac{C(i\rightarrow j)}{kT}\right\}H_z\right)$$

where:

$$A(a\rightarrow j) = (\langle j/\mu_z/j\rangle - \langle a/\mu_z/a\rangle)\ \mathrm{Im}\{\langle a/m_x/j\rangle\langle j/m_y/a\rangle\}$$

$$B(a\rightarrow j) = \mathrm{Im}\sum_{k\neq a}\frac{\langle k/\mu_z/a\rangle}{\hbar\omega_{ka}^{(o)}}(\langle a/m_x/j\rangle\langle j/m_y/k\rangle - \langle a/m_y/j\rangle\langle j/m_x/k\rangle)$$

$$+\sum_{k\neq j}\frac{\langle j/\mu_z/k\rangle}{\hbar\omega_{kj}^{(o)}}(\langle a/m_x/j\rangle\langle k/m_y/a\rangle - \langle a/m_y/j\rangle\langle k/m_z/a\rangle)$$

$$C(a\rightarrow j) = \langle a/\mu_z/a\rangle\ \mathrm{Im}(\langle a/m_x/j\rangle\langle j/m_y/a\rangle)$$

Near an absorption band for well resolved lines but for unresolved Zeeman components, the rotation angle and ellipticity are respectively:

$$\phi(a\rightarrow j) = -\frac{4\pi}{\hbar c} N_a\left\{\frac{2\omega_o\omega^2((\omega_o^2-\omega^2)^2-\omega^2\Gamma_{ja}^2)\ A(a\rightarrow j)}{\hbar((\omega_o^2-\omega^2)^2+\omega^2\Gamma_{ja}^2)^2}\right.$$

$$+\frac{\omega^2(\omega_o^2-\omega^2)}{(\omega_o^2-\omega^2)^2+\omega^2\Gamma_{ja}^2}\left(B(a\rightarrow j)+\frac{C(a\rightarrow j)}{kT}\right)\}H_z \qquad \text{(I28)}$$

$$\theta(a\rightarrow j) = -\frac{4\pi}{\hbar c}N_a\{\frac{4\omega_o\omega^3(\omega_o^2-\omega^2)\Gamma_{ja}A(a\rightarrow j)}{\hbar((\omega_o^2-\omega^2)^2+\omega^2\Gamma_{ja}^2)^2}$$

$$+\frac{\omega^3\Gamma_{ja}}{(\omega_o^2-\omega^2)^2+\omega^2\Gamma_{ja}^2}\left(B(a\rightarrow j)+\frac{C(a\rightarrow j)}{kT}\right)\}H_z \qquad \text{(I29)}$$

while when the Zeeman components are well resolved:

$$\phi(a\rightarrow j) = -\frac{4\pi}{\hbar c}N_a\frac{\omega^2(\omega_o^2-\omega^2)}{(\omega_o^2-\omega^2)^2+\omega^2\Gamma_{ja}^2}Q_a(a\rightarrow j)$$

where $N_aQ_a(a\rightarrow j) = N_{ao}\{Q_{ao}(a\rightarrow j) + B(a\rightarrow j)H_z + C(a\rightarrow j)H_z/kT)\}$

and where $Q_{ao}(a\rightarrow j) = Im(\langle a/m_x/j\rangle\langle j/m_y/a\rangle$

For this case ($/\omega_o - \omega/ << /\omega_o H_z/$), ϕ versus ω has the form of Fig.I9c. Also, as H_z decreases ϕ increases because the lines merge closer together.

The basic aim of the MOR and MCD exercise is to find A,B and C for any $i \longrightarrow j$ transition which will then provide information about the i and j states. Further it might be preferable to calculate θ rather than ϕ since the first is easier to resolve in its components and also ϕ is more susceptible to background rotations.

In order to demonstrate the above facts, Buckingham and Stephens [11] give a simple example of a $^1P \longrightarrow {}^1S$ transition. The state ^1S is non- degenerate ($M_J=0$) while the ^1P is triply degenerate ($M_J=+-1,0$). Therefore equations I26 and I27 give that for no field $\hat{n}_+(^1P-{}^1S)=\hat{n}_-(^1P-{}^1S)$ and $\hat{\phi}(^1P-{}^1S)=0$. For $H_z \neq 0$, the three ^1P states are separated by $eB/4\pi mc$ (Fig. I11). The frequencies of the components are now different and Figs.I11 become Figs.I12. Another point is that the three ^1P ($H_z \neq 0$) levels can be related to the $^1P^M(H_z=0)$ level by the Boltzman relation:

$$N(^1P_{H_z \neq 0}) = N(^1P_{H_z=0})\ (1 - W(^1P_{H_z \neq 0})H_z/kT) \qquad (I30)$$

where $W(^1P^M)=-<{}^1P^M/M_z/{}^1P^M>=e\hbar M/(2mc)$.

$\phi(^1P-{}^1S)$ (to first order in H_z) contains information about the A,B and C terms. The A term occurs when either the initial or the final states of the transition are split by the field, the C term occurs when the ground state is degenerate (and this term is temperature dependent) and finally the B term occurs from the perturbation of the initial and final state

wavefunctions by the magnetic field, which causes them to mix with the other states [11].

The basic principles stated above have been extensively applied to the analysis of molecular spectra. However, for atoms direct observation of the Zeeman effect provides a simple and complete determination of J-values and MOR and MCD have therefore received less attention in connection with symmetry. Another aspect of MCD and MOR is the study of f-values which is the main subject of the present thesis.

10. Absorption and Dispersion Relations for a Line with a Voigt Profile

If the velocity distribution of electrons is Maxwellian, then:

$$P(\xi)\, d\xi = \frac{1}{\sqrt{\pi}\ \xi_o} \exp\ (-\xi/\xi_o)^2\, d\xi$$

is the probability of finding an electron with velocity ξ in the range $(\ \xi\ ,\ \xi+d\xi\ )$. Also $\xi_o=(2KT/m)^{1/2}$. If the observer observes at a frequency ν_1, an atom with velocity ξ absorbs at a frequency $\nu - \xi\nu/c$ [10]. Therefore, the absorption coefficient and the refractive index for a line with a Voigt profile are found by convolving the Lorentzian over a Gaussian, as follows:

$$a_{+-}(\nu)^{Voigt} = \int_{-\infty}^{+\infty} a_{+-}^{LOR}(\nu - \xi\nu/c)\ P(\xi)\ d\xi$$

$$n_{+-}(\nu)^{Voigt} = \int_{-\infty}^{+\infty} n_{+-}^{LOR}(\nu - \xi\nu/c)\ P(\xi)\ d\xi$$

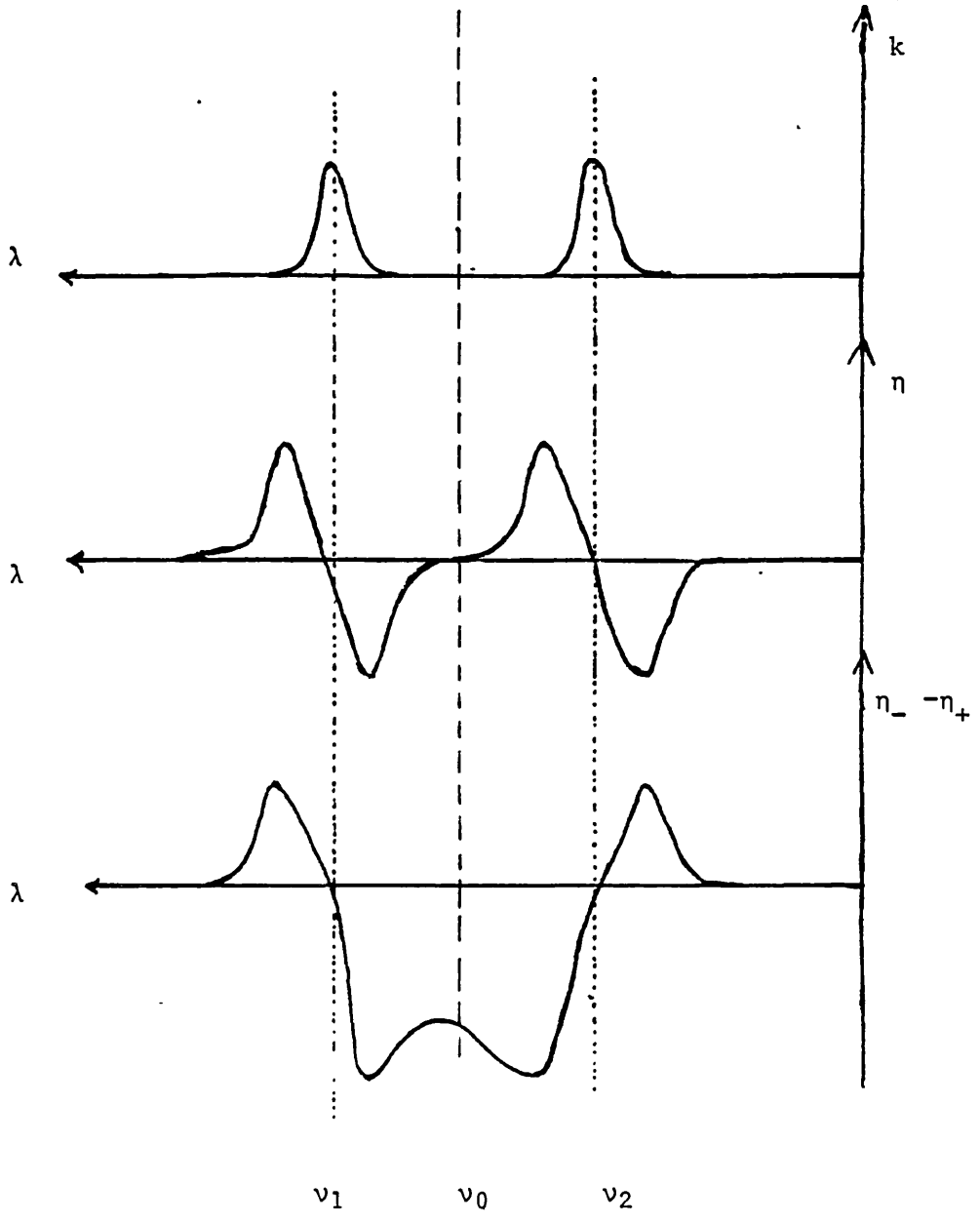

Fig.I9 Refractive index and absorption coefficient curves used to explain the Faraday effect shown in Fig.I8.

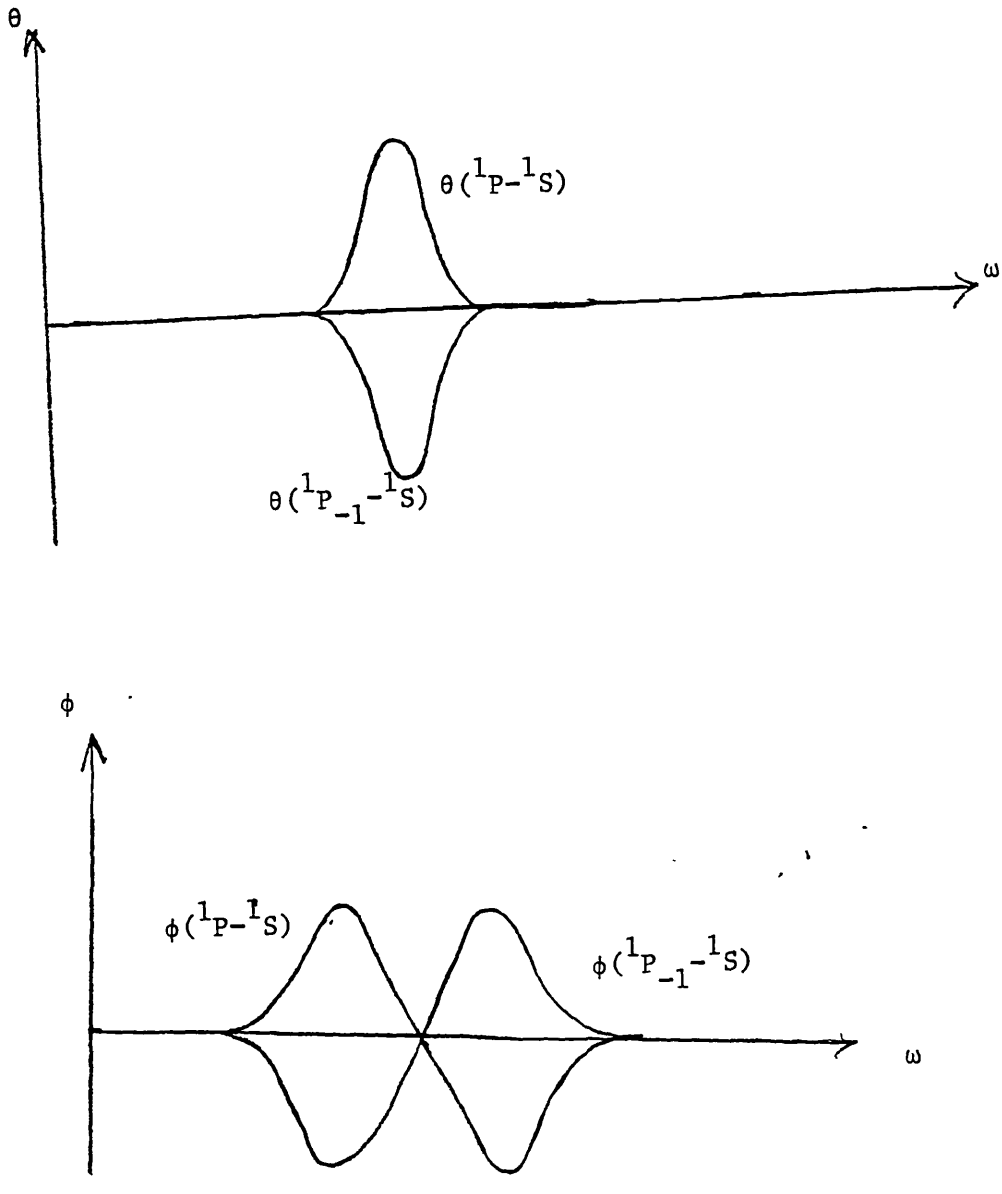

Fig.I11 The Faraday rotation and ellipticity angle curves for the ^1P-^1S transitions in the absence of a magnetic field [11].

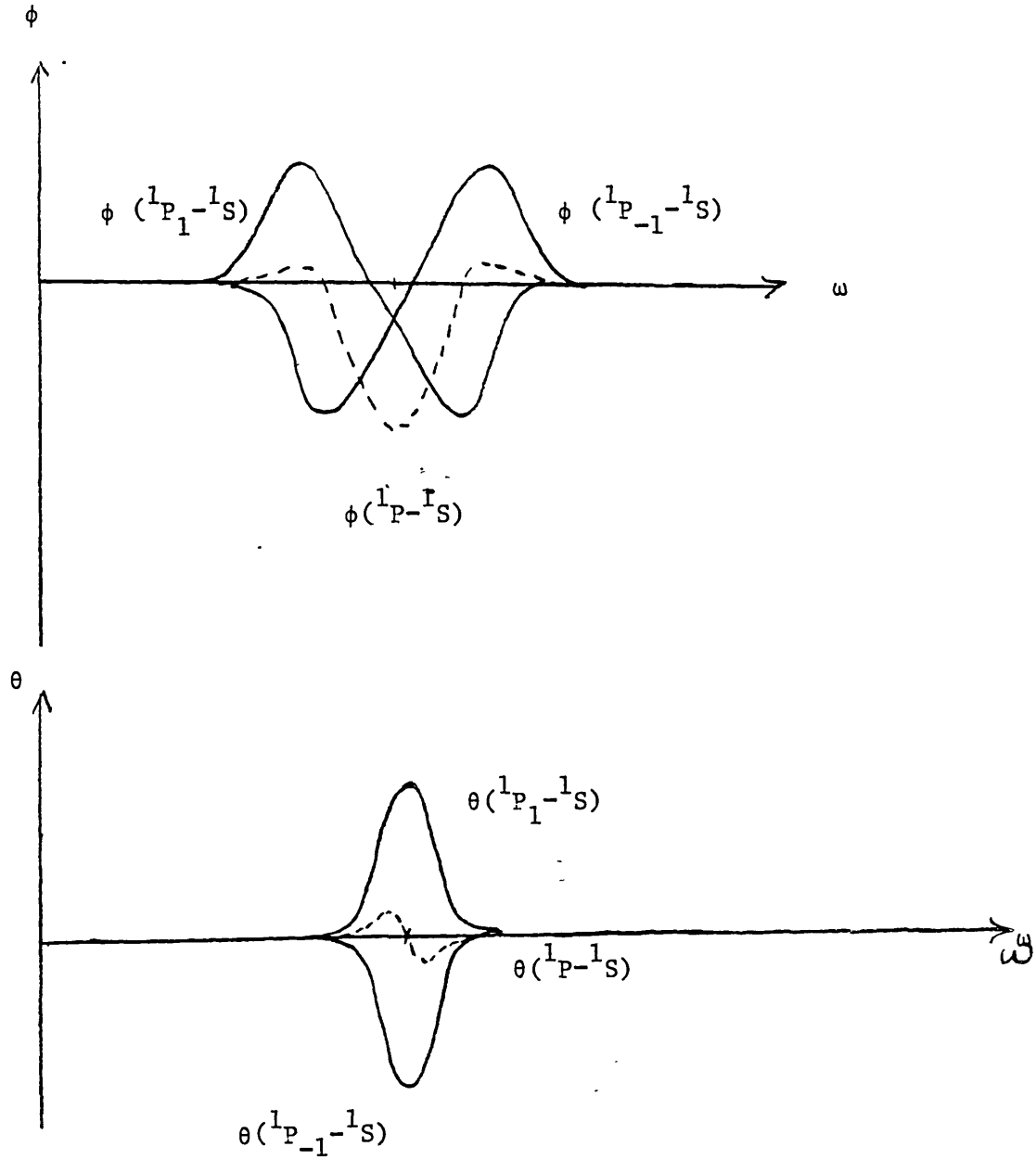

Fig.I12 The Faraday rotation and ellipticity angle curves for the ^1P-^1S transitions in the presence of a magnetic field [11].

After some algebra, the following expressions are obtained:

$$a_{+-}(\nu)^V = \frac{e^2 Nf}{\Delta\nu_D\, mc} \frac{\gamma}{\sqrt{\pi}} \int_{-\infty}^{+\infty} \frac{e^{-y^2}\, dy}{\{(\bar{\nu} \mp \bar{\alpha}) - y\}^2 + \gamma^2} \qquad \text{(I31)}$$

and

$$n_{+-}(\nu)^V = 1 - \frac{e^2 Nf}{4m\,(\nu_o \mp \alpha)\,\Delta\nu_D} \frac{1}{\pi^{3/2}} \int_{-\infty}^{+\infty} \frac{e^{-y^2}\,\{(\bar{\nu} \mp \bar{\alpha}) - y\}\, dy}{\{(\bar{\nu} \mp \bar{\alpha}) - y\}^2 + \gamma^2} \qquad \text{(I32)}$$

where

$$\gamma = \frac{\Gamma}{4\pi\,\Delta\nu_D} \quad , \quad y = \frac{\nu' - \nu_o}{\Delta\nu_D} \quad , \quad \bar{\alpha} = \alpha / \Delta\nu_D \quad , \quad \alpha = \frac{eB}{4\pi mc}$$

and $\bar{\nu} = \nu - \nu_o / \Delta\nu_D$ is the detuning expressed in Doppler widths, $\Delta\nu_D = \nu_o v/c$ and ν' is the variable of integration. As a special case if $\Delta\nu_D >> \Gamma_L$ the Voigt profile resembles a Gaussian and the resulting expressions for a and η would be those corresponding to a Gaussian line profile.

In a recent publication, Hui et al [14] have studied the rapid computation of the Voigt and Complex Error functions. The Complex Error function is:

$$p(z) = e^{-z^2} \left(1 + \frac{2i}{\sqrt{\pi}} \int_0^z e^{t^2}\, dt \right)$$

and they also state that:

$$p(z) \begin{cases} P(z) & \text{if } Im(z) > 0 \\ P(z) + 2e^{-z^2} & \text{if } Im(z) < 0 \end{cases}$$

where

$$P(z) = \frac{i}{\pi} \int_{-\infty}^{+\infty} \frac{e^{-t^2}}{z - t}\, dt$$

By substituting z=s-x+iy , the expression for P(z) is obtained:

$$P(z) = \frac{y}{\pi} \int_{-\infty}^{+\infty} \frac{e^{-t^2}\, dt}{\{(s - x - t)^2 + y^2\}} + i \frac{1}{\pi} \int_{-\infty}^{+\infty} \frac{e^{-t^2}\,(s - x - t)\, dt}{\{(s - x - t)^2 + y^2\}}$$

(I33)

Thus, so far it has been shown that for Im(z)>0 the Complex Error function can take the form of the above equation with clearly separated real and imaginary parts. Hui et al [14] equate in their calculations the Complex Error funcion to a quotient of the form:

$$P(z) = \frac{\sum_{i=0}^{p} a_i x^i}{x^{p+1} + \sum_{i=0}^{p} b_i x^i} \qquad \text{(I34)}$$

and the fits which they obtained for p=3 and p=5 give a maximum relative error of $1.67\ 10^{-6}$ and $1.11\ 10^{-9}$ at reference points chosen between 0 and ∞ .

When this method is coded up and inserted into the computer, taking also advantage of the computer's capability to decompose a complex expression into real and imaginary parts, the real and imginary parts of a Voigt function were obtained. The real part represented the absorption coefficient and the imaginary the refractive index. Then $a_+(\nu)$ and $n_+(\nu)$ were inserted into the formula obtained for the evaluation of the intensity (equation I18).

Hui et al [14] have tabulated values of a_i and b_i for p=5 and p=6. In this work the above formulae (equations I23 and I24) were used to calculate the Voigt expresions with p=6 and the results agreed to 5 decimal figures with the values listed in tables of Abramovitch and Stegun [16]. As a concluding comment to this chapter, the intensity obtained from the above calculations has to be convolved with an apparatus function -taking also into account some other effects which will be discussed in Chapter III- in order to obtain a correct and realistic expression for the intensity of radiation observed on the photographic plate.

The relevance of the ideas introduced in this chapter to experiments recently performed by the Bonn/Imperial College group is explored in greater detail in the next two chapters.

REFERENCES FOR CHAPTER I

General:

1. "Light" by R.W. Ditchburn (Blackie & Son 1955)

2. "Principles of Optics" by M. Born and E. Wolf (Pergamon Press 1965)

3. "Fundamentals of Optics" by F.A. Jenkins and H.E. White (McGraw-Hill 1957)

4. "Elementary Atomic Structure" by G.K. Woodgate (Clarendon Press 1980)

5. "Atomic Spectra" by Kuhn H.G. (Longmans 1962)

6. "Introduction to Atomic Spectra" by H.E. White (McGraw-Hill 1934)

7. "Spectrophysics" by A.P. Thorne (Chapman and Hall 1974)

8. "Electromagnetism" by I.A. Grant and W.R. Phillips (John Wiley and Sons 1975)

9. "Electricity and Magnetism" by W.J. Duffin (McGraw-Hill 1973)

10. "Stellar Atmospheres" by D. Mihalas (W.H. Freeman and Co. 1978)

Special:

11. Buckingham A.D. and Stephens P.J. Ann. Rev. of Phys. Chem., 17, 399 (1966)

12. Stephens P.J. Ann. Rev. of Phys. Chem., 25, 201 (1974)

13. Serber R. Phys. Rev., 41, 489 (1932)

14. Hui A.K., Armstrong B.H. and Wray A.A. J. Quant. Spec. Rad. Transf., 19, 509 (1978)

15. Connerade J.P., J. Phys B., 16, 399 (1983)

16. "Handbook of Methematical Functions" by M. Abramovitch and I.A. Stegun (Nat. Bur. of Standards AMS 55)

17. Buchingham A.D. Symposia of the Faraday Society (1970)

18. Faraday M, Series 3 153 249 (1846) Phil. Magazine 294 (1846)
Experimental Resear. 19th series
Philos. Trans. 1846 VolCXXXVI

19. Lorentz H. La Theorie Electromagnetique de Maxwell (Leydon 1892)

20. Zeeman P. Phil. Magazine Series 5 43 226 (1897)

21. "Resonance Radiation and Excited Atoms" by A.C.G Mithell and M.W.Zemansky (Cambr. Univer. Press 1979)

22. Connerade J.P., Garton W.R.S., Baig M., Hormes J., Stavrakas T.A. and Alexa B. J.de Physiq. C2 43,317(1982)

23. Garton W.R.S., Connerade J.P., Baig M., Hormes J. and Alexa B. J.Phys. B 16 389 (1983)

Chapter II

Background Experiment

1.The Experimental Set-Up

The experiments, the results of which are analysed in the present thesis, were performed by a team from Imperial College and Bonn University on a collaborative project. The object of the present thesis is to present suitable computational methods which were developed for the reduction of the data. We sought to extract as reliable relative f-values as possible, and to make suggestions to improve future experiments in the light of our detailed analysis. The experimental background is as follows: the measurements were performed at the 500 MeV electron synchrotron of the Physikalishes Institute in Bonn, where a laboratory specialising in high resolution VUV spectroscopy has been set up in collaboration with the Blackett Laboratory. The main experimental set-up is shown in Fig.II1.

The source of radiation is an electron synchrotron. Synchrotron radiation is electromagnetic radiation that charged particles emit when they move on circular orbits with highly relativistic velocities. The following are important advantages of Synchrotron Radiation (SR) as a spectroscopic source in the current experiment where photon wavelengths shorter than the visible are involved (Kunz[1]).

a) Linear polarisation with E parallel to the orbital plane (for the present experiments, this was the crucial property).

b) Circular polarisation above and below the orbital plane.

c) The emited radiation is collimated in the instantaneous

direction of flight of the emitting particles (the angular spread is about 1 mrad) and

d) The spectral distribution of the source can be calculatedand and is substantially 'flat' in the wavelength range of interest.

In recent years several publications have dealt with the quantitative properties of SR. In a review paper, Kunz [1]gives the equation of the radiated power off all the orbit in a wavelength $d\lambda$ and an azimuthal angle $d\psi$ to be (ψ is the azimuthal angle, see Fig.1.3 of [1]):

$$I(\lambda,\psi) = \frac{27}{32\,\pi^3}\,\frac{e^2c}{R^3}\left(\frac{\lambda_c}{\lambda}\right)^4 \gamma^8\,(1+(\gamma\psi)^2)^2\left\{K^2_{2/3}(\xi)+\frac{(\gamma\psi)^2}{1+(\gamma\psi)^2}\,K^2_{1/3}(\xi)\right\}$$

where (III)

$\lambda_c := \frac{4\,\pi R}{3}\,\gamma^{-3}$ is the characteristic wavelength

$\xi = \frac{\lambda_c}{2\,\lambda}\,(1+(\gamma\psi)^2)^{3/2}$, $\gamma = E/mc^2$

R=radius of curvature, $k_{1/3}, k_{2/3}$= Modified Bessel functions of the Second Kind.

This equation integrated over all azimuthal angles ψ yields:

$$I(\lambda) = \frac{3^{5/2}}{16\,\pi^2}\,\frac{e^2c}{R^3}\,\gamma^7\left(\frac{\lambda_c}{\lambda}\right)\int_{\lambda_c/\lambda}^{\infty} dn\; K_{5/3}(n)$$

from which it is obvious that the total power per electron , per

second and per unit wavelength interval depends only on λ / λ_c, R and E and therefore a computer program can calculate $I(\lambda)$ for any SR machine or any geometry. Equation II1 can also be integrated over all wavelengths to give the power distribution in ψ :

$$I(\psi) = \frac{e^2 c}{R^2} \gamma^5 (1 + (\gamma\psi)^2)^{-5/2} \left(\frac{7}{16} + \frac{5}{16} \frac{(\gamma\psi)^2}{1 + (\gamma\psi)^2}\right)$$

Integrating equation II1 over ψ and λ , the following is obtained:

$$I_{tot} = \frac{2}{3} \frac{e^2 c}{R^2} \gamma^4$$

Futher Kunz [1] gives the following very useful relations. The angular spread $\Delta\psi$ can be approximated as:

$\Delta\psi = 2/\gamma \, (\varepsilon_c / \varepsilon)^{1/3}$ for $\varepsilon \ll \varepsilon_c$ and $\varepsilon_c = hc/\lambda_c$

and $\Delta\psi = 2/\gamma \, (\varepsilon_c / \varepsilon)^{1/2}$ for $\varepsilon \gg \varepsilon_c$

and also that the total power radiated is:

$$I(\text{Watt}) = 88.5 \, E^4(\text{GeV}) \, j(\text{mA}) \, / \, R(\text{m})$$

where j is the current.

In other papers on SR, originally Schott [2] and then Schwinger [3] stated that synchrotron is linearly polarised in

the orbital plane while the radiation emited into directions above or below it is elliptically polarised with a high percentage of circular polarisation. Heinzman et al [4] have measured experimentally the absolute intensity and the circular polarisation of SR for wavelengths 40 to 100 nm. They found that

the intensity distribution of circularly polarised light in the vertical plane has a FWHM of 3 mrads. They also

found that the intensity decreases as a function of the vertical angle ψ (see Fig.3 of [4] and also Fig.1.3 of [1]) (both results were for λ =100nm). Further they show that the fraction of circular polarisation stays almost constant as a function of λ (at about 80%) depending only on the range of ψ and that it rises from about 75% to 100% as ψ goes from 0 to 2.5mrads. The problems of the dependence of circular polarisation on λ and of having a slight admixture of elliptically polarised light in the incident beam will be connected with the analysis of the results presented in the following chapters and will receive there more attention. Let us now return to the description of the experimental set-up.

The continuum radiation (mostly plane polarised with inevitable fractions of + and - circular polarisation) leaves the 500 MeV synchrotron and is collected by a 65cm long cylindrical bent mirror which focuses only in the horizontal plane. Then the light falls on the vertical slit of a 3-metre normal incidence out-of-plane Eagle spectrograph designed by R.C.M.Learner (1965) and manufactured at Imperial College. It has a 5000 line/mm Jobin-Yvon Al+Mg_2 overcoat holographic grating of 10cm which disperses in the horizontal plane. The

exposure times are in the range of seven minutes to two hours on Kodac SWR plates depending on the level of absorption. Calibration in wavelength was achieved by superposing various emission spectra on the magneto-optical patterns. The resolution of the grating is considered to be the highest currently available in first order. It was vital to be able to obtain the highest resolving power (the instrumental limit is 300000 but in this case it was less because the apparatus function was affected by factors independent of the spectrograph -this will be discussed in a following chapter) because the large grating tilt in the horizontal plane made the optical system very sensitive to the angle between the plane of polarisation of the incident radiation and the rulings of the grating surface.

In this experimental arrangement [8] the radiation emerging from the synchrotron (after being collected by the cylindrical mirror as mentioned above) can be regarded as the radiation emerging from the polariser of the standard experimental set-up for Faraday rotation studies. The diffraction grating of the spectrograph can be regarded as the analyser. Therefore, in principle, with both components 'crossed', no emerging light should be observed (however there will be some because of instrumental imperfections). Furthermore, this is achieved with one optical component (the grating) and no transmission optics. Between the synchrotron and the cylindrical mirror, a superconducting magnet was inserted. In the warm bore of the 50cm-long magnet a wire-wound furnace was used as an absorption cell. As mentioned in an earlier chapter, the plane of polarisation of the light begins to rotate upon its entry in the cell under the influence of the magnetic

field (Faraday rotation). Therefore, the polariser and the analyser will not always be 'crossed', but there will be intensity oscillations in the magneto-optical spectra depending on the rotation that the plane of the light suffered in the cell. It must also be noted that in the standard MOR experiments, the angles of rotation are small (only a few degrees) whereas, in the present instance, angles of many π lead to oscillations of intensity.

The following test was performed to check the polarising efficiency of the grating. A wedge of crystalline quartz with the optical axis running towards the apex, an approximate thickness of 5mm at the centre and an angle between the faces of about 1 min.of the arc was mounted just in front of the spectrograph slit with the axis at 45° to the vertical. The difference between n_+ and n_- (the refractive index for right- and left-hand circularly polarised light in crystalline quartz is approximatelly constant as a function of λ between 2000 and 2500 A). Thus, the optical path difference between positively and negatively polarised light is given by:

$$t (n_+ - n_-) = (n^* + 1/2) \lambda$$

where n^* is an integer (274 for 2190 A) for the plane of polarisation to be rotated by $\pi/2$. Since a wedge was used (instead of a slab or a plate), the fringes had a slope and from this and other data it was estimated that the polarising efficiency of the holographic grating in question was approximately 75%.

The present experiment has been performed on SrI, MgI and BaI as those elements possess singlet principal series and can

exhibit the simple Lorentz doublet. The magnet used is capable of producing fields up to 6.0T. The temperatures of the vapours in the furnace are between 500 C and 1000 C (corresponding to particle densities of about 10^{16} cm^{-3}).

2.Basic Principles of the Magneto-Optical Method

A typical magneto-rotation pattern obtained from the experiments being carried out in Bonn is shown in Fig.II2a. In the middle of the pattern the Lorentz doublet is prominent. On either side of the two Lorentz components the intensity oscillates symmetrically about the field-free resonance wavelength λ_0 and thus the magneto-optical beats are produced. In the experimental set-up, the polariser and the analyser are seen to be crossed (Fig.II1) and as the plane polarised light emerges from the synchrotron and passes through the high density vapour (which is contained between the poles of a magnet) it has its plane of polarisation rotated, according to the Faraday effect, by many turns towards the centre of the absorption lines. So, as the profile is scanned in frequency, the emerging light has its plane of polarisation rotated by integral multiples of $\pi/2$ at different points on the profile due to the fast change in rotation angle as the line is transversed. Starting from the far-wing of the line and moving towards the zero-field line centre, ϕ (the rotation angle) rises from zero to high values and the crossed polarisers transmit a series of "intensity oscillations" which algebraically are represented by equation I18 by the funcion $\sin^2\phi$. As a consequence the electric vector (intensity of radiation) oscillates between the maximum and minimum values.

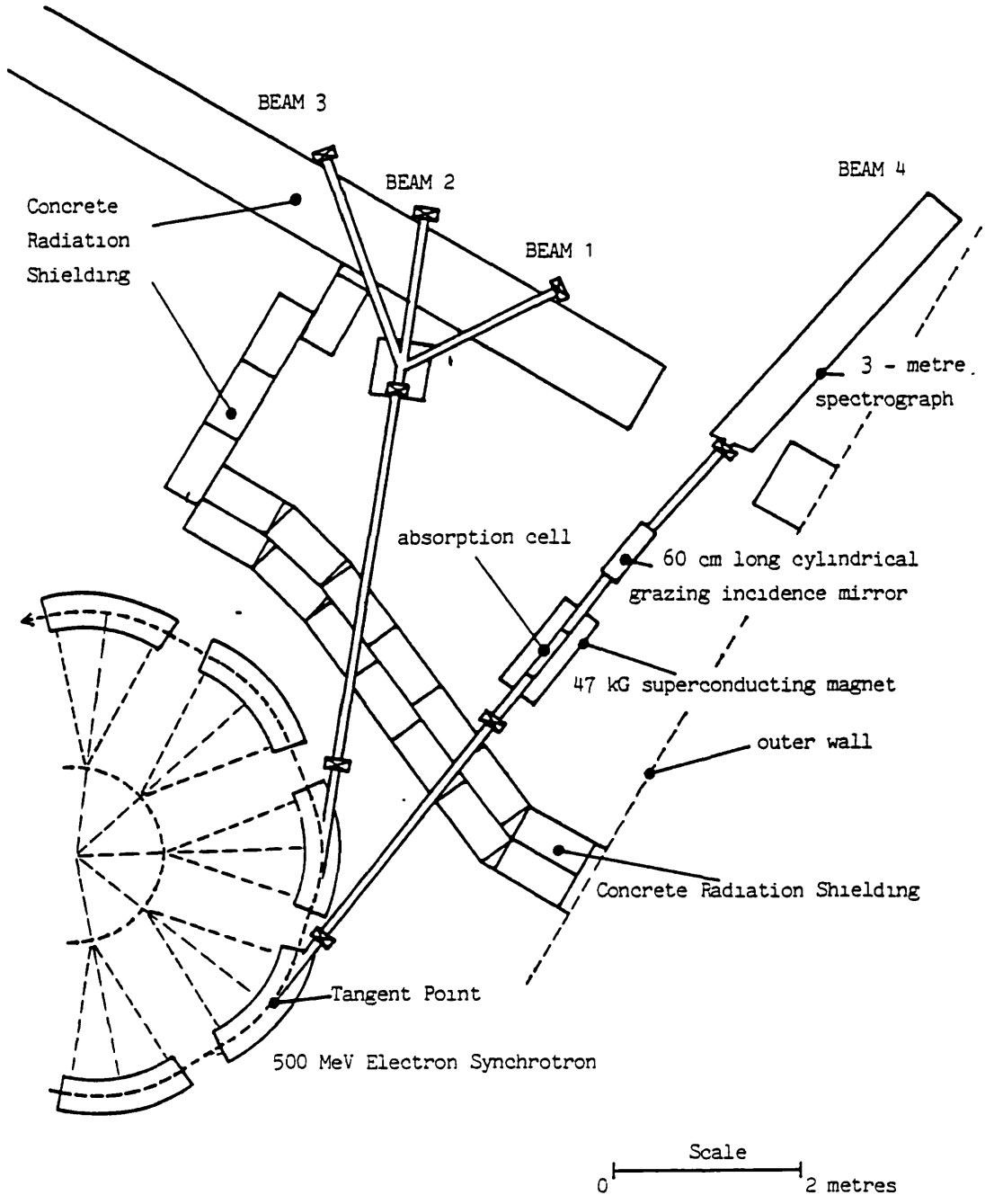

Fig.II1 The experimental set-up for the magneto-optical studies in the Physikalisches Institute in Bonn.

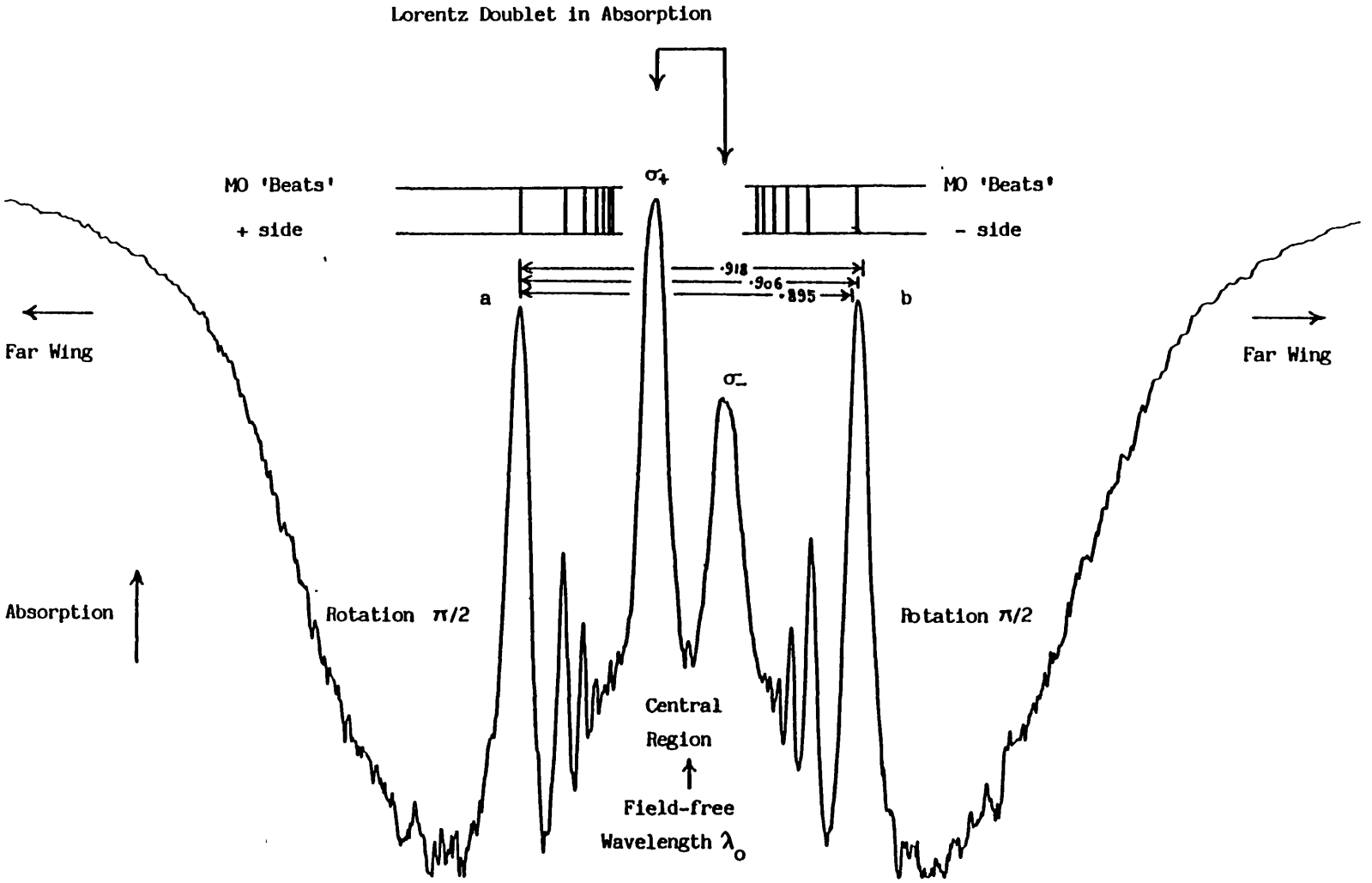

Fig.II2a An experimental magneto-optical spectrum (for n=11 in SrI).

The expressions derived in Chapter I for the intensity transmitted and for the refractive index and absorption coefficient will be restated here for reasons of convenience (see equations I18, I31 and I32):

$$I = \frac{I_o}{4}\{(\exp(-a_+ z/2) - \exp(-a_- z/2))^2 + 4\exp(-(a_+ + a_-)z/2)\sin^2\phi\} \tag{II2}$$

$$a_{+-}(\nu)^V = \frac{e^2 Nf}{\Delta\nu_D\, mc}\frac{\gamma}{\sqrt{\pi}}\int_{-\infty}^{+\infty}\frac{e^{-y^2}\,dy}{\{(\bar{\nu}\mp\bar{\alpha}) - y\}^2 + \gamma^2} \tag{II3}$$

$$n_{+-}(\nu)^V = 1 - \frac{e^2 Nf}{4m\,(\nu_o \mp \alpha)\,\Delta\nu_D}\frac{1}{\pi^{3/2}}\int_{-\infty}^{+\infty}\frac{e^{-y^2}\{(\bar{\nu}\mp\bar{\alpha}) - y\}\,dy}{\{(\bar{\nu}\mp\bar{\alpha}) - y\}^2 + \gamma^2} \tag{II4}$$

from which it can be seen that the intensity formula contains the product NfzB (N is the particle density, f is the oscillator strength, z is the length of the furnace and B is the magnetic field strength). The aim of the calculations in the present work is to obtain a value of NfzB for several members of the Rydberg series, recorded under identical experimental conditions. Relative f-values will be therefore deduced since the quantities N, z and B cancel out. Obviously, knowledge of the exact value of N, z and B is not required although they must be held constant during the experiment. An appropriate value of B, z and N (see below) is of cource required for the calculations. A typical spectral pattern of these calculations is shown in Fig.II2b. There are several approaches to the determination of f- values from magneto-optical spectra.

The first is the far-wing approximation first given by

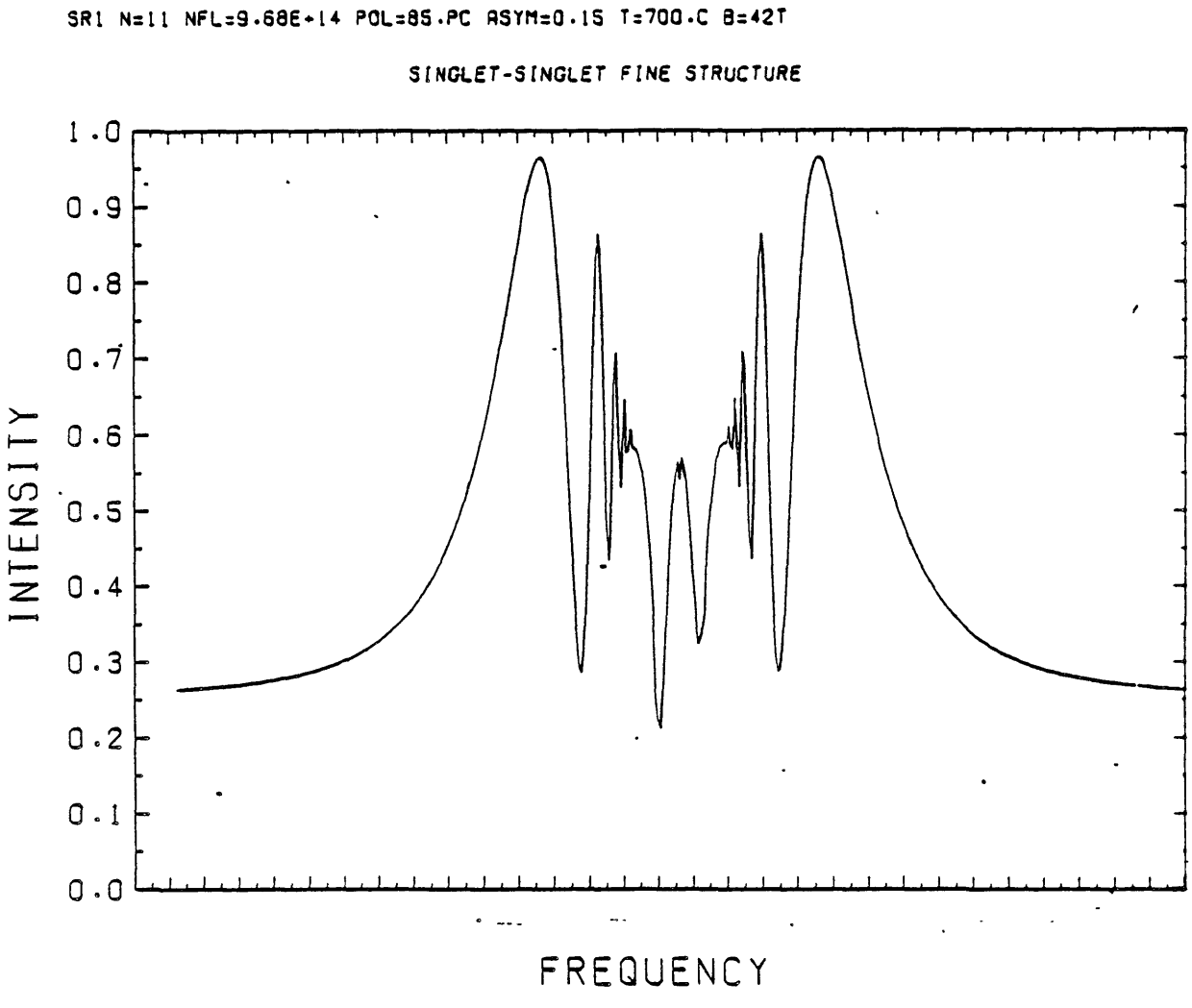

Fig.II2b A theoretical magneto-optical spectrum (for n=11 in SrI).

Mitchell and Zemansky [7]. They relate the rotation angle to N,f,z,B and ν_o (the field-free central frequency) as follows:

$$\phi = \frac{Nfz\ Be^3}{8\pi\ m^2\ c^2} \frac{1}{(\nu - \nu_o)^2} \qquad \text{(II5)}$$

the similarity of this equation with equation I16 is obvious. Equation II5 holds for $\Gamma_L/4\pi \ll eB/4\pi mc \ll \nu_o - \nu$ where Γ_L was defined in Chapter I. From Figs.II2 it can be seen that towards the wings of the line the rotation tends to zero whereas moving in towards its centre the rotation increases until, at $\pi/2$, the transmission through the crossed polarisers is maximum. Moving further towards the line centre, the magneto-optical beats of π ,$3\pi/2$, 2π etc are obtained. Therefore the rotation can be determined, and the accuracy of determination is better for the π peak than for the $\pi/2$ as the first one is sharper and the accuracy of measurement of its exact position is far better. Also, the rotation angles are independent of most non-linearities in emulsion responce which effect relative intensity calculations.

However there are a few reasons for this method not being the most accurate one in determining relative f-values from magneto-optical spectra. These reasons will now be presented (Connerade [6]):

(a) The far-wing formula given by Mitchell and Zemansky [7] stated above, holds best for the outermost rotation peak. But since that one is the broadest it can give information of very poor accuracy.

(b) Connerade [6] has plotted the rotation angle versus frequency, in Fig.2 of that publication, and shows that "under the most ideal conditions only the outermost three or four points can be fitted in this way at the available field strengths". Therefore, there are systematic errors in this analysis which is based on the least accurately determined data.
(c) A careful observation of the experimental spectrum obtained (Fig.II2) shows that regions other than the far-wing, especially the region between the Lorentz doublet, is very sensitive to changes in NfzB.
(d) And finally , the far-wing approximation cannot be applied to partially resolved patterns. These patterns will be discussed in more detail further below in this section.

The second approach is based on the relations for the intensity and for the refractive index and absorption coefficient for a Voigt profile presented in Chapter I and restated in the begining of this section. The intensity must also take into account the polarisation efficiency of the grating, the asymmetry between the two Lorentz components and then it must be integrated over an appropriate apparatus profile. These facts will be discussed in some detail in Chapter III.

As mentioned earlier in this section, the final formula of the intensity will include the product NfzB. An appropriate value for the polarisation, the asymmetry, the width of the apparatus funcion and NfzB are initially inserted as data in the program inserted into the computer to calculate and produce graphically the intensity spectrum. The polarisation, the asymmetry and the FWHM of the apparatus function will be given

the correct value for a certain profile after some trials as they affect a particular part of the spectrum in a certain way (a complete discussion of the choice of their correct values will be postponed until Chapter III). Therefore, only the product NfzB remains to be manipulated for the correct reproduction of the experimentally obtained magneto-optical spectra (using the calculated formulae). In other words, most of the parameters involved in these calculations are held constant from one profile to the next for different profiles recorded on the same plate for identical experimental conditions (minor exceptions to this statement will be discussed in the following chapter). Thus, NfzB must be determined for each profile separately. The difficulty of determining the correct value of NfzB was overcome with the following approach.

The third approach is the Magneto-Optical Vernier technique (MOV) (Connerade [6]). This method is based on the behaviour of the computed spectrum with the variation of the product NfzB. There are two different rates that different parts of the profiles differ. Firstly in the far-wing the pattern varies slowly, moving slightly away from the field-free line centre as NfzB increases (this is in agreement with the far-wing expression given above). Relative intensities remain almost constant as long as the magneto-optical intensity oscillations are outside the Lorentz components. Secondly, in the region between the Lorentz doublet where the rotation angles become much larger, the relative intensities vary very rapidly with the variation of NfzB represented by the $\sin^2 \phi$ factor in equation II2. A demonstration of these facts is given in Fig.II3. In this diagram the x- and y-axes represent the region of the spectrum

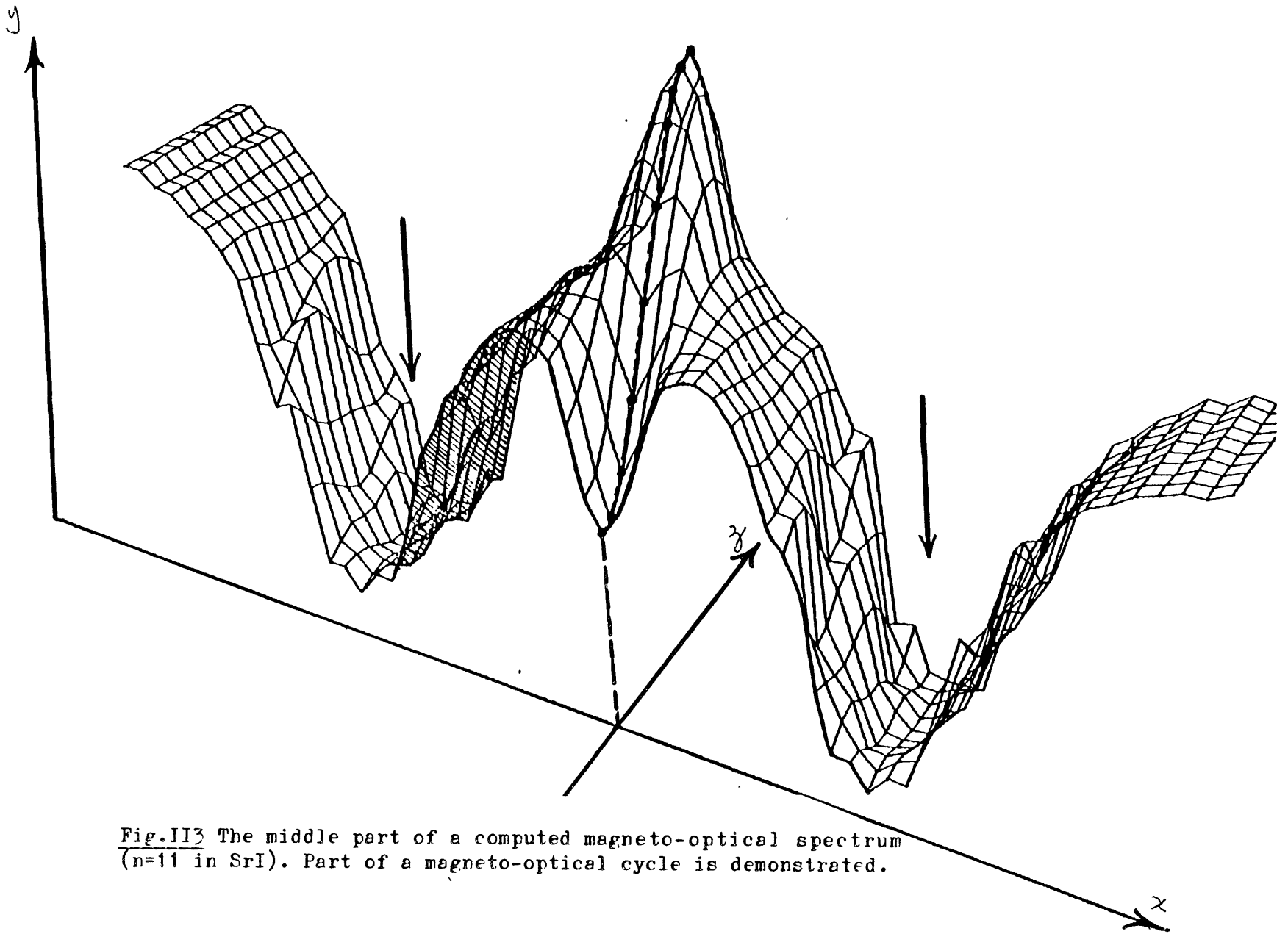

Fig.II3 The middle part of a computed magneto-optical spectrum (n=11 in SrI). Part of a magneto-optical cycle is demonstrated.

between the Lorentz doublet (the x-axis is the frequency and the y-axis is the intensity) and the z-axis is the product NfzB. One period of the fluctuation of NfzB will be refered to as a magneto-optical cycle.

To recapitulate the method used in this piece of work in determining relative f-values the following steps were followed. (i)From the outer parts of the line profile, and with the aid of the far-wing formula NfzB can be determined roughly -to correctness of an order of magnitude. (ii)Afterwards, several magneto-optical cycles are plotted in order to find out whether the values used for NfzB to produce a spectrum cover a magneto-optical cycle. (iii)At the same time, the computer program is made to calculate and write out the actual frequency (or wavelength) distance form the line centre that corresponds to a $\pi/2$ or a π rotation -the choice is made depending on which of the two gives a more accurate reading. Then by knowing the actual dispersion of the plate, it can be checked which cycle gives the closest $\delta\nu$'s (or $\delta\lambda$'s) for the $\pi/2$ or π rotation compared with the experimental results. Finally, (iv)by comparing all the computed spectra within a cycle (from the MCV technique) that has comparable $\delta\nu$'s (for the $\pi/2$ or π rotation) to the experimental values, the correct value for NfzB can be obtained by observing particularly carefully in the middle of the pattern. In this method, the magnetic fields were of the order of 2.0-4.5 Tesla and were kept constant throughout the experiment. The effect of measuring f-values at different field strengths will be discussed in Chapter VI. Further, higher fields (>3.5T) give a high sensitivity and accuracy in the results, where typical f-values were of the order 10^{-4} and the

relative error was under 5%.

A final point in this section will be on non-well resolved magneto-optical patterns. Partially resolved patterns are met at relatively high n-values up to the Rydberg series limit for a given magnetic field strength. As the f-value decreases so does the rotation and eventually the magneto- optical "beats" move into the region of the Lorentz doublet. Therefore it becomes difficult to attach precise labels to the peaks as was done before. As shown by Connerade [6] in his Fig.1C, the MCV technique can still be applied for partially resolved patterns. However in the steps of calculation mentioned above, at the stage where the wavelength (or frequency) spread of the π or $\pi/2$ components is required as a method of checking whether the NfzB value used produces a $\delta\nu$ or $\delta\lambda$ (for π or $\pi/2$) in agreement with the experimentally obtained value, the choice of $\pi/2$ as a rotation angle is compulsory since after that it is not clear which peak is the π rotation. In partially resolved patterns, the outer regions change slowly with increasing n-value, whereas the central intensity changes fast.

REFERENCES FOR CHAPTER II

1 Kunz C. "Synchrotron Radiation" Chapter I edited by C. Kunz. Topics in Current Physics Vol 7 (1979)

2. "Electromagnetic Radiation" by G.A. Schott (Cambridge University Press 1912)

3. Schwinger J. Phys Rev., 75, 1912)

4. Heinzmann U., Osterheld B. and Schafers F. Nucl. Instr. and Methods, 195, 395 (1982)

5. "Fundamentals of Optics" by F.A. Jenkins and H.E. White (McGraw-Hill 1957)

6. Connerade J.P. J. Phys B., 16, 399 (1983)

7. "Resonance Radiation and Excited Atoms" by A.C.G. Mitchell and M.W. Zemansky (Cambridge University Press 1979)

8. Connerade J.P., Garton W.R.S., Baig M., Hormes J., Stavrakas T.A. and Alexa B. J.de Physiq. C2 43 317 (1982)

Chapter III

Calculational Methods and Computational Techniques

In earlier work done on magneto-optical rotation (including both the effects of magnetic circular dichroism and magnetic circular birefringence) done by Connerade ([1] and by Garton et al [2]), it was assumed that the line profile had a Lorentzian shape, that the apparatus smoothing was that of a "top-hat" and the final calcualtions of the spectra were done on a "pet" computer which was a CBM 4032 microprocessor with limited accuracy and resolution.

In the present work, for the sake of improvement of the accuracy of the calculations performed and for the sake of generality, it has been assumed that the line profile has a Voigt shape (by modifying the appropriate parameters it can become Gaussian or Lorentzian), that the apparatus smoothing can be Lorentzian or Gaussian (the triangular has also been investigated) and the calculations were performed as well as the graphical output, on the 174 main computer of the Imperial College. All these aspects will be discussed in greater detail below in this chapter and the great superiority of the produced results to the previous calculations done by Connerade [1] will be demonstrated. This chapter will also include a brief description of the computational and graphical techniques and of the limitations of the computer system used.

In Chapter II, it was mentioned that the grating has a finite polarising efficiency and it was also noted from Fig.II2 that the two Lorentz components are not symmetric in shape to

each other. Polarisation and asymmetry will also be discussed below. In this chapter firstly the various parameters involved in the calculations will be discussed, secondly the apparatus function and thirdly the computational aspects. In particular, section 1 will deal with parameters which can be measured very accurately (eg wavelength), section 2 with parameters that are measured less accurately in the experiment (eg temperature and magnetic field) and their impact on the analysis of the results and sections 3 and 4 with parameters which have to be guessed or matched to the data in the course of the calculation because they cannot be measured directly (eg polarisation,asymmetry and apparatus width respectively). Finally section 5 will deal with some of the aspects of the calculations. The general description of the MOV method of Chapter II and the details of the calculations presented in the present chapter when combined will give the final relative f-value results which will be presented in Chapter VI.

1.Wavelength Determination

Each of the experimental plates that were obtained in Bonn, contained several spectra at different values of the magnetic field and one zero field spectrum. These plates were then microdensitometered at Imperial College and from the zero-field separation of the absorption lines between successive members of the Rydberg series, we were able to find a very exact value of the ratio :wavelength difference/ corresponding distance on the micro- densitometer trace. For the wavelength of each n-value of the principal transitions in alkaline earths that we were interested in, there exist some very reliable

publications such as [3]. Therefore for B≠ 0 each member could be exactly identified and the correct corresponding wavelength λ_o could then be inserted as data in the calculations.

2.The Effect of the Exact Knowledge of the Value of T and B on the Computed Spectra

It was mentioned in the previous chapters that the frequency spread for the intensity in a Lorentzian profile to fall to its 1/e value, was equal to the following expression and also that $\Delta\nu_{(1/e)}^{Dop.}$ entered explicitly the refractive index and the absorption coefficient formulae:

$$\Delta\nu_{(1/e)}^{Dop.} = \frac{\sqrt{2kT/m}\ \nu_o}{c}$$

From this expression, it is obvious that $a_{+-}(\nu)$ and $n_{+-}(\nu)$ and therefore the intensity formula depend in some way on the temperature T.

In the first instance the value of T used in these calculations was the one measured at the outer wall of the absorption cell by our colleagues in Bonn performing the experiment. They used, for the Strontium experiments, a wall temperature of T of 700°C. The effect of varying T on the computed pattern had to be studied and great attention had to be paid in case that the pattern was very sensitive to changes of T if the experimental value does not correspond exactly to that of the vapour. Figs III1,2 and 3 show patterns computed for SrI n=11 with all other parameters held constant and values of temperature of 700 C, 600 C and 1000 C respectively. The patterns were quite similar and it can be said that the pattern with T=1000 C and Nfz=9.66 $10^{14}cm^{-2}$ was identical to the one

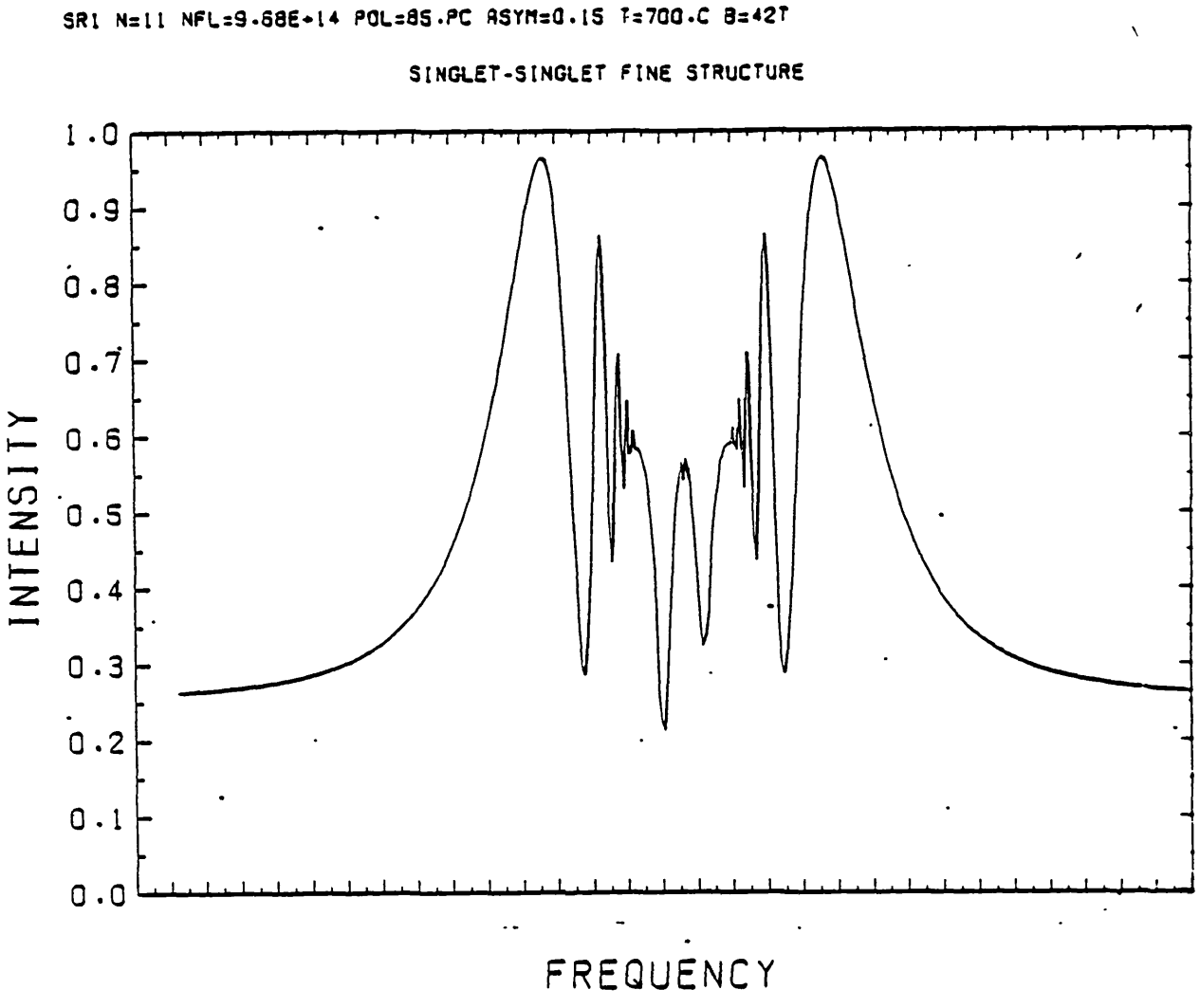

Fig.III1 SrI n=11 pattern calculated with the MOV method at T=700°C and B=4.2T. The polarisation efficiency of the grating was assumed to be 85%, the asymmetry of the two Lorentx components was k=.15 and the half width of the apparatus function was =8.5 10^{10} Hz.

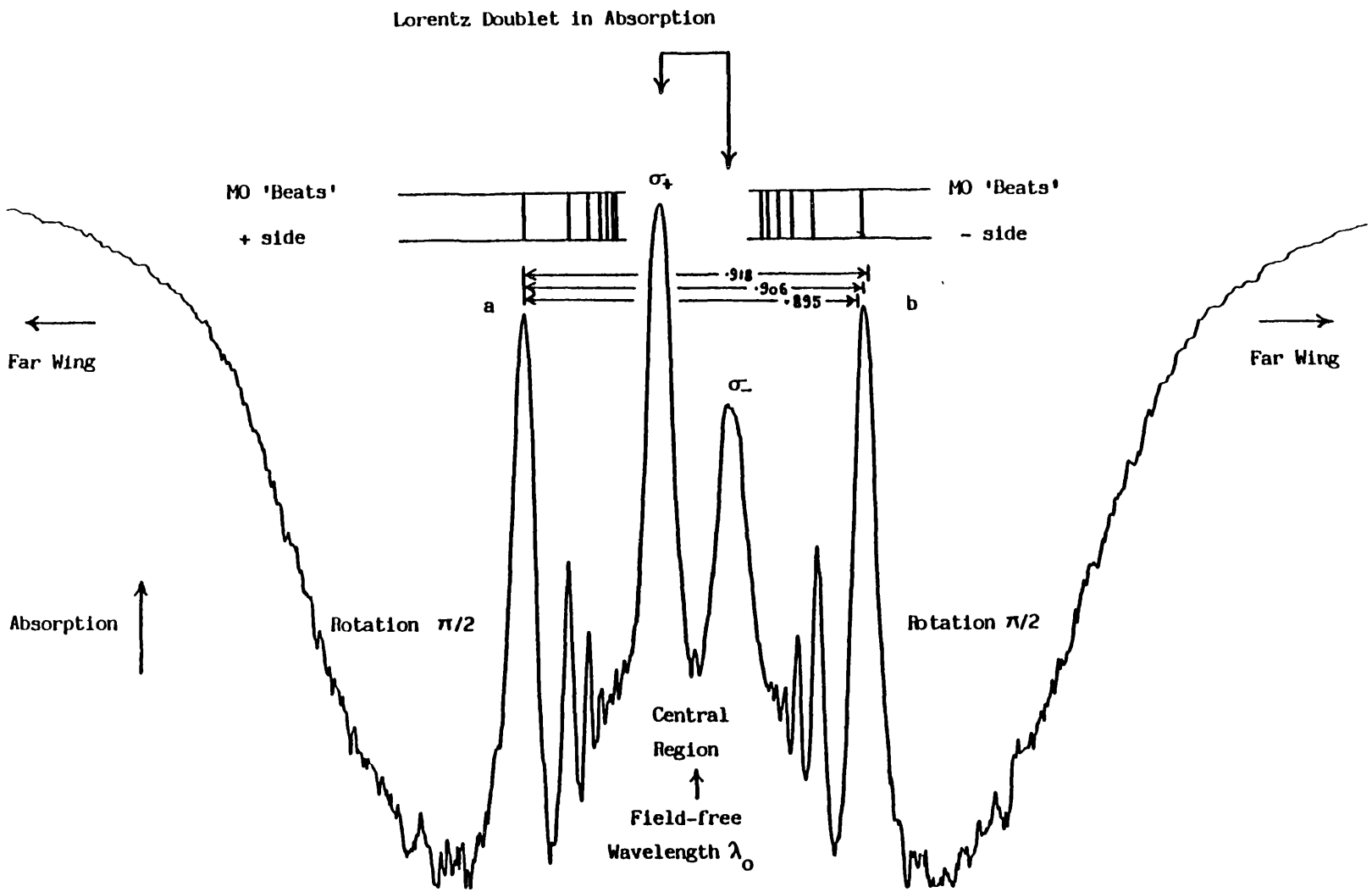

Fig.III1a SrI n=11 experimental pattern obtained in Bonn.

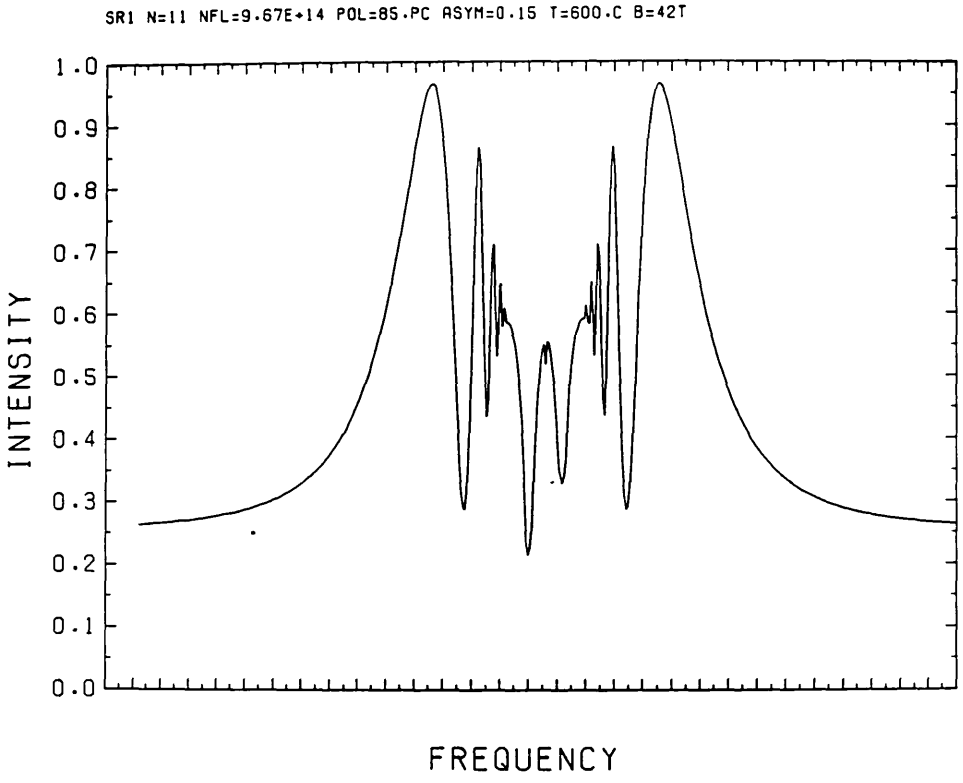

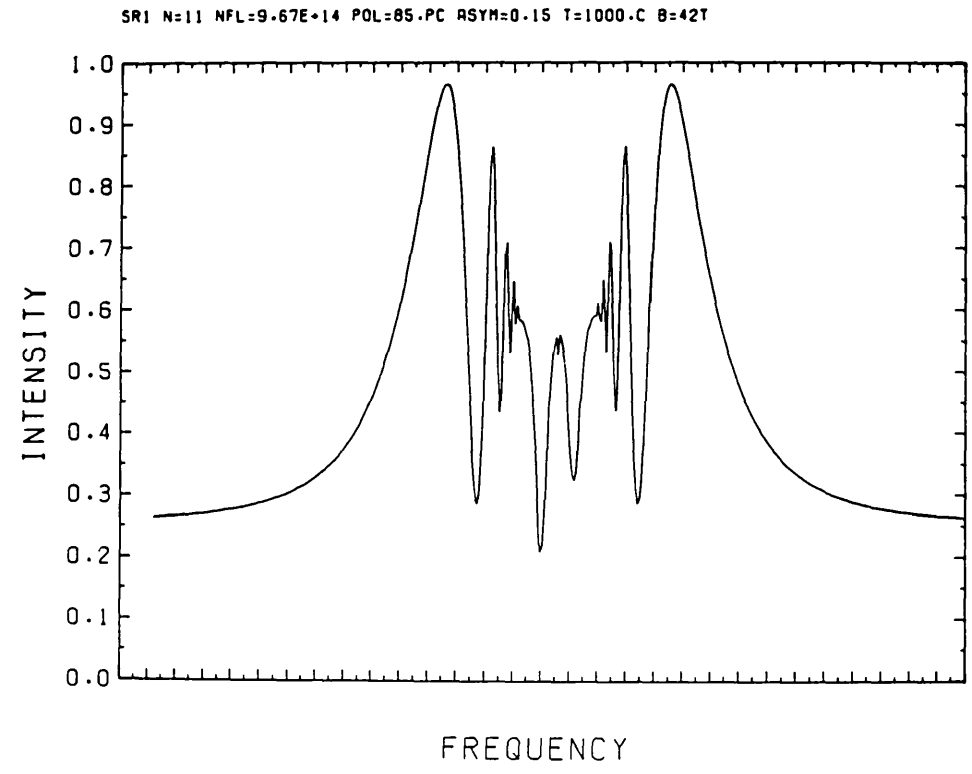

Figs.III2 and 3 SrI n=11 computed spectra. All the parameters used were identical to those of Fig.III1 except T which was 600°C and 1000°C respectively.

with T=600 C and Nfz=9.67 $10^{14}cm^{-2}$ (Figs.III3 and 2 respectively). This implies that a change of 40% in temperature produces a change of 0.1% in determining the f-value which says in other words that tha "approximate" value of T given to us by the experimentalists is more than adequate for correct calculations of the magneto-optical spectra.

The same problem (of doubting the accuracy of given data) arises with the magnetic field. Although in the calculations of relative f-values the B-field contribution cancels, it does though come in the calculations of each individual intensity pattern and the effect of its variation must be studied. Figs.III4 and 5 represent SrI n=11 (identically produced spectra with the same parameters) with B=40T and Nfz=9.67 $10^{14}cm^{-2}$ and B=40T and Nfz=9.63 $10^{14}cm^{-2}$ respectively. From these two figures and Fig.III1a it is obvious that Fig.III5 is much closer to the experimental spectrum. This means that in order to produce identical patterns if the B-field if one goes from 40T to 42T then its Nfz value must go from 9.67 $10^{14}cm^{-2}$ to 9.63 $10^{14}cm^{-2}$, ie a 5% inacurracy in determining B produces a 0.4% error in determining the value of Nfz of a particular member of the series. The above argument was for the n=11 member (the lowest in our experimental data) series. We have also found that as n increases the variation of the central (and important) part of the M-O patterns of each n as a function of Nfz decreases. We find that this source of systematic errors will produce at most a 0.4% error in determining the Nfz value for a 5% error in determining B. Errors in determining the value of the magnetic field are not usually greater than that 5% because then we can cross-check the experimetnal B-field given data with the

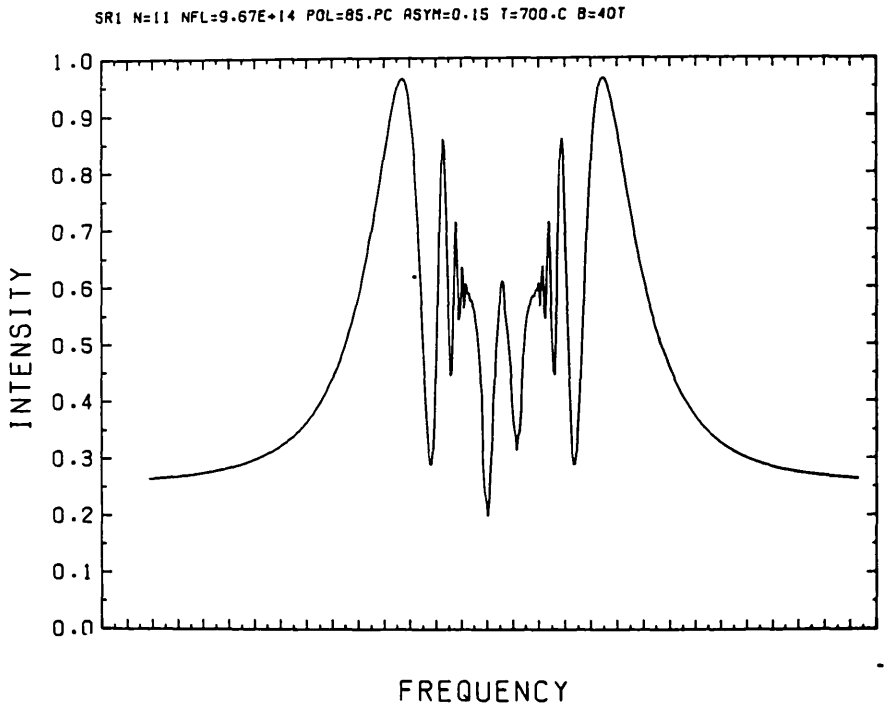

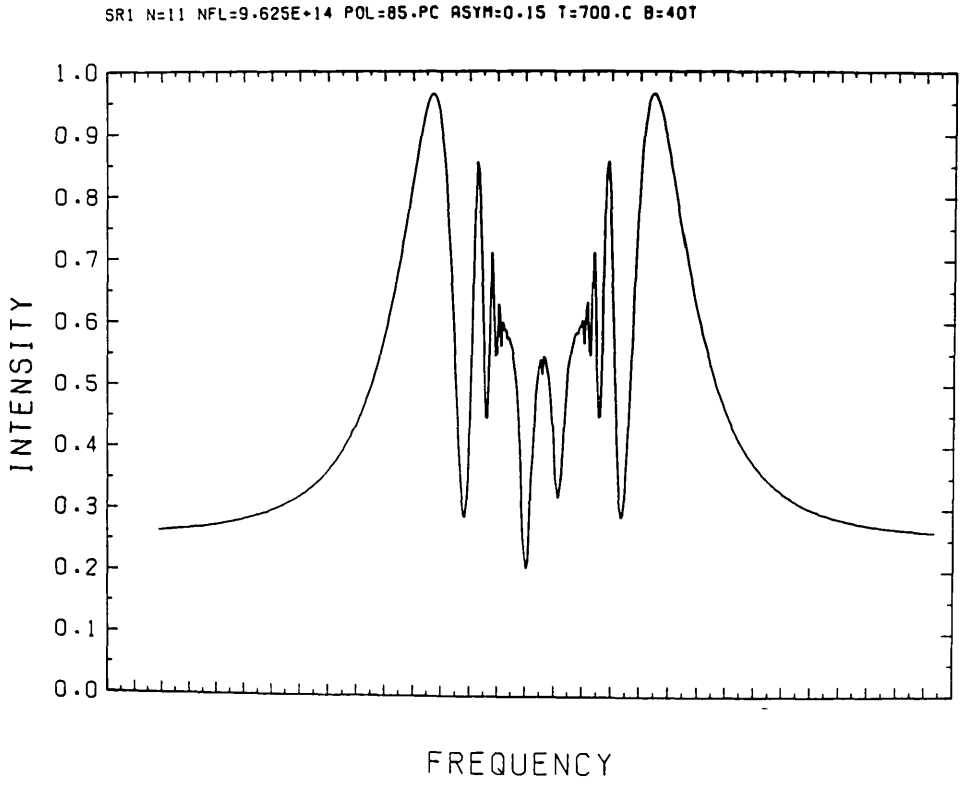

Figs.III4 and 5 SrI n=11 computed spectra. All the parameters used were identical to those of Fig.III1 except that B=4.0T for both figures and Nfz=9.67 10^{14} and 9.63 10^{14} respectively.

distance between the two Lorentz components ($eB/4\pi mc$). In summary, errors in the exact knowledge of temperature and magnetic field of 40% and 5% respectively produce only errorrs in Nfz of the order of a few tenths of a percent. Therefore, as far as this aspect is concerned, the MOV method is quite reliable.

3.Polarisation of the Grating and Asymmetry of the Lorentz Doublet

When the set-up of this experiment was described in chapter II, it was mentioned that the polarising efficiency of the grating was not 100% but something like 70-80%. Therefore the formula for the intensity derived in Chapter I (equation I18) must take into account the effect of the non- 100% efficient grating by multiplying the above expression by P/100 where P is the polarisation efficiency of the grating.

The intensity formula now becomes after taking into account the above facts:

$$I = \frac{I_o}{4}\frac{P}{100}\left(\left(e^{-a_+z/2} - e^{-a_-z/2}\right)^2 + 4e^{-(a_++a_-)z/2}\sin^2\phi\right) + \frac{100-P}{100} I_o e^{-(a_++a_-)z}$$

The above expression for the intensity, yields a symmetric Lorentz doublet pattern (ie the effect of "asymmetry" has not been considered yet). We use the expression introduced by Connerade [1] to account for the imperfect polarisation efficiency of the grating. A justification for this term is as follows: consider the radiation which has passed through the system to consist of two parts. Firstly polarised light and secondly a small fraction of light of random polarisation.

Integrating the origingal expression for the intensity over all angles, gives an intensity proportional to:

$$I' = I_o \int_{-\pi}^{+\pi} (e^{-a_+ z/2} - e^{-a_- z/2})^2 + 4e^{-(a_+ + a_-)z/2} \sin^2\phi) d\phi$$

which equals:

$$= I_o /4\pi \; 2 (e^{-a_+ z/2} + e^{-a_- z/2})$$

Since a_+ and a_- are non-zero in different regions then (up to a constant) we get the same behaviour as that proposed by Connerade [1]. It was mentioned in section 2 of Chapter II that the values of polarisation and asymmetry were found by the "trial and error" method. Some illustrative examples will show how this was done. Fig.III6 shows the SrI n=11 symmetric magnetorotation spectrum evaluated assuming that the grating is a perfect polariser (ie P=100%). From the above equation it can be seen that in the far wing both terms tend to zero and from section 2 of Chapter I (Inverse Longitudinal Zeeman effect) it can be seen that the symmetric Lorentz doublet was half the depth of the maximum amplitude (in intensity). The rest of the pattern is as expected with the intensity oscillations discussed in the two previous chapters. If in the same pattern every parameter remains constant, and the calculations are repeated with P=85%, Fig.III7 will be produced. Here again all the main features exist, such as the magneto-optical beats as well as the Lorentz doublet, with the only difference the intensity of various parts of the profile has changed since Fig.III6. For example, the far wing does not have zero intensity now, but (100-85)/100 I_o(since a_+ and a_- are almost zero out in the far

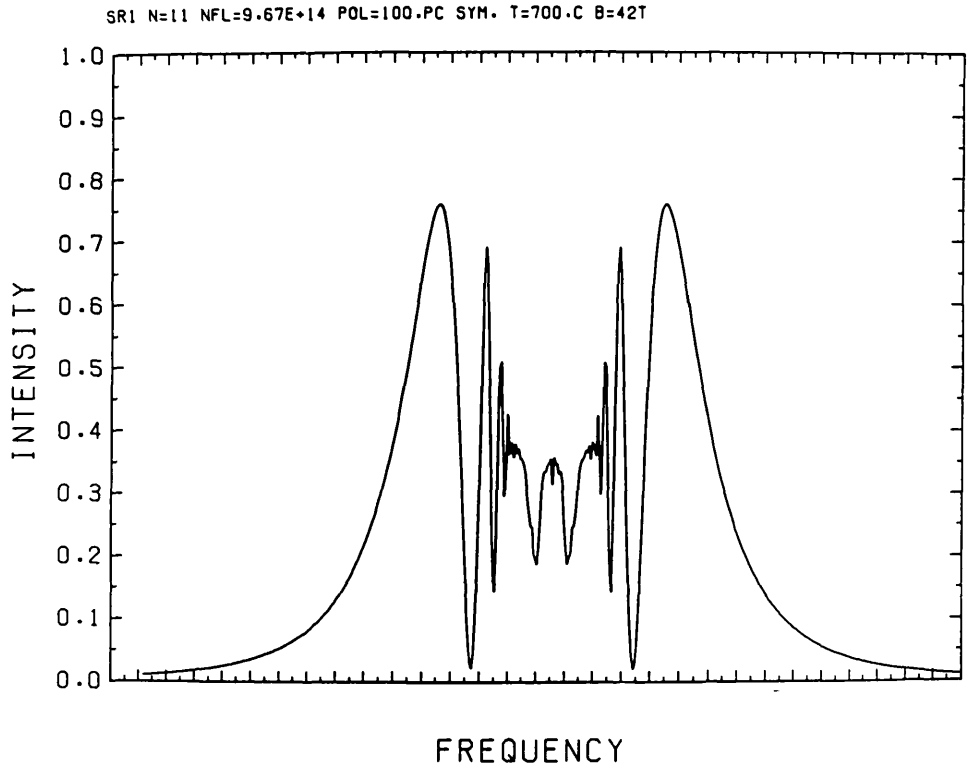

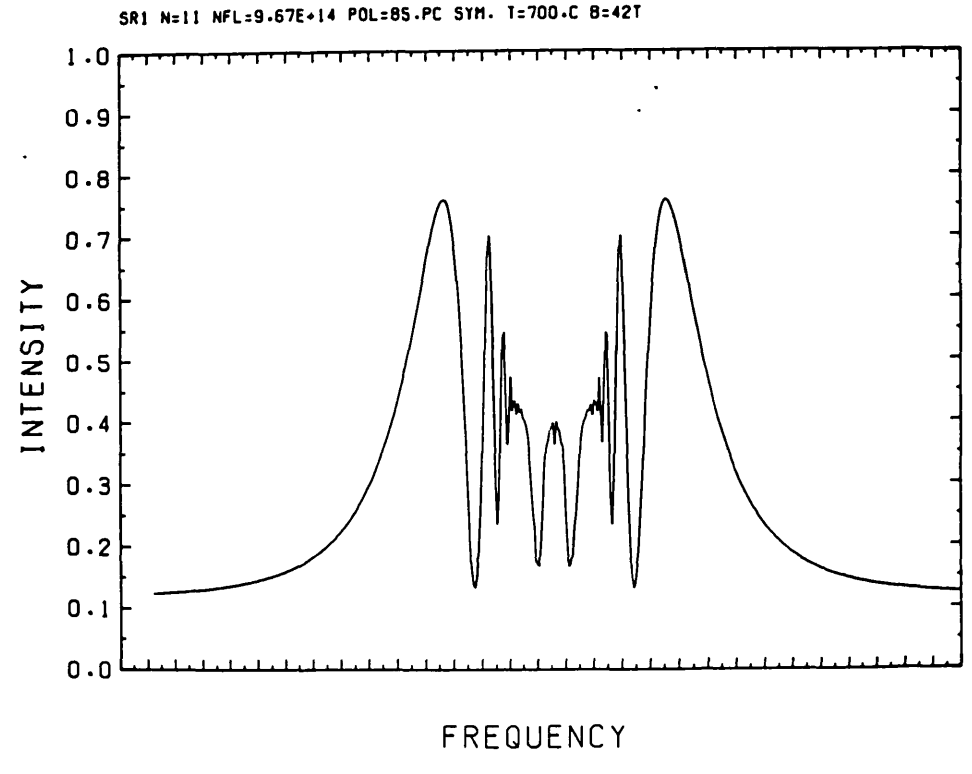

Figs.III6 and 7 SrI n=11 computed spectra. T=700°C, B=4.2T and Nfz=9.67 10^{-14} for both figures. The pattern was assumed to have identical Lorentz components and also to have 100% and 85% polariasation efficiency respectively.

wing) which is shown in Fig.III7. Apart from the $\pi/2$ rotation intensity peaks which remain constant in intensity, the rest of the pattern is shifted upwards (not by a constant amount everywhere as might be expected from the second factor of the previous equation since it depends on a+ and a- which are frequency dependent; see section 10 of Chapter 1). Therefore, as the polarising efficiency of the grating decreases, there is an upward inhomogeneous shift of the pattern with a simultaneous increase in intensity and emphasis on the Lorentz components with respect to the magneto-optical fringes. Fig.III8 is the same as Figs.III6 and 7 with the only difference that it is evaluated with P=40%. The observations stated above are even more prominent in this exmaple. In the extreme case where P=0% it is obvious from the previous equation that only the two absorption peaks will be revealed as in the inverse Zeeman effect since the first term vanishes and the second term represents just pure absorption. This is shown in Fig.III9. At this point, it must be stressed that the insertion of the polarisation efficiency in the intensity formula and its calculation, only serves the purpose of trying to reproduce as well as posssible the experimental spectrum. Since it only affects the level of intensity of the Lorentz components by moving the complete pattern up or down does not influence the middle part of the magneto-optical pattern, it plays no role whatsoever in the determination of the relative f-values.

Next in this section, the asymmetry with respect to the line centre of the two Lorentz components in Fig.III1a will be studied and an explanation of the effect will be attempted. A first guess might be to explain this asymmetry by any of the

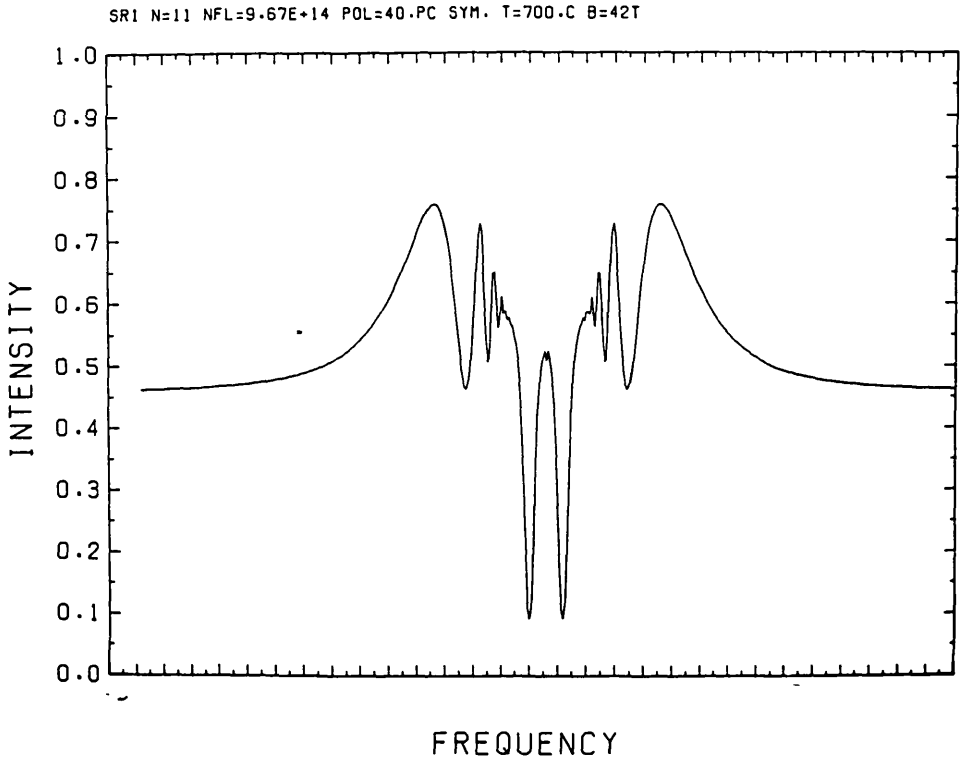

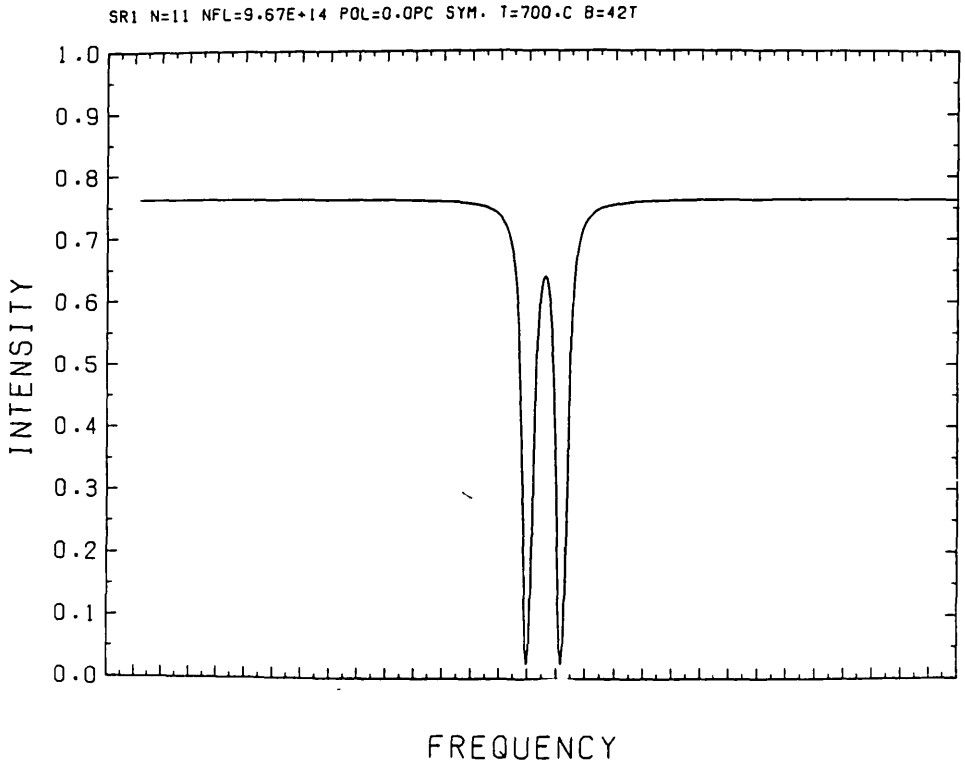

Figs.III8 and 9 SrI n=11 computed spectra. All parameters used were identical to those of Fig.III6 and 7 except that P=40% and 0% respectively.

following processes which lead to antisymmetric Faraday effects [4]. As the magnetic field is increased, the processes in order of significance are: a)the Back-Goudsmit effect which breaks the coupling of I and J in hypefine structure, b)the Pachen-Back effect which breaks the LS coupling and thus mixes singlet and triplet states.

All the effects associated with anti-symmetric rotation would act at the same time on all the part from the line centre field-free intensity point to the far-wing (the + or - depending on the sign of the antisymmetric rotation) through the refractive indices and the absorption coefficients, which are related to each other through the Kramers-Kroning relations and cannot therefore be separately changed. But Fig.III1a indicates that within the experimental errors the pattern is symmetrical about the line centre with the only exeption of the one Lorentz component being stronger in intensity that the other. This makes the explanation of the effect by any antisymmetry of the Faraday effect impossible and another explanation must be found.

Another possible cause of the effect is some ellipticity of the incident radiation. It was mentioned in section 1 of Chapter II [8] that together with the plane polarised radiation (in the orbital plane) there is also some elliptically polarised radiation that emerges from the synchrotron. If the experimental conditions are such that the acceptance angle is out of the orbital plane, then there will be inevitably an amount of circularly polarised radiation added to the plane polarised one. Such an admixture will only strengthen one of the two Lorentz components while leaving the rest of the pattern unaffected, ie circularly polarised light of a given sense will be absorbed by

the Lorentz component on one side of the pattern and not by the corresponding Lorentz component on the other side. It was found that very good results from these calculations were obtained for an admixture of circularly polarised light of a few % of the incident beam. In terms of the algebra involved in these calculations, this can be achieved by adding to the intensity formula a factor equal to:

$$k\, e^{-a_+ z} \quad \text{or} \quad k\, e^{-a_- z}$$

Therefore the intensity equation now becomes:

$$I = I_o/4 \cdot P/100 \left((e^{-a_+ z/2} - e^{-a_- z/2})^2 + 4e^{-(a_+ + a_-)z/2} \sin^2\phi\right) + k\, e^{-az}, + (100-P)/100 I_o e^{-(a_+ + a_-)z}$$

If in the extra term the negative absorption coefficient is inserted, then the new pattern produced by using the above equation and P=100% will give Fig.III10. Comparing Figs.III6 and 10 it can be seen that the latter has every point of the spectrum shifted by an amount equal to the constant used k, exept the negative Lorentz component which has the same strength of intensity in both figures. Therefore, the asymmetry of the Lorentz doublet can be reproduced computationally having a very good resemblance to the actual experimental spectrum. When the asymmetry (in this case k=0.15) is included in the previous calculations that gave Figs.III6 to 9, then Figs.III10,11,1 and 12 are produced. It must be mentioned again that the only reason for including the asymmetry factor in the calculations is the achievement of a very good theoretical reproduction of the experimental spectra. It should also be stressed that we cannot distinguish between grating effects and effects due to impure

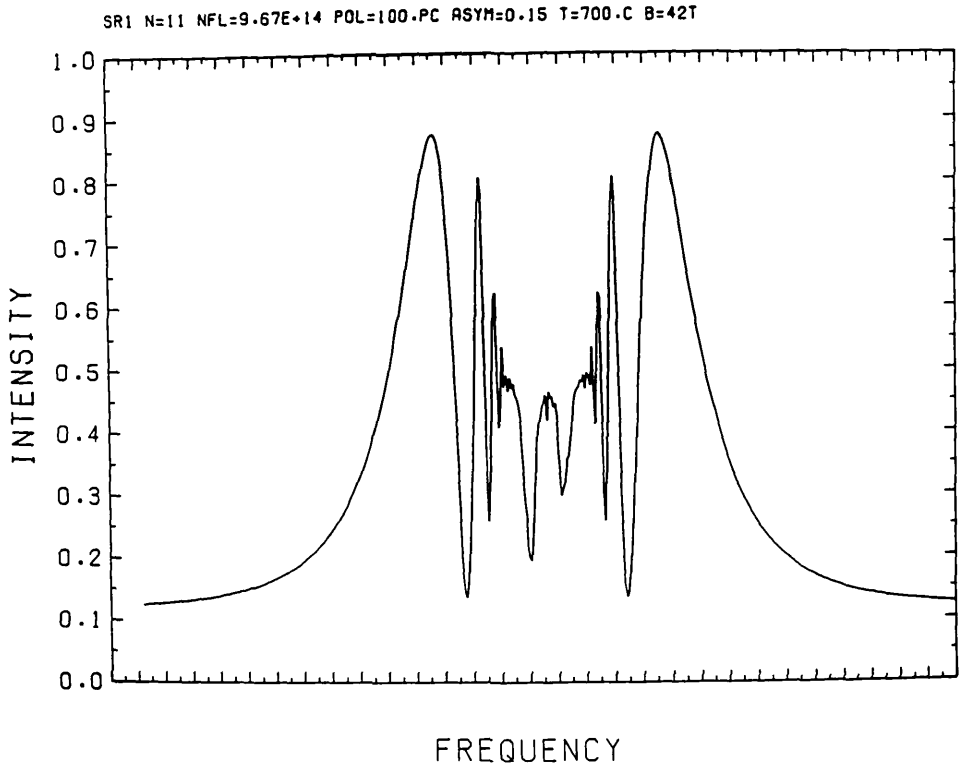

Fig.III1C SrI n=11 computed spectrum. The temperature, B-field and Nfz values were identical to those of Fig.III1. The pattern was calcuelted with k=.15 and P=100%.

source polarisation by our calculations. Clearly, future experiments should test these ideas, *eg.* by moving the experiment out of plane and trying different gratings.Its existence does not alter the shape of the centre of the line in any way and therefore it does not affect the relative f-value determinations. Figs.III10,11,1 and 12 show that their form is affected by the values of P and k; a decrease of P emphasising the Lorentz components and shifting the pattèrn upwards while an increase of k making the difference between the two Lorentz components even larger. Figs.III13 to 16 were calculated with k=0.35 and P=100%,85%,40% and 0% respectively. All the above examples lead to the concluding comment, that roughly it can be said that an increase in the asymmetry coefficient leads the two Lorentz components into having a greater intensity difference (asymmetry) while a decrease in the value of the polarisation emphasises the Lorentz doublet with respect to the rest of the pattern and at the same time shifts upwards the whole of the pattern. Thus it can be said with certainty that there is no other way in determining the exact values of P and k apart from trying several pairs of them and observing the result, always bearing in mind how each of them can affect the magneto-optical pattern. Of cource, the correctness criterion for P and k will be the resemblance of the co$^{m}_{\lambda}$puted spectrum to the corresponding n-value experimental one. Illustrations of this statement are given through Figs.III17 to 20 for SrI n=11. The inconsistency in variation of P with the n-value (ie wavelength) is still an open question that must be answered in the near future. However, the irregular variation of k with wavelength is to be expected according to the grating manifacturers.

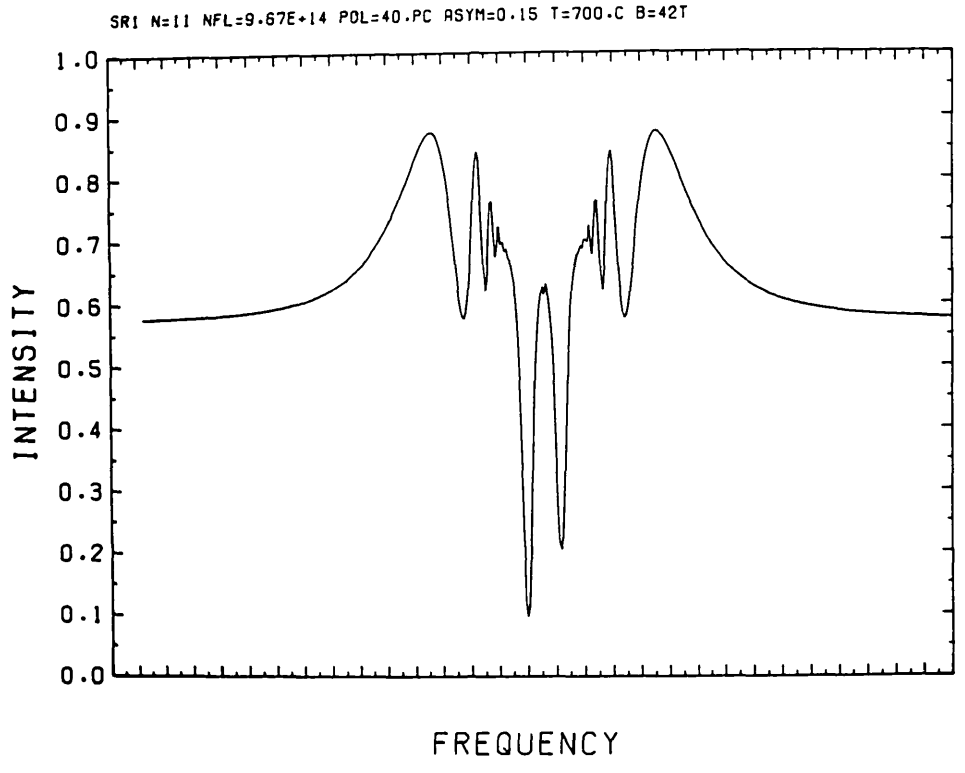

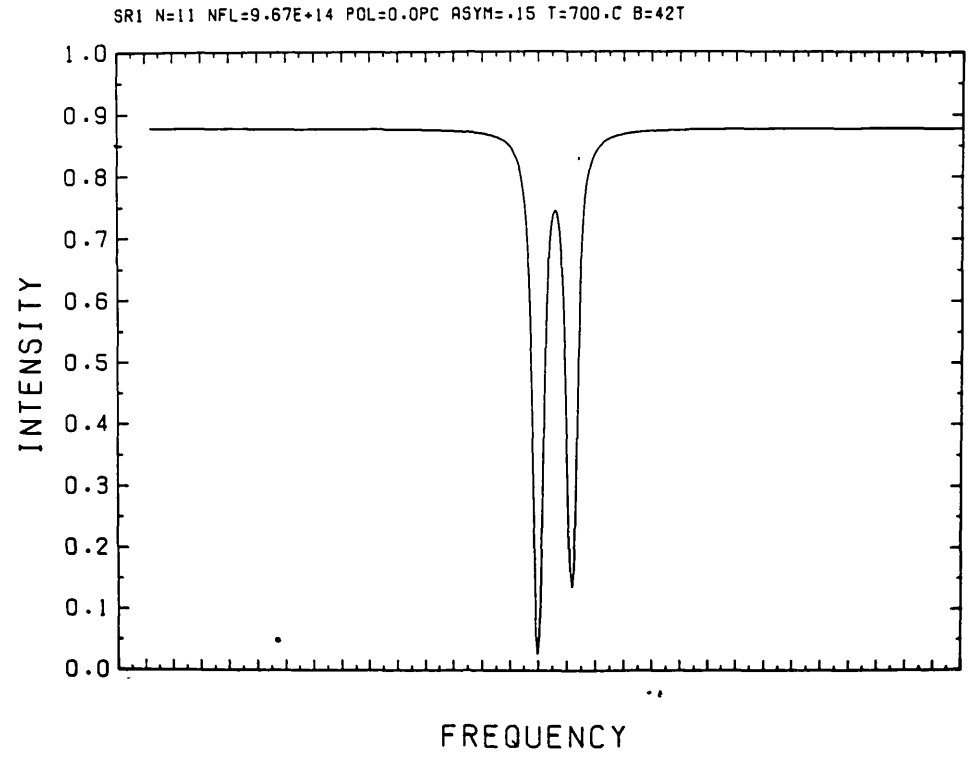

Figs.III11 and 12 SrI n=11 computed spectra. All parameters used were identical to those of Fig.III10 except that P=40% and 0% respectively.

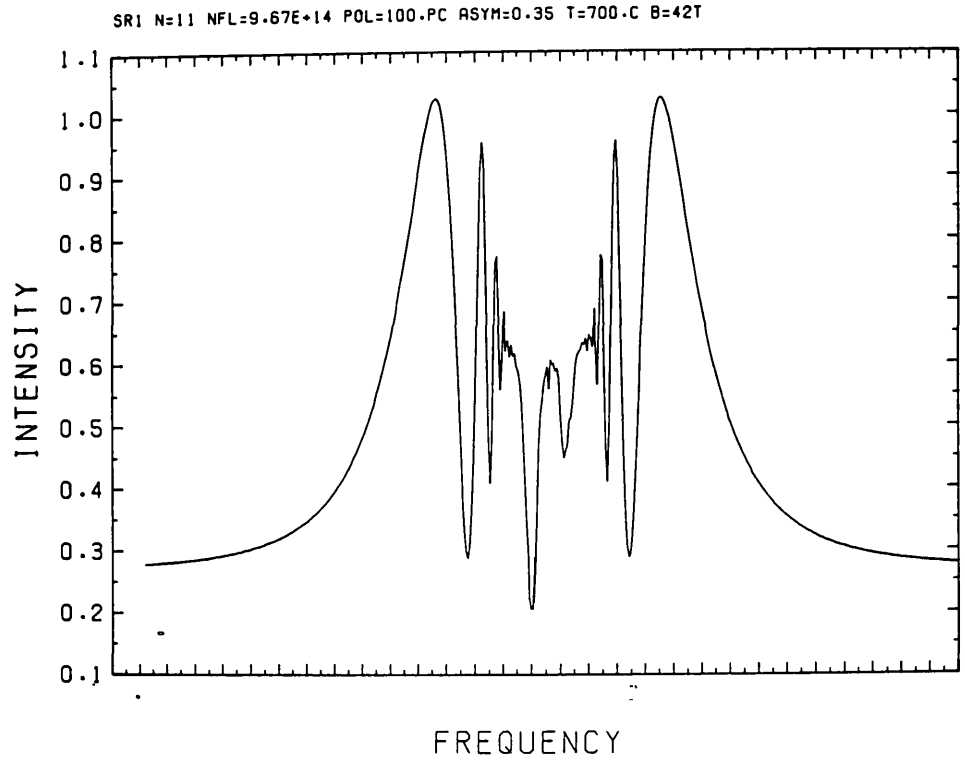

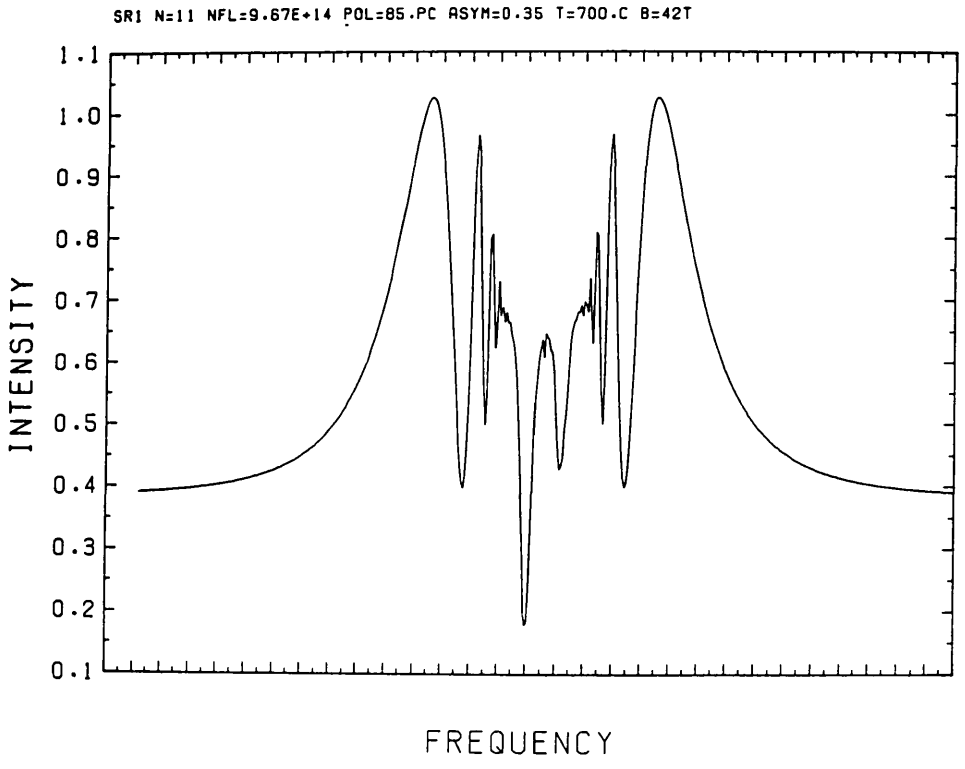

Figs.III13 and 14 SrI n=11 computed spectra. All paramters used were identical to those of Fig.III1 except that k=.35 and P=100% and 85% respectively.

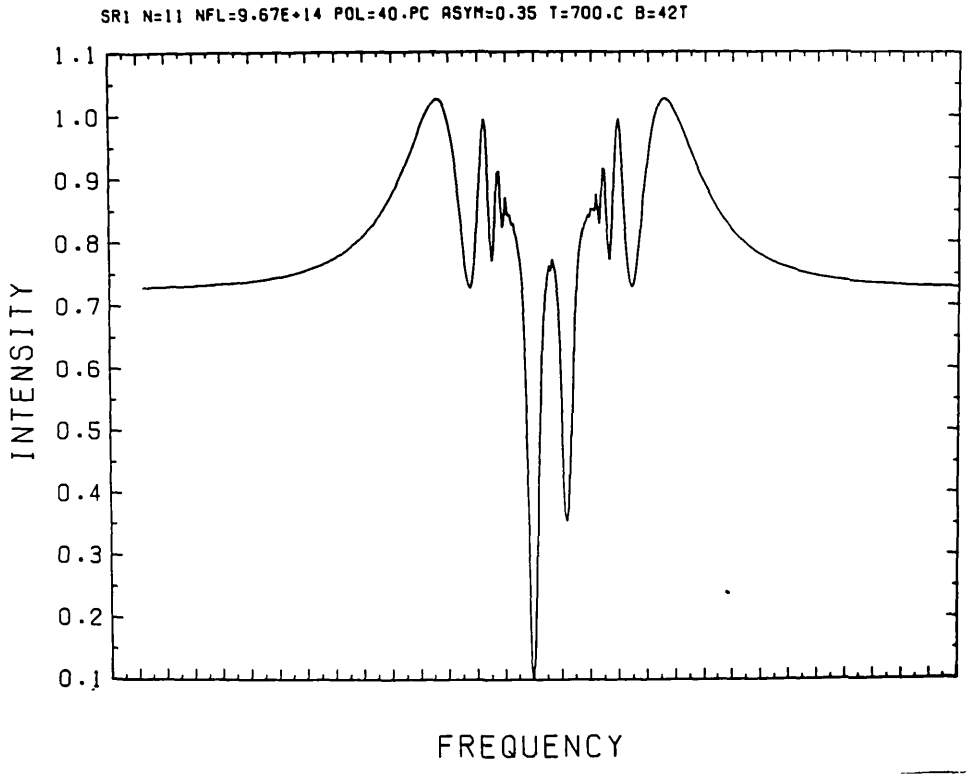

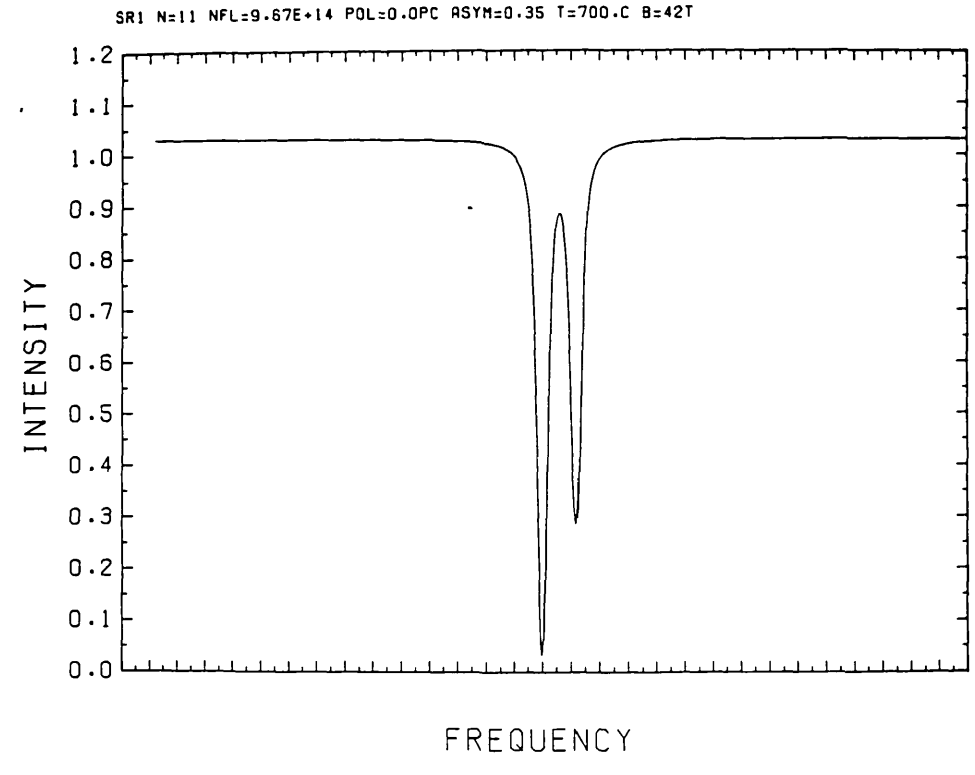

Figs.III15 and 16 SrI n=11 computed spectra. All parameters used were identical to those of Figs.III13 and 14 except that P=40% and C% respectively.

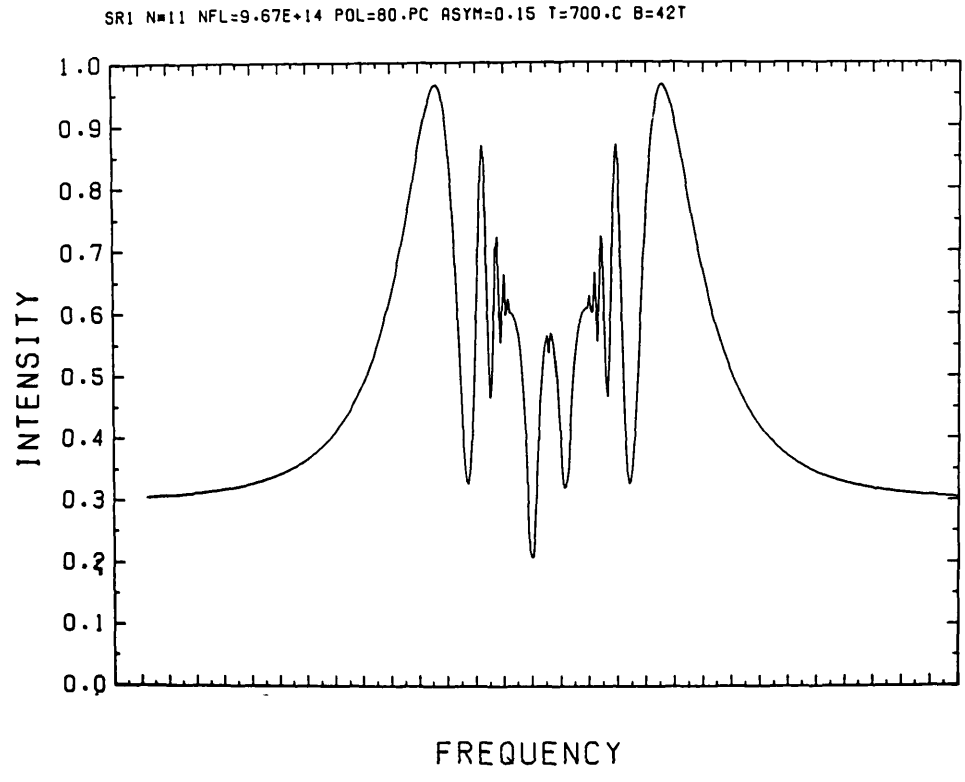

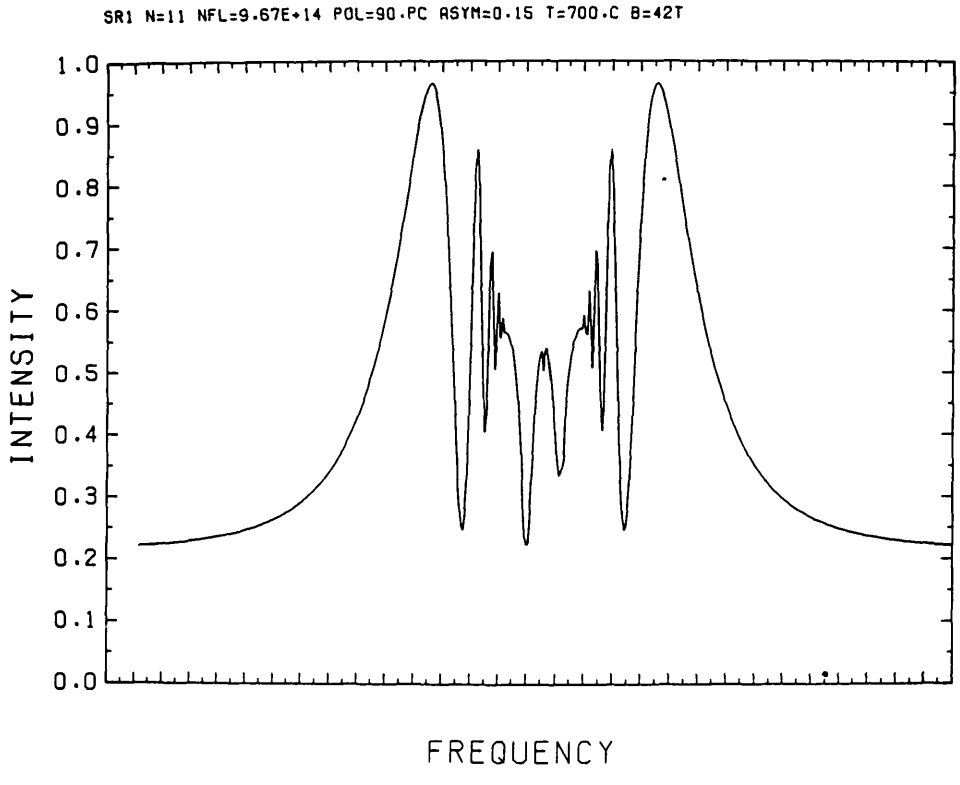

Figs.III17 and 18 SrI n=11 computed spectra. All parameters used were identical to those of Fig.III1 except that k=.15 for both figures and P=80% figures and 90% respectively.

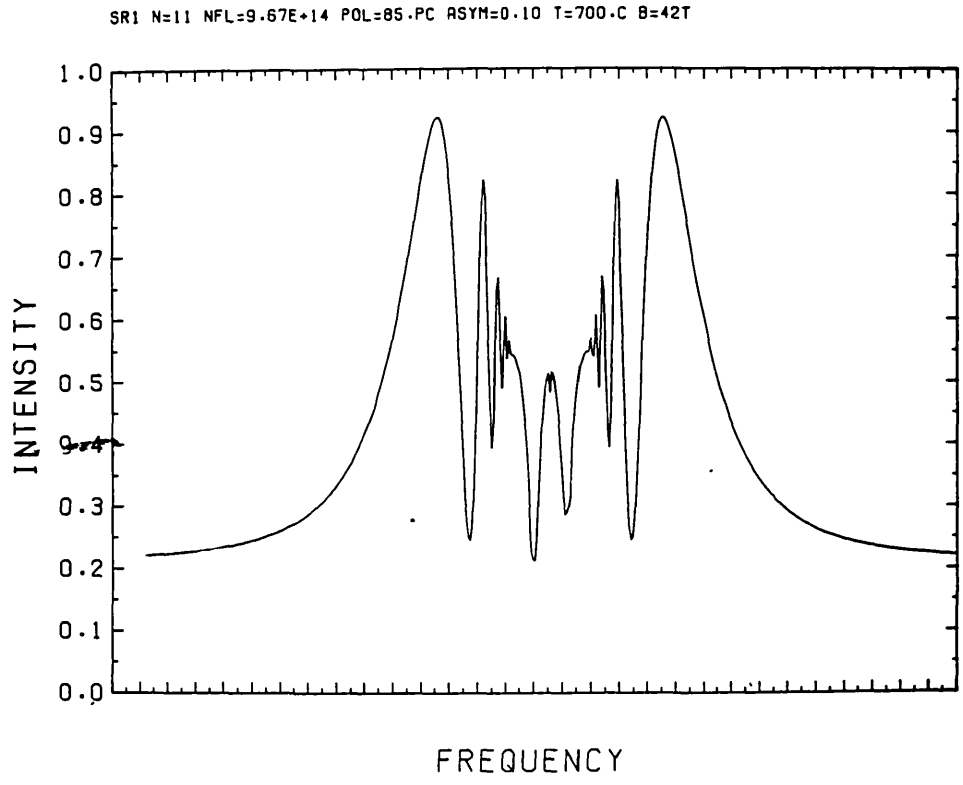

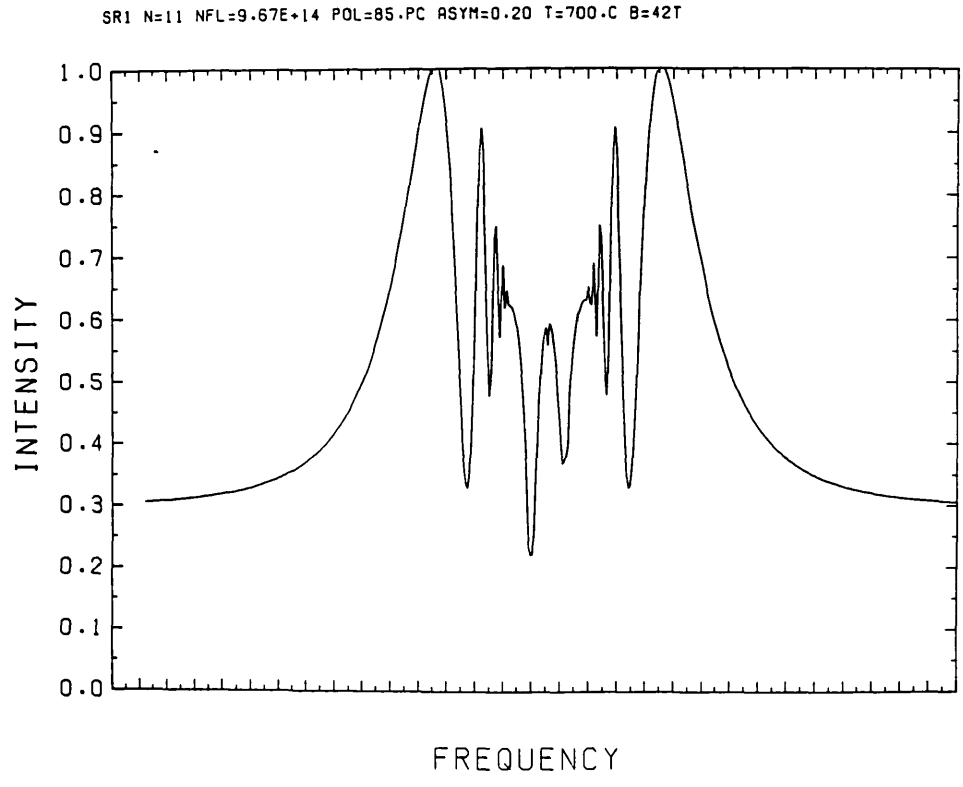

Figs.III19 and 20 SrI n=11 computed spectra. All parameters used were identical to those of Figs.III17 and 18 except that P=85% for both and figures and k=.10 and .20 respectively.

4.The Apparatus Function

It was mentioned in a previous chapter that the calculated intensity of radiation at the end of the furnace must be convolved over an appropriate apparatus function in order to obtain the final and correct expression for the intensity observed on the photographic plate. It must be said that the apparatus function is not simply the instrumental function of the spectrograph, which could be determined for example by analysing a zero-field profile. Effects such as the fluctuations of the density of the absorbing vapour or of the B-field during the exposure must be included in the apparatus function. The apparatus smoothing equation is:

$$I^{Final}(\nu) = \int_{-\infty}^{+\infty} I(\nu - \nu^*)\, L(\nu^*)\, d\nu^* \qquad \text{(III1)}$$

where $L(\nu')$ is the apparatus function whose form will be discussed below, and $I(\nu')$ is the intensity (see equation III7 of section 5 of this chapter). Fig.III21 shows the intensity spectrum before being smoothed by an apparatus function.

In the present calculations at each frequency point of the spectrum, the numerical integration of the apparatus function convolution is performed from $-2\,\Delta\nu_{APP}$ to $+2\,\Delta\nu_{APP}$ (where $\Delta\nu_{APP}$ is the FWHM of a Lorentz apparatus function). 100 frequency steps are required to perform the convolution integration numerically with sufficient accuracy. This process is repeated 1000 times, for the 1000 frequency points that construct the final pattern.

In the work previously done by Connerade [1] on the magneto- optical vernier method (MOV) it was assumed that the

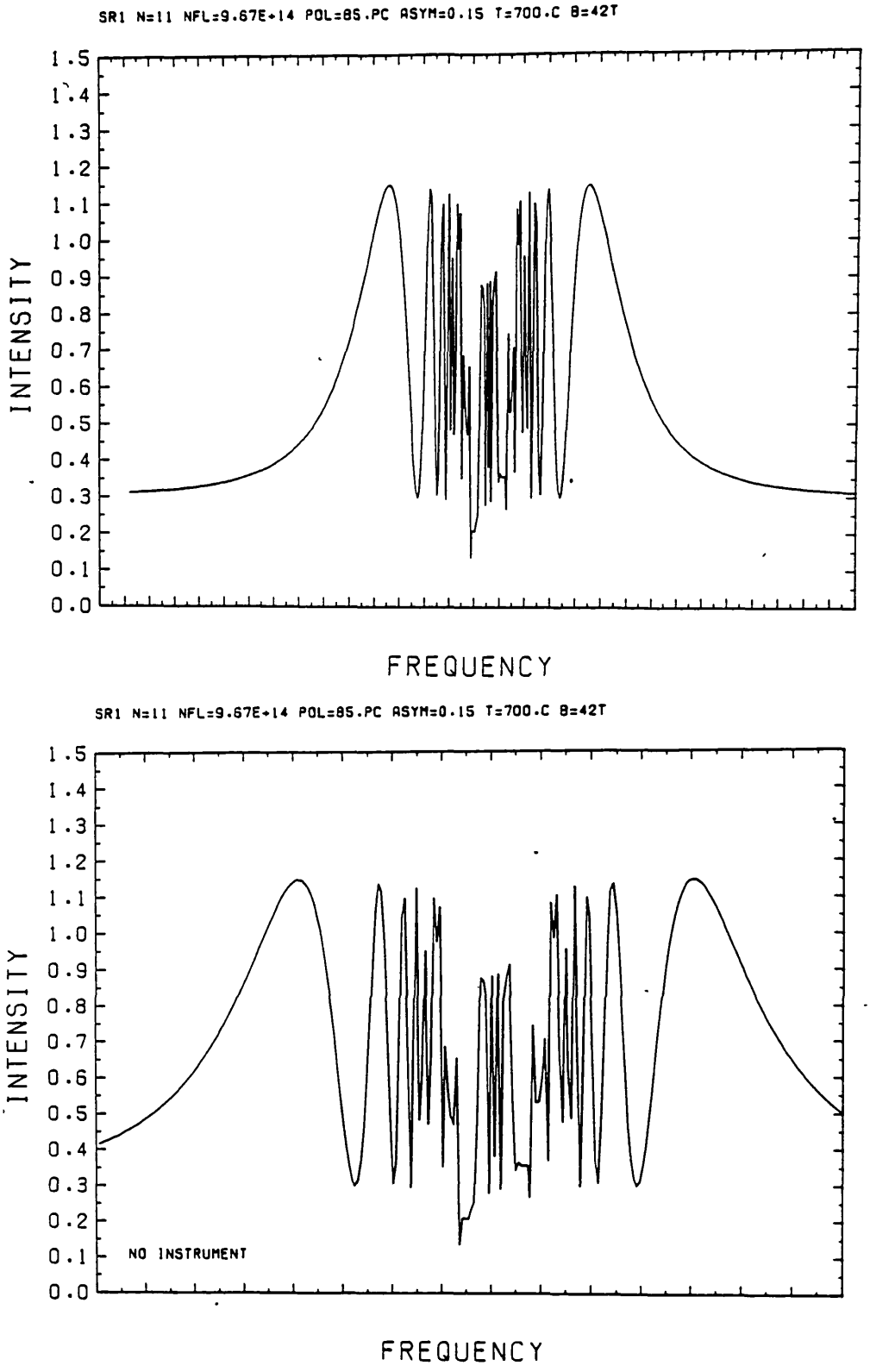

Fig.III21 A magreto-optivel pattern (and in an expanded form) of the n=11 SrI line without apparatus smoothing. The parameters used were identical to those of Fig.III1.

apparatus function was of a simple "top-hat" shape and no investigations were made either on the accuracy of the numerical aspects or of the influence of this arbitrary choice of profile. This section of the present chapter will be devoted to a detailed discussion on these two problems -which were crucial for the establishment of the MOV method as a practical tool for studying M-O spectra. Indeed, the motivations for the theoretical study and computational developments which together form the subject matter of the first seven chapters of this thesis were (i) establishing the reliability of the MOV approach for some simple atomic spectra and (ii) providing suitable theoretical tools in the form of documented computer codes for the reduction and analysis of future experiments.

In the present section the following three types of profiles are investigated: Lorentzian, Gaussian and triangular. The "top-hat" one has already been investigated before [1]. The Lorentzian and the Gaussian were considered as more reasonable representations of the physical situation and are extensively studied. The triangular function was also considered for its simplicity of representation but is a somewhat crude approximation and will be given only limited attention. Section 4 of this chapterr contains subsections 4a,4b and 4c. Section 4a deals with the correct determination of the FWHM value of a Lorentzian apparatus profile. It will be seen that exactly the same method applies to the determination of the FWHM value of a Gaussian function. Section 4b will deal with the numerical calculation of the convolution integral. It will tackle the question of how many points to use accross a numerical integration and also the effect that the replacement of infinity

limits of the apparatus integration with finite values has on the profiles. Finally, section 4c defines the Gaussian and triangular profiles, states some of the algebra needed to ensure that all profiles have exactly the same value of FWHM as the Lorentzian one and also studies the effect of replacing the infinity integration limits with finite ones. Intercomparisons between magneto-optical spectra obtained using the three above-mentioned apparatus functions with and without apparatus smoothing will finally be made. At this point, we compare our results with experimental data.

4a. Determination of the Correct FWHM Value of a Lorentzian Apparatus Function

The simplest method of determining the FWHM of the Lorentzian apparatus function in question is to treat it as an unknown. The check of this correctness will be the reproduction of the observed magneto-optical pattern (eg Fig.III1a for SrI n=11).

For this reason calculations with 100 steps between $+2\Delta\nu_{APP}$ and $-2\Delta\nu_{APP}$, (these assumptions will be justfied in subsequent sections) and with varying $\Delta\nu_{APP}$ were performed. Figs.III22 to 27 show the computed spectrum for SrI n=11 for values of $\Gamma_{APP}=2\pi\ \Delta\nu_{APP}$ equal to $8.5\ 10^{10}$, $4.00\ 10^{10}$, $6.00\ 10^{10}$, $9.50\ 10^{10}$, $11.00\ 10^{10}$ and $15.00\ 10^{10}$ respectively. From the figures it is obvious that the pattern calculated with $\Gamma_{APP}=8.50\ 10^{10}$ is the closest to the observed spectrum (Fig.III1a). As Γ_{APP} increases and the apparatus width becomes greater and smoothes the intensity spectrum more and more, there are less and less intensity oscillations and they are comparatively weaker. The opposite effect occurs as Γ_{APP} decreases with with more

stronger and sharper "intensity oscillations" occurring as a result. In Figs.III22 to 27 it can be easily seen that the middle part of the spectrum lying between the two Lorentz components is quite sensitive to any changes of Γ_{APP} not because it affects in any way directly the calculations, but because the bandwidth associated with the apparatus function is effective in smoothing the spectrum in the sensitive and important to our calculations middle part.

It is necessary therefore to try and find out with some greater accuracy the magnitude of this effect and the subsequent tolerance error. Fig.III25 shows the pattern produced from the calculations using $\Gamma_{APP}=9.50\ 10^{10}$ (a value of Γ_{APP} is chosen for these quantitative arguments close to the one considered best -the $8.50\ 10^{10}$- for reasons of greater accuracy because the greater the deviation from the correct value of Γ_{APP} the more obvious the error becomes) and with $Nfz=9.67\ 10^{14}$ (as used for Fig.III1 which is considered the best attempt for SrI n=11) while keeping all the other parameters constant. It can be seen that the middle part deviates from the experimental pattern. Fig.III28 is identical to Fig.III25 in Γ_{APP} and the other parameters and calculations exept that here $Nfz=9.66\ 10^{14}$ and produces a pattern whose middle part is much closer to the experimental spectrum. Therefore a pattern with $\Gamma_{APP}=8.50\ 10^{10}$ and $Nfz=9.67\ 10^{14}$ (Fig. III1) is almost identical to a pattern with $\Gamma_{APP}=9.50\ 10^{14}$ and $Nfz=9.66\ 10^{14}$, ie a change of about 11% in the apparatus width produces only an error(deviation) of 0.1% in the resulting pattern and therefore in the determined f-value. This shows that the pattern is slightly dependent on the apparatus function width -just to

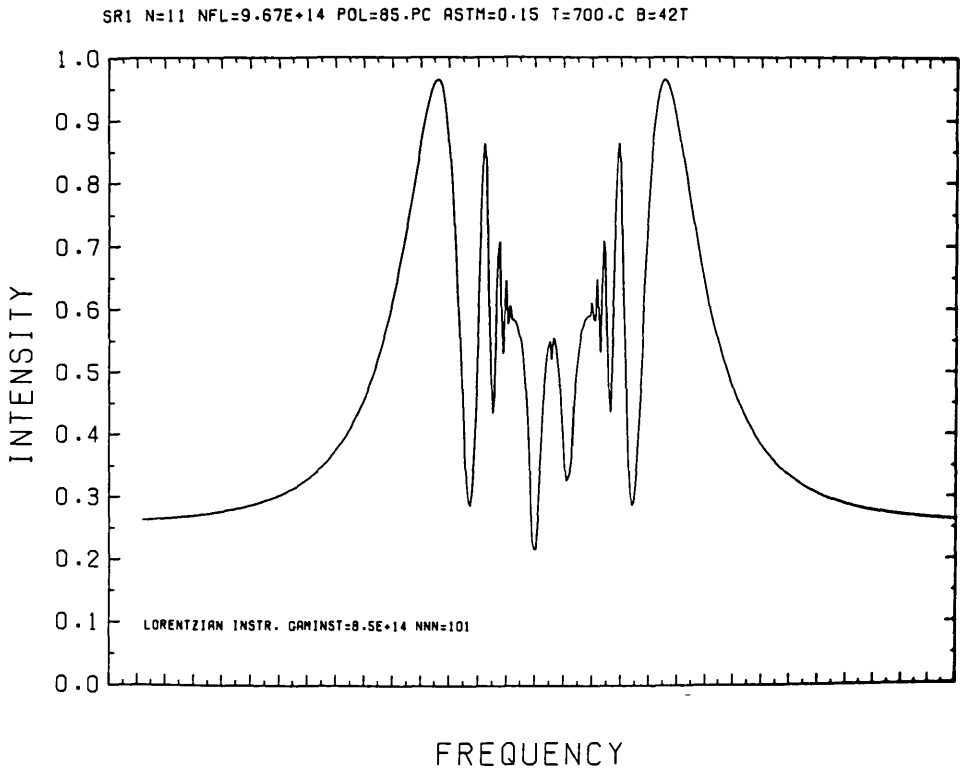

Fig.III22 This figure is identical to Fig.III1, but is repeated here for reasons of convenience.

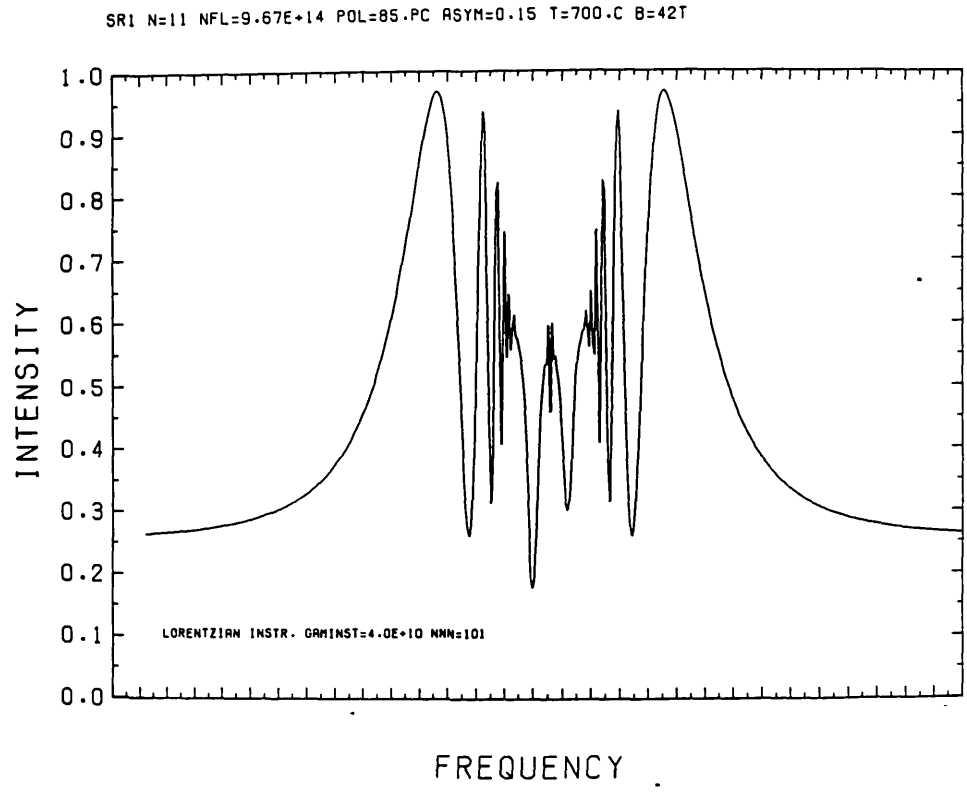

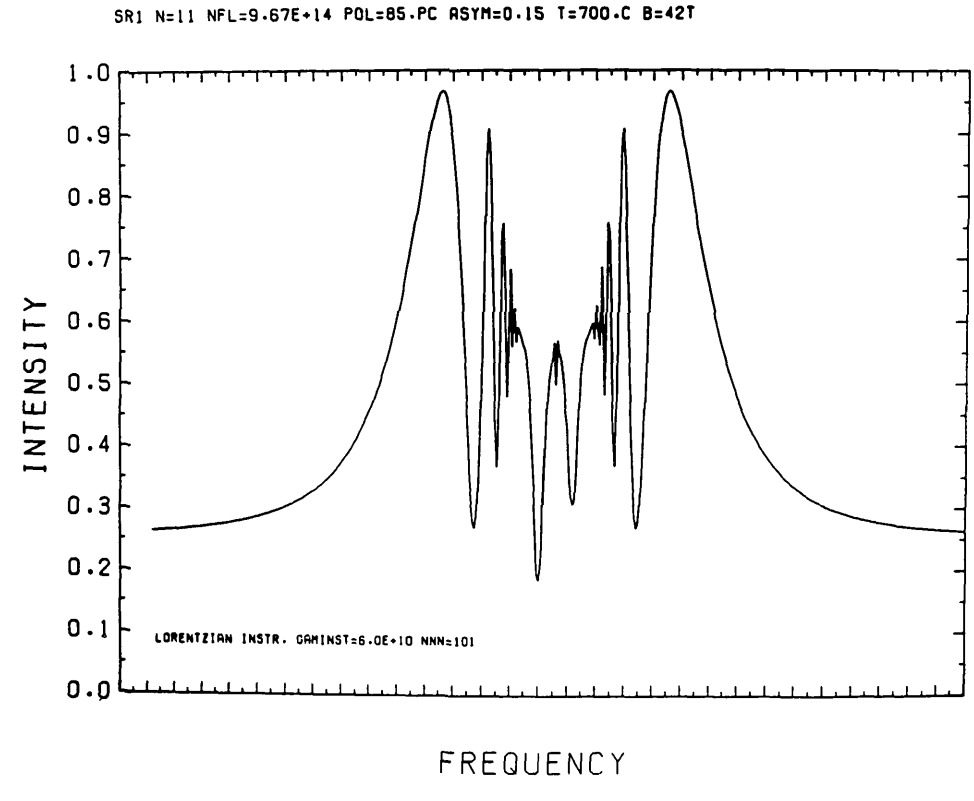

Figs.III23 and 24 SrI n=11 computed spectra. All parameters used were identical to those of Fig.III1 except that the apparatus width was $4.0\ 10^{10}$ and $6.0\ 10^{10}$ respectively.

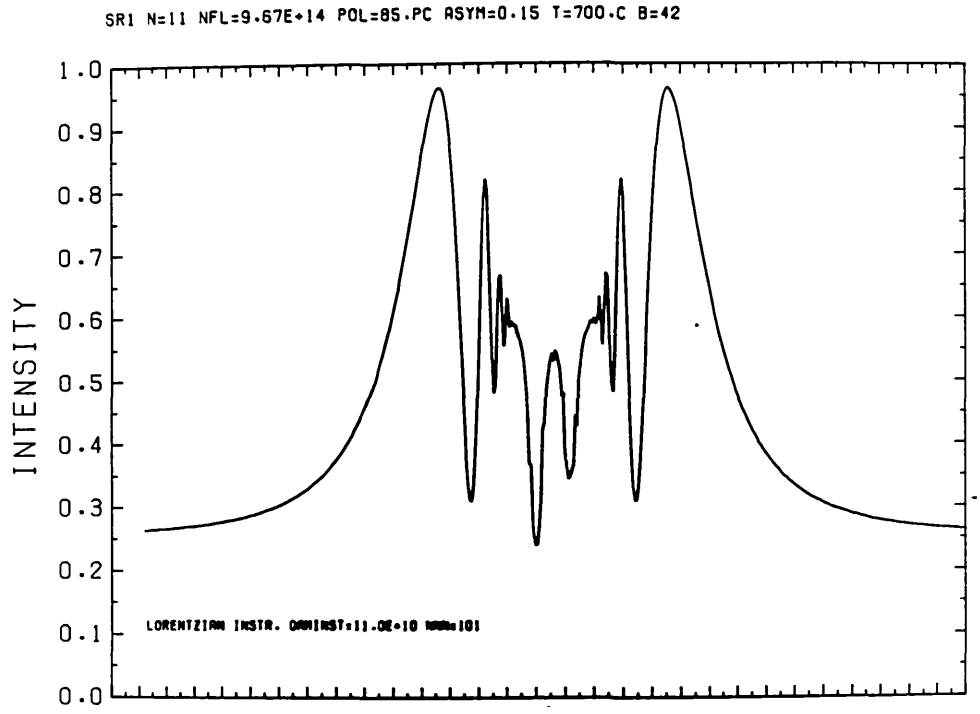

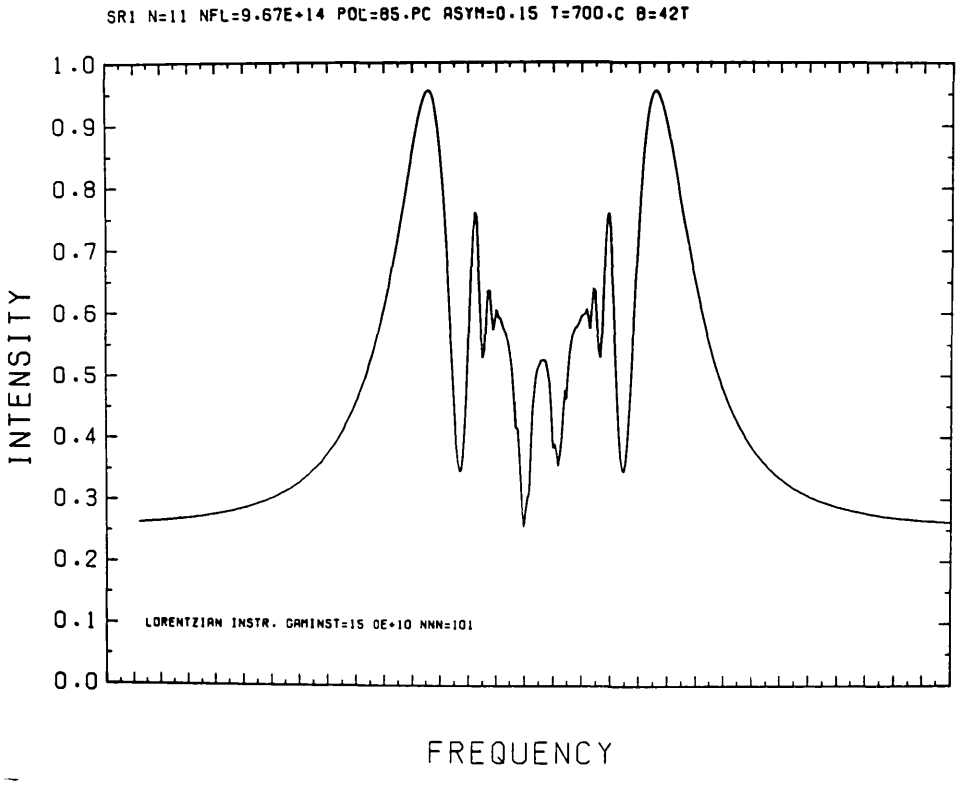

Figs.III26 and 27 SrI n=11 computed spectra. All parameters used were identical to those of Fig.III1 except that the apparatus width was 11.0 10^{10} and 15.0 10^{10} respectively.

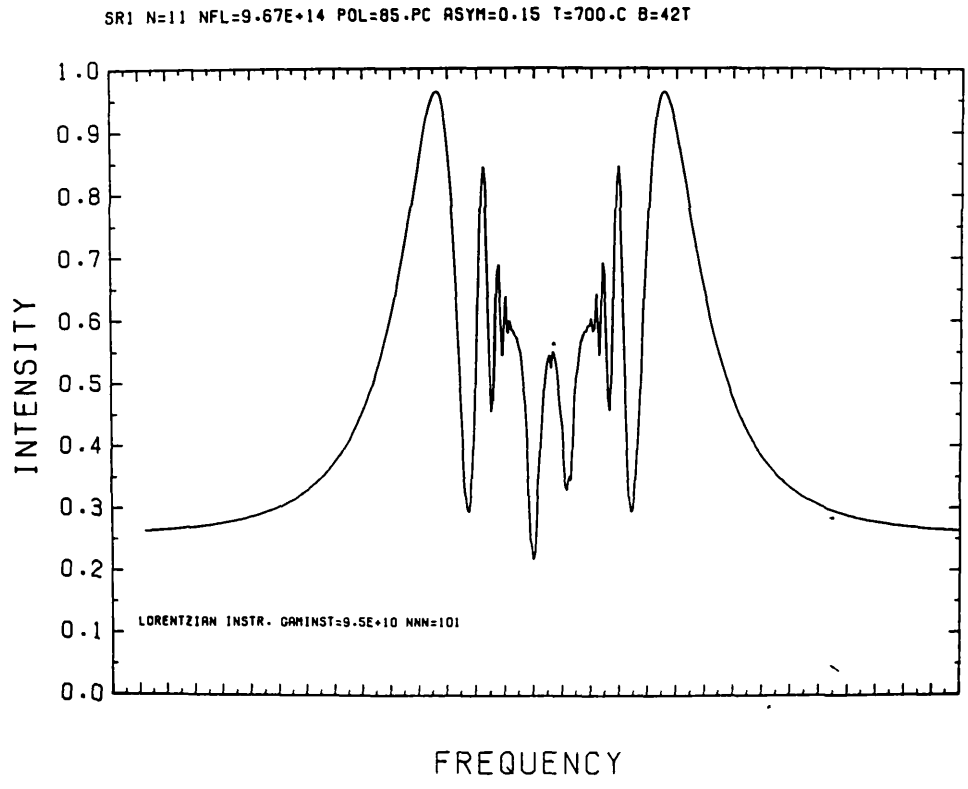

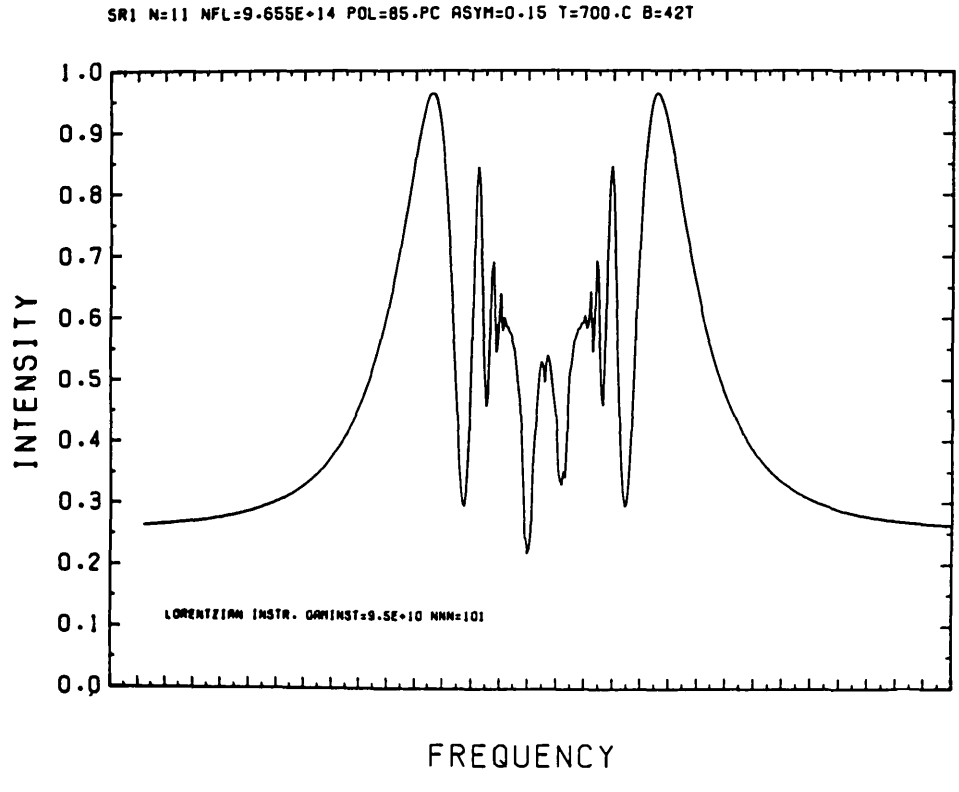

Figs.III25 and 28 SrI n=11 computed spectra. All parameters used were identical to those of Fig.III1 except that the apparatus width was $9.5\ 10^{10}$ and Nfz=$9.68\ 10^{14}$ and $9.655\ 10^{14}$ respectively.

produce the visual resemblance with the experimental results-but that no great accuracy in the knowledge of the exact apparatus width is necessary.

4b.Numerical Calculation of the Convolution Integral

It was said above that at each frequency point ν the intensity was convoluted with the Lorentzian apparatus function over a distance $+2\ \Delta\nu_{APP}$ to $-2\,\Delta\nu_{APP}$ taking 100 points in between, ie:

$$I(\nu) = \int_{+2\Delta\nu_{APP}} I(\nu - \nu^*)\, L(\nu^*)\ d\nu^* \qquad \text{(III2)}$$

$$= \sum_{l=1}^{l=100} I\left\{\nu - \left(2-4\left(\frac{101-1}{100}\right)\right)\Delta\nu_{APP}\right\}. L\left(2-4\left(\frac{101-1}{100}\right)\Delta\nu_{APP}\right).\frac{4\Delta\nu_{APP}}{100}$$

Figs.III29,30,31,1 and 32 represent the spectrum of SrI n=11 calculated with the same parameters and $\Gamma_{APP}=8.50\ 10^{10}$ and $Nfz=9.67\ 10^{14}$ but having different number of steps in the convolution summation, ie 21,51,81, 101 and 161 respectively. From Figs.III29 to 32 and Fig.III1a which is the experimental figure, it is obvious that a very good quality of the computed spectrum is produced when the number of steps between $+-2\ \Delta\nu_{APP}$ is greater or equal to 100. Fig.III32 which is calculated with 161 steps and takes 1.6 times the computer time required to calculate the spectrum with 101 steps (Fig.III1) and the two figures are almost identical. Therefore in all the calculations the optimum number of steps was considered to be 100.

In the calculations described so far, the convolution of the intensity profile with the apparatus function at a particular frequency point ν of the spectrum was considered to cover the $+2\Delta\nu_{APP}$ to $-2\Delta\nu_{APP}$ frequency range. This means that

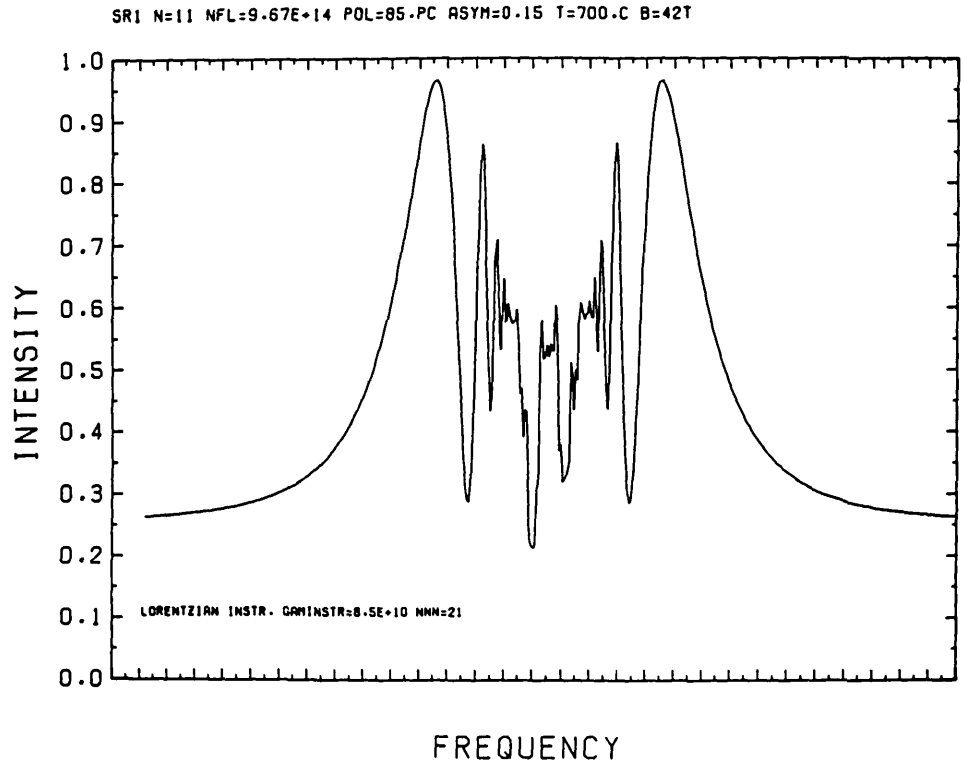

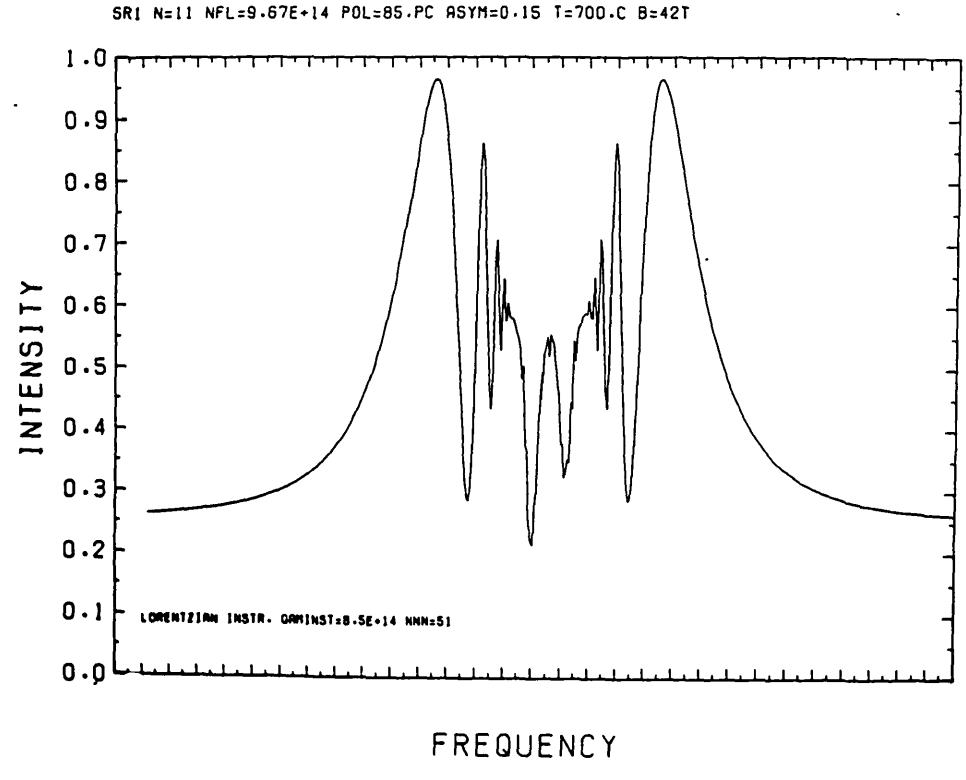

Figs.III29 and 30 SrI n=11 computed spectra. All parameters used were identical to those of Fig.III1 except that the number of steps between two successive freqeuncy points was 21 and 51 respectively as opposed to the 101 of Fig.III1.

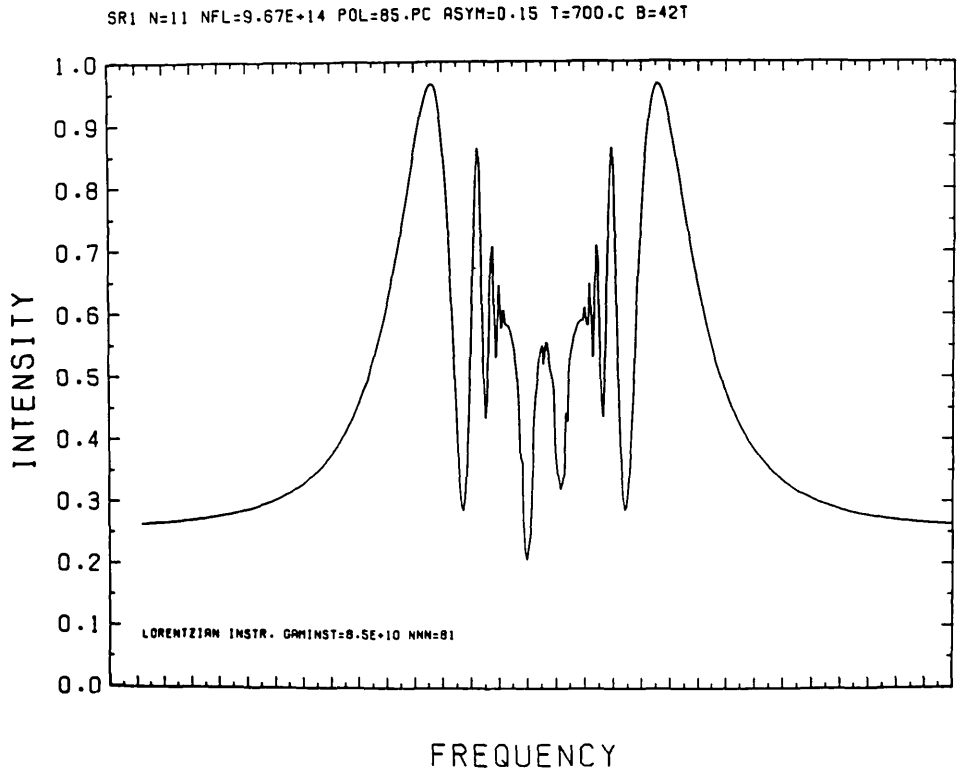

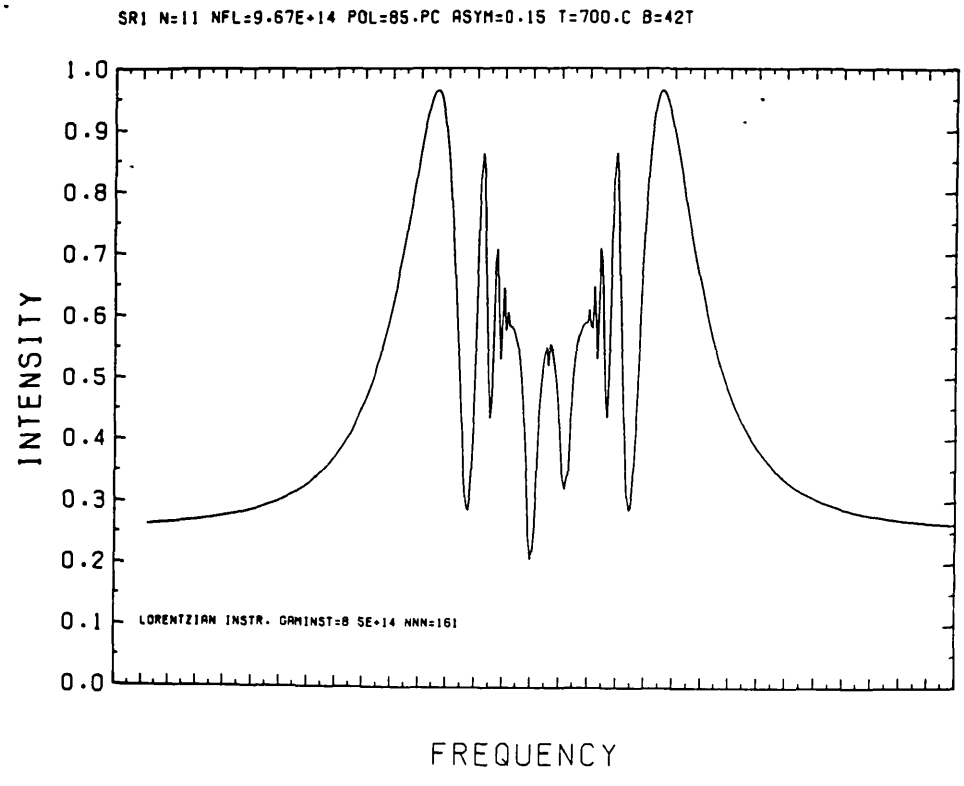

Figs.III31 and 32 SrI n=11 computed spectra. All parameters used were identical to those of Fig.III1 except that the number of steps between two successive frequency poirts was 81 and 161.

the Lorentz function is taken up to the following point symmetric about the frequency point ν_o mentioned in equation III2: $L(\pm 2\ \Delta\nu_{APP}) =$

$$\frac{4}{\Gamma_{APP}} \frac{(\Gamma_{APP}/4\pi)^2}{(2\Delta\nu_{APP})^2 + (\Gamma_{APP}/4\pi)^2} = \frac{4}{\Gamma_{APP}} \frac{1}{17} = I_o/17$$

ie this can be represented schematically as:

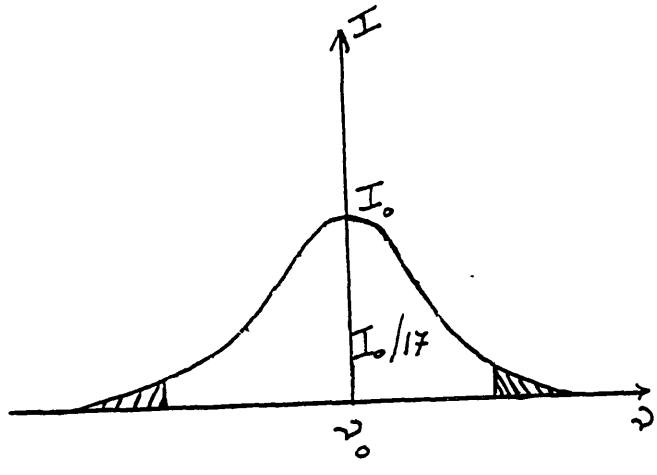

From the above, it is obvious that the assumption of replacing the infinity limits of the convolution integral with $+2\ \Delta\nu_{APP}$ and $-2\ \Delta\nu_{APP}$ can include information up to (1.-0.058) of the total intensity (ie. that $0.058*I_o$ is left out), after which a greater accuracy is not absolutely necessary for good quality results but which would greatly increase the computing time since as seen above the steps of the summation cannot be smaller than $4\ \Delta\nu_{APP}/100$. Therefore from the above facts it is justified to assume that a frequency step in the numerical calculation of the convolution integral must be greater or equal to about $4\ \Delta\nu_{APP}/100$ and that it is adequate to replace the infinity

limits of this integration with +-2 $\Delta\nu_{APP}$ as this goes out to 0.058 of the Lorentzian and gives us almost all the necessary information whilst keeping the computing time at a reasonable level.

4c.Study and Comparison of Lorentzian, Gaussian and Triangular Apparatus Functions

So far the apparatus function used in the calculations, had a Lorentzian form:

$$L(\nu^*)\, d\nu^* = \frac{\Gamma_{APP}\ /4\pi^2}{(\nu - \nu^*)^2 + (\Gamma_{APP}\ /4\pi)^2} \qquad \text{(III4)}$$

where $\Gamma_{APP}=2\pi\ \Delta\nu_{APP}$ and where $\Delta\nu_{APP}$ is the full width half maximum intensity corresponding frequency spread. The above expression is already normalised, since:

$$\int_{-\infty}^{+\infty} L(\nu^*)\, d\nu^* = \frac{4}{\Gamma_{APP}} \int_{-\infty}^{+\infty} \frac{(\Gamma_{APP}\ /4\pi)^2\, d\nu^*}{(\nu\ -\nu^*)^2 + (\Gamma_{APP}\ /4\pi)^2} = 1 \qquad \text{(III5)}$$

Fig.III1 shows the spectrum of SrI n=11 calculated with a Lorentzian apparatus function with $\Gamma_{APP}=8.50\ 10^{10}$ and with using 100 points to calculate the convolution integral at every frequency point of the pattern.

It is useful to see the effect of another apparatus profile of the same FWHM intensity on these calculations. A Gaussian has the form:

$$\overset{G}{L}(\nu^*) = \frac{1}{\sqrt{\pi}} \frac{1}{\Delta\nu_{1/e}^{APP}} e^{-(\nu-\nu^*)^2/(\Delta\nu_{1/e}^{APP}\ )^2} \qquad \text{(III6)}$$

where $\Delta\nu_{APP}^{(1/e)}$ is the full frequency width at the 1/e intensity. For the above assumption to hold (ie both Gaussian and

Lorentzian profiles to have the same FWHM), we have:

$$L^G(\text{half maximum}) = \frac{1}{\sqrt{\pi}} \frac{1}{\Delta\nu_{1/e}^{APP}} \frac{1}{2} = \frac{1}{\sqrt{\pi}} \frac{1}{\Delta\nu_{1/e}^{APP}} e^{-(\nu-\nu_{\frac{1}{2}})^2/(\Delta\nu_{1/e}^{APP})^2}$$

which means that the $FWHM^G = 2(\nu_{1/2} - \nu_o) = 2\,\Delta\nu^{APP}_{1/e}\sqrt{\ln 2}$ and since the $FWHM^L = \Delta\nu_{APP} = \Gamma_{APP}/2\pi$ it is concluded that:

$$\Delta\nu_{1/e}^{APP} = \frac{\Gamma_{APP}}{4\pi\sqrt{\ln 2}}$$

and this can be inserted into the Gaussian profile:

$$L^G(\nu^*)\,d\nu^* = \frac{e^{-(\nu-\nu^*)^2/(\Delta\nu_{1/e}^{APP})^2}}{\sqrt{\pi}\cdot\Delta\nu_{1/e}^{APP}}$$

The above function is already normalised since:

$$\int_{-\infty}^{+\infty} L^G(\nu^*)\,d\nu^* = \int_{-\infty}^{+\infty} \frac{e^{-x^2}\,dx}{\sqrt{\pi}\,\Delta\nu_{1/e}^{APP}} = 1 \qquad \text{with} \quad x = \frac{\nu - \nu^*}{\Delta\nu_{1/e}^{APP}}$$

The usual calculations were performed for SrI n=11 keeping all the parameters constant (including $\Gamma_{APP}=8.50\ 10^{10}$) but this time replacing the Lorentzian apparatus function with the Gaussian one just described. From these calculations Fig.III33 was produced. Comparing Figs.III1 and 33 it can be easily seen that the ones computed with the Gaussian function have sharper and stronger in intensity magneto-optical beats. This is due to the fact that the Lorentzian function is flatter and its maximum intensity point is lower than the Gaussian, ie:

$$L^{Lor}(\nu_o) = 4/\Gamma_{APP}$$

whereas:

$$L^G(\nu_o) = \frac{1}{\sqrt{\pi}\ \Delta\nu^{APP}_{1/e}} = \frac{4}{\Gamma_{APP}} .\pi\sqrt{\ln 2}$$

which means that the Gaussian maximum is $\sqrt{\pi \ln 2}$ times stronger than the Lorentzian one.

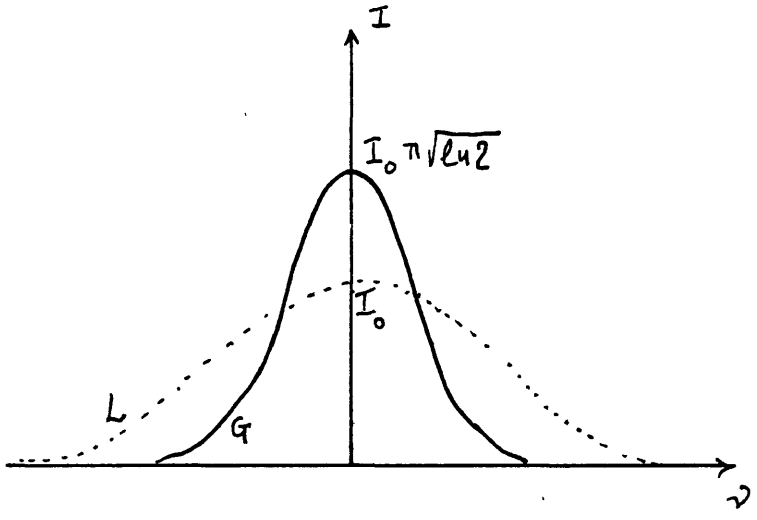

The above figure shows schematically the comparison of the Gaussian with the Lorentzian. Figs.III1 and 33 are computed with all the parameters and calculations identical (exept that Fig.III1 is for a Lorentzian apparatus profile whereas Fig.III33 is for a Gaussian one) including the assumption that the numerical convolution at any frequency point goes from $-2\,\Delta\nu_{APP}$ to $+2\,\Delta\nu_{APP}$. It was shown in section 4b of the present chapter that for the Lorentzian case the calculations go out to 0.058 of the total intensity which is of quite adequate accuracy. Similarly, for the Gaussian case it can be said that:

$$L^G(\pm 2\Delta\nu_{APP}) = \frac{\exp -(2\Delta\nu_{APP})^2/(\Delta\nu_{App(1/e)})^2}{\sqrt{\pi}\ \Delta\nu^{APP}_{1/e}} = e^{-4\ \ln 2}/\Delta\nu^{APP}_{1/e}\sqrt{\pi} = e^{-4\ \ln 2} I_o$$

the $+-2\Delta\nu_{APP}$ assumption includes information up to 0.0625 times the maximum intensity which is excellent accuracy. Fig.III34 shows the calculation of the SrI n=11 pattern where the solid line is produced with a Lorentzian apparatus function and the dashed line with a Gaussian while every other parameter is held constsnt in the two cases. As expected the Lorentzian pattern is less sharp and weaker than the Gaussian. This was shown in the above figure (the Lorentz function is more spread towards the wings and has a weaker peak at the centre). Furhter it was shown that the $+-2\ \Delta\nu_{APP}$ assumption loses all the information after 0.058 Io in the Lorentz case, while 0.0625 $\times\ I_o$ in the Gaussian.

A third type of apparatus function tried in the present calculations was assumed to have a triangular form, ie:

$$L^{T}(\nu^*)\ d\nu^* = \frac{2\pi}{\Gamma_{APP}}\ Max\left(\ 1 - \frac{\nu^*}{\Gamma_{APP}}\ \right)$$

In this case the limits of the convolution integral extended from $-2\ \Delta\nu_{APP}$ to $+\ 2\ \Delta\nu_{APP}$ with 50 steps accross and therefore the area under the triangle is normalised again, ie:

$$\text{Area} = 1/2\ \text{base*height} = (1/2)\ 2\Delta\nu_{APP}\ \frac{2\pi}{\Gamma_{APP}} = 1$$

and the height of the triangle was $2\ \pi/\ \Gamma_{APP}$ like the Lorentzian case. Fig.III35 compares the SrI n=11 pattern produ ced with a Lorentzian profile (solid line) and with a triangular one (dashed line). Computationally this latter type of apparatus function is much preferable as its calculation is much quicker and cheaper than exponentials or inverse squares. Further the triangular pattern on Fig.III35 resembles roughly to the

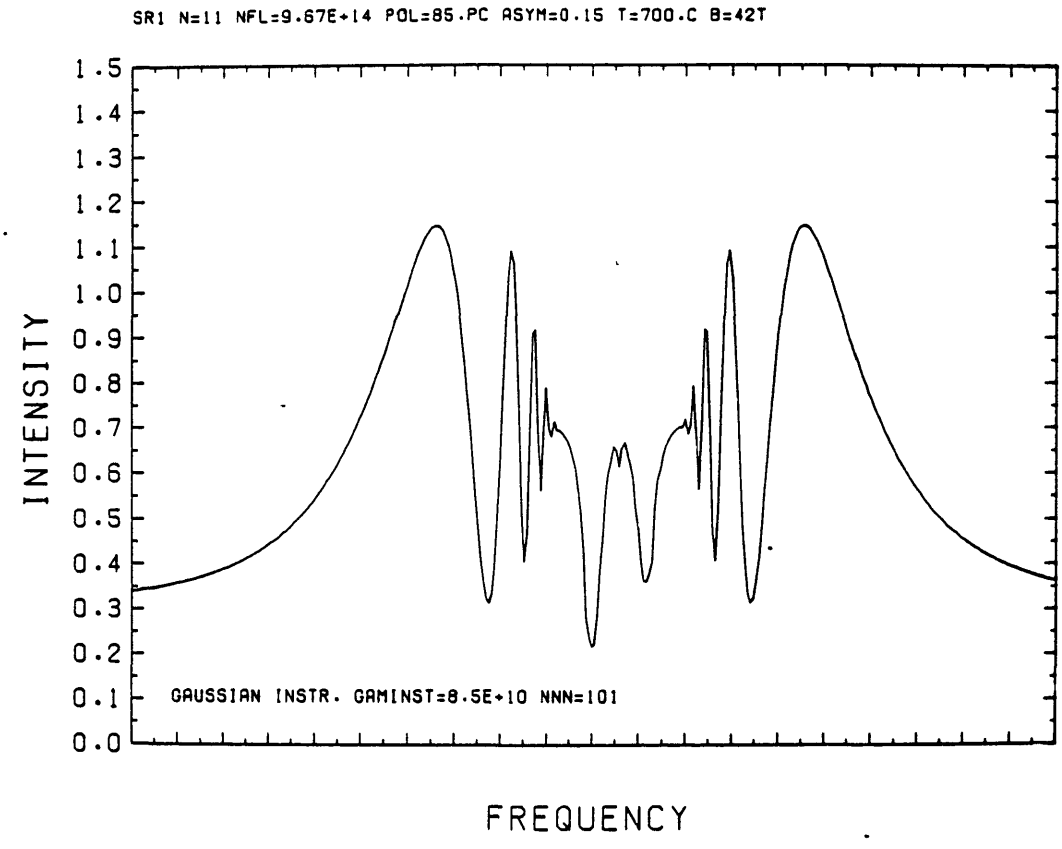

Fig.III33SrI n=11 computed spectrum with a Gaussian apparatus profile. All other parameters used were identical to those of Fig.III1.

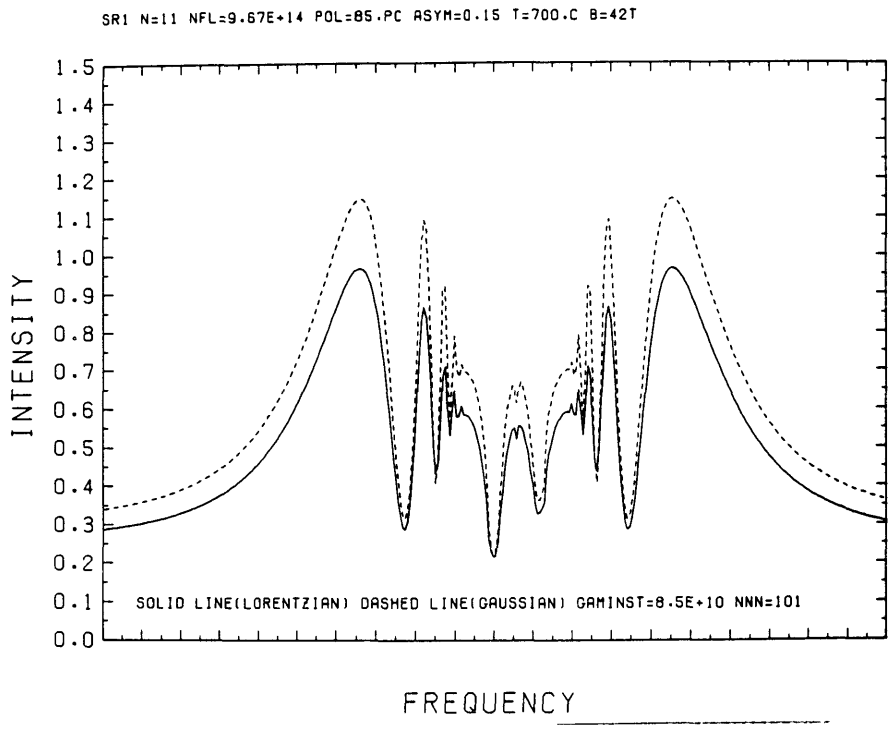

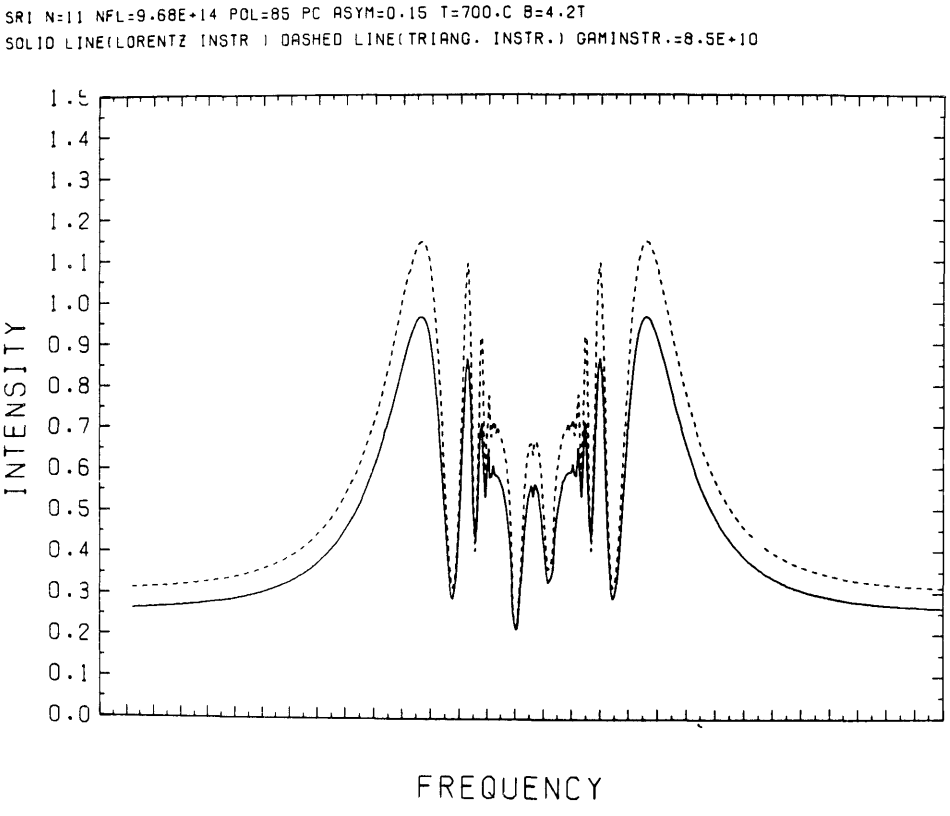

Figs.III34 and 35 SrI n=11 computed spectra with (a) a Gaussian (dashed line) and a Lorentzian (solid line) and (b) a triangular (dashed line) an a Lorentzian (solid line) apparatus function. All parameters used were identical to those of Fig.III1.

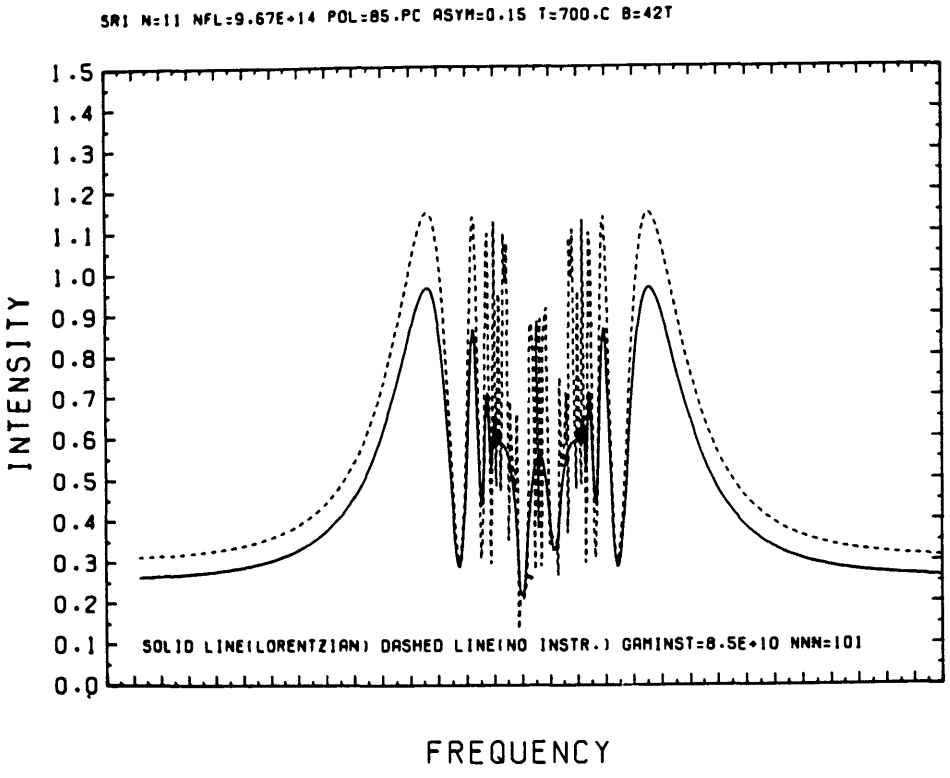

Fig.III36SrI n=11 computed spectrum with a Lorentzian apparatus smoothing (solid line) and with no smoothing (dashed line). All the parameters used were identical to those of Fig.III1.

experimental spectrum of Fig.III1a, but however the Lorentzian or the Gaussian are more realistic.

Finally, as a concluding comment to this section, the magneto- optical spectrum was plotted without a smoothing apparatus function and Figs.III21 and 21a were produced. As expected, the magneto-optical beats were very strong and sharp and the $\pi/2, \pi, 3\pi/2$ etc intensity maxima and minima remain at the same intensity level until the Lorentz componenets are reached (in this case they are more squared than in the smoothed case). The smoothing effect of the apparatus function can be readily demonstrated in Fig.III36 where it can be seen how it chops off the peaks of the beats of the unsmoothed pattern. Also the rotation peaks in the Lorentzian spectrum do not remain at a constant level but decrease more and more until they reach the Lorentz doublet.

5.Computational Techniques

In Chapter I the equation of the emitted intensity from the furnace was derived as well as more appropriate expressions for the refractive index and absorption coefficient for a line with a Voigt profile. Then it was assumed that after inserting $n_{+-}(\nu)$ and $a_{+-}(\nu)$ in the intensity formula, $I(\nu)$ must be smoothed over the apparatus profile $L(\nu)$ which might be Lorentzian, Gaussian or triangular. Therefore the following integration has to be performed:

$$I^{final}(\nu) = \int I(\nu - \nu^*)\, L(\nu^*)\, d\nu^*$$

where

$$L(\nu^*) = \frac{\Gamma_{APP} / 4\pi^2}{\nu^{*2} + (\Gamma_{APP}/4\pi)^2}$$

is the Lorentzian apparatus smoothing. This implies that $a^V_{+-}(\nu - \nu^*)$ and $n^V_{+-}(\nu - \nu^*)$ have to be calculated in the computer code and then synthesise $I(\nu - \nu^*)$ according to:

$$I(\nu-\nu^*) = I_0/4\ \{(e^{-a^V_+(\nu-\nu^*)z/2} - e^{-a^V_-(\nu-\nu^*)z/2}) +$$

$$4\, e^{-(a^V_+(\nu-\nu^*) + a^V_-(\nu-\nu^*))z/2} \sin^2((n^V_+(\nu-\nu^*) - n^V_-(\nu-\nu^*))z/2)\}P/100$$

$$+(100- P)/100\ I_0 e^{-(a^V_+(\nu-\nu^*) + a^V_-(\nu-\nu^*))z} + k\, e^{-a^V_\pm(\nu-\nu^*)\, z} \qquad \text{(III7)}$$

As mentioned in section 10 of Chapter I, the absorption coefficient can be related to the real part of the Complex Error function and the refractive index to the imginary part, since:

$$a^V_\pm(\nu-\nu^*) = \frac{\sqrt{\pi}\ e^2\ Nf}{\Delta\nu_D\ m\ c}\ \frac{a}{\pi} \int \frac{e^{-y^2}\, dy}{\left(\frac{\nu-\nu_0\ -\nu^* \mp A}{\Delta\nu_D} - y\right)^2 + a^2}$$

and

$$n^V_\pm(\nu-\nu^*) = 1 - \frac{e^2\ Nf}{4m\sqrt{\pi}(\nu_0 \pm A)\Delta\nu_D}\ \frac{1}{\pi} \int \frac{e^{-y^2}((\nu-\nu_0-\nu^* \mp A)/\Delta\nu_D - y)\, dy}{\left(\frac{\nu-\nu_0-\nu^* \mp A}{\Delta\nu_D} - y\right)^2 + a^2}$$

where y,a,A and $\Delta\nu_D$ were defined in section 10 of Chapter I and since:

$$\mathrm{Im}(P(z)) = \frac{1}{\pi} \int_{-\infty}^{+\infty} \frac{e^{-t^2}\ (s-\alpha - t)\, dt}{(s-\alpha-t)^2 + \beta^2}, \quad \mathrm{Re}(P(z)) = \frac{\beta}{\pi} \int_{-\infty}^{+\infty} \frac{e^{-t^2}\, dt}{\beta^2 + (s-\alpha-t)^2}$$

where I(z) is the Complex Error function and $z = s - \alpha + i\beta$, it can be said that: $a^V_\pm(\nu-\nu^*) = C_1 * \mathrm{Real}\left(Z\left(\frac{\nu - \nu_0\ -\nu^* \mp A}{\Delta\nu_D} + iA\right)\right)$

where $n_{+}^{V}(\nu-\nu^*) = 1 - C_2^{\pm} * \text{Imaginary} \left(Z \frac{\nu - \nu_o - \nu^* \mp A}{\Delta\nu_D} + iA \right)$

$$C_1 = \frac{e^2\sqrt{\pi}Nf}{\Delta\nu_D\, mc} \quad , \quad C_2^{\pm} = \frac{e^2\, Nf}{4m\sqrt{\pi}(\nu_o \pm A)\, \Delta\nu_D}$$

and $Z(\omega)$ is the Complex Error function with $\omega = (\nu - \nu_c - \nu^* \mp A)/\Delta\nu_D + iA$. From the paper of Hui et al [5] a quick method for solving for the real and imaginary parts of a complex error function, can provide in this case quick and accurate solutions for $a^{V}_{+-}(\nu - \nu^*)$ and $n^{V}_{+-}(\nu - \nu^*)$.

After the refractive index and the absorption coefficient were obtained at a frequency $(\nu - \nu^*)$, the apparatus convolution was performed. In the present work, the apparatus convolution was not performed from $-\infty$ to $+\infty$ (as this is physically impossible) but was performed instead between $+2\ \Delta\nu_{APP}^{N}$ and $-2\ \Delta\nu_{APP}^{N}$ (where $\Delta\nu_{APP}^{N}$ is the FWHM) taking 100 points of summation in between. These two assumptions had to be made for the sake of realistically inexpensive computing time and were justified previously in section 4 from the quality of the results obtained. The whole computed spectrum consisted of 1000 frequency points (from +24*A to -24*A).

Schematically, the sequence of the calculations performed can be shown as follows:

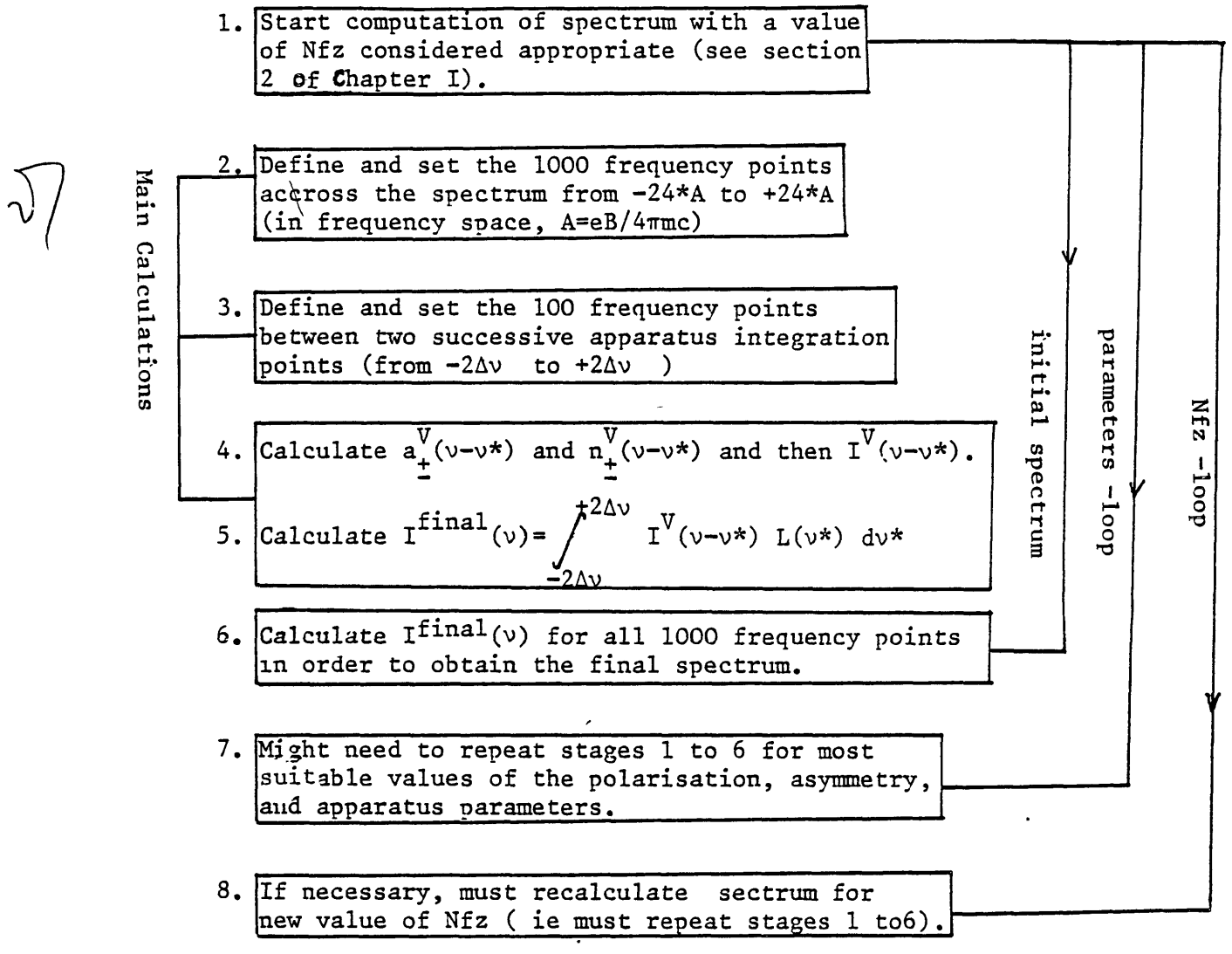
Main Calculations
1. Start computation of spectrum with a value of Nfz considered appropriate (see section 2 of Chapter I).
2. Define and set the 1000 frequency points across the spectrum from -24*A to +24*A (in frequency space, A=eB/4πmc)
3. Define and set the 100 frequency points between two successive apparatus integration points (from -2Δν to +2Δν)
4. Calculate $a_{\pm}^{V}(\nu-\nu^*)$ and $n_{\pm}^{V}(\nu-\nu^*)$ and then $I^{V}(\nu-\nu^*)$.
5. Calculate $I^{final}(\nu)=\int_{-2\Delta\nu}^{+2\Delta\nu} I^{V}(\nu-\nu^*)\, L(\nu^*)\, d\nu^*$
6. Calculate $I^{final}(\nu)$ for all 1000 frequency points in order to obtain the final spectrum.
7. Might need to repeat stages 1 to 6 for most suitable values of the polarisation, asymmetry, and apparatus parameters.
8. If necessary, must recalculate sectrum for new value of Nfz (ie must repeat stages 1 to6).
initial spectrum
parameters -loop
Nfz -loop

All these calculations were performed on the 174 IBM main college computer interactively. Once the values for the intensity of the spectrum were obtained as a function of frequency, it was desirable to obtain a graphical output of these results and also to be able to determine the value of $\delta\nu$ that corresponded to a $\pi/2$ or π rotation as this was necessary to determine, from the comparison from the experimentally obtqained spectra whether our computed spectrum was in the correct magneto-optical cycle. The latter was easily calculated by the computer by making use of the fact that the intensity is at a maximum for rotation angle $\pi/2$ and at a minimum at rotation angle π. A new piece of code was added at the end of the previously described program in order to search for these intensity maxima and minima. The computer time used now was almost twice than before inserting the extra code to calculate the $\delta\lambda(\pi, \pi/2)$ distance. In this work, three types of graphics routines were used. The first was a 3-dimentional graphics routine necessary to produce the MOV cycles where the x-axis was the frequency, the y-axis was the intensity and the z-axis was the product Nfz. The second type of graphics was an accurate presentation of the results requiring a large volume of output with many graphs on each file (each graph was performed with a different Nfz value -within the correct magneto-optical cycle- and by carefully observing the middle of the pattern and comparing it with the experimental spectra, the correct value of Nfz could be deduced. Finally, the third type of graphics used, was very accurate, with very good resolution, labelling possibilities and with the ability to have several curves on the same graph -ideal for producing the best and final

computed spectra. All these three types will be discussed now in more detail, but before proceeding to this it must be said that in all three cases, the values of the intensity and frequency must be first obtained and then use one of the three programs to obtain the desired graphical output.

The Imperial College Computer Centre common plotting library, is a collection of Fortran-callable routines based on a package provided by Calcomp and improved by the ICCC and the University of London Computer Centre personnel. The library enables users to produce graphical output on the microfilm plotter and on the Tektronix graphics terminals.

The first type of graphics required in this work, was used to plot 3-dimensional graphics and exists in the ICCC routine library under the name "Surface" [6]. It produces a succession of curves plotted on to a regular grid. From a representative 3-dimensional graph for SrI n=11 (Fig.III37) it can be seen that the graph cannot be used for a quantitative analysis and therefore its application is mainly pictorial. There are several different functional possibilities that can be requested by the user such as the elimination of any hidden lines in the graph in order to improve the visual clarity of the surface, height clipping, changable viewing angle amd perspective distance, rotation of the axes and picture magnification. Matching microfilm hardcopy of any displayed surface picture (on the Tektronix terminal) can also be produced. There is a limit of 10000 points to be plotted per graph. In the present calculations for the sake of economising computing time only the region between the two Lorentz components was plotted in the (x-y) plane (Fig.III37).

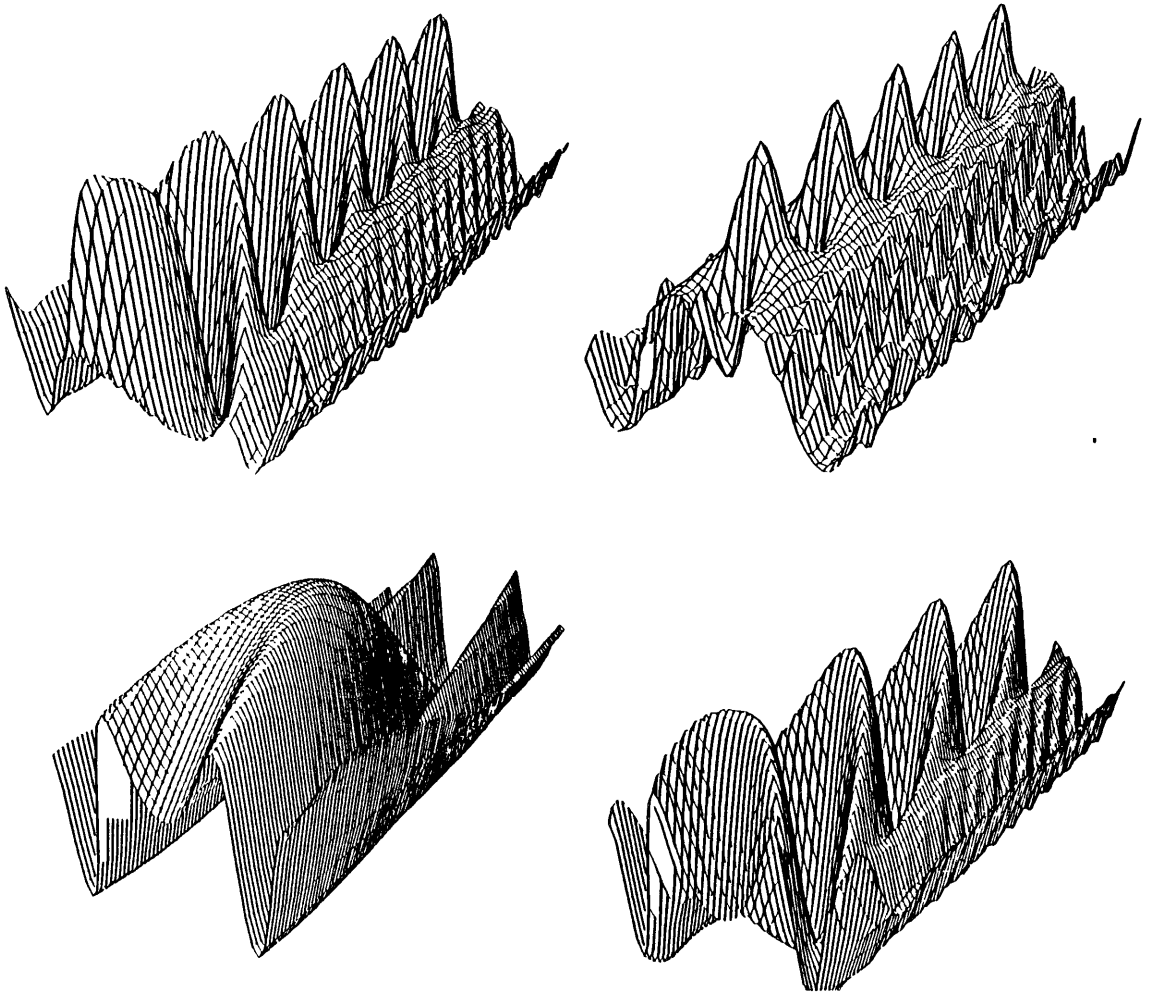

Fig.III37 MOV cycles for n=11,16,24 and 18 for SrI. The sensitivity of the cycle structure to changes in Nfz decreases as n increases under otherwise identical experimental conditions.

The second graphics routine was stored in the ICCC library under the name "Simple" [7]. This routine as well as every graphics routine, consists of a number of plotting functions each of which in tern is made up of many basic plotting movements. The functions performed by this plotting routine include the establishing of a plot origin, drawing straight lines or curves (scalling arrays of points to be plotted over a given length of plot, drawing various symbols and finally drawing and labelling axes. This graphics routine can provide a changable overall size of the graph, displacement of the origin, production of symbols at specified positions and the x- and y-axes. As in the previous case, the graph produced by "Simple" can be transferred to microfilm hard copy where a single "picture" is prepared on a grid of 16000*16000 points and each point can be at any of 30 levels of intensity. Therefore the most detailed graphics with excellent resolution can be produced on microfilm and the drawing speed is very fast since the drawing is dove by an electron beam. All the computed graphical spectra presented in this thesis were originally produced on microfilm and then developed. Another property of the "Simple" routine which was taken advantage of for these calculations, was the fact that with some modifications in the commands several graphs (corresponding to different Nfz values) could be produced one after the other on the same piece of microfilm so that the observation of the middle part of the pattern and the comparison with experimental results was a comparatively easy task (Fig.III38). This saved plenty of time and effort. Although the routine described next produces much more tidy graphs it does not possess the above property, which is so useful, that

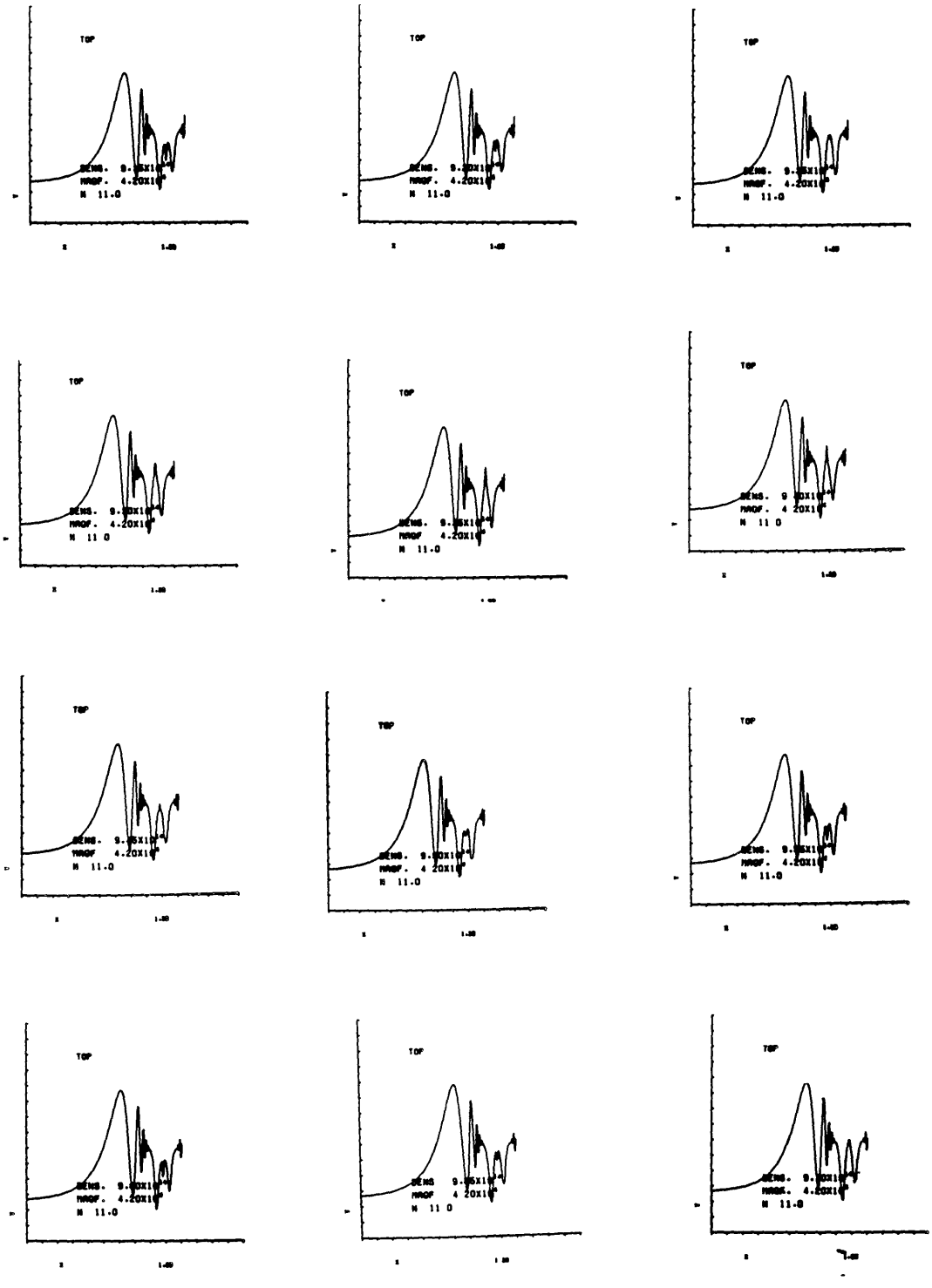

Fig.III38SrI n=11 MCV cycle. The sensitive dependence of the middle part on the product Nfz is obvious.

"Simple" had to be used at this stage of calculations.

Finally, the next routine used for the plotting of the final versions of the spectra was called "Gplot" and was originally developed by A.Bradshaw. It is basically of the same form as the "Simple" routine (and uses most of its functions and subroutines) but has the options of labelling the axes, flexible start and end values, a linear or logarithmic x- and y- mesh, a selection of various types of curves and the possibility of having more than one curve between the same set of axes. Also, the axes form a rectangle which produces a very "good-looking" graph and also prints the specified intervals on both axes. At this final point of the calculations and the computational description, some theoretical MOV patterns for SrI n=11,15,20 and 25 will be shown together with their corresponding experimental patterns (Figs.III39 and 40). The excellent quality of reproduction is the proof we need to conclude that the MOV method is correct.

6.Limitations of the Method

This section will be devoted to recapitulate the points mentioned previously which might be a source of error to our calculations and which are limitations of the method.

a) From the "given" data uncertainties can exist in the temperature and the B-field. For the n=11-27 SrI example that we studied thoroughly, 40% and 5% uncertainties in the above quantities respectively produce a 0.1% and 0.4% error in the determination of f-values. In future experiments, it is clear that the B-field should be surveyed more carefully within the magnet and its variations with time should be monitored more

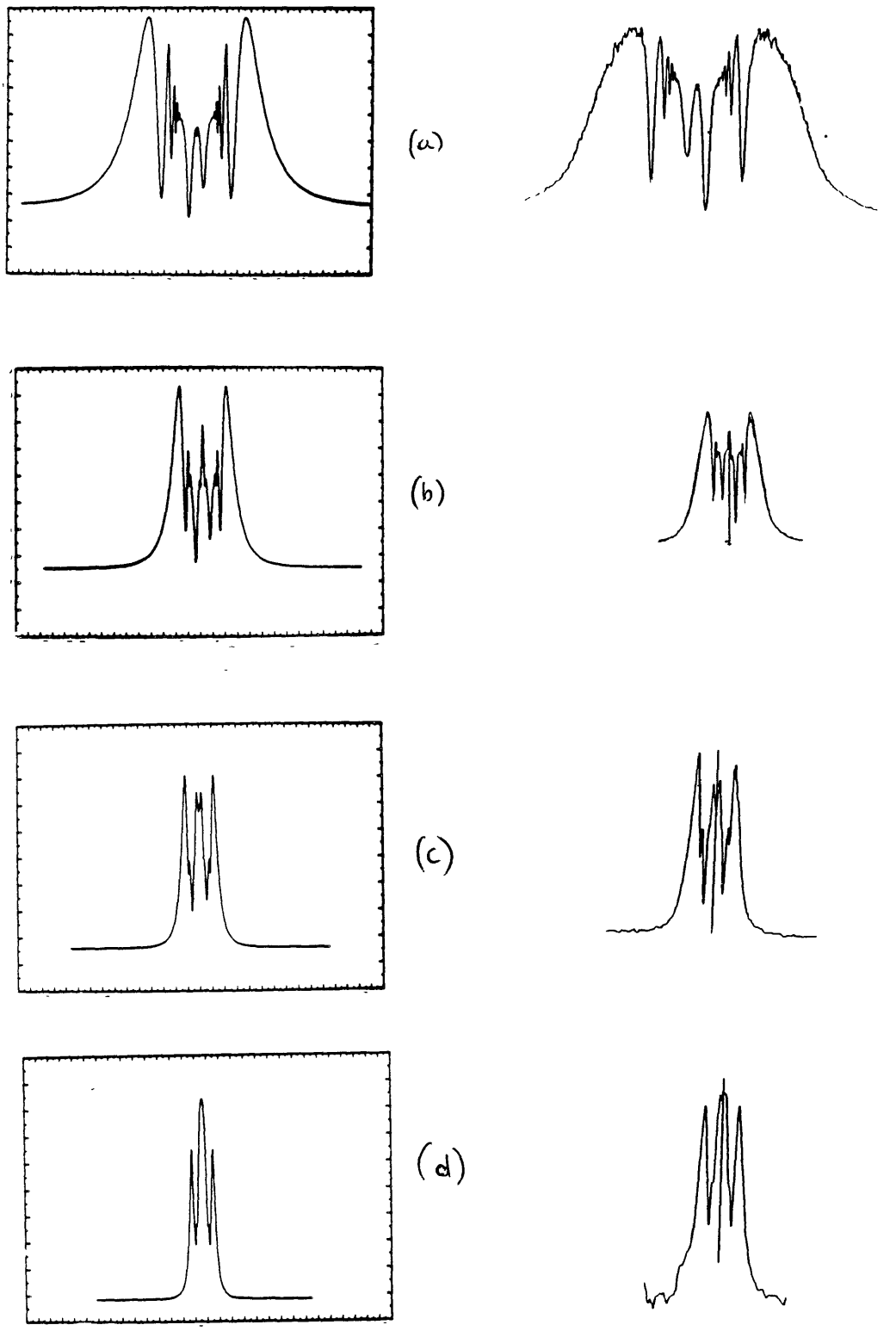

Figs.III39 and 40 SrI n=11,15,20 and 25 spectra theoretical and experimental in quite good agreement.

Plase note that figs (a) and (b) are reversed in energy scale with respect to the data.

exactly. Temperature data is less crucial but is also required.

b) From the "chosen" data uncertainties can exist in the value of the FWHM of the apparatus function and it was found that an 11% change in the apparatus width produces only an error of 0.1% in Nfz. The optimum number of steps between two successive integration points can easily be determined as well as the integration limits can be chosen such that the calculated profile tends almost to the value it would have with the infinity limits. It would seem that the closer the apparatus function can be to the true experimental function, the better the data will be since the maximum number of oscillations of intensity will be observed. Thus future experiments should concentrate on stabilising the vapour column (eg. by using test pipes) and using more stable superconducting magnets.

c) The particular values of the polarisation of the grating and of the pattern asymmetry play no detectable role in determining the correct value of Nfz but only affect the appearance of the spectra. Therefore, we believe that one need not worry about these two factors until the others mentioned above have been attended to.

d) The following practical problem did not occur during our present calculations but might very easily do so in the future. There is a limited number of frequency points across the spectrum and of points between two integration steps that the presently available College computer can store and calculate. However we believe that this problem will only arise if it is required to double the resolution or to study many members of a series on one run (see for "overlapping lines" MOV technique that tackles two or more lines simultaneously Chapter V).

Conclusions

In this chapter the smoothing of the spectrum by the apparatus function was introduced and compared to an unsmoothed pattern. At each frequency point, the apparatus convolution procedure was performed by a numerical integration extending over $+-2\,\Delta\nu_{APP}$ (FWHM intensity frequency spread) with 100 summation steps in between. Both these assumptions were justfied. Then, three types of apparatus smoothing were used to compute the spectrum and were compared to the experimental pattern of Fig.III1a. Although the $+-2\,\Delta\nu_{APP}$ assumption allows the Gaussian function to go out up to 0.0625 times its maximum value and up to 0.058 for the Lorentz case, both of them produced very good results. The fact that the MOV method was so independent of the exact type of apparatus profile used, was a great advantage and a further proof of its correctness and reliability. A triangular function was also used (more as a test than as a real possibility) and it produced results of the correct general shape. Also all the computational details and techniques were described in this chapter.

It was also seen that a large variation in tem perature affected the determination of f-values very little (0.1%) while a 4.5% variation of the B-field affected them only by 0.3%. In what follows it will be assumed that the experimental values were correct, but it is worth noting that they need not be determined with the greatest accuracy. It was also seen how the polarisation and asymmetry terms added to the original intensity formula improved the appearance of the patterns without however affecting the f-value determination.

As a concluding remark to this chapter it must be said that the more soundly based MCV method with the Voigt line profile, the more realistic apparatus function and the more elaborate calculations on a large computer turned out to yield a big improvement on the early magneto- optical calculations by Connerade [1]. The results obtained with the improved method will be presented in Chapter VI.

REFERENCES TO CHAPTER III

1. Connerade J.P. J. Phys B., 16, 399 (1983)

2. Connerade J.P., Garton W.R.S. Baig M.A., Hormes J., T.A. Stavrakas and Alexa B. Tour de Physique, 43, C2-317 (1982)

3. Parkinson W.H. Reeves E.M. and Tomkins F.S. J. Phys B., 9, 157 (1976)
   Mitchell C.J. J. Phys B., 8, 25 (1975)
   Penkin N.P. and Shabanova L.N. Optics and Spectroscopy, 12, 1 (1962)

4. Forson E.N. and Wilets L. Adv. in At. and Mol. 16, 343 (1980) (Academic Press - New York 1980)

5. Hui A.K., Armstrong B.H. and Wray A.A. J. Quant. Spec. Rad. Trans., 19, 509 (1978)

6. ICCC Bulletin 4.22/2

7. ICCC Bulletin 4.11/1

8. Kunz. C. "Synchrotron Radiation" Chapter 1 edited by C. Kunz. Topics in Current Physics Vol 7 (1979)

9. "Electromagnetic Radiation" by G.A. Schott (Cambridge University Press 1912)

10. Schwinger J. Phys Rev., 75, 1912)

11. Heinzmann U., Osterheld B. and Schafers F.

Nucl. Instr. and Methods, 195, 395 (1982)

Chapter IV

Some Brief and General Comments on Transition Probabilities

In recent years the determination of atomic transition probabilities has become a very active research area with several hundreds of research articles having as a result to increase the number of lines for which we know the transition probabilities from 10^5 to 10^6 (for an excellent and general reference on transition probabilities see Wiese [1] and references therein).

Atomic transition probabilities and lifetimes are needed in the following fields:(i) Astrophysics: transition probabilities are vital for the determination of stellar element abundances.(ii) Space Physics: far UV and soft x-ray emission spectra from highly ionised species in the solar corona are interpreted with the use of atomic transition probability data.(iii) Plasma Physics: transition probabilities, especially those of stable gases, are used for plasma diagnostics.(iv) Thermonucler Fusion Research: in order to study energy loss problems due to small but heavy element impurities in tokamak devices, transition probabilities are necessary.(v) Development of Laser Systems: in order to achieve the most desirable population inversion in a laser, the knowledge of transition probabilities is vital for the determination of level populations and lifetimes, and (vi) Isotope Separation: in order to separate isotopes, knowledge of transition probability data of the transitions involved in stepwise laser excitation and photoionisation is needed. Finally atomic transition

probabilities can be a very sensitive test of atomic theory. The accuracy of theoretical results can be compared with observations either of transition energies or of transition probabilities thus we can have a measure of the quality of the radial eigenfunctions. Of the two, atomic transition probabilities are a much more sensitive means of checking atomic theory because they depend on the overlap between initial and final wavefunctions rather than on a single wavefunction.

The rates at which energy is absorbed or emitted by an atom are related to the Einstein coefficients. These coefficients are defined and explained in Appendix AIV together with a classical and quantum-mechanical description of the calculation of the absorption coefficient. In the same appendix, some approximate methods for calculating transition probabilities for light elements are also given.

Atomic transition probabilities can be obtained experimentally from emission and absorption measurements. There are two basic difficulties associated with each of these methods. The first is the correct measurement of the intensity which must be compared to that of a standard source and the second is the determination of the populations of the relevant levels. For relative measurements this latter problem disappears but otherwise it can only be overcome if LTE conditions apply and if the temperature is known. For both emission and absorption, attention must also be paid that the line in question is optically thin and, in emission, that there is no continuum radiation arround (which would shift the base line from its true position) and for absorption measurements that the resolution of the instrument is good and that the stray

scattered light can be made minimal as well as the radiation absorbed from the wings of the line. Another basic technique for measuring transition probabilities is the "hook" technique where opacity and intensity calibration problems are non-existent but which fails if the lines are weak or if they overlap with each other. All these methods are discussed in greater detail in Appendix AIV. The beam foil, the delayed coincidence and the Hanle methods can give us life-times and they are also discussed in the same appendix. They have relatively simple experimental set-ups but are very susceptible to radiation trapping effects which affect the level populations.

The MCV method decribed in this thesis, does not depend on the optical thickness of the vapour. This is a very basic advantage over the usual absorption techniques previously discussed (as well as in Appendix AIV). The MCV method gives relative f-value results, thus having the same problem of determining the population density of the level in question, a problem which all the absorption and emission measurements have, if absolute f-values are to be determined. The MCV method can be applied successfully to overlapping lines (see Chapter V) where the "hook" technique fails. Unlike the MCV method, the "hook" technique involves an interferometer and the wavelength regime that it can operate in is determined by the wavelength regime for which interferometers are available. In all the techniques for measuring atomic transition probabilities (absorption, emission and MCV) attention must also be paid so that the column density is not very low, thus producing very weak lines. The Hanle method (which also involves a magnetic field like the MCV method) can produce absolute f-values by giving us the life-time

of the transitions in question. However, for the Hanle effect to be success fully applied, we need quite strong lines and long wavelengths as apposed to the MOV method where such restrictions are not required. If there are more than one lower levels that the upper level k can combine with ($\tau_k = 1/\sum_i A_{ki}$), then it is not possible to determine the transition probability of one particular line from the measured life-time of level k. This is another important restriction of the Hanle method.

References to Chapter IV

1. Wiese W.L. Progress in Atomic Spectroscopy Part B., 1101(1979) (Eds.Hanle H. and Kleinpoppen Plenum Publ. Corp. 1979)

Chapter V

Some Further Extensions of the MOV Method

Introduction

This chapter will be devoted to some extensions of the magneto- optical method discussed so far in this thesis. With the overlapping lines technique it is now possible to calculate accurately the spectra of two lines which are very close to each other. In the first section of this chapter a criterion of the applicability of the method will be derived as well as the method itself will be described. Section 2 will show that the M-O method is still applicable for singlet to triplet transitions while section 3 will justify the neglect of hyperfine structure. Section 4 will show that the Weingeroff method [1] of measuring absolute f-values cannot be applied to our case since it is exclusively applicable in the wings of the lines. Finally in Appendix AV second order magnetic field effects will be discussed.

1.Overlapping Lines

In this section the influence of overlapping patterns on the measurement of relative f-values will be assessed and an experimental example of overlapping lines will be given. The reason we need to investigate this is that very often it is required to determine by refractive index measurements the f-values of two lines lying very close to each other.

It is an interesting question to see how the proximity of another line (either from an impurity or from another

transition) can influence the experimental results. This can be a very important difficulty to the MOV method. The problem is more prominent among the higher members of a Rydberg series even before configuration mixing effects begin to prevail (a discussion on l-mixing will follow in section 5), which become so closely spaced that there is no longer enough interval between two succesive members for a properly resolved magneto-optical pattern to develop without overlap.

If two adjacent lines are sufficiently far from each other to produce two independent magneto-optical patterns then we will proceed as described in the earlier part of this thesis to calculate the relevant quantities and there will be no cancellation of rotation in either of the lines. Otherwise, there will be some cancellation of rotation and more specifically the positive rotation due to one transition will be cancelled by the negative rotation due to the other when the patterns are sufficiently close to begin merging together. The transition from one category to another is quite abrupt as can be seen from Figs.V1 and V2. It is therefore necessary (a) to try and find the quantitative condition at which this overlapping effect becomes important and (b) also to modify the theory to take this into account once this is so. These two points will now be discussed in some greater detail as follows:

(i) Firstly, we will try and derive a practical criterion for the conditions under which overlap is significant. The Faraday rotation ϕ is given by:

$$\phi(\nu) = \frac{\pi\nu}{c} z(n_+ - n_-) \qquad (V1)$$

where n_{+-} are the refractive indices, given by (equation I22):

$$n_{\mp}(\nu) = 1 - \frac{e^2 Nf}{\pi^{3/2}\Delta\nu_D 4m} \frac{1}{(\nu_0 \pm \alpha)} \int_{-\infty}^{+\infty} \frac{e^{-y^2}((\bar{\nu} \mp \bar{\alpha}) - y)\, dy}{((\bar{\nu} \mp \bar{\alpha}) - y)^2 + \gamma^2}$$

where the various parameters have been defined in section 10 of Chapter I. In the region of interest, $\gamma^2 << ((\bar{\nu} - \bar{\alpha}) - y)^2$ and therefore $n_{+-}(\nu)$ becomes:

$$n_{\mp}(\nu) = 1 - \frac{e^2 Nf}{\pi^{3/2}\Delta\nu_D 4m} \frac{1}{(\nu_0 \pm \alpha)} \int_{-\infty}^{+\infty} \frac{e^{-y^2}((\bar{\nu} \mp \bar{\alpha}) - y)\, dy}{((\bar{\nu} \mp \bar{\alpha}))^2}$$

From the above equation it is obvious that there is a singularity at $\bar{\nu} \mp \bar{\alpha} = y$. Therefore an analytic expression is only possible if:

$$(\bar{\nu} \mp \bar{\alpha}) - y \longrightarrow (\bar{\nu} \mp \bar{\alpha}) \qquad \text{(V2)}$$

ie that $\bar{\nu} \mp \bar{\alpha} >> y$

So, for $\bar{\nu} \mp \bar{\alpha} >> y$, the refractive indeces become:

$$n_{\mp}(\nu) = 1 + \frac{e^2 Nf\sqrt{\pi}}{4\sqrt{\pi}m\, \Delta\nu_D\, (\nu_0 \pm \alpha)\pi\, (\bar{\nu} \mp \bar{\alpha})}$$

and no numerical integration is necessary. Inserting these values in the rotation angle formula, we obtain:

$$\phi(\nu_{lim}) = - \frac{Nfz\, Be^3}{8\pi\, m^2c^2\, (\nu_0^2 - \alpha^2)((\nu_{lim} - \nu_0)^2 - \alpha^2)} \nu_{lim}(\nu_{lim} - 2\nu_0) \qquad \text{(V3)}$$

The above formula is used to calculate the rotation due to the impurity line ν_o the frequencies ν_{lim} where a measurement is being carried out. We estimate that if $\phi(\nu) \gtrsim 10^o$, then a full calculation of the profile of the impurity line is required for an accurate result. The approximations associated with this method are: (a) the fact that we choose arbitrarily the condition $\phi(\nu) > 10^o$ and (b) that $\bar{\nu} \pm \bar{\alpha} >> y$ ($\bar{\nu} \pm \bar{\alpha} = 50y$ is adequate) for an analytic solution to be possible. However in spite of these approximations taken into account, the method is still superior to the far-wing approximation given by Mitchell and Zemansky [4].

(ii) Secondly, once it is established that the lines are so close together that they do overlap, the theory must be altered to take this into account. In the code used so far and described in the previous chapters of this thesis,the rotation angle due to each line (if they were alone) $\phi(\nu)_{line1}$ and $\phi(\nu)_{line2}$ respectively were calculated initially. Then the rotation angle $\phi = \phi_1 + \phi_2$ was inserted in the intensity formula and the overlapping lines' intensity spectrum was produced. From Figs.V1 and V2 it can be seen that this theory agrees excellently with experiment over a wide range of parameters.

2.Possibility of Application of the Present M-C Method to (^1S-^3P) Transitions

It is a very interesting question to investigate how the theory should be set up for a singlet-triplet transition and what kind of results one should expect to get.

As mentioned in section 3 of Chapter I for typical values of ζ(LS) the fields we are working with (B<10 Tesla) are

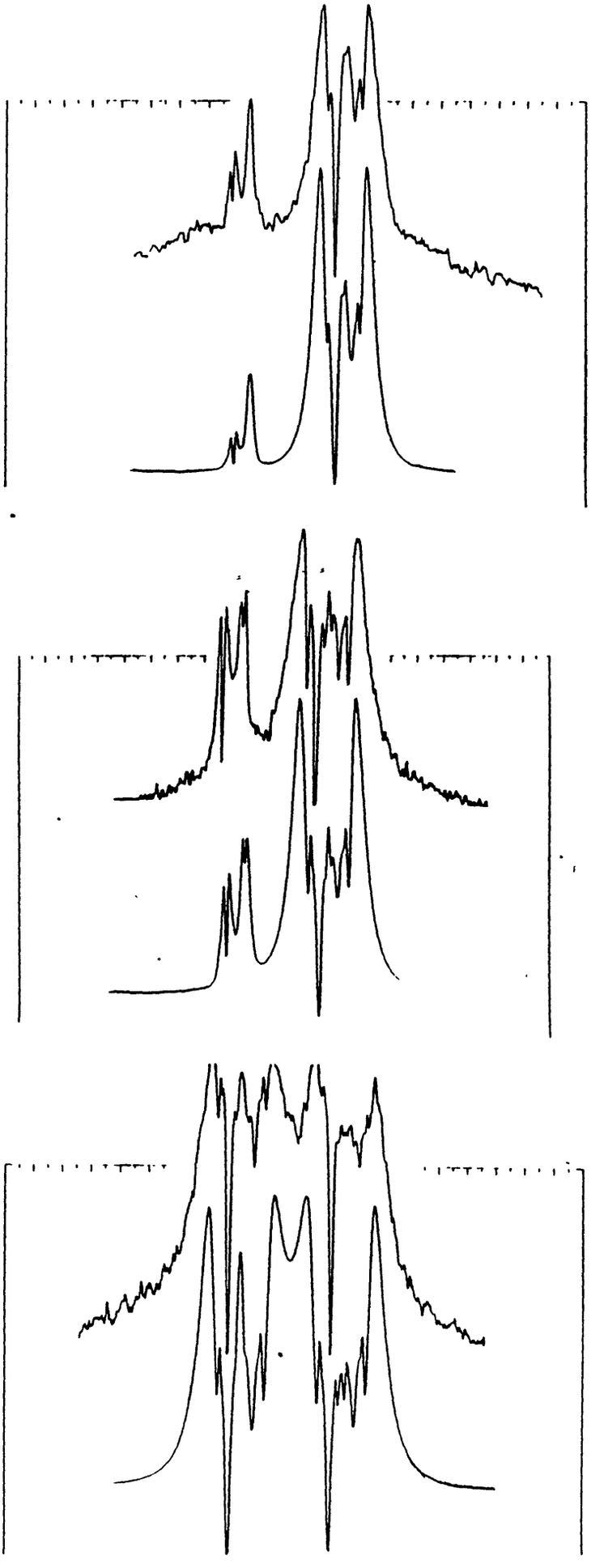

Fig.V1 Overlapping patterns for PaI and SrI at T=775°C and (a) B=2.0T, (b) B=2.5T and (c) B=3.0T.

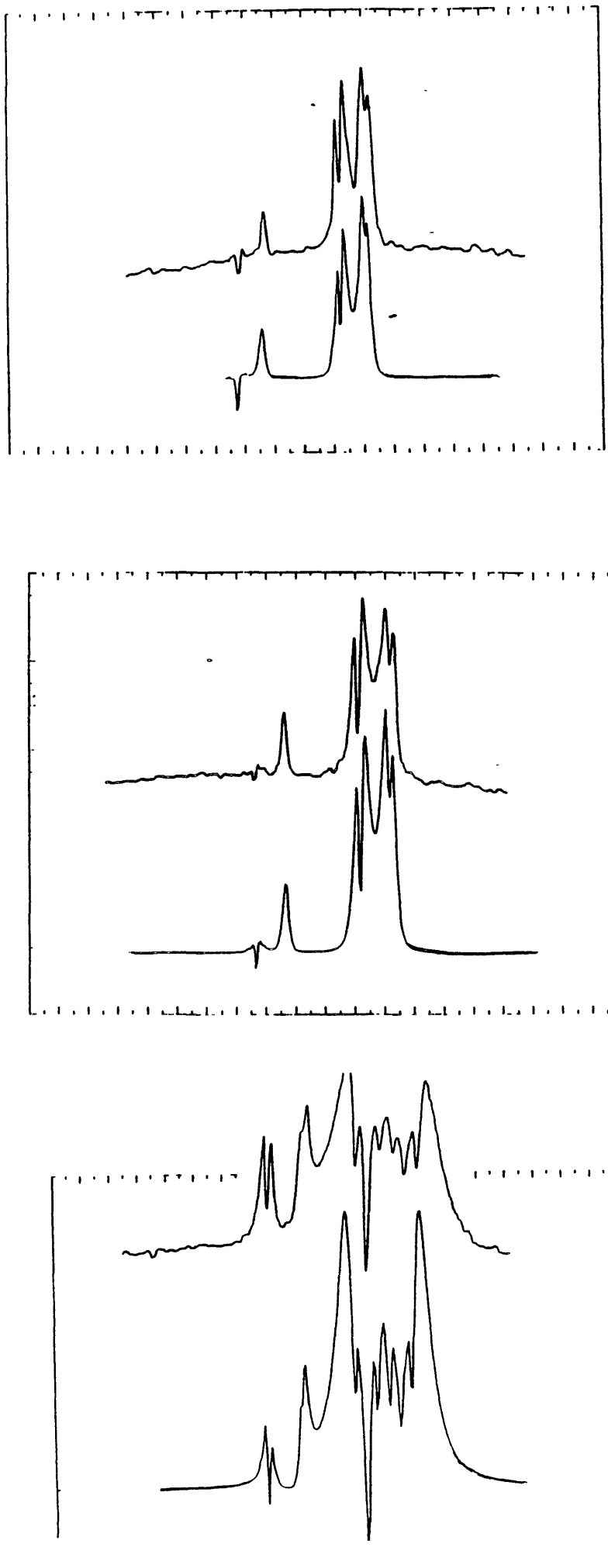

Fig.V2 Overlapping patterns for BaI and SrI at T=900°C and (a) P=3.0T, (b) P=3.5T and (c) P=4.3T.

classified in the low-field category form equation I3. Therefore the frequency of any allowed transition will be stated again to be equal to:

$$h\nu = h\nu_0 + \mu_B B(g_J' M_J' - g_J M_J) \qquad (V4)$$

Also the selection rules are:

$$\Delta M_J = 0, \pm 1$$

$$M_J = 0 \not\rightarrow M_J' = 0 \quad \text{if } \Delta J = 0$$

In the present problem (applied to SrI) the following energy levels are involved: $(^1S_0)$,$(^3P_0)$,$(^3P_1)$ and $(^3P_2)$. In particular:

1) $1s^2(^1S_0)$ has S=0, L=0, J=0, M_J=0 and g_J=1 from equation I 7

2) $1s5p(^3P_0)$ has S=1, L=1, J=0, M_J=0 and g_J=0

3) $1s5p(^3P_1)$ has S=1, L=1, J=1, M_J=0 ± 1 and g_J=3/2

4) $1s5p(^3P_2)$ has S=1, L=1, J=1, M_J=0 ± 1 ± 2 and g_J=3/2

Considering the selection rules we get that:

1. $(^1S_0) \rightarrow (^3P_0)$ is a forbidden transition since M_J=0$\rightarrow$ M_J=0 and Δ J=0.

2. $(^1S_0) \rightarrow (^3P_1)$ is allowed because of break down of the ΔS selection rule and for ΔM_J=0 we get the π-polarisation and for ΔM_J=+-1 the σ-polarisation. The frequency of the two possible transitions is given by: $h\nu\ (^3P_1 \xrightarrow{M_J=+1} {}^1S_0) = h\nu_0 + 3/2\ \mu_B B$

$$h\nu\ (^3P_1 \xrightarrow{M_J=-1} {}^1S_0) = h\nu_0 - 3/2\ \mu_B B$$

and finally,

3. $(^1S_0)\not\rightarrow(^3P_2)$ is forbidden transition since $\Delta J=2$.

Mitchell and Zemansky [1] give the far-wing expressions for such transitions which are functions of α_s and β_s where α_s are the Lande g- factors noted so far as g_J and where β_s are the intensities for the circularly polarised components. They state that according to Kuhn's theory the refractive index is given by:

$$n_{\pm}(\nu) = 1 + \frac{e^2 Nf}{4\pi m \nu_0} \sum_s \frac{\beta_s}{\nu - \nu_0 \mp \alpha_s} \qquad (V5)$$

From the tables that Mitchell and Zemansky [1] give :s denotes the fine structure components with s=1, $\alpha_1=3/2$ and $\beta_1=1$ for $(^1S_0)\rightarrow(^3P_1)$ transitions. Therefore, the Zeeman splitting factor for singlet-triplet transitions is 3/2 α instead of α hat was the factor for singlet-singlet transitions.

The computer code that was used to obtain singlet-triplet magneto- optical spectra was the one described in the previous chapters of this thesis with the exception of the modification of the appropriate wavelength and the splitting factor. Fig.V3 shows the spectrum obtained from the $5s^2(^1S_0)\rightarrow 5s11p(^3P_1)$ transition with the same Nfz input data as the best spectrum of $5s^2(^1S_0)\rightarrow 5s11p(^1P_1)$.

It can be seen that the very middle of Fig.V3 exhibits the same basic features as the corresponding part of the singlet-singlet spectrum shown in Fig.II2. Obviously since the Lorentz separation is different for the singlet-triplet spectrum the remaining part between the two Lorentz components is slightly different for the two cases. Fig.V4 shows the refractive index

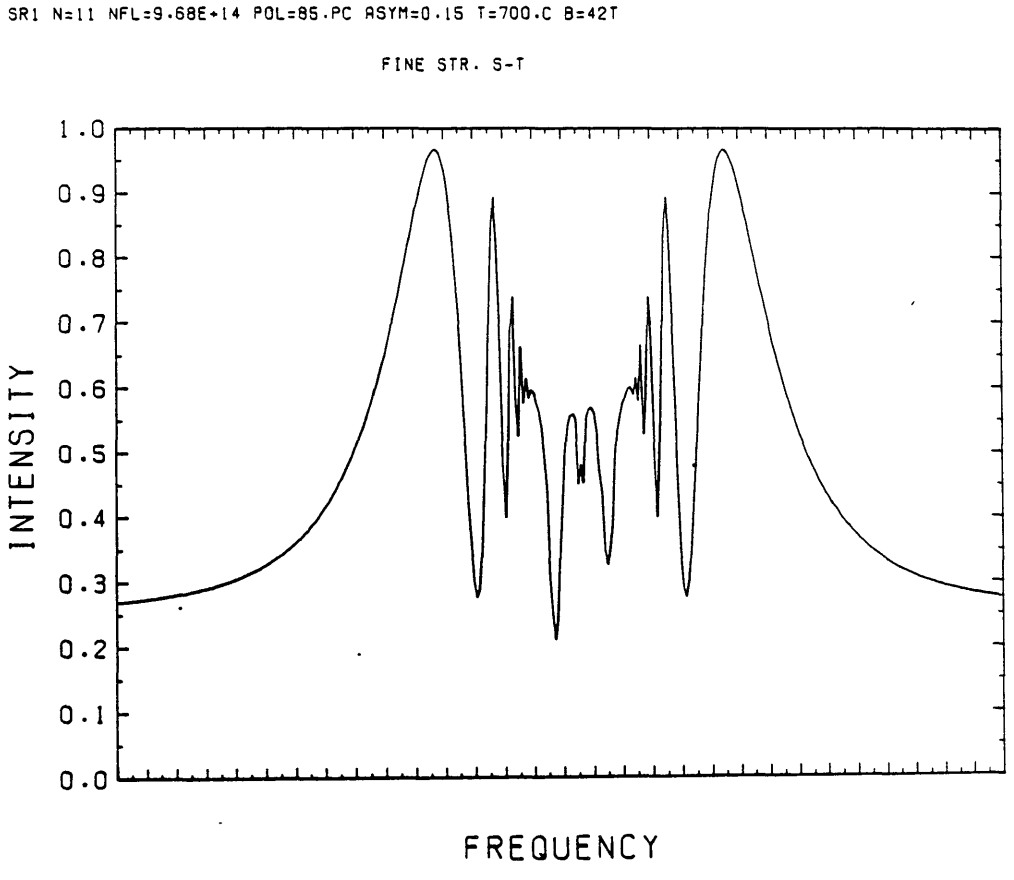

Fig.V3 ($^1S - {}^3P$) computed magneto-optical spectrum for n=1 ^1SrI, polarisation efficiency=85%, asymmetry constant=.15 and Nfz=9.68 10^{14}.

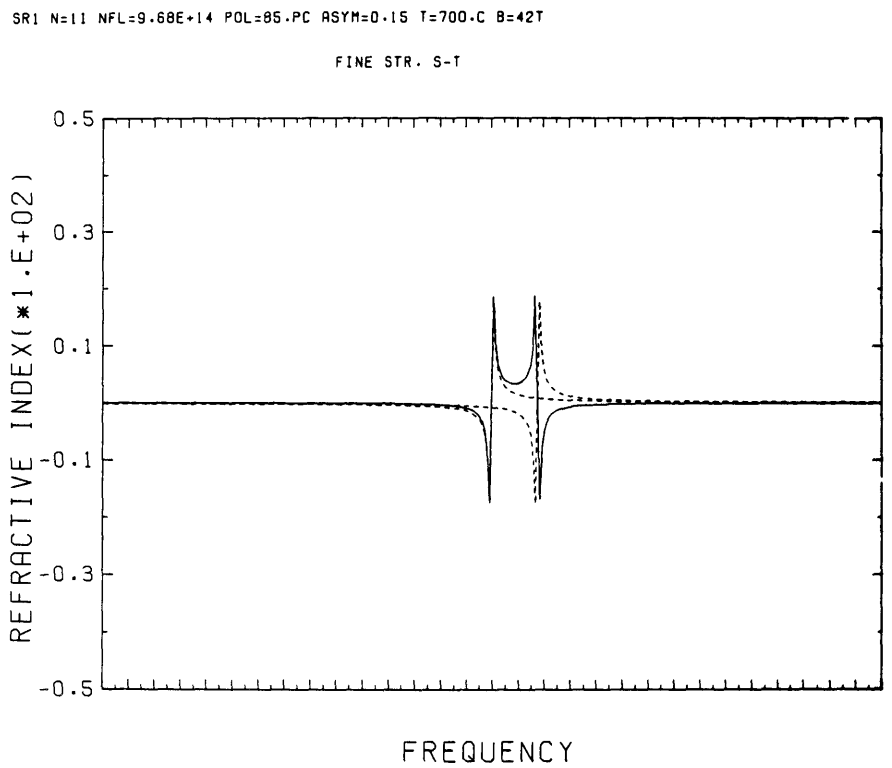

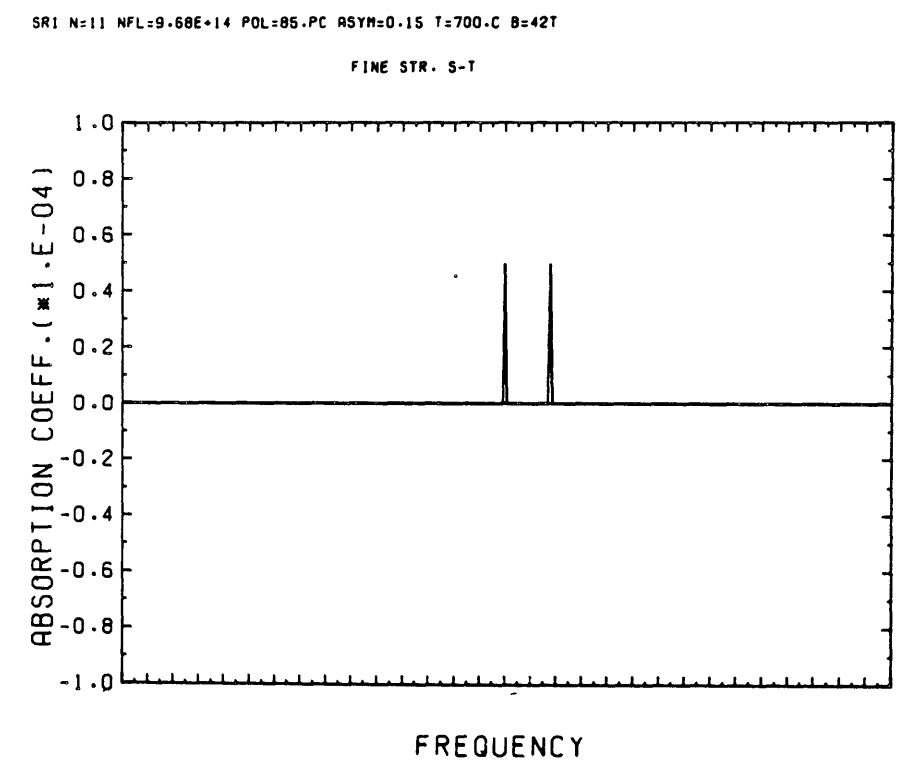

Fig.V4 Computed refractive index and absorption coefficient curves for a ($^1S - {}^2P$) transition.

and absorption coefficient curves that correspond to singlet-triplet transitions. For different Nfz input values, the centre part of the pattern "oscillates" up and down, thus making the MOV method still applicable.

3.Magneto-Optical Spectra with Hyperfine Structure Included

So far in this work hyperfine structure has been assumed to be negligible in all the calculations. Although intuitively one would expect the effect of hyperfine structure to be extremely small it will nevertheless be useful to prove it. For simplicity we will only deal with hyperfine structure in the $(^1S_0)\dashrightarrow (^1P_1)$ case of transitions encountered in the experimental spectra obtained in Bonn and not in the $(^1S_0)\dashrightarrow (^3P)$ hypothetical lines considered in the previous section.

In section 4 of Chapter I we saw that the energy shift was:

$$\Delta E = g_J \mu_B B M_J - g_J' \mu_B B M_J + A M_I M_J \qquad (V6)$$

Since $A \propto [J(J+1)+S(S+1)-L(L+1)]/4J(J+1)$ for the singlet levels involved L=J and S=0 we get that for both A=0. Therefore the last term in the energy shift formula vanishes. Also for both levels (from equation I7) $g_J=1$. Therefore

$$\Delta E \text{ for } (^1S_0) \text{ level is } = \mu_B B M_J - g_I' \mu_B B M_I$$

and

$$\Delta E^* \text{ for } (^1P_1) \text{ level is } = \mu_B B M_J^* - g_I' \mu_B B M_I^*$$

Recalling the $\Delta M_I = +-1$ and $\Delta M_J = +-1$ selection rules we obtain that the energy of allowed transitions is given by:

$$E = h\nu_o + \Delta E^* - \Delta E = h\nu_o + \mu_B B(M_J^* - M_J) - g_I' \mu_B B(M_I^* - M_I)$$

For $\Delta M_J = +1$, $\Delta M_I = +1$ $\qquad E = h\nu_o + \mu_B B - g_I' \mu_B B$

$\Delta M_J = +1$, $\Delta M_I = -1$ $\qquad E = h\nu_o + \mu_B B + g_I' \mu_B B$

$\Delta M_J = -1$, $\Delta M_I = +1$ $\qquad E = h\nu_o - \mu_B B - g_I' \mu_B B$

$\Delta M_J = -1$, $\Delta M_I = -1$ $\qquad E = h\nu_o - \mu_B B + g_I' \mu_B B$

From the above energies it can be seen that the difference in energy $h\nu_o$ of the unperturbed levels is shifted by amounts $+- \mu_B B$ to give the two Lorentz σ-polarisation components and in turn each of these two components is shifted by an amount $+- g'_I \mu_B B$ due to the hyperfine structure.

The reason why intuitively we expected that the effect of hyperfine structure would be unimportant is because the hyperfine energy shift is 1836.13 times smaller than the fine energy shift and also smaller than the line Doppler width by two orders of magnitude. Therefore, the hyperfine energy splitting will be lost in the width of the line.

Another point which should be examined is the distribution

of nuclear spins in the common isotopes of the elements in question. From nuclear tables (see any standard nuclear physics textbook, eg Enge [2]), the following data is obtained:

Element	Isotope Abundance %	Muclear Spin
Sr I	82.56%	0+
	7.00%	9/2+
	9.86%	0+
	0.56%	0+
Ba I	71.66%	0+
	11.32%	3/2+
	7.81%	0+
	6.59%	3/2+
	2.42%	0+
	0.10%	0+
	0.10%	0+
Mg I	78.70%	0+
	10.13%	5/2+
	11.17%	0+

For all three elements we are interested in (Sr, Ba and Mg)

it can be seen that arround 70-80% of their isotope abundance do not possess a nuclear spin. However in the present calculations the worst case was considered and we assumed that we had 100% isotope abundance with nuclear spin. We then had to include the two Zeeman components and the four hyperfine ones. Mitchell and Zemansky [1] state that the refractive index has to be calculated by the method of Kuhn but we have to sum over all the Zeeman and hyperfine components as follows:

$$n_{\pm}(\nu) = 1 + \sum_{i} \frac{e^2 Nf}{4\pi m \nu_0} \sum_{si} \frac{\beta_{si}}{\nu - \nu_i \mp \alpha \alpha_{si}}$$

where i denotes the hyperfine components, s the fine components and the other parameters have their usual meaning. β_s was assumed to be equal to 1/2 since at the limit of zero hyperfine structure the sum of the two hyperfine components had to equal the intensity of the corresponding Lorentz line.

The calculated magneto-optical intensity pattern with hyperfine structure is shown in Fig.V5 and as expected is identical with the spectrum obtained with only fine structure (Fig.V3). Fig.V shows the energy level diagram for the hyperfine structure case of the $(^1S_0) \rightarrow (^1P_1)$ transition.

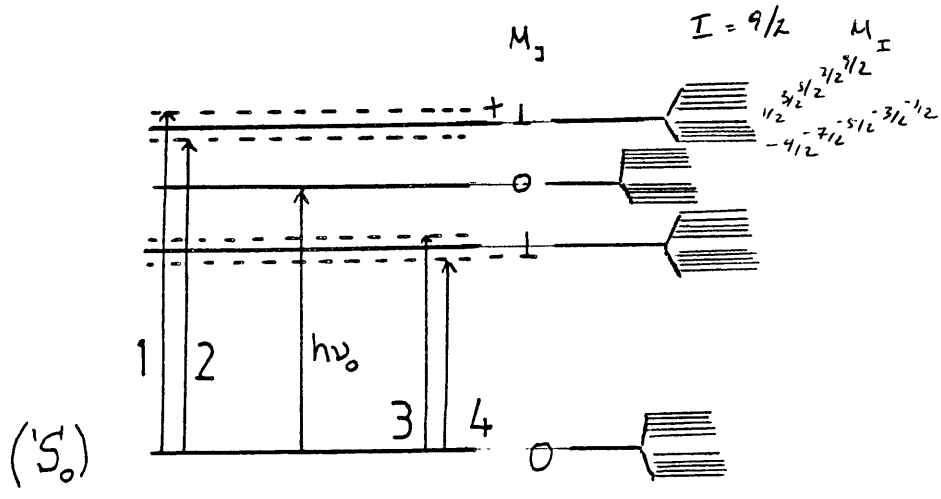

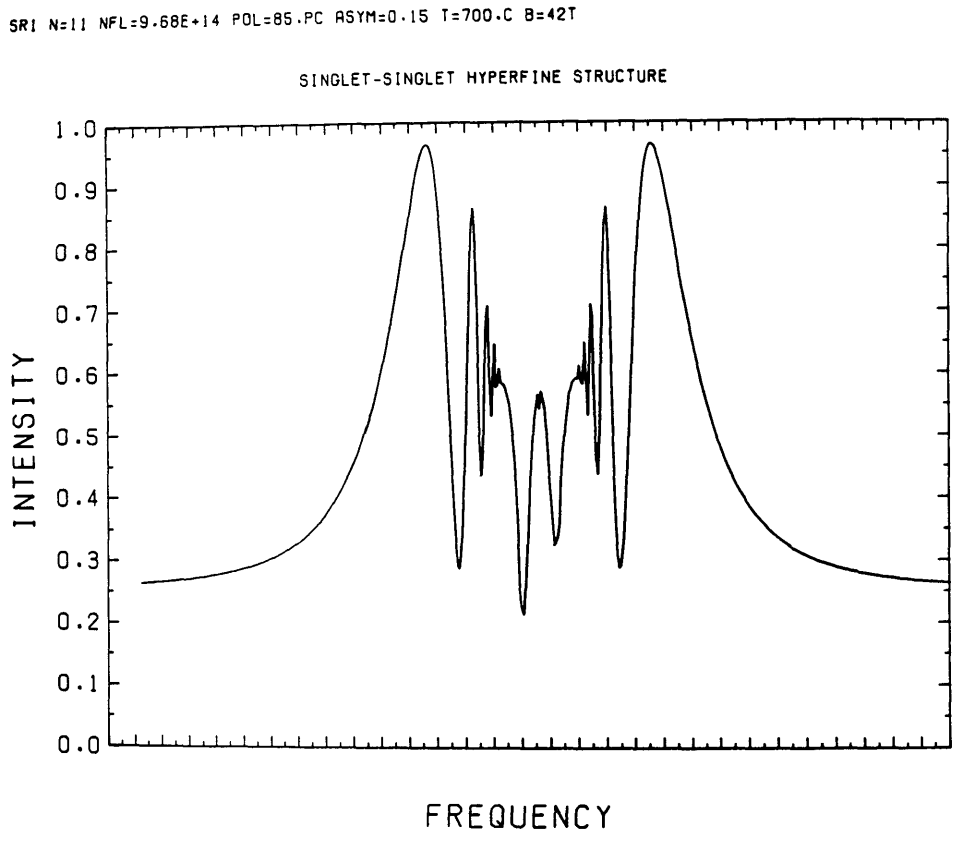

Fig.V5 Computed magneto-optical spectrum including the effect of hyper- fine structure for n=11 SrI, polarisation efficiency=85%, asymmetry constant=.15 and Nfz=9.68 10^{14}.

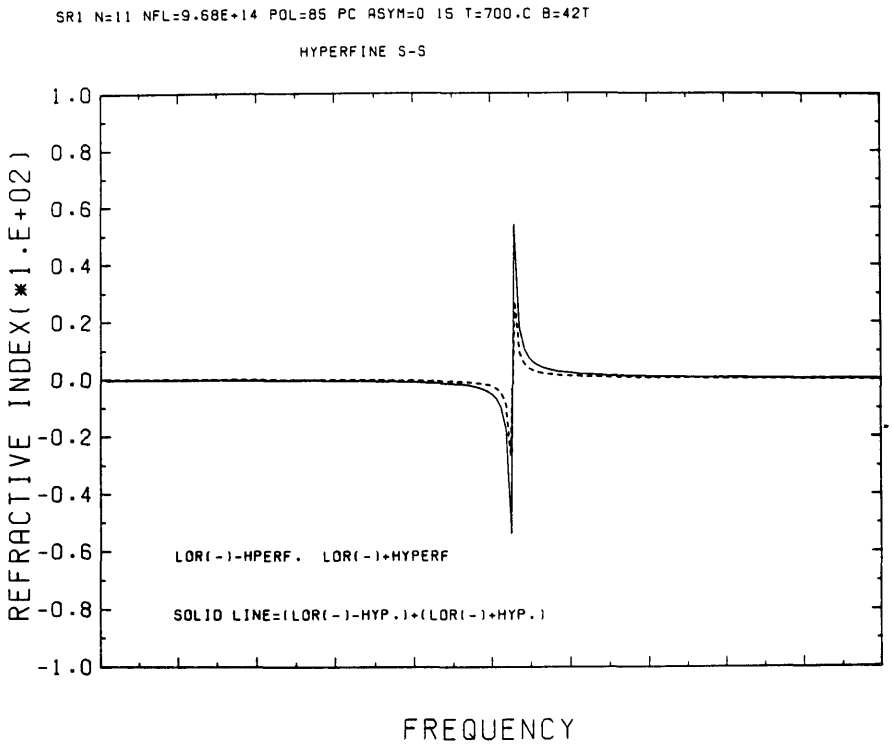

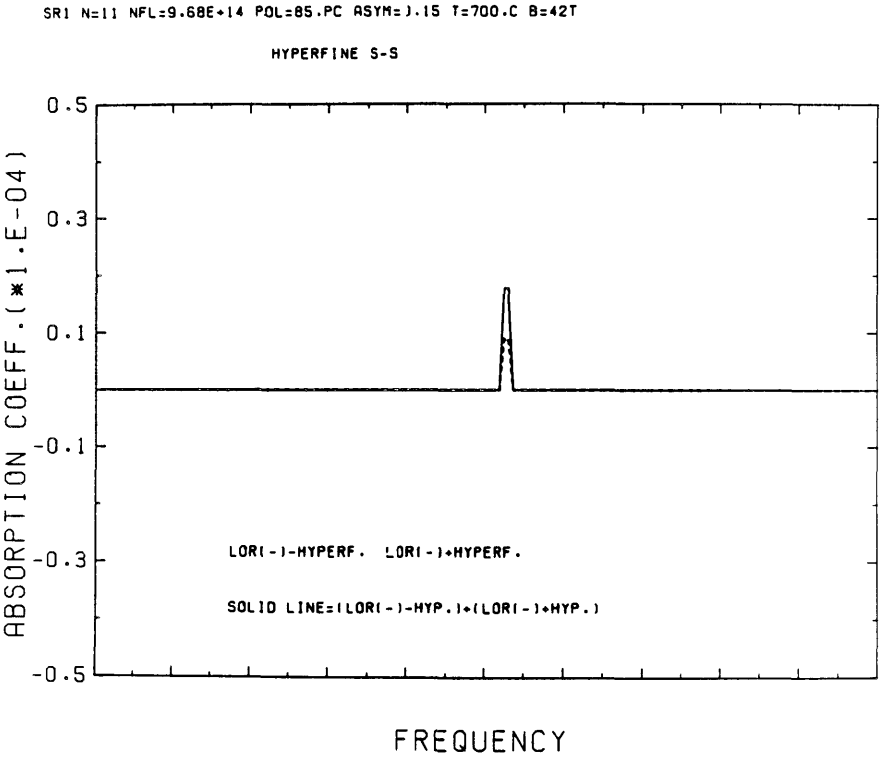

Fig.V6 Schematic representation of the $^1P(F_J=+1)$ levels with hyperfine structure.

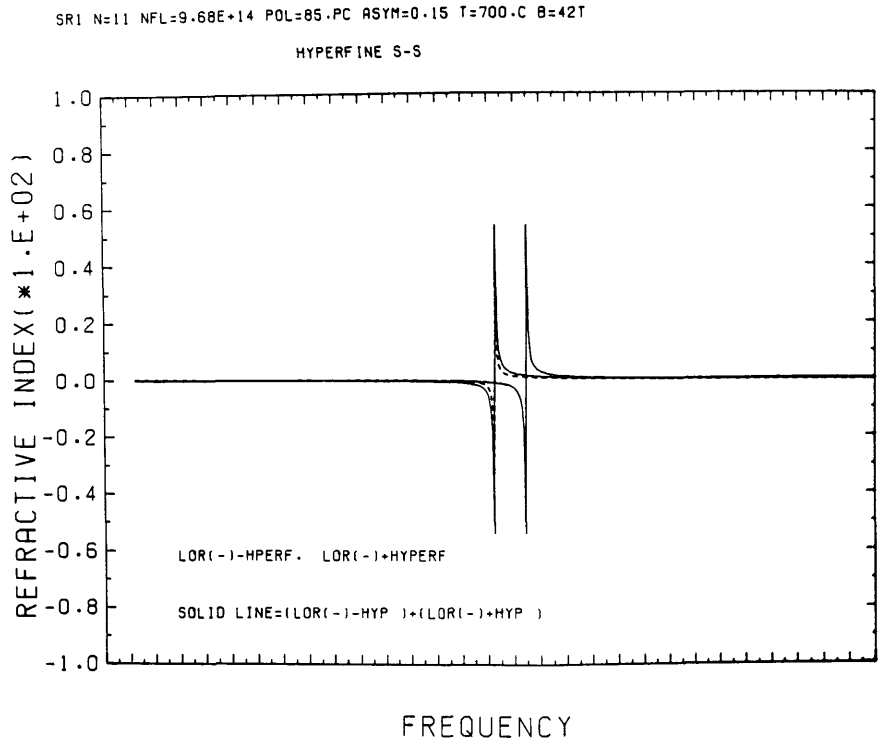

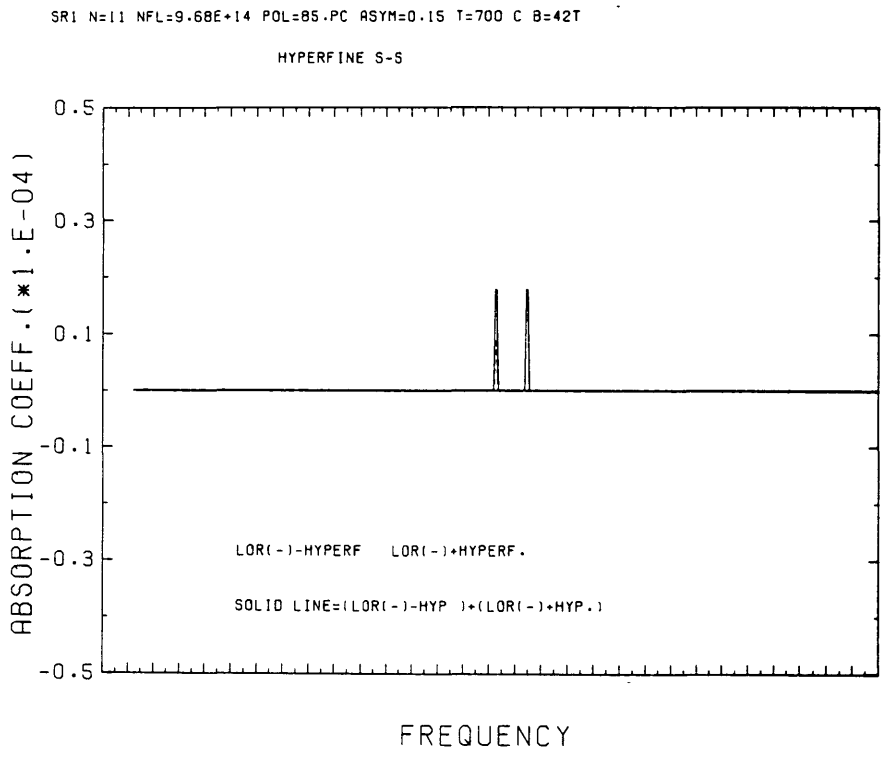

Fig.V7 Computed refractive index and absorption coefficient curves when hyperfine structure is included in the calculations.

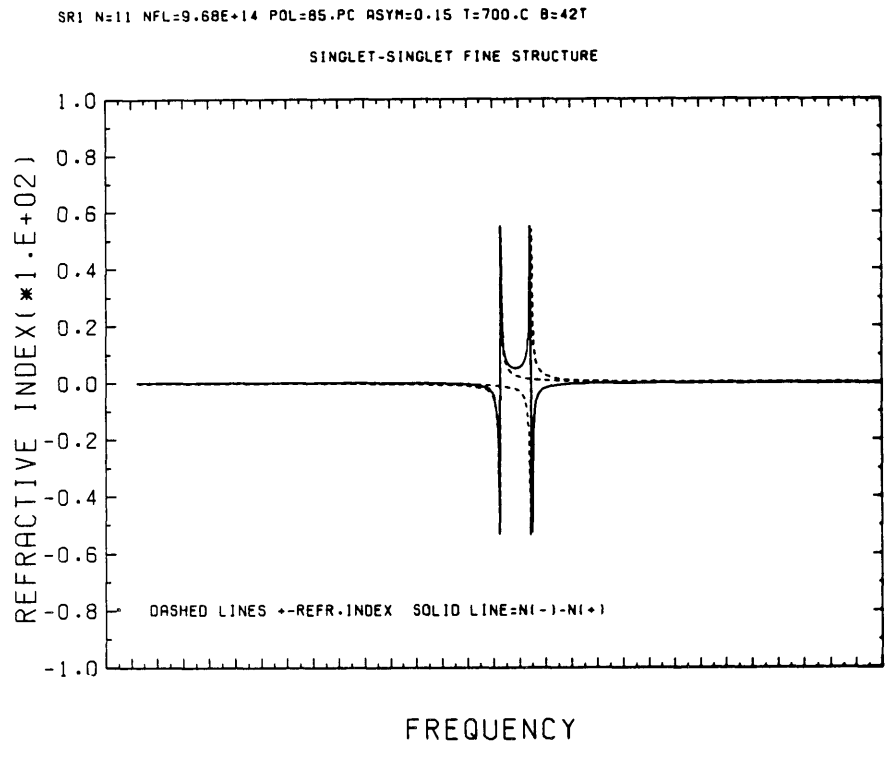

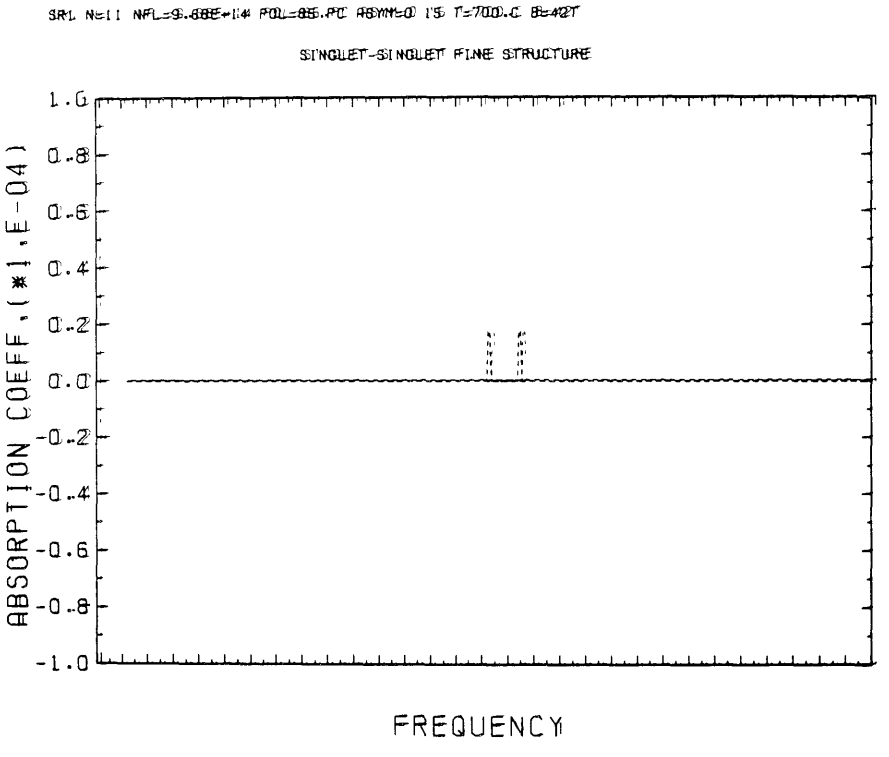

Fig.V8 Computed refractive index and absorption coefficient curves when only fine structure is included in the calculations.

Also the refractive indices and absorption coefficients were plotted verus frequency for the transitions 1 and 2 respectively in Fig.V7. Since, as stated above, the refractive index is the summation of all hyperfine components weighted appropriately, Fig.V7 which represents that summation is identical with Fig.V8 which represents the refractive index for the fine case. The same results can be deduced from an expanded scale.

4.Investigation of Measuring Absolute f-values from the M-O Spectra by Applying the Weingeroff Method

Weingeroff in 1931 [1] devised a method of measuring atomic lifetimes of some atomic resonance states by a magnetic rotation measurement which does not require knowing the vapour pressure data.

In this paper [1] ϕ denoted the angle of rotation of the analyser from the crossed position (ϕ =0) and I was the intensity of light due to the magnetic rotation and the continuous background. Stephenson [3] showed that absolute f-values could be measured by using a null method on the intensity pattern, ie setting I=0 and noting the position of the analyser, say ϕ_o, at which the absorption line coincides with the continuous background. This would give another equation to the system and therefore the unknown product (Nz)f would reduce only to f.

For our case even if the photographic recording allowed transmitted and absorbed intensities to be "balanced" accurately and even if the integration over the profile to determine a ratio of transmitted to absorbed intensity was feasible, there is one basic difference with the Weingeroff method that would

make the latter inapplicable to this case. Weingeroff assumes that the absorption coefficient given by Mitchell and Zemansky [4] and Plaskett [5] is:

$$k_\nu = \frac{\sqrt{\pi}\ e^2\ Nf}{mc\ \Delta\nu_D}\ \left(e^{-(\Delta\nu/\Delta\nu_D)^2} + \frac{A\ \Delta\nu_D^{\,2}}{4\pi\ \Delta\nu_D \sqrt{\pi}\ \Delta\nu^2} \right)$$

and then becomes:

$$\frac{\sqrt{\pi}\ e^2 Nf}{mc\ \Delta\nu_D}\ \ \frac{A\ \Delta\nu_D^{\,2}}{4\pi\Delta\nu_D \sqrt{\pi}\ \Delta\nu^2}$$

where $\Delta\nu_D$ is the Doppler width. That is, his theory is applicable only to the far-wings of the magneto-optical line and when the central regior of the line is completely absorbed (this is so when the length of the absorbing column or the pressure of the absorbing vapour are very high).

So, it is evident that, since the present method (MOV)is based on the detection of features at the very centre of the line, that the Weingeroff method is not applicable to the data.

REFERENCES TO CHAPTER V

1. Weingeroff M. Z. Phys. 67, 679 (1931)

2. "Introduction to Nuclear Physics by H.A. Euge (Addison-Wesley 1982)

3. Stephenson G. Proc. Roy. Soc. 464 (1950)

4. "Resonance Radiation and Excited Atoms" by A.C.G. Mitchell and M.W. Zemansky (Cambridge University Press 1971)

5. Plaskett H. Mon. Not. Roy. Astr. Soc. 107, 117 (1947)

Chapter VI

Results from the Magneto-Optical Method

In the previous chapters the magneto-optical method for determining relative f-values was described, examined and discussed. This chapter will present the results obtained. Section 1 of the present chapter will deal with SrI for several members of the Rydberg series (n=11,25). The results will be compared to those of Parkinson, Reeves and Tomkins [1]. Section 2 will five the results for MgI for members n=7,14 and for three different field strengths. Section 3 will present the results for BaI for a single member $6s^2(^1S_0)\rightarrow 6s15p(^1P_1)$ with a close lying Strontium $5s^2(^1S_0)\rightarrow 4d5p(^1P_1)$ impurity line for a wide range of parameters and the validity of the overlapping lines' technique will be demonstrated. Finally, the results for Magnesium will indicate that there seems to be a dependence of the f-values on the applied magnetic field. This was the motivation to study more carefully the work of others on this aspect as well as to try and find an approximate theoretical method to see how f-values were affected by externally applied magnetic fields. These facts will be discussed in Chapter VII which follows.

1.Strontium Results

The physical background and the computer code described in Chapters I to III were used to measure the relative f-values of SrI. The experimental plates obtained in Bonn contained members of the pricipal series starting from n=11 and ending after n=30.

But since after n=28 the pattern of each Rydberg member overlapped very much with the next member and the spectrum was a continuous succession of peaks, it was not possible to see any definite rotation or any specific Lorentz components. At that point l-mixing had started showing up and would be followed by n-mixing. Therefore our analysis had to stop at n=28. For each n it was found that a slightly different value of the polarisation parameter had to be used since the polarising efficiency of the grating was wavelength dependent. The asymmetry parameter was also changed for each n and not in a systematic way but this was to be expected according to the grating manufacturers. The value of the apparatus FWHM for optimum results was found to be 8.50 10^{10}. Having the aim and criterion of the best reproduction of the experimental spectrum with our computational method, the values of the product Nfz that gave the best results are shown in column 2 of table VI1. Column 3 of the same table shows the f-values obtained when our Nfz products are normalised to the f-values of $5s^2(^1S_0)\text{-->}5s11p(^1P_1)$ of Parkinson, Reeves and Tomkins [1].

We adopt the standard approach of quantum defect theory [2] to plot the differential oscillator strength versus quantum numbers. The general solution to Schrodinger's equation for $r>r_o$ can be written as:

$$\psi(\nu,r) = N_\nu \, (f(\nu,r)\cos\pi\mu - g(\nu,r)\sin\pi\mu)$$

where $f(\nu,r)$ and $g(\nu,r)$ are the regular and irregular solutions to Schrodinger's equation, $\mu\pi$ represents their relative phase and N_ν is a normalisation factor. Further N_ν is proportional to $(n-\mu)^{-3/2}$ for negetive electron energies and

n	Nfl (cm^{-2})	f	Height (cm)	P(%)	Width (cm)	A	n*
11	9.69(14)	.00284	.582	85	.0467	.15	8.372
12	5.74(14)	.00168	.417	84	.0335	.15	9.346
13	3.97(14)	.00116	.309	79	.0248	.08	10.330
14	2.71(14)	.00079	237	80	.0190	.05	11.319
15	1.99(14)	.000583	.182	83	.0146	.13	12.311
16	1.42(14)	.000416	.144	83	.0116	.10	13.302
17	1.13(14)	.000312	.116	83	.00932	.05	14.30*
18	.930(14)	.000272	.094	86	.00761	.01	15.301
19	.698(14)	.000204	.078	86	.00629	.05	16.294
20	.567(14)	.000166	.066	88	.00527	.02	17.292
21	.427(14)	.000125	.055	92	.00445	.04	18.290
22	.361(14)	.000106	.047	87	.00379	.08	19.293
23	.299(14)	.000087	.041	87	.00326	.08	20.288
24	.255(14)	.000074	.035	85	.00282	.06	21.286
25	.217(14)	.000064	.031	90	.00246	.00	22.288
26	.172(14)	.000051	.026	90	.00216	.01	23.273
27	.160914)	.000047	.024	90	.00190	.05	24.281
28	.121(14)	.000035	.021	90	.00169	.06	25.273

$\Gamma_{\perp} \simeq 4.5\ 10^{8}$ Hz B = 4.2 T $\Gamma_{App} = 8.5\ 10^{10}$ Hz

P = polarization A = asymmetry

Table VII Sr I f-value results normalised to n=7 of (1) and data extracted for QDT plots.

N_ν is independent of energy for positive electron energies. As $r \rightarrow \infty$ the function $\psi(\nu, r)$ must tend to zero, ie:

$$\lim_{r \rightarrow \infty} \psi(\nu, r) \longrightarrow 0$$

which implies that $\sin(\nu + \mu) = 0$ ie that $n = \nu + \mu$ where ν is the effective quntum number, n is the principal quantum number and μ is the quantum defect. The frequency of a transition for the alkaline earths is given by:

$$T_\infty - T_{n^*} = \frac{R}{(n^*)^2}$$

where T_∞ is a constant which has the frequency of the series limit and R is the Rydberg constant. Since two successive values of n^* differ by approximately unity, $n^*_2 = n^*_1 + 1$ we can say that

$$T_{n_1^*+\frac{1}{2}} = T_{n_2^*-1+\frac{1}{2}} = T_{n_2^*-\frac{1}{2}} \qquad \text{and also} \qquad T_{n_1^*-\frac{1}{2}} \equiv T_{n_1^*+\frac{1}{2}}$$

or, equivalently :

$$\underset{n_1^*}{\bullet} \qquad T_{n_1^*+\frac{1}{2}} = T_{n_2^*-\frac{1}{2}} \qquad \underset{n_2^*}{\bullet} \qquad T_{n_2^*+\frac{1}{2}}$$

Returning to Starace's paper [2] it can be said that the product $f^*(n-\mu)^3$ will produce a spectrum of oscillator strengths that varies slowly from one discrete level to another and also joins smoothly in the continuous spectrum of oscillator strengths. It is therefore convenient to plot the results as consecutive rectangles (whose height is $\nu^3 f/2R$ and width $2R/\nu^3$) whose total area equals the f-value. Columns 4 and 5 of table VI1 show these quantities for n=11,28 for SrI while column 6 gives n^*. Fig.VI1 shows such a plot of renormalised oscillator

strengths as a function of energy. It also shows the smooth join which is obtained between the present data (rectangles) and the photoionisation cross-section of SrI measured by Hudson et al [8]. Although the shape of the graph at high n is much more satisfactory than the one obtained from earlier measurements by the "Hook" technique [1], there are still departures from the straight line in Fig.VI1 which are not well understood, especially for n=18 and for n=25, 26,27 and 28. The jump between n=17 and n=18 is present in the "Hook" data of Parkinson Reeves and Tomkins [1] and is even more prominent than in the present data. This departure form linearity falls well outside the errobars and therefore there must be another reason for this. On examining more carefully the spectrum between n=17 and n=18 we found an impurity line at 2201.42 A due to the $7p(^1P_1)$ in CaI. Since this absorption line shows a pair of intensity maxima (Fig.VI8) (magneto-optical rotation) it must mean that the impurity is mixed with the Strontium vapour inside the absorption cell. From the known f-value of the Calcium transition [1], the Ca/Sr ratio in the vapour was calculated and found to be about $1C^{-4}$. It must be noted that the commercially available "pure" samples of Ca,Sr and Ba from eg Alpha or Koch might contain about 1/2% metalic impurities which is a rather high level.

The values n=25,26,27 and 28 lie below the "best" straight line through this data points and this discrepancy increases systematically as the f-value increses. However there must be a reason for this trend occuring. It might be due to perturbations in the f-value produced by the externally applied magnetic field. Garton and Tomkins [3] mention that l-mixing satellites

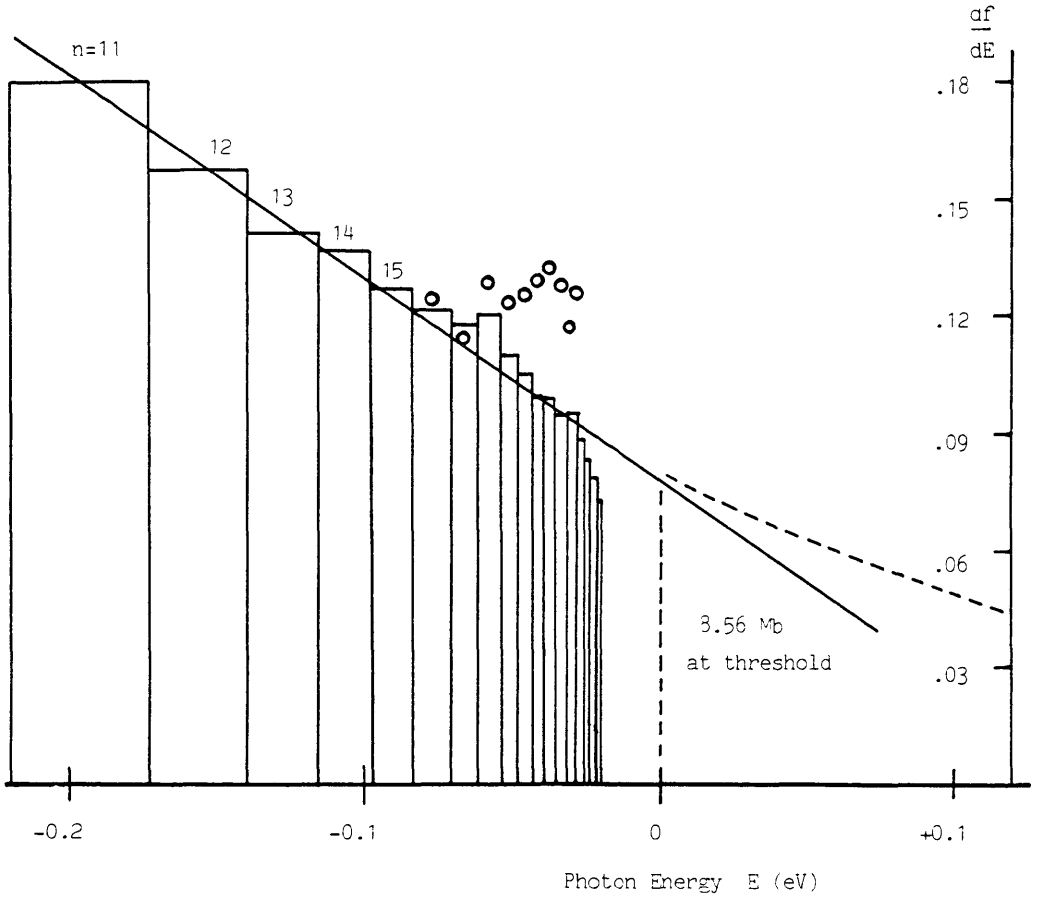

Fig. VI I

Plot of renormalised oscillator strengths as a function of energy for the principal series of Sr I showing the smooth join which is obtained between the present data (rectangles) and the photoionisation cross section of Sr I as measured by Hudson et al.(1969), scaled up by 1.5. This is compared with 'hook data' by Parkinson Reeves and Tomkins (1976-open circles), who suggest a scaling factor of 1.9 for the data of Hudson et al.(1969). A scaling factor of 1.7 was suggested by Lutjens(1972) The 'hook' values for n=11 to 15 are very close to the present values and are omitted for clarity At high e the present measurements still show some departures from a straight line and this is discussed in the text.

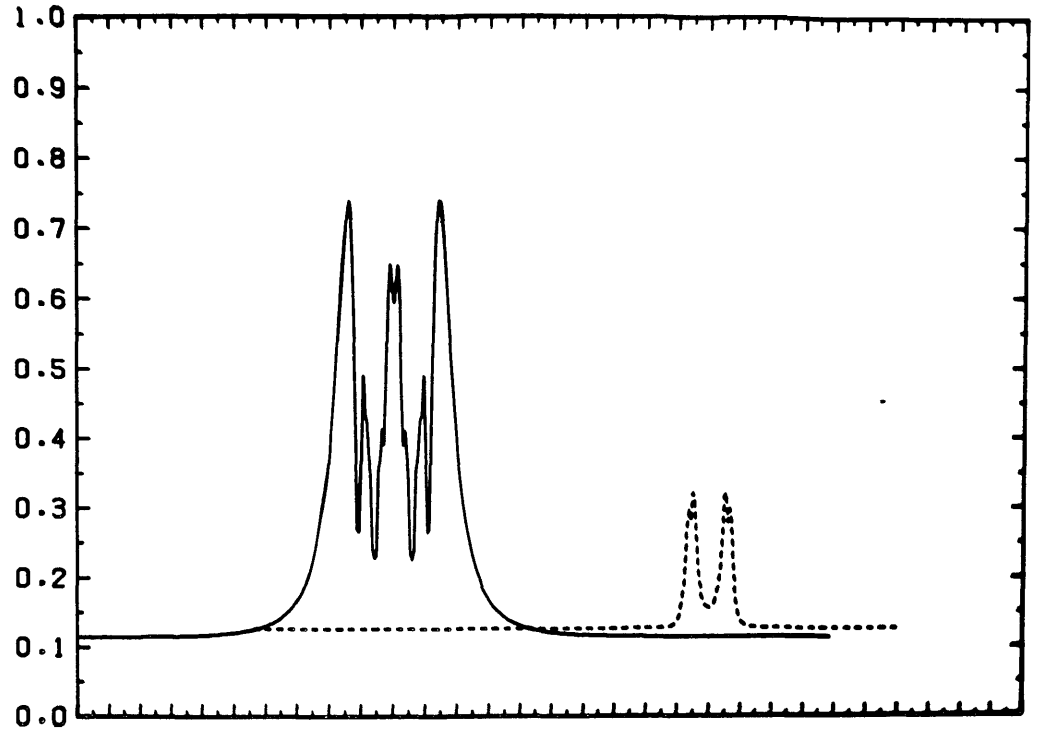

Fig.VI8 The computed MOV CaI impurity pattern next to the n=17 line of SrI.

start appearing arround n=30 in fields of 4.0 Tesla and it seems that our spectra show that the data becomes difficult to interprete at about n=28 at 4.2 Tesla. Although this is still speculative it might provide a good explanation of the observed effects. A much more systematic investigation has to be carried out with spectra obtained at different magnetic fields in order to reach a definite conclusion concerning the variation of f-values with applied magnetic field at that n-regime.

Relative f-values for the principal series in SrI for members with n=11 to n=28 were also given by Connerade [4], where the initial and not refined form of the MOV technique was applied. A simple dispersion theory and a "top-hat" apparatus smoothing was employed [4]. Fig.VI2 shows the results from [4], the experimental spectrum and the much improved present results (for all three cases SrI n=11 was considered a good example). Although the overall features of the two calculated spectra were the same, the present ones that were produced with more elaborate calculations and with a finer mesh, gave a much more detailed structure of the central part of the line which is in excellent agreement with the experimental pattern. The improvement is not surprising since: (a) we considered a Voigt line profile where Doppler broadening dominates instead of approximating the line profile by standard dispersion theory and (b) we used a Gaussian or a Lorentzian smoothing profile to represent overall apparatus function, which is physically more reasonable than the "top-hat" function.

2.Magnesium Results

Following an identical procedure to the one described in

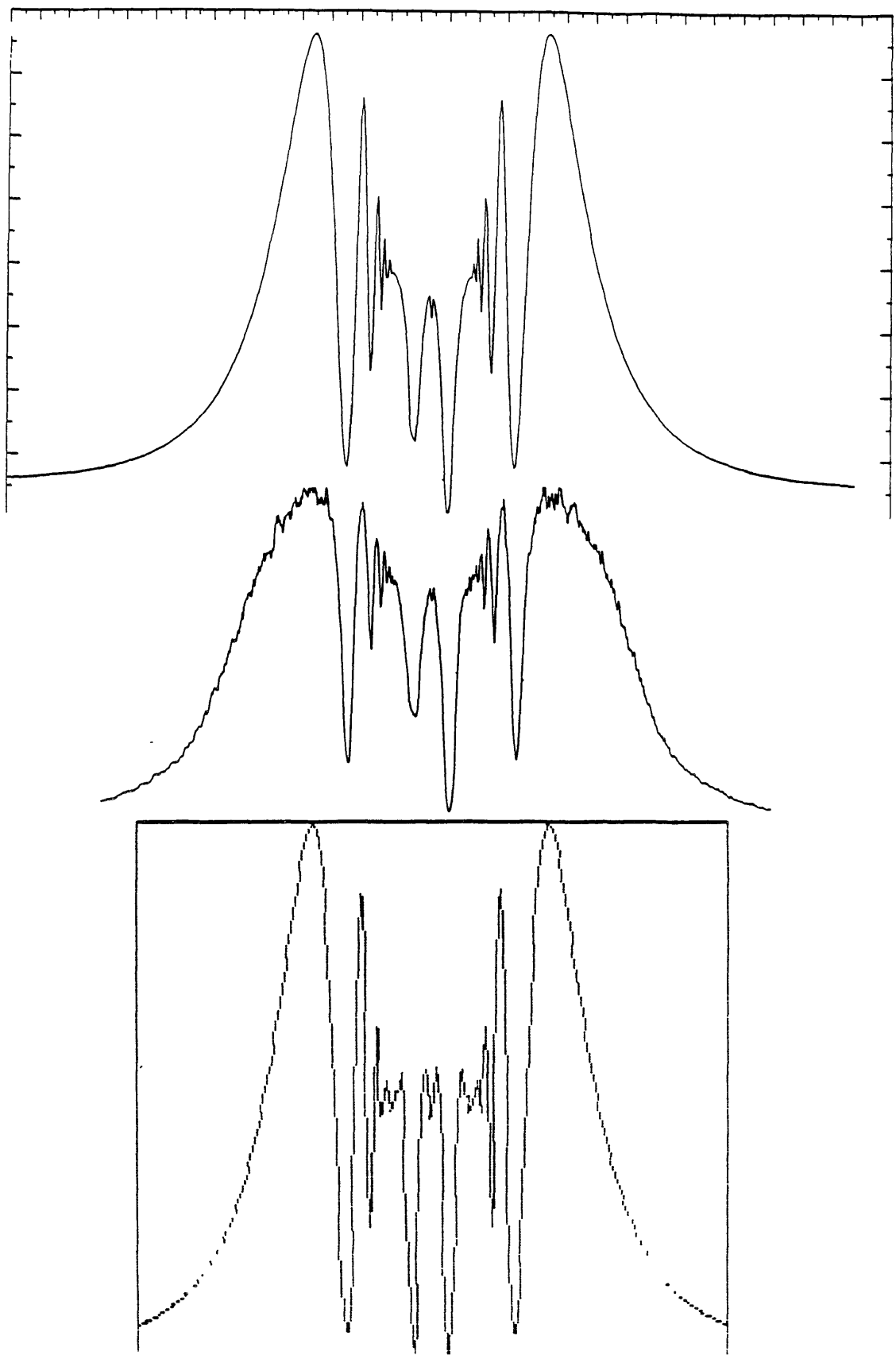

Fig.VI2 Comparison between (a) present calculations, (b) the experimental magneto-optical spectrum and (c) Connerade's (reference [4] of Chapter VI) (all patterns were for n=11 of SrI).

the previous section, relative f-values for the principal series of MgI for n=7,14 for three different field strengths (B=2.4, 3.7 and 4,5 Tesla) were obtained. The apparatus FWHM was 11.8 10^{10}.

The results are presented in tables VI2,3 and 4 for the three fields in increasing order. Fig.VI3 shows the QDT method plot for the three field strengths with all the f-values normalised to the n=7 f-value of Mitchell [5]. The three different lines definitely signify that there is a B-field dependence of the f-values since each one of them falls well outside the error-bar region of the other two lines. Fig.VI4 shows again a QDT method diagram but this time all the f-values were normalised to the n=8 f-value of Mitchell [5].This was done in case Mitchell's n=7 f-value was incorrect. However, the same behaviour was obtained.

In the next chapter there will be an extended discussion on the dependence of atomic transition probabilities with externally applied magnetic fields. However, form our results it is only possible to deduce that the two quantities (f-values and B-fields) are experimentally related.

In order to be able to produce more informative computational results, two things must be done on the experimental side: firstly, in order to repeat our analysis to even higher fields in search for a trend, an upgrading of the superconducting magnet will be required and secondly, it would be desirable to have series of spectra which were taken when the field is (i) increasing and (ii) when it is decreasing. This latter requirement would rule out any random evaporation processes which might substantially alter the column densities

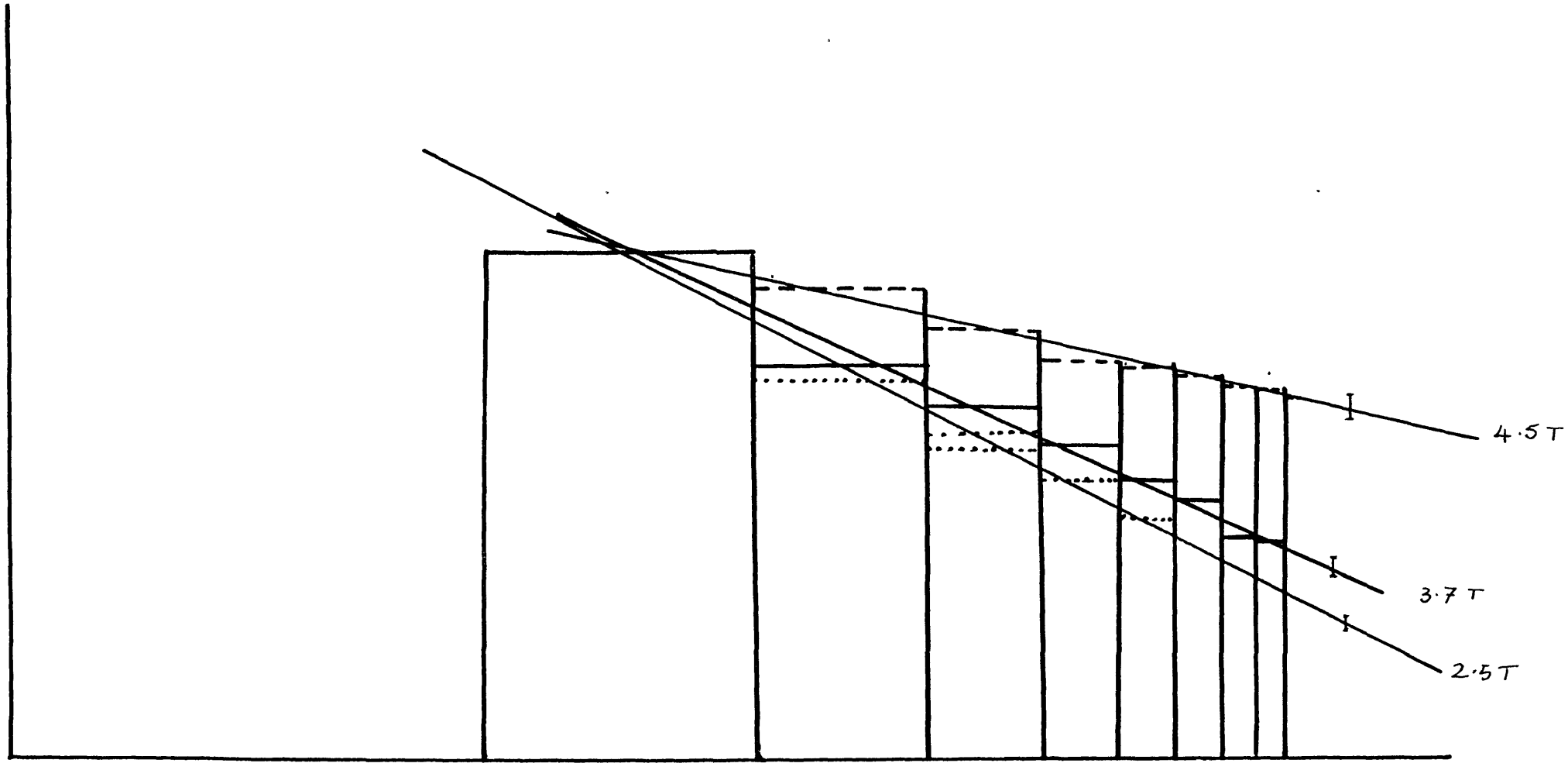

Fig.VI3 Quantum defect theory f-value plot for MgI for B=2.5,3.7 and 4.5T calculated with the MOV method. All results were normalised to the n=7 value of Mitchell (reference [5] of Chapter VI).

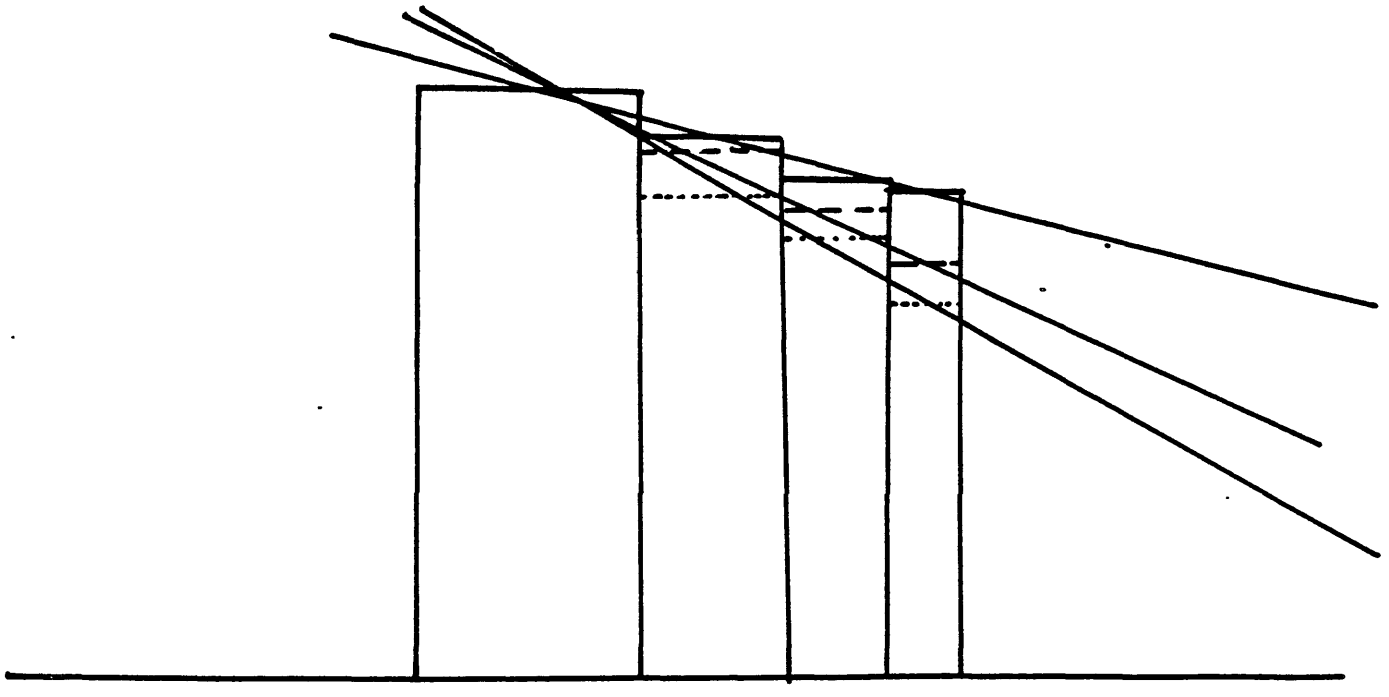

Fig.VI4 Quantum defect theory f-value plot for MgI for P=2.5,3.7 and 4.5T calculated with the MCV method. All results were normalised to the n=8 value of Mithcell (reference [5] of Chapter VI).

n	Nfl (cm^{-2})	f	Height (cm)	P(%)	Width (cm)	A	n*
7	8.50(14)	4.11(-3)	.0316	55	.130	.30	5.9584
8	4.97(14)	2.409-3)	.0294	70	.0816	.30	6.9561
9	3.07(14)	1.48(-3)	.0272	74	.0544	.20	7.9546
10	1.97(14)	9.52(-4)	.0250	72	.0381	.20	8.9533
11	1.41(14)	6.82(-4)	.0246	72	.0277	.20	9.9527
12	1.04(14)	5.0*(-4)	.0241	74	.0208	.24	10.9516
13	.775(14)	3.74(-4)	.0234	74	.0160	.24	11.9513
14	.605(14)	2.92(-4)	.0233	74	.0125	.24	12.9507
15	.470(14)	2.27(-4)	.0227	70	.0100	.24	13.9504

$\Gamma_{App} = 11.8 \times 10^{10}$ Hz $\Gamma_{\perp} \approx 4.5 \times 10^{8}$ Hz

Table VI2 Mg I f-value results normalised to n=7 of (5) and data extracted for QDT plots (B=4.7T).

n	Nfl (cm^{-2})	f	Height (cm)	P(%)	Width (cm)	A	n*
7	1.12(15)	4.11(-3)	.0316	65	.130	.30	5.9584
8	5.50(14)	2.018(-3)	.0247	70	.0816	.40	6.9561
9	3.30(14)	1.211(-3)	.0223	70	.0544	.40	7.9546
10	2.05(14)	7.52(-4)	.0197	70	.0381	.40	8.9533
11	1.33(14)	4.88(-4)	.0176	70	.0277	.40	9.9527
12	.929(14)	3.41(-4)	.0164	70	.0208	.40	10.9516
13	.598(14)	2.19(-4)	.0137	70	.0160	.40	11.9513
14	.465(14)	1.76(-4)	.0136	70	.0125	.40	12.9507

$\Gamma_{App} = 11.8 \times 10^{10}$ Hz $\Gamma_L = 4.5 \times 10^{8}$ Hz

Table VI3 As for Table VI2 but for B=3.7T.

n	Nf1 (cm^{-2})	f	Height (cm) P(%)	Width (cm) A	n*
7	1.10(14)	4.110(-3)	.0316 60	.130 .30	5.9584
8	.535(14)	1.998(-3)	.0245 70	.0816 .40	6.9561
9	.292(14)	1.091(-3)	.0200 80	.0544 .40	7.9546
10	.185(14)	6.912(-4)	.0181 80	.0381 .40	8.9533
11	.116(14)	4.33(-4)	.0156 80	.0277 .40	9.9527

$\Gamma_{App} = 11.8\ 10^{10}$ Hz $\Gamma_L \simeq 4.5\ 10^{8}$ Hz

Table VI4 As for Table VI2 but for B=2.5T.

	PS*	MW**	PRT***	Present
f1 ($5d8p\ ^3P_1$)	.0022	.00251	.00191	
f2 ($15p\ ^1P_1$)	.0018	.00209	.00148	
R=f1/f2	1.22	1.201	1.291	1.366± 0.01
f2 (corr)	.0016	.00184	.00139	

*stands for Penkin and Shabanova (1962)
** stands for Miles and Wiese (1969)
*** stands for Parkinson Reeves and Tomkins (1976)

Table VI5

f-values of the Ba lines at 2432.52 Å ($5d8p\ ^3P_1$) and at 2428.15 Å ($15p\ ^1P_1$) and their ratio R as obtained by various authors.

of the furnace.

3.Barium Results

In this section the computational results obtained for Ba will be presented. The procedure of the calculations was identical to the one followed in the cases of SrI and MgI. This time the FWHM of the apparatus function was found to be 7.60 10^{10} for best results.

Unfortunatelly, although we had at our disposal a number of magneto- optical spectra obtained at various furnace temperatures and at various field strengths, the particle density of the furnace happened to be quite low so that the rotation was rather small for the majority of the series members. Therefore, the spectra were rather insensitive to changes in Nfz over the range n=7,to n=10 and as a consequence much of the experimental data was left unused.

From the field-free absorption spectrum it can be seen that there was a Strontium impurity line at 2428.09 A ($4d5p(^1P_1)$ in SrI) which was only 0.68 A away from the 2427.41 A ($15p(^1P_1)$ in BaI) transition . Since BaI and SrI have different vapour pressures, very small variations in temperature allow large variations in relative concentration of the two elements. The experimental results indicated that patterns of comparable scale could be obtained from both lines over a range of furnace temperatues 700 ^{o}C to 1000 ^{o}C. In section 1 of Chapter V the problem of overlapping lines was tackled and discussed and in this section it is actually applied. The results obtained were in excellent agreement with the experimental patterns, for a wide range of magnetic fields and temperatures. This altered the

degree of overlap of the patterns over a wide range. All these facts are shown in Figs. VI5 and 6. Thus, the computed spectra that the overlapping lines' technique and applicability criterion discussed in Chapter V were verified and we conclude that this theory can account for the structure of the observed patterns over the full range, from treating the two lines completely separately where they keep their individual identities to the case where the patterns penetrate each other sufficiently to coalesce with cancellation of the positive rotation due to one line by the rotation due to the other.

Fig.VI6 was recorded during a run at high temperature, when some of the sample had evaporated and the Nfz product (on which the accuracy of the MOV depends) was <1/20th of the value of Fig.VI5 at the same field strength. The large rotation angles on the data of Fig.VI5 shows that this time less sample had evaporated and so accurate values for the ratio R of the intense $5d8p(^1P_1)$ line to the $15p(^1P_1)$ line were obtained. The ratio R is plotted against $\delta\lambda$ (the spread in wavelength of the impurity pattern) and shown in Fig.VI7 from which we see that the accurate f-values of overlapping lines can be extracted from the data even in presence of overlap, provided that a detailed analysis of the structures is performed. Earlier authors using other techniques did not take into account for the effect of the SrI impurity in the spectrum. In the previous work done, the uncertainties in determining the correct value of the vapour pressure, made it difficult to examine correctly the errors in R. Therefore, Penkin and Shabanova [6] quote an absolute 8-15% error and state that the relative f-values were measured with "great accuracy" without giving it in numbers. Table VI5 gives

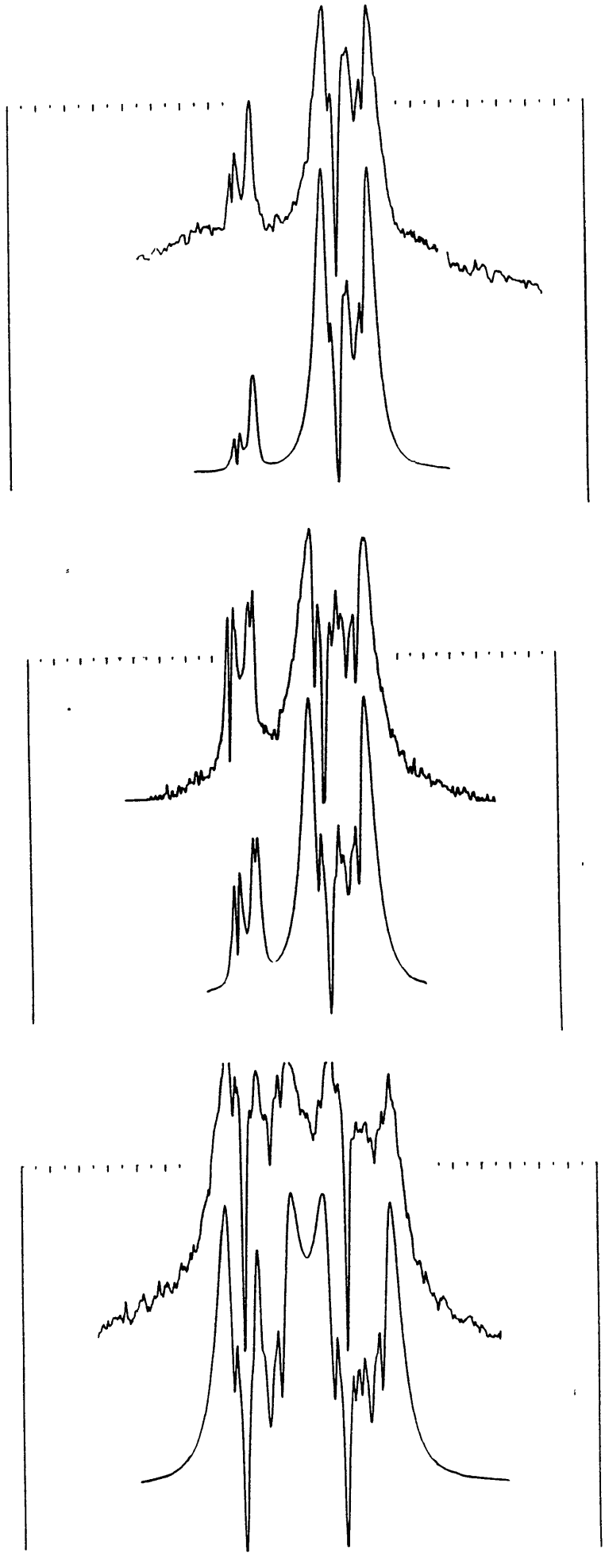

Fig.VI5 Overlapping patterns for BaI and SrI at T=775°C and (a) B=2.CT, (b) B=2.5T and (c) B=3.CT.

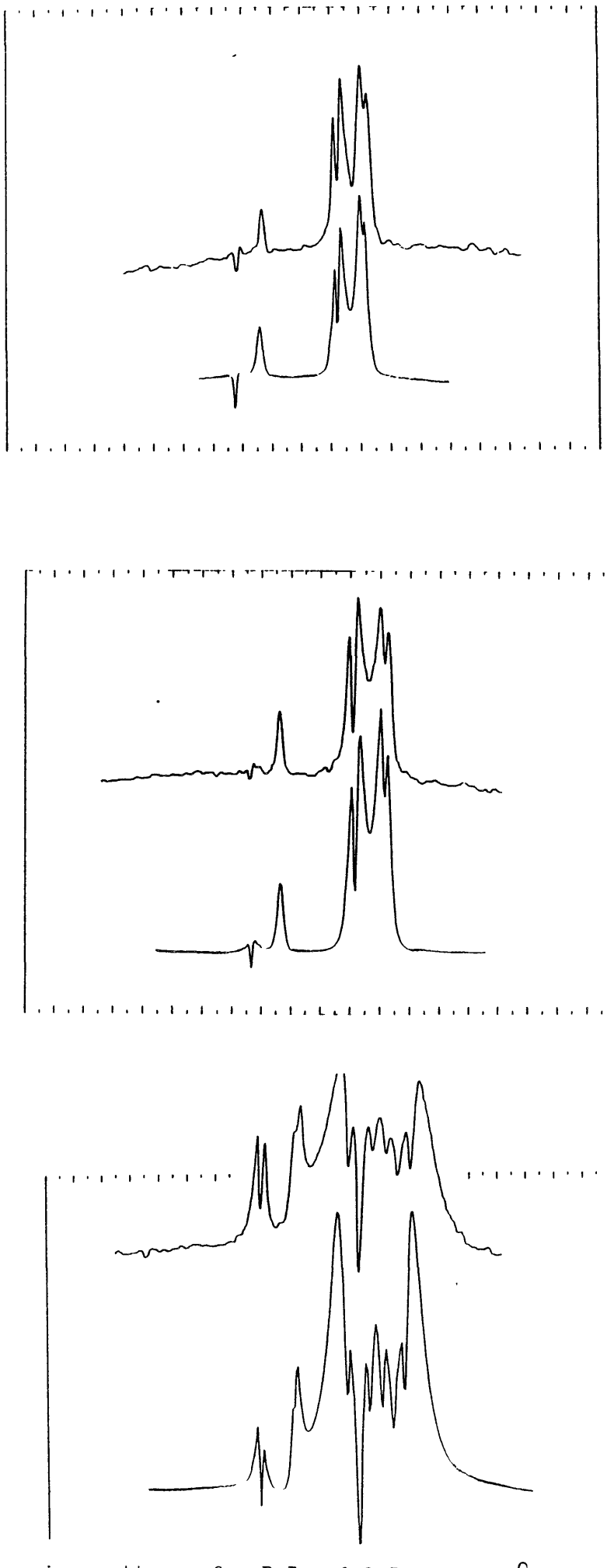

Fig.VI6 Overlapping patterns for PaI and SrI at T=900°C and (a) P=3.0T, (b) P=3.5T and (c) P=4.3T.

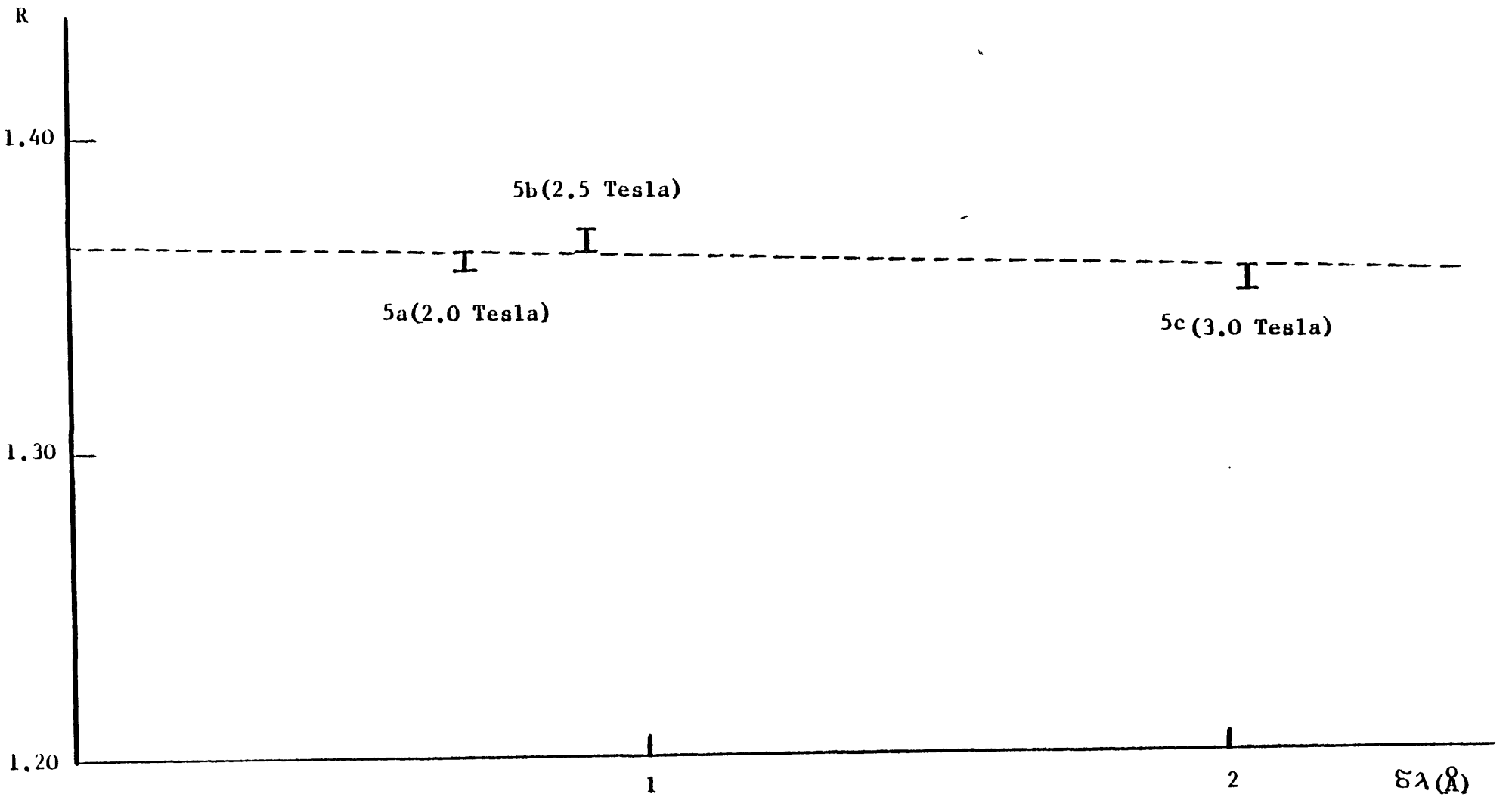

Fig.VI7 The ratio R of the f-values (defined in the text of Chapter VI) plotted as a function of the wavelength interval spanned by the impurity line, showing that R is very nearly independent of the overlap.

the relevant data. If we assume that earlier authors were not aware of the existence in their spectra of this SrI impurity line and that this fact caused systematic errors in their work and if we also take our value for R, we obtain corrected values for f_2 which for each set of data, are smaller than the published ones. Thus we believe that the overlap with the SrI impurity line caused these systematic errors from 11% (Penkin and Shabanova [6], Miles and Wiese [7]) to 6% (Parkinson Reeves and Tomkins [1]). These errors are within the errorbars these authors give but are still large for relative f-value measurements. Again it is worth noting (see comment above) that the commercially available samples of "pure" Ba contain about 1/2% of metallic impurity.

REFERENCES TO CHAPTER VI

1. Parkinson M.H., Reeves E.M. and Tomkins F.S. J. Phys. B., 9, 157 (1976)

2. Starace A.F. ("Photoionization and Other Probes of Many-Electron Interactions", p.335 N.Y. Plenum Publ. Corp. 1976)

3. Garton W.R.S. and Tomkins F.S. Astrophys. J., 158, 839 (1969)

4. Connerade J.P. J. Phys B., 16, 399 (1983)

5. Mitchell C.J. J. Phys B, 8, 25 (1975)

6. Penkins N.P. and Shabanova L.N. Optics and Spectroscopy, 12, 1 (1962)

7. Miles B.M. and Wiese W.L. Atomic Data 1, 1 (1969)

8. Hudson R.D., Carter V.L. and Young P.A. Phys.Rev. Lett. 180 77 (1969)

Chapter VII

Calculation of f-Values and Their B-Field Dependence

This chapter presents calculations of the f-values of high Rydberg states ($7<n<27$) for the principal series of the alkaline earths. We also calculate the dependence of the f-values on the externally applied magnetic field. There are two elements to these calculations:
firstly the calculation of the f-values using a Hartree-Fock code in L-S coupling and
secondly by expanding the relevant eigenfunctions in terms of L-S eigenfunctions.

Section 1 uses the method described by King [1] to investigate the potential problem of having a $^1P_1$ level rather close to a $^3P_1$. We find that for cases of interest they are not sufficiently close to cause problems with the MCV method, but should they do the overlapping lines technique described in Chapter V could be applied. Section 2 presents some results from a code written by Clark and Taylor [6, 7] on high-n hydrogenic f-values in medium magnetic fields. In section 3 we outline a method by which we can approximately account for the B-field dependence of the f-values of high n states. Following a brief introduction to Hartree-Fock calculations (section 4), in section 5 we discuss the necessary modifications which are needed to model high-n states. The details of these calculations are presented in section 6. Finally, results from the method are presented and discussed in section 7.

An important element to the work discussed in this chapter

is the calculation of the total interaction Hamiltonian (including B-field effects) and its solution for the coefficients of the corresponding eigenvectors. Although this work is described excellently in [1], we have included a description of it as appendix (Appendix AVII). Finally, Appendix BVII contains a qualitative review of the research by other workers on the f-value dependence on very high ($>10^{3}$T) magnetic fields.

1.Discussion on the Results of Appendix AVII and their Application to the MCV Method

Using the total Hamiltonian matrix described in Appendix AVII and the appropriate input data for the energy and the electrostatic and spin-orbit parameters for SrI King [1] obtained that the two σ -components (M_J=+-1) of the singlets were quite dissimilar after a certain n-value for a particular field with the $+\sigma$ being more broadened as the field and principal quantum number increased. This was obviously due to the fact that the vector coupling at that point had changed (the B-field contribution to the coupling had started to dominate the spin-orbit and the electrostatic) and as a result the $^3P_1$ line approached the $^1P_1$ one and hence the apparent broadening. In particular King [1] stated that for high laboratory field strengths (10T) spin decoupling (disappearance of the $^3P_1(+\sigma)$ state and merging with the $^1P_1(+\sigma)$ one) occured at n=23.

From the above discussion (and from Appendix AVII) it can be concluded that for intermediate field strengths there will be a $^1P_1$ and a $^3P_1$ state very close together. In Chapter V the MCV method was successfully applied to the singlet- triplet

transitions (section 2 of Chapter V). In the same chapter the overlapping lines' problem was also tackled (section 1). Therefore it is possible to apply the MOV method to the Paschen-Back effect as will now be shown qualitatively:

(a) Use King's total Hamiltonian matrix to evaluate the eigenvalues (energy levels) and the coefficients of the eigenvectors of an (s-p) configuration of the element in question for any field strength.

(b) Having obtained the correct energies of the levels for the applied magnetic field B it will be probably found that the $^1P_1$ and $^3P_1$ levels are very close together. Then, the overlapping lines' criterion will be applied to the $^1S_0$-$^1P_1$ and $^1S_0$-$^3P_1$ lines. If the lines are found to be sufficiently far apart they will be calculated as two separate cases, otherwise the overlapping lines method will have to be applied. Finally,

(c) Since we know that singlet-triplet transitions exhibit MOV behaviour in their centre part, then the $^1S_0$-$^3P_1$ line will be no-problem in the Paschen-Back calculations whether treated separately from the $^1S_0$- $^1P_1$ line or as a part of a complex spectrum.

However, as stated above, the Paschen-Back point seemed to be arround n=23 [1] for B-fields under 10T (for SrI) and therefore for our particular strontium spectra we could say that for n< 23 the present calculations are completely reliable as far as the neglect of neighbouring triplet states is conserned. Using the singlet-triplet (M_L =1) computed energy separation [1] for SrI n=21 at B≅6.0T we can see that it is equivalent to

about 5 Zeeman splittings and also that the triplet has only 4% intensity. Therefore the $^3P_1$ neglect in our MCV calculations is also justified by the fact that it is sufficiently far away from the $^1P_1$ line and also that it is so weak that would not be observed.

2.A Brief Cutline of the Work of C.W.Clark and K.T.Taylor Relevant to the Quadratic Effect in Hydrogen Rydberg Series

Following the experimental results of Garton and Tomkins [3] of the quadratic Zeeman effect in high Rydberg series much theoretical work on this topic had to be done. Although the basic quantum-mechanical physics of an atom in a magnetic field have been understood since the 1930's , many more phenomena exhibited have not yet been explained in a satisfactory manner. The motion of the electron at large distances r from the ionic core inside magnetic fields of the order of 10 T have been treated classically by Edmonds and Pullen [4] and semi-classsically by Edmonds [5] whereas its behaviour near the core has been treated quantum- mechanically by Fano ([6] and references therein). This section of the present chapter will be devoted to describing how Clark and Taylor [**6, 7**] have calculated hydrogenic wavefunctions and energy levels for high Rydberg states in magnetic fields. The Rydberg states have to be high ones since only for those the force excerted by the laboratory magnetic field on the (outer) electron is comparable or greater than the forces due to the remainder of the atom. They have not extended their work to other elements and unfortunately there are no experimental data available on hydrogen for comparisor whereas there exist for

other elements. This work of Clark and Taylor provides the only source of study of the behaviour of high Rydberg hydrogen states in laboratory attainable magnetic fields.

In their work they have made some assumptions which will now be stated. They have neglected all the relativistic terms in the interaction of the nucleus with the electron and there is no spin orbit interaction in their calculations. Consequently they are in the Paschen- Back regime. This assumption can be justified as follows: the energy difference between two states with $j=l\pm1/2$ is given by:

$$\Delta E_l = \frac{Z^4 \alpha^2}{2n^3 l(l+1)} \qquad (a.u)$$

where α is the fine structure constant. The diamagnetic shift is given by:

$$H_D = \beta^2 n^4 / Z^2$$

The above two effects become comparable when $\Delta E = H_D$, ie when:

$$\beta = \frac{Z^3 \alpha}{(2n)^{7/2} \sqrt{l(l+1)}}$$

For B=4.7T the two shifts are comparable at arround n=6. Further the linear Zeeman effect is $H_L = \beta(l_z + 2s_z)$ which they assume to be approximately equal to βl_z and the ratio:

$$H_L / \Delta E = \frac{l^2(l+1)\ 2n^3}{Z^4\ \alpha^2}$$

is usually much greater than unity indicating that it is justifiable to neglect the spin-orbit interaction in the present circumstances.

The second assumption made was that they set [7] as zero the centre of mass momentum of the atom although in a real experiment there would be a random thermal motion. The effect of a centre of mass motion is the same as if there was an electric field perpendicular to B and this Stark effect could be treated by perturbation theory.

The magnetic field B=Bz is considered to be in the z-direction and the vector potential is $\underline{A}=-1/2\ \underline{r}_{\wedge}\underline{B}$. The Schrodinger equation is also:

$$(-\tfrac{1}{2}\nabla^2 - 1/r + \beta L_z + \tfrac{1}{2}\beta^2 r^2 \sin^2\theta)\Psi = E\Psi$$

where $\beta=eB/2mc$, βl_z is the linear Zeeman energy and $1/2\ \beta^2 r^2 \sin^2\theta$ is the quadratic diamagnetic energy. If the linear Zeeman energy is subtracted from both terms of the above equation we have:

$$(-\tfrac{1}{2}\nabla^2 - 1/r + \tfrac{1}{2}\beta\ ^2 r^2 \sin^2\theta)\Psi = \varepsilon\Psi$$

The Coulomb potential 1/r becomes equal to the quadratic potential $1/2\ \beta^2 r^2 \sin^2\theta$ for r= a few thousand Bohr radii and for $\beta=10^{-5}$. Therefore for smaller radii near the core, where we have low n eigenstates, the diamagnetic effect can be treated as a perturbation or even neglected. Near the ionisation point the density of states and the coupling increases very much and this perturbative approach stops being valid.

Continuing with the description of the work of Clark and Taylor [6, 7] the reasons for choosing the Sturmian functions to diagonalise the Hamiltonian as well as a few words about these functions will now follow. The type of wavefunction that would be used had to take account of the large influence of the magnetic field (through the quadratic potential $1/2\ \beta^2 r^2 \sin^2\theta$ at large values of r and of the Coulomb potential (1/r) at smaller values of r (where the magnetic effects are negligible). Such a function would be of the form:

$$\Psi(\underline{r}) = \sum_l A_l f_l(\varepsilon,r)\ Y_{lm}(\underline{r})$$

where $f_l(\varepsilon,r)$ are the Coulomb functions of energy ε and A_l are coefficients. The hydrogenic wavefunctions could be suitable functions with reasonable accuracy at small r's and using a small number of terms. However, for two basic reasons [7], the discrete hydrogenic wavefunctions are thought to be unsuitable and instead the Sturmian wavefunctions are used: the first is that the computer needs a long time to compute the r^2 matrix elements and if a more efficient (Gauss-Laguerre) scheme is used

a very large number of matrix elements will need to be calculated and secondly and mainly that the discrete hydrogenic basis is not complete. If part of the hydrogenic continuum is included, the calculations converge to the wrong result. These two basic disadvantages can be overcome by using the Sturmian functions as first pointed out by Edmonds [8]. The wavefunction Ψ is expanded as:

$$\Psi = \sum_{n,l} \Psi^{(z)}_{nl} \cdot S^{(z)}_{nl}(r)\, Y_{lm}(r)$$

where the Sturmian functions $S_{nl}(z)$ are given by:

$$S^{(z)}_{nl}(r) = \sqrt{\frac{(n-l-1)!}{2(n+l)!}}\ (\zeta r)^{l+1} \cdot L^{(2l+1)}_{n-l-1}(zr)$$

where $L^{(2l+1)}_{n-l-1}(zr)$ is the associated Laguerre function and is defined as:

$$L^{(\alpha)}_{n}(x) = \binom{n+\alpha}{n} /F/(-n,\alpha+1;x)$$

The matrix elements of the magnetic interaction are given by:

$$Q_{nl,n'l'} = \int_0 r^2 S^{(\zeta)}_{nl}(r)\ S^{(\zeta)}_{n'l'}(r)\, dr$$

with $/l-l'/\leq 0,2$ and vanishes unless $/n-n'/\leq 3$. Expressions of $Q_{nl,n'l}$ and $Q_{nl,n'l+2}$ for $/n-n'/=0,\pm1,\pm2,\pm3$ are given in appendix 1 of [7].

A very important property of the Sturmian basis set is the fact that any positive value can be given to the variable z. When z=2/n then hydrogenic values are been produced (for zero field). For n>10 the above comment stops being true (as noted by Edmonds) even if 60 Sturmian functions per partial wave were included. Clark and Taylor [7] have found that higher values of z than 2/n must be used for such cases. A disadvantage of the Sturmian basis is that $S^{(z)}_{nl}(r)$ is orthogonal for 1/r and therefore the ovelap matrix is not diagonal in n but instead tridiagonal. However, this scheme is convenient since the vector components are ordered by increasing quantum numbers l and n respectively. The number of components that is required obeys a certain criterion and can therefore be determined [7]. For the results of [7] and for satisfactory convergence of oscillator strengths and energy levels thirty lower partial waves consistent with m and parity were used.

Using all the above, the equation for ψ_{nl} becomes an eigenvalue problem of the form:

$$H\,\Psi = \varepsilon\, B\,\Psi$$

where H is a banded matrix because of the selection rules ($\Delta n=0,\pm1,\pm2,\pm3$ and $\Delta l=0,\pm2$). Clark and Taylor used Crawford's algorithm ([7] and references therein) to solve the above equation, by finding the eigenvalues when H and B are both banded matrices and then by inverse iteration determining the eigenvectors. For these long calculations they used 2000

Sturmian functions to obtain the eigenvectors and the computer was the SERC CRAY-1. Such an inormously large computer was necessary for its speed of calculations and its large storage capacity. Once the eigenvectors had been calculated the dipole matrix elements and hence the oscillator strengths were easily obtained by inverse iteration [7].

Next in this description of Clark's and Taylor's work on the oscillator strength determination for high Rydberg series in the presence of moderate magnetic fields come a few words on the convergence of the calculations through the stability of the f-values with respect to the variable z. As the energy and the principal quantum number increase, the corresponding eigenfunctions move further away from the nucleus. This can be compensated up to a cerain degree by decreasing z but at some point this stops being useful. There an "unstable" energy region has been reached. The convergence of Clark's and Taylor's calculations is established as follows [12 , 13]: There is a certain range of values for z for a particular section of the spectrum over which the f-values and the energies are very stable.Then once this is established, n and l can be varied to obtain the required accuracy of convergence.

Finally the results of Clark's and Taylor's work for high Rydberg members (n=6,28) for hydrogen and for several magnetic field strengths will now be presented. Drs Clark and Taylor kindly provided us with their code and we ran it for B-fields and n values that we were interested in, ie B=2.5,7.5 and 20.0 Tesla and 2<n<28. From Figs.VII1,2 and 3 where the resulting f-values are plotted against energy we can see that for the low n's the usual discrete Rydberg pattern is obeyed very well while

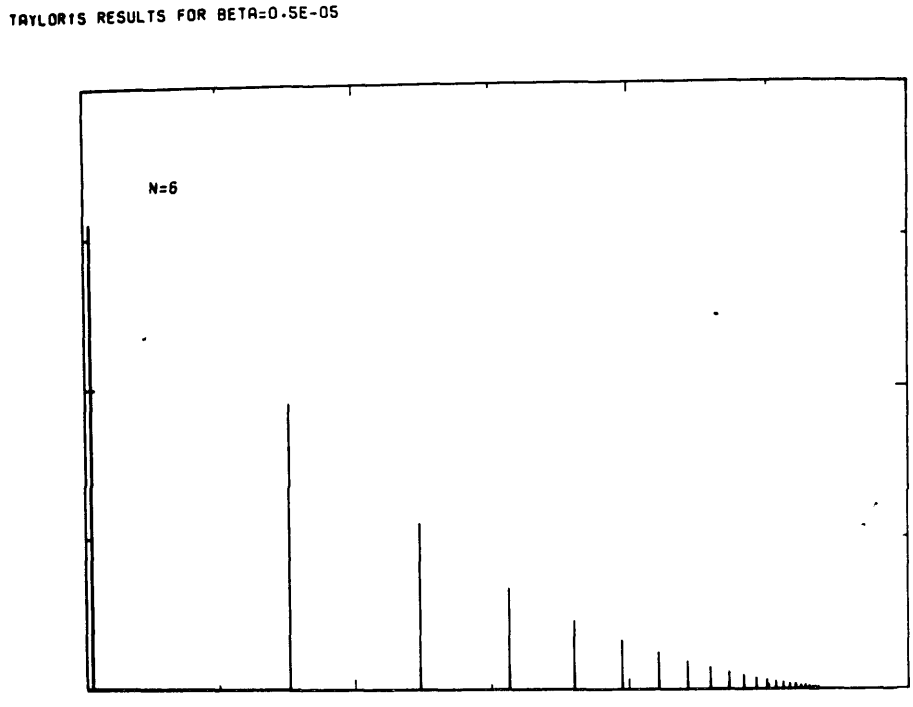

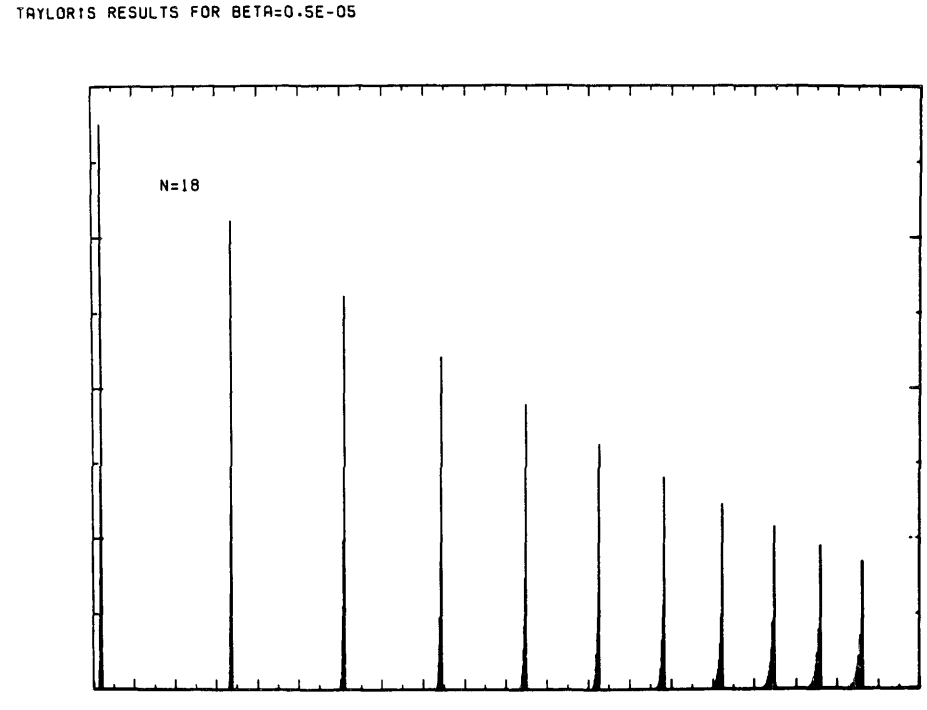

Fig.VII1

Results using Clark's and Taylor's code for hydrogenic f-values against energy for B=2.5 Tesla.

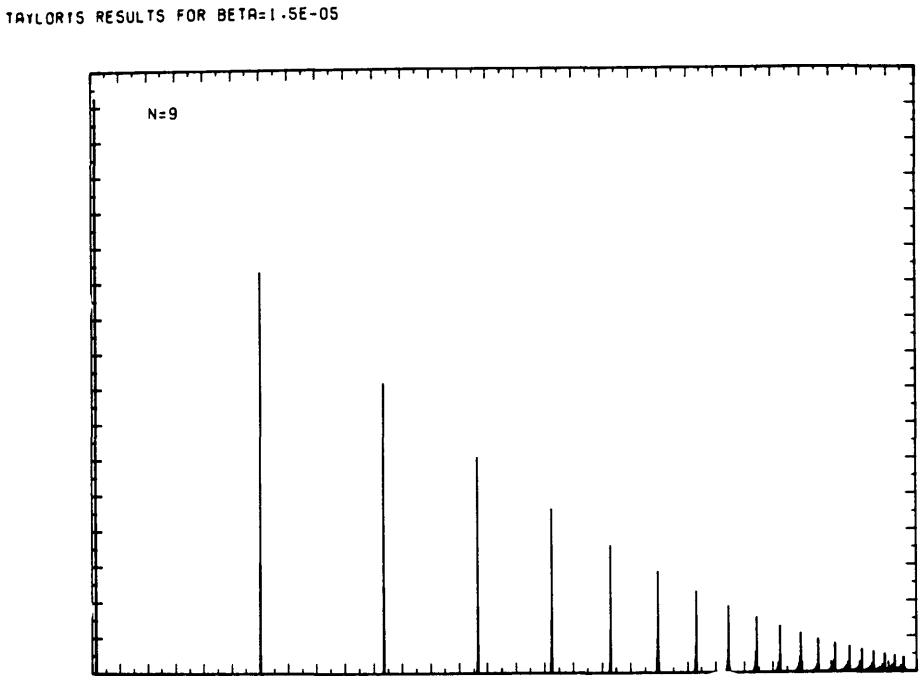

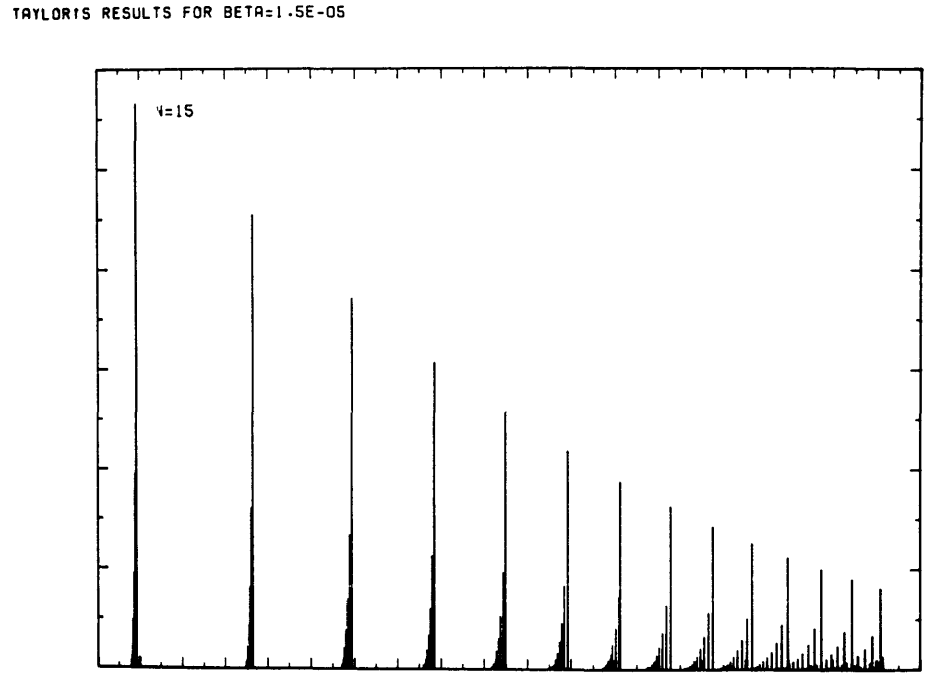

Fig.VII2

As Fig.VII1 but for B=7.5 Tesla.

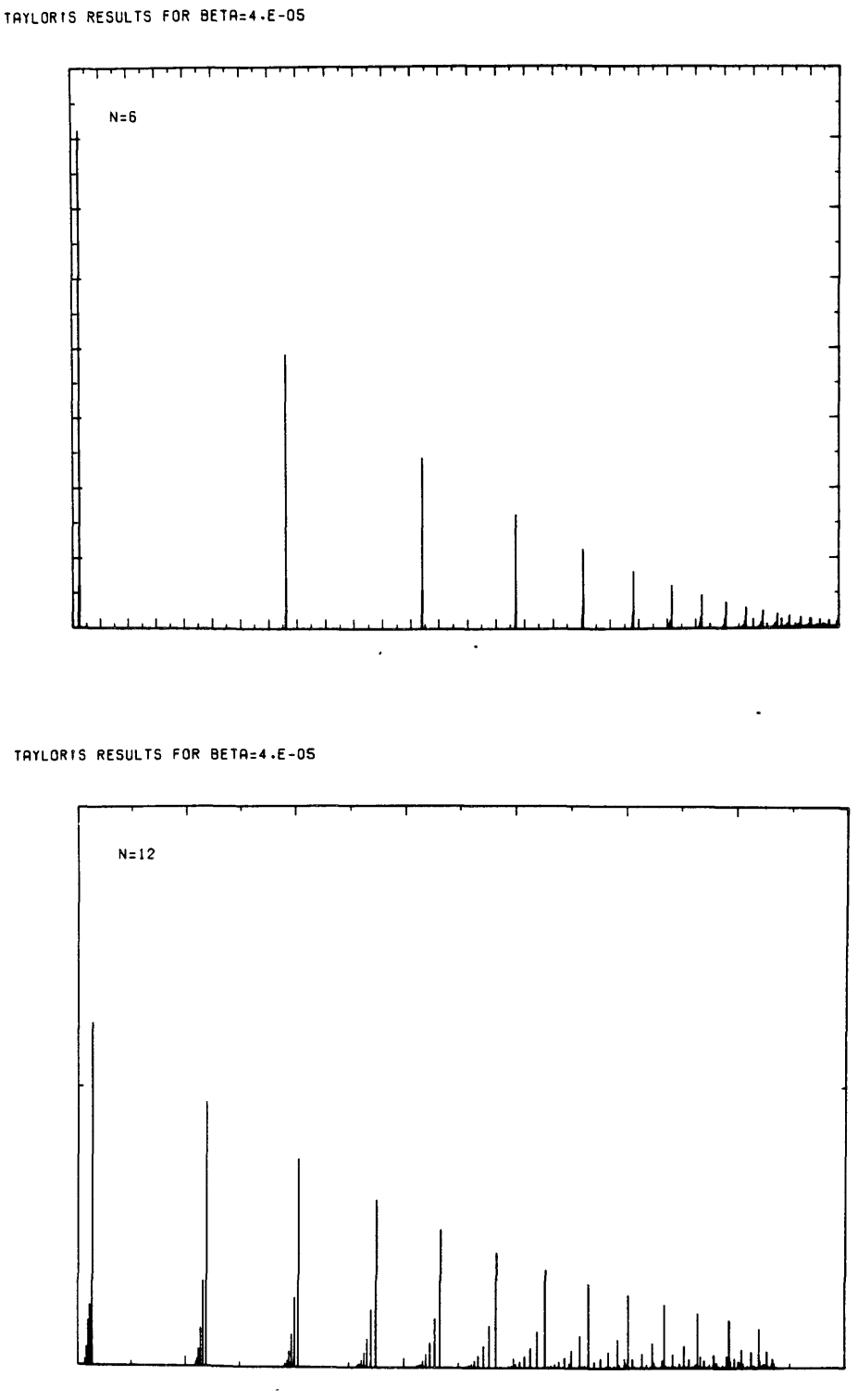

Fig.VII3

As Fig.VII1 but for B=19.5 Tesla.

as n increases we begin to see the configuration mixing effects. It can also be seen that for this case (M=+1) the l-mixing is weak and the weight of the oscillator strength is on the principal line (as opposed to the M=0 case [12, 13]) where the f-values are more equally distributed amongst all levels with the same n-value). As the field increases, basically the same features are exhibited only l-and n-mixing becoming more obvious and more dominant at much lower n's. For high fields (B>50T) the program failed to converge.

3.An Approximate Theoretical Method to Calculate f-Values in the Presence of External Magnetic Fields

As seen in the previous sections of this chapter several authors have attempted to study more carefully the dependence of f-values with an externally applied magnetic field. However most of them but two (Clark and Taylor) have dealt with very high magnetic fields ($>10^3$T) which are found in stellar plasmas. Clark and Taylor have studied the quadratic B-field f-value dependence at lower fields (<50T) for high Rydberg hydrogenic members but in their work they assumed that they were in the complete Paschen-Back regime with l and s being decoupled. Therefore, there was a need to study this effect for a higher element and when the linear Zeeman effect is valid and also for any value for the magnetic field. In particular we tried to find how the f-values of the principal series of the alkaline earths (our test element was MgI since we already had some experimental plates on magnesium taken at several field strenghs) varied with the magnetic field.

We needed to investigate how the following expression:

$$/\langle \Psi(\text{ground state}) /\underline{D}/ \Psi(1s^2 2s^2 2p^6 3snp)\rangle /^2$$

(VII1)

depended on P and n.

From the previous sections of this chapter, using King's work [1] we can obtain a matrix of the coefficients of the eigenvectors as a function of the magnetic field, is:

$/^1P_1^*\rangle$	α_1	β_1	γ_1
$/^3P_2^*\rangle$	α_2	β_2	γ_2
$/^3P_1^*\rangle$	α_3	β_3	γ_3

Table VII1 Matrix of coefficients of eigenvectors obtained from [1].

Therefore, each of the new eigenvectors Ψ_1, Ψ_2 and Ψ_3 can be expressed as a linear combination of the old LS allowed eigenfunctions $/^1P_1\rangle$,$/^3P_2\rangle$ and $/^3P_1\rangle$ as follows:

$$\Psi_1 = \alpha_1 /^1P_1\rangle + \beta_1 /^3P_2\rangle + \gamma_1 /^3P_1\rangle$$
$$\Psi_2 = \alpha_2 /^1P_1\rangle + \beta_2 /^3P_2\rangle + \gamma_2 /^3P_1\rangle$$
$$\Psi_3 = \alpha_3 /^1P_1\rangle + \beta_3 /^3P_2\rangle + \gamma_3 /^3P_1\rangle$$

(VII2)

Arbitrarily we chose to call $/^1P_1^*\rangle, /^3P_2^*\rangle$ and $/^3P_1^*\rangle$ the resulting eigenvectors Ψ_1, Ψ_2 and Ψ_3 in order of decreasing energy (the reason for this is that the program used, opperates in such a way that ouputs the eigenvectors in order of decreasing corresponding eigenvalues). For low B- fields, this nomenclature is consistent with the conventional naming of $/^1P_1^*\rangle$ as the function that contains the highest contribution of the $/^1P_1\rangle$ (ans similarly for $/^3P_2^*\rangle$ and $/^3P_1^*\rangle$ that contain most $/^3P_2\rangle$ and $/^3P_1\rangle$ respectively) but for highest fields the situation changes as will be seen in the text that follows.

Coming back to the f-value problem we see that we have to evaluate the following:

$$/\langle 3s^2/\underline{D}/\Psi_1\rangle/^2 = /\alpha_1\langle 3s^2/\underline{D}/^1P_1\rangle/^2 + /\beta_1\langle 3s^2/\underline{D}/^3P_2\rangle/^2 + /\gamma_1\langle 3s^2/\underline{D}/^3P_1\rangle/^2$$

$$/\langle 3s^2/\underline{D}/\Psi_2\rangle/^2 = /\alpha_2\langle 3s^2/\underline{D}/^1P_1\rangle/^2 + /\beta_2\langle 3s^2/\underline{D}/^3P_2\rangle/^2 + /\gamma_2\langle 3s^2/\underline{D}/^3P_1\rangle/^2$$

$$/\langle 3s^2/\underline{D}/\Psi_3\rangle/^2 = /\alpha_3\langle 3s^2/\underline{D}/^1P_1\rangle/^2 + /\beta_3\langle 3s^2/\underline{D}/^3P_2\rangle/^2 + /\gamma_3\langle 3s^2/\underline{D}/^3P_1\rangle/^2$$

(VII3)

Using the fact that in LS coupling:

$$\langle(^1S_o)/\ \underline{D}\ /^3P_2\rangle \quad \text{and} \quad \langle ^1S_o/\underline{D}\ /^3P_1\rangle$$

are zero, then we have to find the following:

$$f(\Psi_1) = /\alpha_1\ \langle 3s^2(^1S_o)/\underline{D}/3snp(^1P_1)\rangle/^2$$

$$f(\Psi_2) = /\alpha_2\ \langle 3s^2(^1S_o)/\underline{D}/3snp(^1P_1)\rangle/^2$$

$$f(\Psi_3) = /\alpha_3\ \langle 3s^2(^1S_o)/\underline{D}/3snp(^1P_1)\rangle/^2$$

(VII4)

The coefficients α_1, α_2 and α_3 can be obtained from King's program if we input the wavelength and the electrostatic and spin-ordit parameters of the transitions in question (in units of cm^{-1}). The wavelengths for n=7 to 27 can be used [14] and the other two parameters can be calculated by a Hartree-Fock program that calculates radial functions which will be discussed later. Therefore at this point we could do two things: 1)either assume that $\langle 3s^2(^1S_0)/\underline{D}/3snp(^1P_1)\rangle=1$ and knowing the α's see how $f(\Psi_1)$, $f(\Psi_2)$ and $f(\Psi_3)$ vary relatively to each other with the B-field and the n-value and also α_1^2 (or α_2^2 or α_3^2) versus P-field (or n-value) would show how f- values depend on B (or n) or 2) try and calculate $\langle 3s2(^1S_0)/\underline{D}/3snp(^1P_1)\rangle$ and using the above equations and the α's from King's program [1] we would see how f-values depended on B and n in an absolute way. In the present work we prefered to do the latter which seemed more interesting. To calculate these electric dipole transitions we have used a program that was initially developed by Fischer and Saxena [9] which uses the radial functions obtained from Multi-Configurational Hartree-Fock calculations [10]. The next sections will be devoted to a brief and general discussion on the Hartree-Fock problem, to the description of the oscillator strength program used and the results obtained.

4.Brief Discussion on Hartree-Fock Calculations

In the work described in this thesis use has been made of the Multi-corfiguration hartree-Fock program of Froese Fischer [10]. A non- standard aspect of this work is its application to high n states. In this and the next section we will discuss briefly what Hartree-Fock codes do and describe the adaptations

needed to Fischer's code to model high n states.

The Hartree-Fock method has been used over the last 50 or so years to obtain approximate solutions to Schrodinger's equation in many electron atoms and ions. A vast literature exists and two books [11, 12] are devoted to the numerical aspects of these problems. Here we will briefly outline what Hartree-Fock calculations involve (apart from reference [11] another excellent but shorter review on H-F calculations used was [13]).

Our aim was to solve the non-relativistic Schrodinger equation for an N electron system in the field of a massive point charge (+eZ):

$$H\,\Psi = E\,\Psi$$

$$H = \tfrac{1}{2}\sum_{i=1}(\nabla_i^2 + 2Z/r_i) + \sum_{i>j} 1/r_{ij} \qquad \text{(VII5)}$$

Instead of solving equation VII5 the Hartree-Fock method seeks solutions to:

$$\hat{H}\,\Phi = E\,\Phi$$

$$\hat{H} = \sum_{i=1}^{N} (-\tfrac{1}{2}\nabla_i^2 + Z/r + V(r)) \cong H$$

Now if Φ is expressed as the product:

$$\Phi = \phi(1)\phi(2)\ldots\phi(N)$$

which satisfy:

$$(-\tfrac{1}{2}\nabla_i^2 + Z/r_i + V(r_i))\ \phi(i) = E_i\ \phi(i) \qquad \text{(VII6)}$$

additionally (because of spherical symmetry) we can express:

$$\phi\ (r,\theta,\phi,\sigma) = \frac{1}{r} P(r)\ Y_{lm_l}(\theta,\phi)\ \chi_{m_s}$$

P(r) satisfies:

$$\left(d^2/dr^2 + 2Z/r - 2V(r) - l(l+1)/r^2 - \varepsilon \right) P(r) = 0$$

$$\varepsilon = -2E_i \qquad \text{(VII7)}$$

subject to the boundary condition $P(0)=P(\infty)=0$. Thus the one electron wavefunction may be described in the Hartree-Fock method by $\{nlm_lm_s\}$.

There are symmetry requirements which must be imposed on Φ so that it behaves in the same manner, with the interchange of two electrons, as the proper eigenfunction Ψ. This can be achieved by expressing Φ as a Slater determinant:

$$\Phi = (N!)^{-\frac{1}{2}} \begin{vmatrix} \phi_1(1) & \cdots & \cdots \\ \cdots & \cdots & \cdots \\ \cdots & \cdots & \phi_N(N) \end{vmatrix} \qquad \text{(VII8)}$$

In the Hartree-Fock method the radial equation VII7 for ϕ's with the same l need not be the same. The orthogonality of radial wavefunctions with the same l is thus not assured but conventionally is imposed.

$$\int \phi_{nlm_l m_s} \phi_{n'l'm_l'm_s'} d\tau = \delta_{nn'} \delta_{ll'} \delta_{m_l m_l'} \delta_{m_s m_s'} \tag{VII9}$$

This is an additional constraint and not a property of the equations.

Further properties which should be possed by Φ can be seen by noting that H is independent of S^2 and S_z (so must commute with it) and also commutes with L^2 and L_z. Therefore we expect:

$$L^2\Phi = L(L+1)\phi \ , \ S^2\phi = S(S+1)\phi$$

$$L_z\phi = M_L\phi \quad \text{and} \quad S_z\phi = M_S\phi$$

to hold. This means that it may not be appropriate to express Φ as a single Slater determinant. Fischer uses:

$$\Psi(\gamma LS) = \sum_{j=1}^{NCFG} c_j \Phi_j(n_1l_1, n_2l_2, \ldots, n_Nl_N, SL) \tag{VII10}$$

where NCFG is the number of configurations and imposes that $\langle \Phi_i / \Phi_j \rangle = \delta_{ij}$.

The method used to solve for the wave function relies on a variational principle. This can be introduced by considering the exact solution of equation VII2C, $/\Psi\rangle$. Obviously, we have that:

$$\langle \psi / H-E / \psi \rangle = 0 \tag{VII11}$$

If we define $\delta \langle \Psi / A / \Psi \rangle$ by:

$$\lim_{\epsilon \to 0} \frac{d}{d\epsilon} \left(\langle \psi' / A / \psi' \rangle \right), \; / \psi' \rangle = / \psi \rangle + \epsilon / \delta \psi \rangle$$

where $/ \delta \Psi \rangle$ is an arbitrary perturbation, then

$$\delta \langle \psi / H-E / \psi \rangle = \langle \delta \psi / H-E / \psi \rangle + \langle \psi / H-E / \delta \psi \rangle = 2 \langle \delta \psi / H-E / \psi \rangle = 0$$

(VII12)

Hartree-Fock calculations aim to find approximate numerical solutions to the equations. They use the analogs of equations VII11 and VII12:

$$\langle \Phi / H-E / \Phi \rangle = 0 \qquad \text{(VII11')}$$

$$\langle \delta \Phi / H-E / \Phi \rangle = 0 \qquad \text{(VII12')}$$

and are considered to define the "best" solution for a given numerical approximation. The description of $/ \Phi \rangle$ and $/ \delta \Phi \rangle$ is restricted by the finite numerical model. So equations VII11' and VII12' only imply:

$$(H-E) / \Phi \rangle = R$$

where R is a residual error which is orthogonal to $/ \Phi \rangle$ and any $/ \delta \Phi \rangle$. The solution to equations VII11' and VII12' leave

$$E(\Phi) = \langle \Phi / H / \Phi \rangle \; / \; \langle \Phi / \Phi \rangle$$

stationary with respect to first order pertubations in / Φ>. This is the basis of the method of solution of the Hartree-Fock equations. The energy is given by [11]:

$$E_{total}(\gamma LS) = \sum_{j=1}^{NCFG} c_j^2 E_1(\text{average}) + \sum_{k_m m=1}^{NCFG} a_m c_{jm} c_{j'm} F^{k_m}(i_m j_m; i'_m j'_m) + \sum_{m=1}^{NCFG} b_m c_{jm} c_{j'm} G^{k_m}(i_m j_m; i'_m j'_m) + \sum_{m=1}^{NCFG} d_m c_{jm} c_{j'm} R^{k_m}(i_m i_m j_m; i'_m i'_m j'_m)$$

where $a_m, k_m, i_m, j_m, i'_m, j'_m$ and $b_m, k_m, i_m, j_m, i'_m, j'_m$ are inputed in the program as data for the F^k and G^k terms respectively.

(VII13)

$F^k(nl,n'l') = R^k(nl,n'l';nl,n'l')$ and $G^k(nl,n'l') = R^k(nl,n'l';n'l',nl)$

where $R^k(\alpha,\beta;\alpha',\beta') = \iint P(\alpha;r)\, P(\alpha',r) U^k(r,s) P(\beta;s)\, P(\beta',s)\, dr ds$

where $U^k(r,s) = s^k/r^{k+1}$ for $r \geqslant s$

and $= r^k/s^{k+1}$ for $r < s$

The energy must be stationary with respect to changes both in the c coefficients and all the P(n,l)'s. This is achieved iteratively by alternatively finding the c's which give a stationary state for final products and then finding the

P(n,l)'s which give a stationary state for fixed c's. There are, of course, many other levels of iteration since the equations are highly non-linear. The conditions that E(total) ve stationary lead to an equation for the P(n,l)'s of the form:

$$\left(d^2/dr^2 + \frac{2}{r}(Z-Y(nl,r)) - \varepsilon_{nl,nl} - l(l+1)/r^2 \right) P(nl,r) =$$

$$2X(nl,r)/r + \sum_{n'} \varepsilon_{nl,n'l} P(n'l,r)$$

$$\text{where } Y(nl,r) = \sum_{n'l',k} \frac{A_{nl,n'l',k}\, Y^k(n'l',n'l;r)}{n'l'/n'l'}$$

$$X(nl,r) = \sum_{n'l'=nl,k}{}' \frac{B_{nl,n'l',k} Y^k(nl,n'l',r) P(n'l',r)}{n'l'/n'l'}$$

(VII14)

$$\text{and} \quad A_{nl,n'l',k} = (1+\delta_{nl,n'l'}) a_{nl,n'l',k} / q_{nl}$$

$$B_{nl,n'l',k} = b_{nl,n'l',k} / q_{nl}$$

$$\delta I(nI) = - \int Q(nl,r) LP(nl,r)\, dr$$

$$\delta F^k(nl,n'l') = 2(1+\delta_{nl,n'l'}) \int Q(nl,r) P(nl,r) (1/r) Y^k(n'l',n'l',r)\, dr$$

$$\delta G^k(nl,n'l') = 2 \int Q(nl,r) P(n'l',r) (1/r) Y^k(nl,n'l',r)\, dr$$

The coefficients in equation VII14 depend on the other P(n,l)'s and hence iteration is required. Constraints which have been introduced, orthogonality and normalisation, must be accounted

for in the numerical solution. The Lagrange multipliers (described in any mathematics standard textbook as [22]) can be used to do this.

5.Solution of the Radial Equation for Large n States

The grid used in the program of Froese-Fischer [10] and in associated programs is given by:

$$\rho_j = \log_e Zr_j \qquad \text{(VII15)}$$

with $\rho_i = -A + B(j-1)$ $(j=1,2,\ldots M)$. This gives the values of the radius at mesh points as:

$$r_0 = 1/Z\ e^{\rho_i} \qquad \text{(VII16)}$$

Values of A=-4 and B=1/16 are recommended [10] for most applications. This mesh has two advantages over a mesh uniformly spaced in r. Firstly high resolution is provided near the origin where P(nl,r) is expected to change rapidly (it is a singular point). Secondly by transforming to ρ as the independent variable, and also tranforming the dependent variable in equation VII14, it is possible to perform the calculations more economically.

A problem occurs if we wish to have states with $n \geq 10$. For these cases the increments between successive mesh points, Δr, becomes too large at large values of r for the value of B=1/16. Using this value of B we found that the results became very unphysical at large r. P(nl,r) was no longer smooth as can be seen in Figs.VII4 and 8 where the outer region contained straight lines rather than curves. By solving for P(nl,r) on a

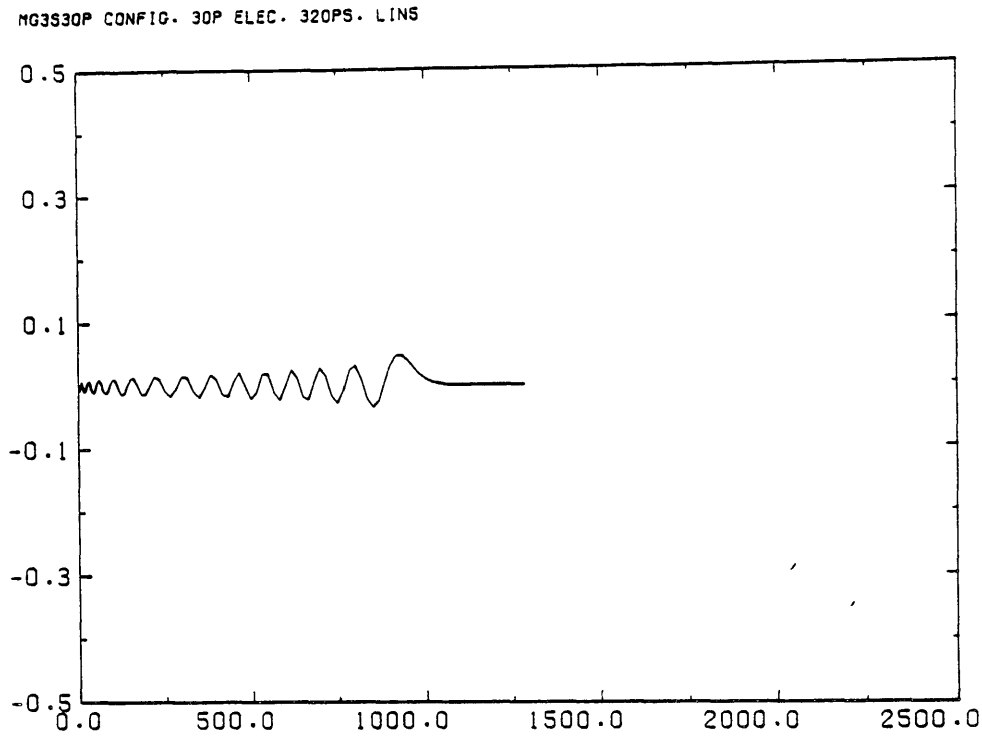

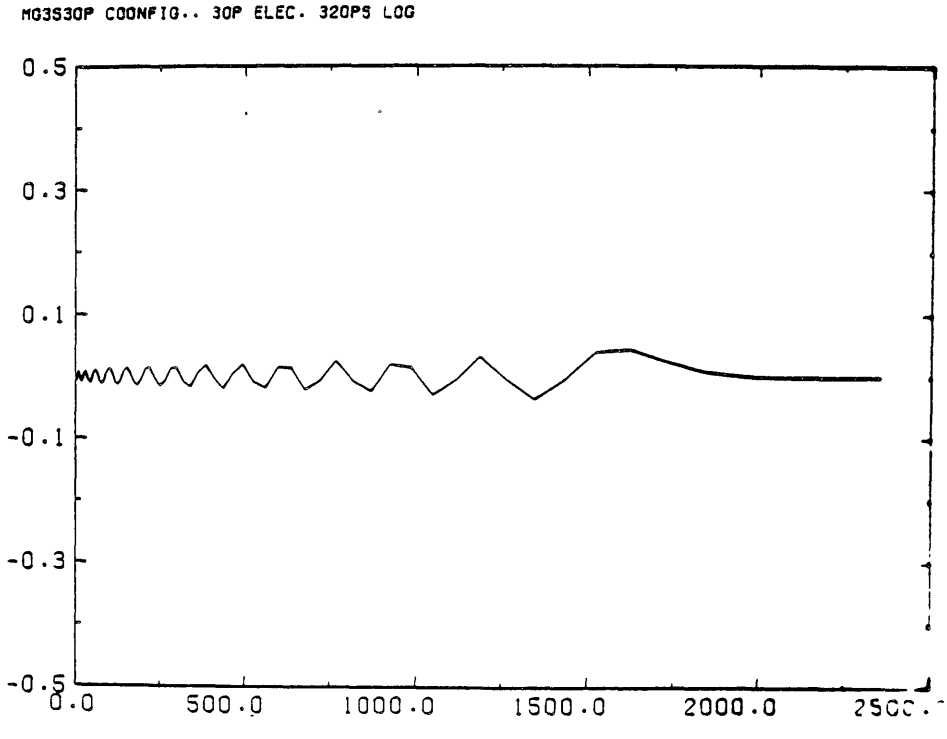

Figs.VII 5 and 4 Computed radial wavefunction for the 3s3Op configuration for MgI on the logarithmic mesh given by [16] and on the "linear 5" mesh (see text), both for 320 points.

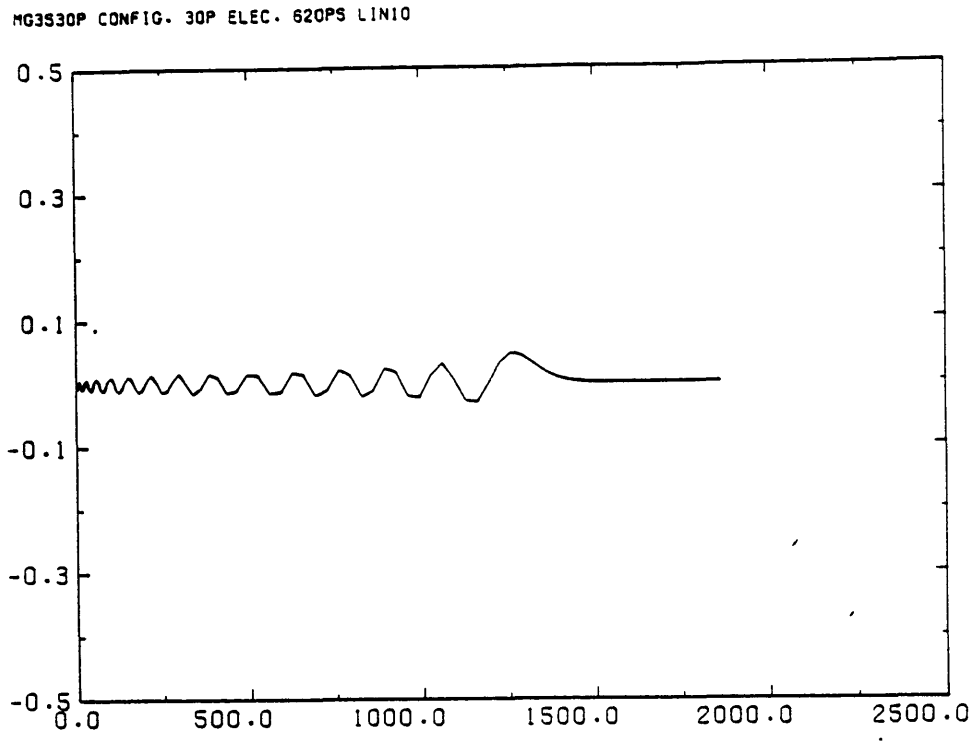

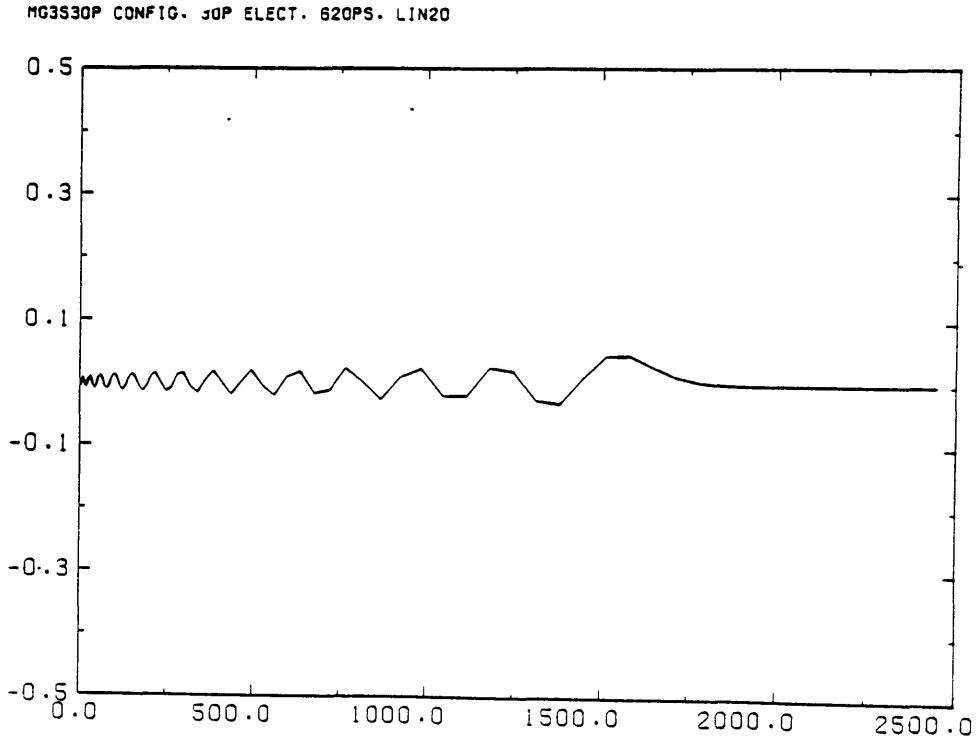

Figs.VII6 and 7 As Figs.VII4 and 5 but for "linear 10" and "linear 20" radial grids respectively (both for 620 points accross).

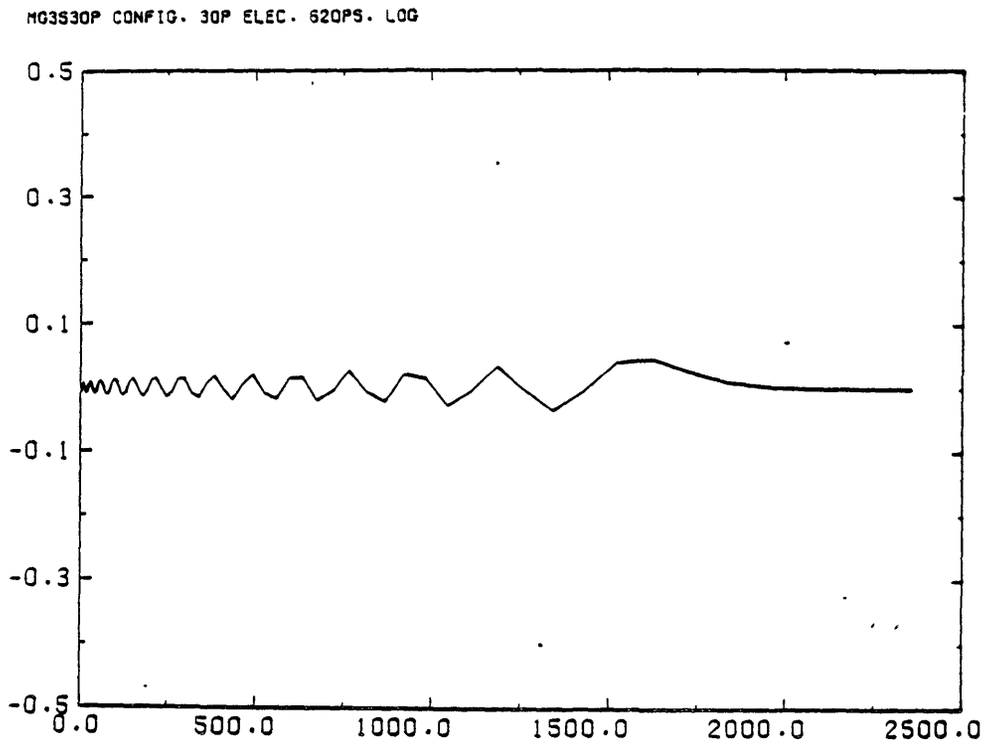

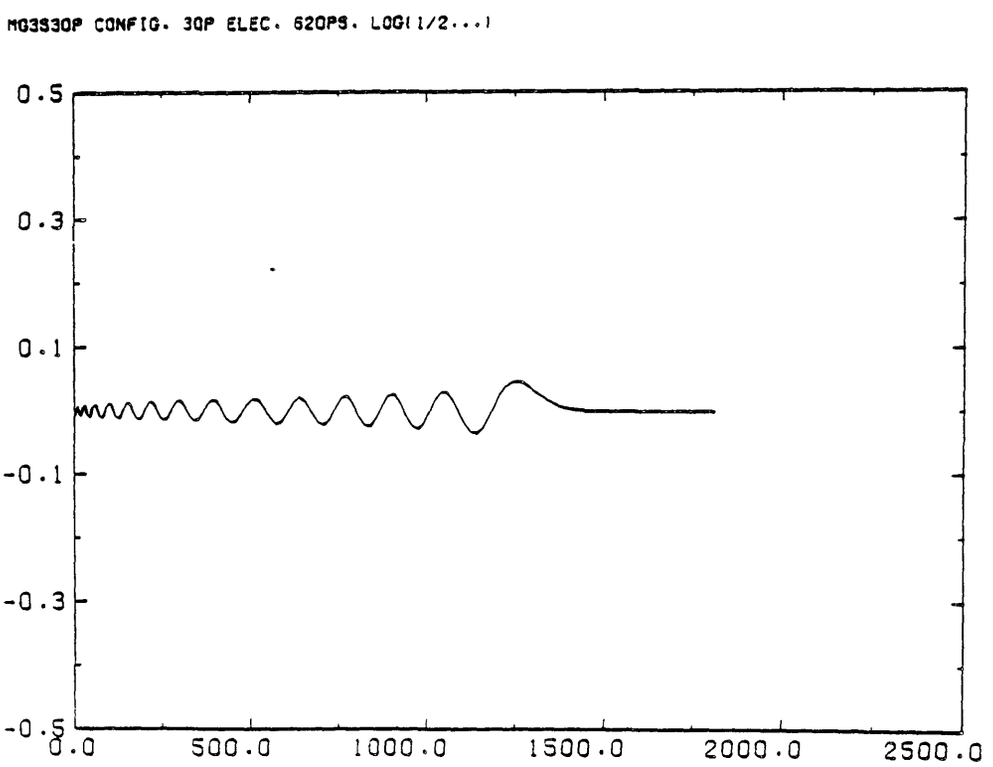

Figs.VII8 and 9 As Figs.VII4 and 5 but on the *logarithmic* radial mesh suggested by [16] and on the "1/2" logarithmic radial mesh suggested by the present calculations (see text), both for 620 points accross.

mesh where Δr was given by the maximum of $1/z \exp(\rho_{i+1}) - 1/z \exp(\rho_i)$ (=5,10 and 20 and for different number of mesh points shown in Figs.VII5,6 and 7 respectively) and Δr_{max} smooth solution to the finite difference equations could be obtained. Such a mesh spacing is however incompatible with other parts of the program and also with other programs which we used to produce the f- values. (The program of [10] which uses $\rho = \alpha r + \beta \log_e r$ as a variable would be more appropriate for overcoming these problems). Instead we used a smaller value of B. A suitable value of B, and increasing the number of points untill no further improvement in the results is found. Very good results have been achieved for n in the range 7 to 30 for A=-4, B=1/32 and 620 mesh points as seen in Fig.VII9. Also the number of nodes is correct. If we were not limited by the storage capacity of the computer, the mesh interval would have been futher decreased and more points would have been included. Fig.VII10 shows the radial functions for the inner electrons which behave in the expected way. Therefore, so far we have seen how to obrtain the radial functions for high-n states in the MgI principal series.

6.The Calculational and Computational Aspects of the f-Value Determination Procedure

The second program used in this work was originally developed by Fischer and Saxena [9] and calculated oscillator strengths using the multi- configuration radial functions obtained from the previous program. In this program, both length and velocity oscillator strengths are calculated (which are defined as):

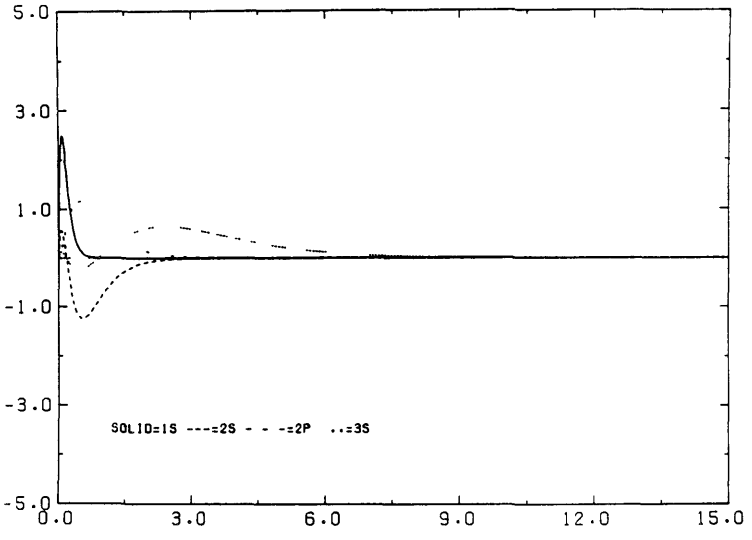

Fig.VII10

The computed radial functions of the inner electrons (3s3s-3s30p).

Length form:

$$gf = \frac{2}{3} \Delta E\,(2S+1) \left\langle \gamma LS / \sum_i r_i / \gamma' L' S \right\rangle^2 \qquad \text{(VII17)}$$

Velocity form:

$$gf = \frac{2}{3} \frac{1}{\Delta E} (2S+1) \left\langle \gamma LS / \sum_i \nabla_i / \gamma' L' S \right\rangle^2 \qquad \text{(VII18)}$$

Let us suppose that we have to calculate the matrix elements:

$$\langle \gamma LS/Q/\gamma' L' S \rangle$$

where Q is a tensor of rank 1 (as in equations VII 7 and 8′) and where the initial and final states are defined respectively as:

$$\Psi(\gamma LS) = \sum_i^n a_i \, \Phi(\gamma_i LS)$$

and

$$\Psi(\gamma' L' S) = \sum_i^n a_i \, \Phi(\gamma' L' S) \qquad \text{(VII19)}$$

Also

$$\langle \gamma LS/Q/\gamma' L' S \rangle = \sum_i^{m} \sum_j^{m'} a_i a_j' \langle \gamma_i LS/Q/\gamma_j' LS \rangle$$

This equation reduces to one-electron integrals' expression as:

$$\langle \gamma LS/Q/\gamma' LS \rangle = \sum_k a_{ik} a'_{jk} c_{ikjk} \langle n_k l_k / Q / n'_k l'_k \rangle \qquad \text{(VII20)}$$

More technically speaking, the mixing coefficients a_j and the radial functions were calculated in the previously described MCHF code [10] while the coefficients C_{ikjk} used to convert equation VII19 to one-electron integrals were calculated in a lengthy and complicated program originally developed by Robb [15] but subsequently modified for clearer spectroscopic notation by Fischer and Saxena [16].

The matrix elements in length and velocity form are given respecively by:

$$\langle nl/Q/n'l' \rangle = (-1)^{l_{max}-l} \sqrt{l_{max}} \int_0^\infty P_{nl}(r) r P_{n'l'}(r)\, dr$$

and

$$\langle nl/Q/n'l' \rangle = (-1)^{l_{max}-l+1} \sqrt{l_{max}} \int_0^\infty P_{nl}(r) \left(d/dr + \frac{l(l+1)-l'(l'+1)}{2r} \right) P_{n'l'}(r)\, dr$$

where $l_{max} = \max(l,l')$ and $P_{nl}(r)$ and $P_{n'l'}(r)$ are the radial wavefunctions. As mentioned by Fischer and Saxena [9] the numerical integrations were performed using Simpson's rule and

Stirling's formula for the length and velocity expressions respectively.

All three programs used for finding the f-values were obtained from the Computer Physics Communications Library at Queen's University in Belfast. Unfortunately, to obtain the correct results, it was not just a question of loading them and running them on the computer here at Imperial College. Apart from the very complicated task of changing in all programs the radial mesh spacing for high-n states correct $P_{nl}(r)$ behaviour, we also had to convert all the programs from double precision to single precision because our computer has a word length greater or equal to 48 bits and so double precision should not be used.

The following tables show briefly the input data and output results from the three codes used.

1) number of cases, input, output, tape (a)

2) for each case: order of tensor operator

whether tensor operator is or not spin dependent

maximum number of orbitals

output tape (b)

3) nl labelling of all the electrons

4) number of configurations and the number of shells in each configuration

5) the ln labelling of each electron (for each occupied shell) and the occupation number. And finally,

6) the coupling of the individual shells and then the coupling of shells (parentage notation)

Inserted in program AAKP (22)

DATA1..... coefficient of one-electron reduced matrix element and indices of the electrons involved.

1) label of the atom and term, atomic number,

number of points, number of wavefunctions,

number of wavefunctions to be made self-consistent with the core to remain fixed,

number of configurations, number of F^k, G^k and R^k integrals.

2) configuration data (labels and weights).

3) For each electron: label, n and l quantum numbers,

estimated screening parameter,

type of method to solve differential equation.

4) The value of the F^k, G^k and R^k integrals if any are present and the index of electrons they refer to.

5) Type of outputing, number of sweeps through the differential equations and the number of equation solved after the sweep through the system.

Inserted in program ACRF (16)

DATA2 ..... Amongst other data we obtain the radial functions and the mixing coefficients

1) DATA1

2) DATA2

3) label and atomic number for the atom,
number of radial functions,
label and number of configuration of initial and
final states a nd multiplicity (2S+1) value.

4) energy and configuration of initial and
final states.

Inserted in program ACRZ (15)

RESULTS..... Oscillator strength of the

transition in length and velocity form.

7.Results

In the f-value program we needed to insert the radial functions of the 1s,2s,2p,3s and np electrons for the principal series of Magnesium. The first four radial functions were obtained by running the Hartree-Fock program for the ground state and the fifth radial function was obtained from the (3snp) excited state. Since the f-value expressions both for length and velocity depend strongly on ΔE, an accurate value of it should be inserted in the code and was considered best (also mentioned by Fischer and Saxena) rto use the experimetnal values. We obtained the follwing f-values (table VII2) for the principal series of MgI (3s3s-3snp, n=7 to 27).

Ideally, one would expect that the length and velocity oscillator strengths should be identical. However, in our results they differ by a factor of approximately two. The same discrepancy (of a factor of two) was recently observed by Griffin et al [17] for the $3p^6 3d(^2D)-3p^5 3d^2(^2D)$ and (^2F) transitions in Ti^{+3} who also used Hartree-Fock wavefunctions to calculate the transition probabilities. Tiwary et al [18] state that FH calculations do not take properly into account correlation effects with neighbouring energy states, which are in some cases substancial and subsequently they used the sophisticated configuration interaction (CI) wavefunctions produced by a code written by Hibbert et al [19]. Considering the above facts and that also Kelly's paper [20] who stated that the geometric mean of the length and velocity values reduces the correlation problems, we calculated these geometric means. Also, we normalised all our results to the n=7 f-value of Fitchell [21] as we had done in Chapter VI. The ratio f(n=7)/f(n=8) of our present calculations (=1.646) compared quite well with the one obtained from Fitchell's values [21] (=1.756).

n	f_l	f_v	f_g
7	4.110(-3)	1.850(-3)	2.757(-3)
8	2.492(-3)	1.127(-3)	1.675(-3)
9	1.635(-3)	7.426(-4)	1.102(-3)
10	1.132(-3)	5.162(-4)	7.644(-4)
11	8.141(-4)	3.693(-4)	5.483(-4)
12	6.116(-4)	2.779(-4)	4.123(-4)
13	4.646(-4)	2.140(-4)	3.153(-4)
14	3.653(-4)	1.668(-4)	2.468(-4)
15	2.899(-4)	1.338(-4)	1.969(-4)
16	2.343(-4)	1.084(-4)	1.594(-4)
17	1.945(-4)	8.975(-5)	1.321(-4)
18	1.628(-4)	7.466(-5)	1.102(-4)
19	1.350(-4)	6.274(-5)	9.203(-5)
20	1.165(-4)	5.361(-5)	7.903(-5)
21	9.968(-5)	4.607(-5)	6.776(-5)
22	8.758(-5)	3.97(-5)	5.896(-5)
23	7.506(-5)	3.455(-5)	5.092(-5)
24	6.573(-5)	3.0141(-5)	4.471(-5)
25	5.718(-5)	2.660(-5)	3.889(-5)
26	5.083(-5)	2.343(-5)	3.451(-5)
27	4.527(-5)	2.065(-5)	3.057(-5)

Table VII2 f-values (in length and velocity form and the geometric mean) obtained from the present calculations.

Unfortunately, Mithell stops at n=8 and therefore no more comparisons can be made. A final comment on these zero-field calculated results is that the oscillator strength decreases as n increases which obeys the same general trend that we found from the experimental data (analysed with the MOV method). Our f-values are shown plotted against energy and n-value in Figs.VII11 and 12 respectively.

Having obtained the zero-field f-values, and the matrix coefficients from King's program we will now present the results that we obtained for the f-value B-field and n-value dependence. Figs.VII13 and 14 show the B- field dependence (for 3s3s-3s19p for MgI) of the $/^1P_1^*>$, $/^3P_2^*>$ and $/^3P_1^*>$ states for M=+1 and -1 respectively. We can see that in the range of 0 to 6 Tesla (which is of experimental interest), there is a negligible B-field effect on all but the $/^3P_2>$ f-value. The large jump of the the $/^3P_2^*>$ and the $/^1P_1^*>$ f-values is a consequence of the convention that we have used to label the states (this has been commented on previously) and is a result of the $/^1P_1^*>$ and $/^3P_2^*>$ states crossing. Fig.VII15 presents the same information but grouped according to the state (for the + and - M components). Finally, Figs.VII16,17 and 18 present the same results but for nine different n-values (in the range 7 to 27) which all show the same trends as noted above.

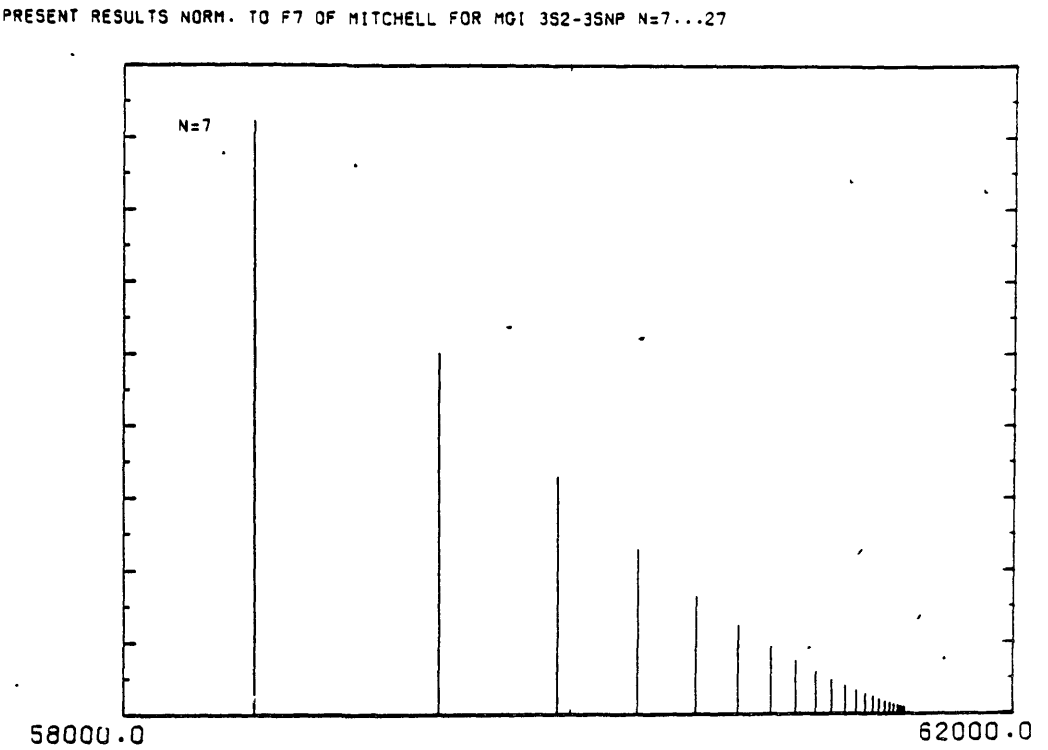

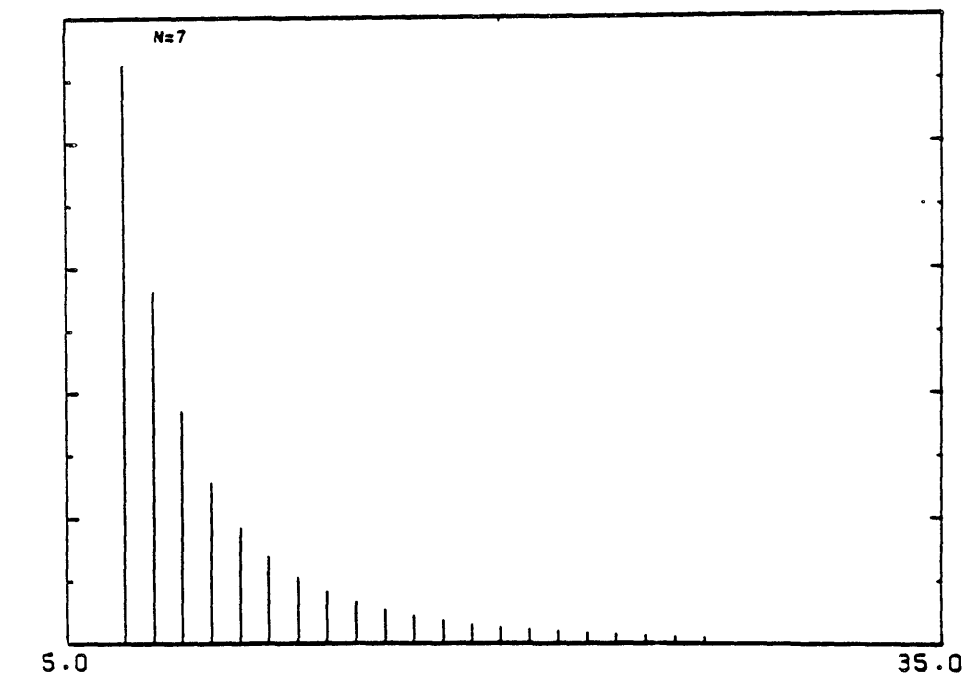

Figs.VII11 and 12 Computed zero field f-values with present calculations versus energy and n-value respectively for the principal series of MgI (with $7<n<27$).

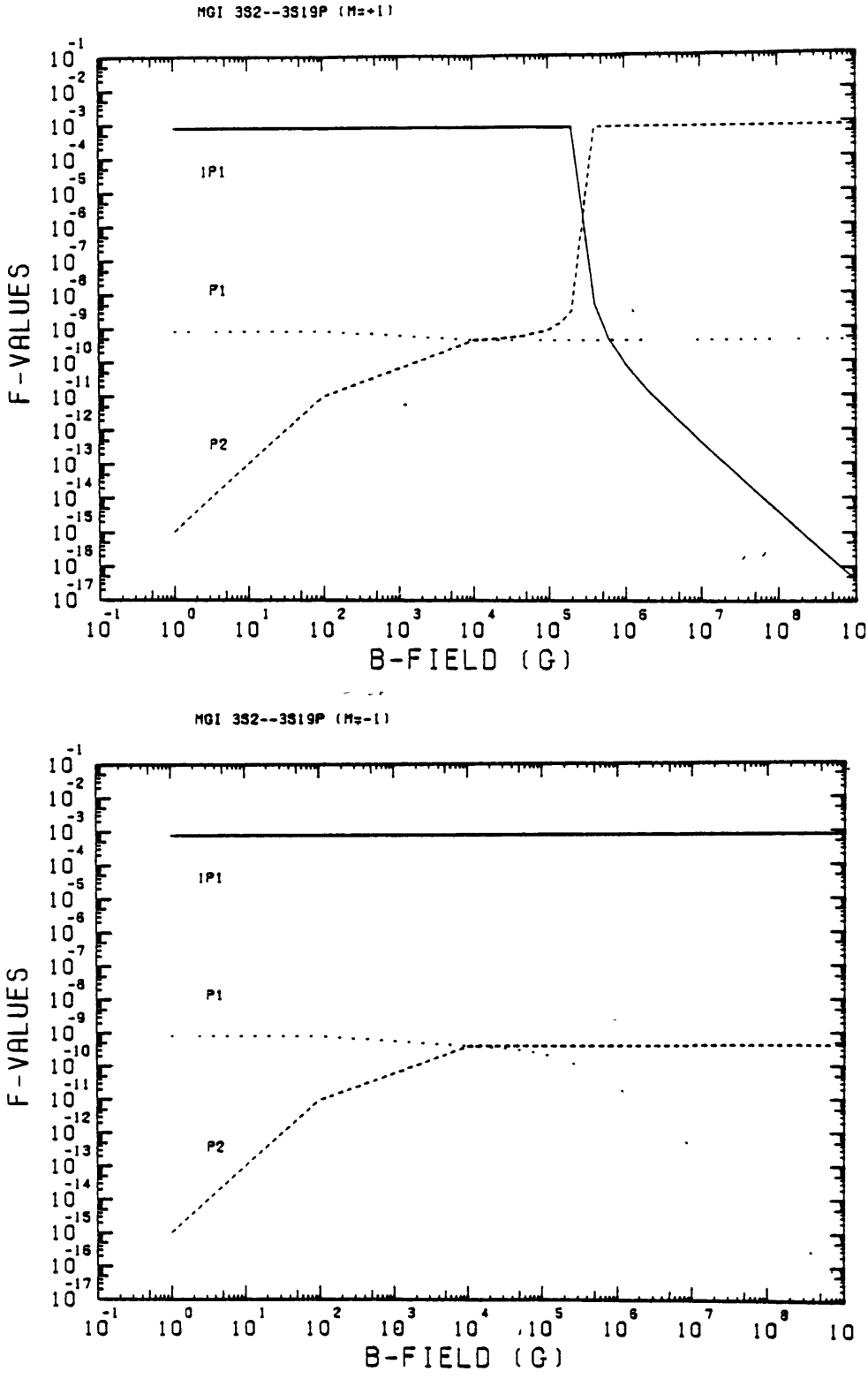

Figs.VII13 and 14 The P-field dependence of the f-values ($3s3s$-$3s19p$ transition for MgI) according to the present calculations of the $/^1P_1^*>$, $/^3P_2^*>$ and $/^3P_1^*>$ states for M=+1 and M=-1 respectively (see text for $/^1P^*>$ notation).

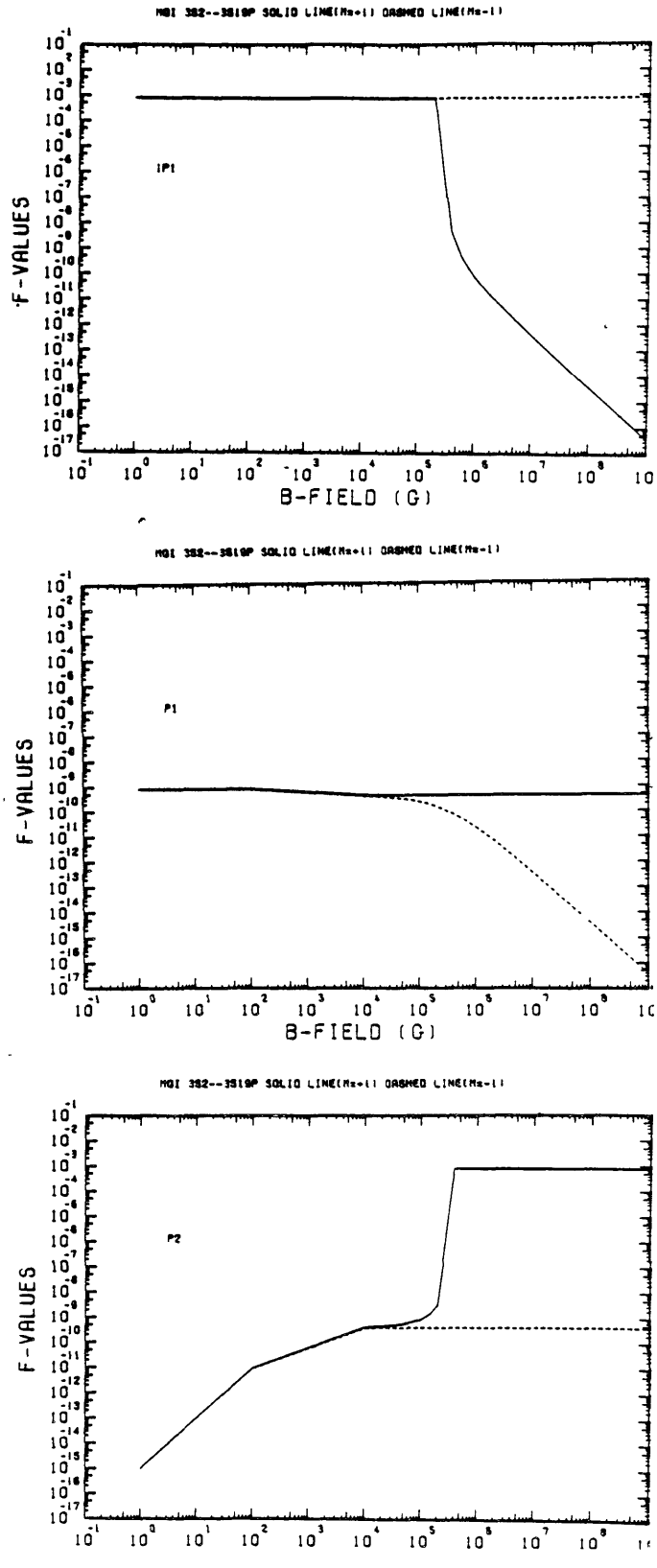

Fig.VII15

The same information as in Figs.VII13 and 14 but grouped differently.

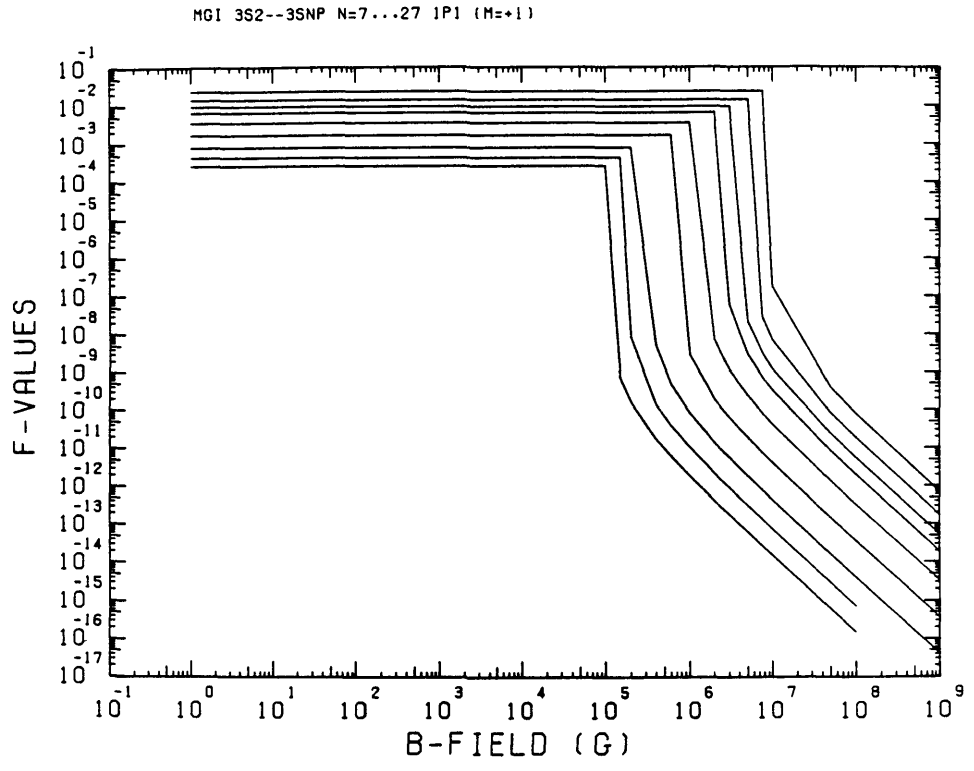

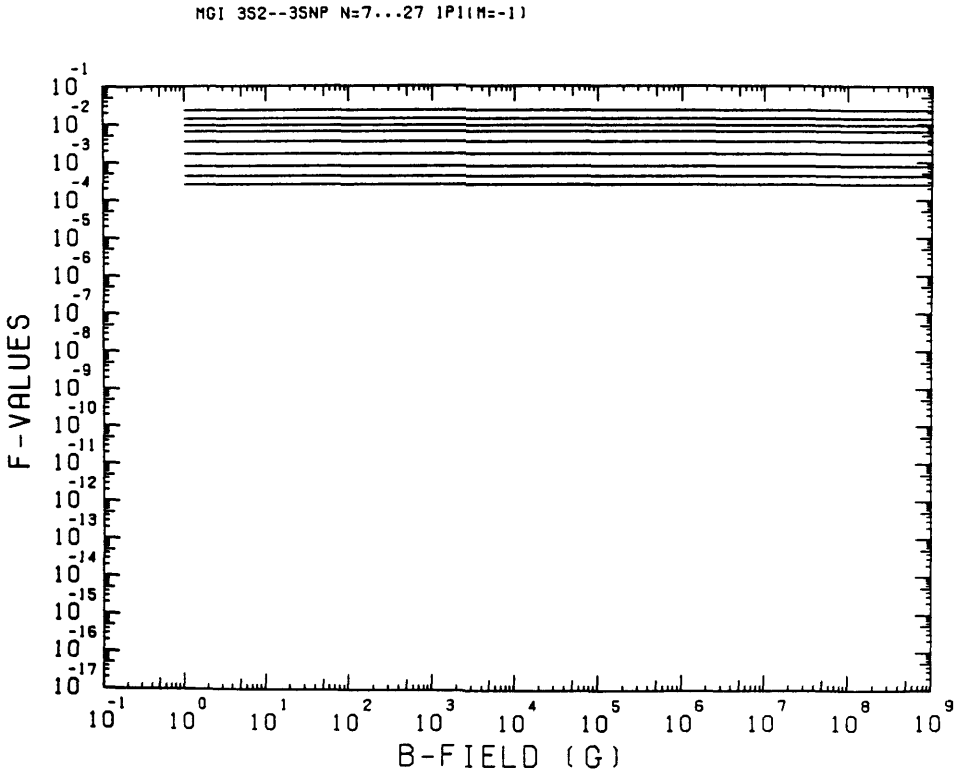

Figs.VII16,17 and 18

As Figs.VII13 and 14 but for different n's in the range 7 to 27.

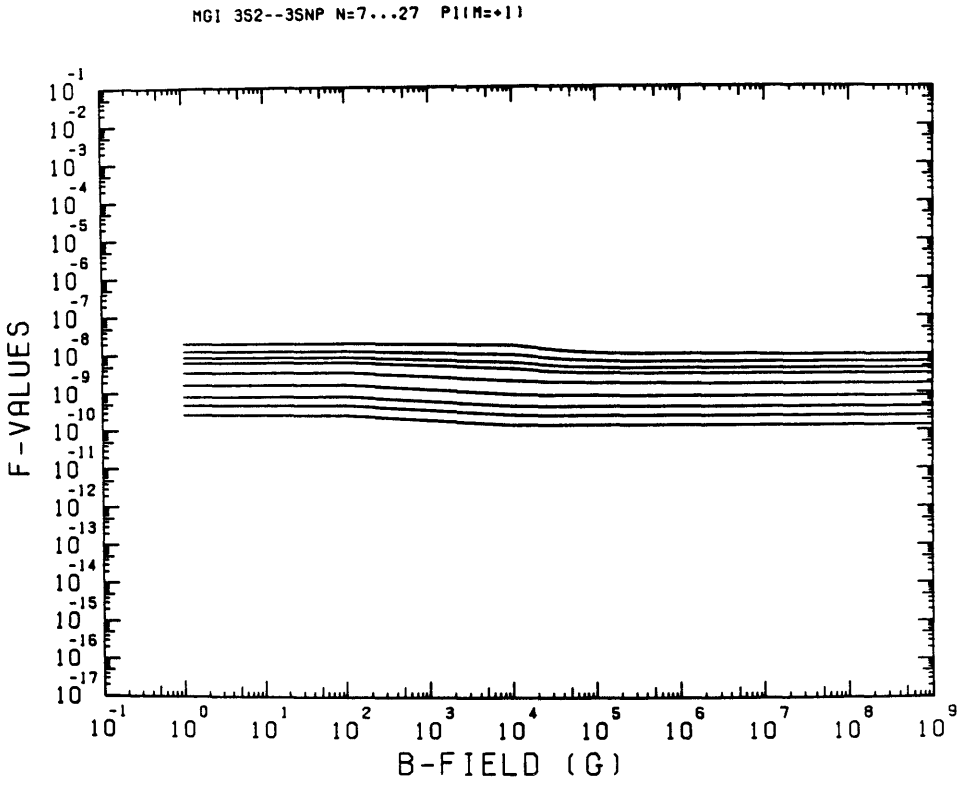
MGI 3S2--3SNP N=7...27 P1(M=+1)
F-VALUES
B-FIELD (G)

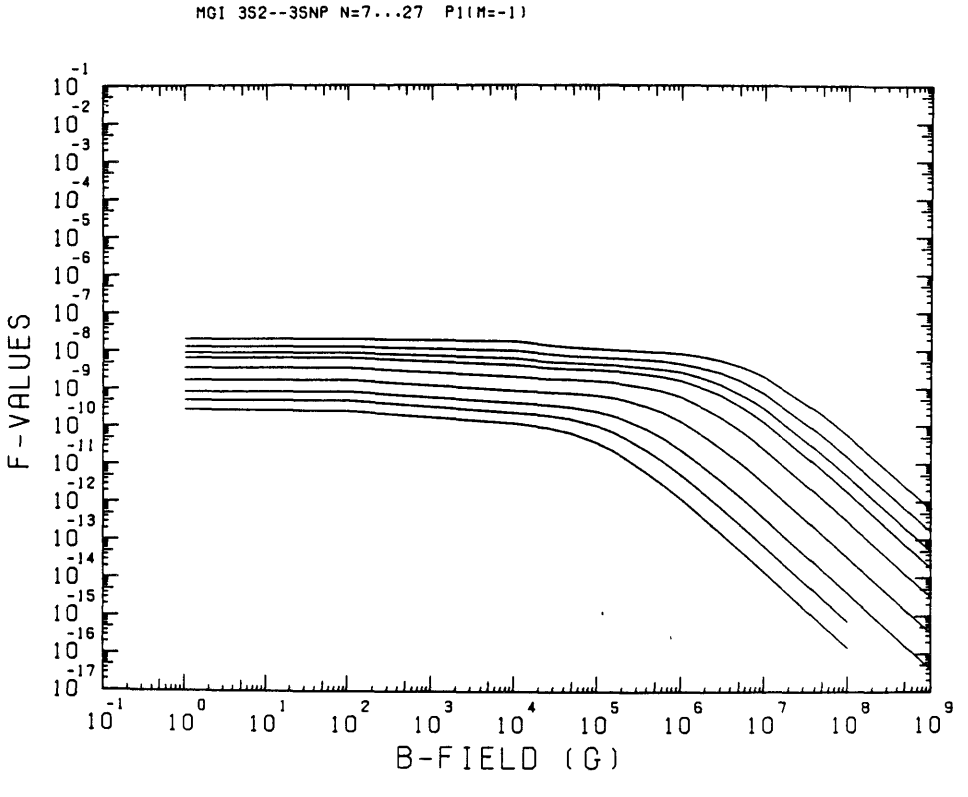
MGI 3S2--3SNP N=7...27 P1(M=-1)
F-VALUES
B-FIELD (G)

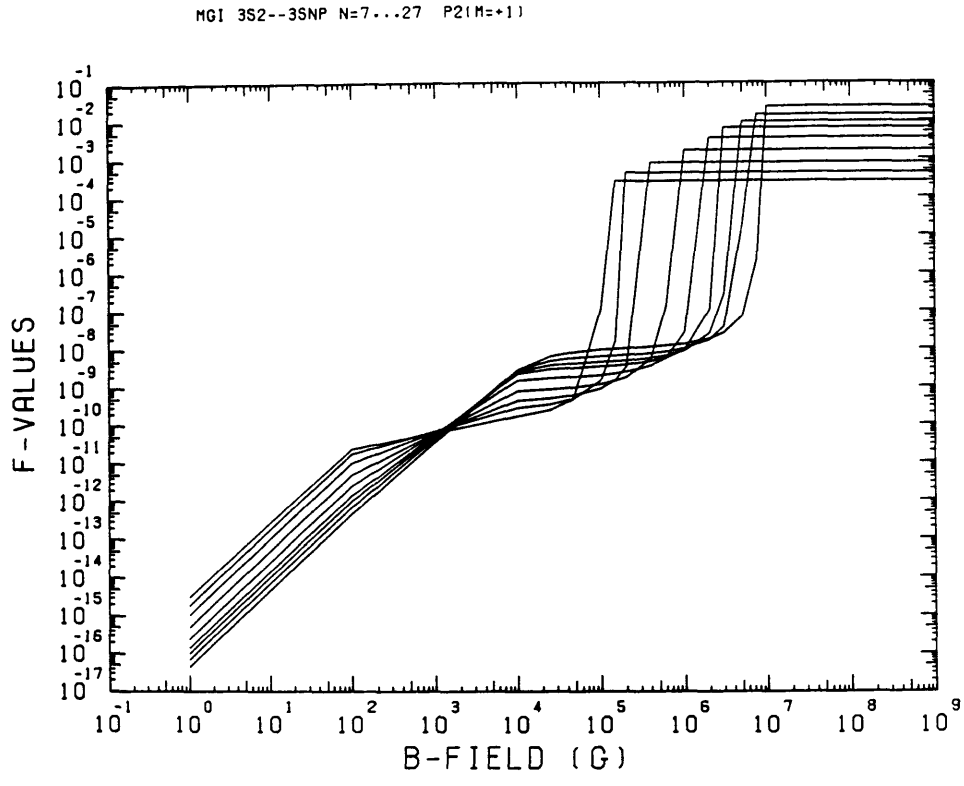
MGI 3S2--3SNP N=7...27 P2(M=+1)
F-VALUES
B-FIELD (G)

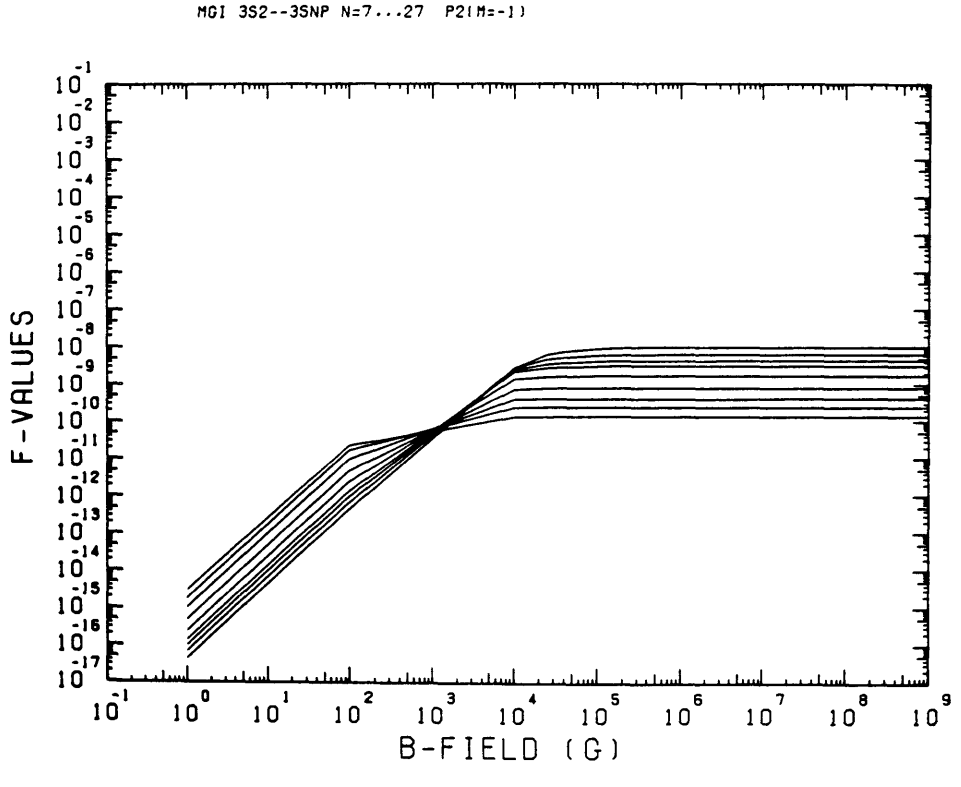
MGI 3S2--3SNP N=7...27 P2(M=-1)
F-VALUES
B-FIELD (G)

References for Chapter VII

1. King P.W. PhD Thesis (University of London, 1972)
2. "Quantum Theory of Atomic Structure" by J.C.Slater Vols.I and II (McGrawhill 1963)
3. Garton W.R.S. and Tomkins F.S. Astrophys. J., 158, 839 (1969)
4. Edmonds A.R. and Pullen R.A. (I.C. preprints ICTP 79-80/28 (1980)
5. Edmonds A.R. Jour. de Phys., 31, C4-71 (1970)
6. Clark C.W. and Taylor K.T. J. Phys. B., 13, L737 (1980)
7. Clark C.W. and Taylor K.T. J.Phys. B., 15, 1175 (1982)
8. Edmonds A.R. J. Phys. B., 6, 1603 (1973)
9. Fischer C. and Saxena K.M.S. Comput. Phys. Commun., 9, 381 (1975)
10. Fischer C. Comput. Phys. Commun., 1, 151 (1969)
11. "The Hartree-Fock Method for Atoms" by C.Froese-Fischer (J.Wiley 1977)
12. "The Calculation of Atomic Structures" by D.R.Hartree (J.Wiley 1957)
13. Cohen M. and McEachran Adv. in Atom. and Mole. Phys., 16, 1 (1980)
14. Brown C.M., Naber R.H., Tiford S.G. and Ginter M.L. Appl. Optics, 12, 1858 (1973)
15. Robb W.D. Comput. Phys. Communic., 6, 132 (1973)
16. Fischer C. and Saxena K.M.S. Comput. Phys. Commun., 9, 370 (1975)
17. Griffin D.C., Pottcher C. and Pindzola M.S. Phys. Rev. A., 25, 1374 (1982)

18. Tiwary S.N., Kingston A.E. and Hibbert A. J. Phys. B., 16, 2457 (1983)

19. Hibbert A., Kingston A.E. and Tiwary S.N. J. Phys. B., 15, L643 (1982)

20. Kelly M. Phys.Rev.

21. Mitchell C.J. J. Phys. B., 8, 25 (1975)

22. "Mathematical Methods for Scientists" by Stephenson J, (Longman 1961)

Chapter VIII

A Brief Theoretical Background to Plasma Diagnostic Techniques

In this chapter we introduce some concepts related to the use of emission spectroscopy of laser produced plasmas. In, particular we discuss the estimation of plasma properties from the intensity ratios of spectral lines, since this is the subject of the next chapter (and [16]). This introduction is brief and excludes some topics which are not of immediate importance to the understanding of this chapter, such as non-ideal effects (Burgess [17]), the effects of a spatial gradient and a detailed treatment of NLTE radiation transport [18] and the important topic of plasma line shapes [19]. More complete introductions to plasma spectroscopy are given by the excellent reviews of McWhirter [20] and Gabriel and Jordan [21].

1.Introduction

In recent years lasers of very high irradiance have been developed (of the order of 10^{11}-10^{18}W/cm^2). When these powerful lasers are focused on gaseous or solid targets, they ionise them and convert a thin layer of the surface of the target into a plasma. These laser produced plasmas (LPP's) have very high density and pressure (10^{-3}-10g/cm^{-3} and 10^{-2}-4000 Mbar), temperature of the order 10-10000 eV, very small size and short life-time. The reason why LPP's have attracted a great deal of scientific interest recently is because of intereset in inertially confined fusion (ICF) (an excellent general review article on LPP's is given by Key and Hutcheon[1]). In the

present work only the spectroscopy of LPP's will be discussed. Spectroscopy is an important plasma parameter diagnostic technique. Our aim is to interpret the spectrum of radiation emitted from a plasma using a theoretical model in which all the possible radiative and collisional processes that ionise the plasma and populate the various excited states are taken into account.

Atomic physics and astrophysics have been a very useful source of basic information but there is always a certain degree of error in the data which makes theoretical predictions obtained from the plasma model of limited accuracy. In the following sections of this chapter we will consider the standard models of ionisation of the plasma, the population of excited states and the connection of these two with the line and continuum intensities. Then we will discuss how the temperature of the plasma can be diagnosed and how line ratios and Stark broadening can be related to the density of the plasma [2] and finally, the effects of opacity on ionisation will be considered.

2.Local Thermodynamic Equilibrium Model

Complete thermodynamic equilibrium (TE) requires that every process (collisional or radiative) and its inverse must occur at equal rates by the principle of detailed balance. It is often the case that radiative processes are not followed by their inverse (if the plasma is optically thin). In local thermodynamic equilibrium (LTE) it is assumed that "all the thermodynamic properties of the material are the same as their thermodynamic equilibrium values at the local values of T and

density throughout the entire atmosphere" [3]. If the density is low so that radiative rates dominate collisional rates the LTE assumption will not be valid. At higher densities where collisional rates dominate and the populations of excited states are in detailed balance, LTE prevails. When the plasma is in LTE, the free electrons will have a Maxwellian velocity distribution and the populations of the excited states and ionisation stages will be given by the Boltzman and Saha equations respectively:

$$\frac{n(i)}{n(j)} = \frac{g(i)}{g(j)} \exp\left(\frac{\chi(i,j)}{kT_e} \right)$$

$$\frac{n(z+1,gr)\ n_e}{n(z,gr)} = \frac{g(z+1,gr)}{g(z,gr)} 2\left(\frac{2\pi mkT_e}{h^2} \right)^{3/2} \exp\left(\frac{\chi(z,gr)}{kT_e} \right)$$

where n(i), n(j), n(z+1,gr) and n(z,gr) are the populations densities of the various levels designated by their quantum numbers i,j and gr respectively. g(z,gr) is the statistical weight of level gr of ionisation stage z, x(i,j) is the energy between bound levels i and j and x(z,gr) is the ionisation potential of the ion of charge z in its ground state [4].

McWhirter [4] has suggested the criterion for LTE to hold between levels i and j to be (where radiative decay rates give about 10% deparures form LTE):

$$n_e n(i)\ X(T_e,i,j) \geqslant 10 n(i)\ A(i,j)$$

where $X(T_e,i,j)$ is the de-excitation coefficient and A(i,j) is the atomic transition probability. By substitution of the appropriate values it becomes:

$$n_e \geqslant 1.6\ 10^{12} \sqrt{T_e}\ \chi(i,j)^3 \quad cm^{-3}$$

The energy difference between bound levels decreases as n increases; hence a lower value for the density is required to maintain the higher n- states in LTE or in other words for a certain n only the higer n-values will be in LTE. This is called partial LTE. Another condition which must be fullfilled if the plasma is to be maintained in LTE is that the equilibration time must be small compared to the time needed for plasma parameters to change [2].

3.Coronal Model

In the previous section we considered the case where collisional rates are balanced by their inverse processes and the plasma was in LTE. In the coronal model collisional ionisation balances with radiative recombination and collisional excitation with spontaneous decay (we are assuming again an optically thin plasma) [4].

Collisional ionisation and three-body recombination can be represented as:

$$e + N(z) \rightleftharpoons N(z+1) + e^- + e^-$$

and radiative recombination and photoionisation can be represented as:

$$e^- + A(z+1) \longrightarrow A(z) + h\nu$$

where $h\nu$ is the energy of the emmited photon. Collisional ionisation and radiative recombonation are proportional to n_e and three-body recombination is proportional to n_e^2 . If the plasma is optically thin and the radiation density is low, the

photoionisation is also low. At low n_e, radiative recombination dominates over three-body recombination and the coronal equilibrium arises from a balance between collisional ionisation and radiative recombination [4], ie:

$$n_e n(z,gr)\ S(T_e,z,gr) = n_e n(z+1,gr)\ \alpha(T_e,z+1,gr)$$

where $S(T_e,z,gr)$ is the collisional ionisation coefficient and $\alpha(T_e,z+1,gr)$ is the radiative recombination coefficient.

Unlike the LTE case, knowledge of atomic parameters is required to calculate the population densities (and not knowledge of the density). As pointed out by Burgess [5] , the radiative recombination should be corrected for dielectronic recombination. The radiative recombination coefficient $\alpha\ (z,gr)$ is replaced by $\alpha(z,gr) + \alpha(z,tot_d)$ where $\alpha(z,tot_d)$ is the dielectronic rate coefficient summed over all relevant levels [1]. By comparing values of $\alpha(z,gr)$ and $\alpha\ (z,tot_d)$ given by McWhirter [4] and Donaldson and Peacock [6] respectively, it can be seen that for the temperature range of interest in fusion, the dielectronic recombination coefficeint exceeds $\alpha(z,gr)$ by approximately one order of magnitude for some cases.

In the coronal limit the collisional excitation rate from level i to level j must balance all the possible radiative decay rates from levels k (where k<j) to level j, ie:

$$X(T_e,i,j)\ n_e n(i) = n(j) \sum_{k<j} A(j,k)$$

Several authors have attempted to calculate collisional excitation and ionisation rates and some forms will be discussed in the next chapter.

The coronal model holds when the radiative decay of a level dominates over collisional decay, ie:

$$\sum_j A(i,j) \gg n_e \cdot X(i,j) \qquad \text{(VIII1)}$$

McWhirter [4] also states that there is a limit to the principal quantum number after which the previous inequality is not satisfied. Therefore considering only states with $n<6$ and equation VIII1, he gives the upper limit of the electron density for the coronal approximation to be:

$$n_e \leqslant 5.6\ 10^8\ (Z+1)^6 \sqrt{T_e}\ \exp\left(\frac{1162\ (Z+1)^2}{T_e}\right)$$

McWhirter [4] has also shown that the relaxation time (of a LPP) τ for the formation of the last ionisation stage is comparable to the time-scale on which the parameters of the plasma change and hence a time dependent calculation is required.

4.Collisional-Radiative Model

At intermediate densities all the collisional and radiative processes must be taken into account. However it may be possible to neglect stimulated rates (eg stimulated decay and photoionisation). The C-R model includes collisional transitions and spontaneous radiative decay between bound levels, collisional ionisation from any bound level, three-body recombination (or radiative recombination) into any bound level (and finally autoionisation from a doubly excited ionic level to the next ionic stage and electron capture). In the high density limit where all collisional rates dominate, the LTE model

prevails and in the limit of low density where radiative rates dominate, the coronal model prevails.

Although LPP's are of great scientific interest there are not many publications on C-R calculations with LPP's parameters. In order to obtain population densities in the intermediate regions one must either use a sophisticated computer program accounting for all the possible processes and levels or an approximate model considering the most important processes. The first has been attempted by scientists at the Lebedev Institute calculating level populations of H-like and He-like ions with parameters similar to those of LPP's , by Lee [7], Seely [8] and in Chapter IX of this thesis calculating H-, He- and Li-like ions with LPP's parameters for Si and Al plasmas. The latter has been attempted by several authors, one amongst them being McWhirter. In a paper [4] he considers one property of the plasma which simplifies greatly the calculations. This property is that as n(the principal quantum number) increases and the energy difference decreases, the collisional rates dominate over radiative between bound levels and therefore above a certain level one may use LTE equations to calculate the population ratios.

Numerical solutions for hydrogenic ions have been calculated by Bates et al [9], McWhirter and Hearn [10] and several other authors. Bates et al [9] and McWhirter and Hearn [10] include tables of the collisional ionisation and the radiative recombination rates.

5.Dielectronic Satellites

When an ion captures a free electron to form a doubly excited state, dielectronic recombination takes place [3], ie:

$$A^{+Z}(n,l) + e(E,l''+l) \longrightarrow A^{+(Z-1)}(n',l+l;n'',l'')$$

and then stabilises radiatively:

$$A^{+(Z-1)}(n',l+l;n'',l'') \longrightarrow A^{+(Z-1)}(n,l;n'',l'') + h\nu$$

Alternatively, the doubly excited state can decay by autoionisation to give a free electron and the initial ion. These doubly excited levels of ions from the next lower ionisation stage form satellite lines (lines very close to the resonance lines). Since resonance lines of He- and H-like ions are usually optically thick and their satellite lines are not, the latter may be a more useful density diagnostic.

6.Methods of Diagnosing T_e

The rates at which radiation is emitted and absorbed by a plasma consisting of photons and electrons, having thickness D and density ρ are given respectively by Cillie [11] as:

$$n(\nu) = \frac{n_e n_p}{4\pi\rho} \frac{2^6\pi^3}{(6\pi)^{3/2}} \left(\frac{m}{kT_e}\right)^{\frac{1}{2}} \frac{e^6}{c^3m^2} \exp(-h\nu/kT_e)$$

and

$$\chi(\nu) = \frac{n_e n_p}{4\pi\rho} \frac{2^6\pi^3}{(6\pi)^{3/2}} \left(\frac{m}{kT_e}\right)^{\frac{1}{2}} \frac{e^6}{hcm^2} \frac{1}{\nu^3}(1-\exp(-h\nu/kT_e))$$

And the solution of the radiative transfer equation is:

$$I(\nu) = \eta(\nu) \frac{1- \exp(-\chi(\nu)\rho D)}{\chi(\nu)}$$

where the symbols have their usual meaning.

At low frequencies (IR) $\chi(\nu)\rho D$ will be large and the spectrum will be that of a Black-Body. At higher frequencies (Visible, UV and soft x-rays) the spectrum may be dominated by Bremsstrahlung and radiative recombination.

6.1 IR Measurements

At the IR region of the spectrum the main source of radiation is due to transitions between free electrons. The intensity of radiation emitted form the plasma (again of thickness D and density ρ) is given by [4]:

$$I(\nu) = \frac{2h\nu^3}{c^2 (\exp(h\nu/kT_e) -1)} (1- \exp(-\chi(\nu)\rho D))$$

where

$$\chi(\nu) = \frac{n_e n_p}{4\pi\rho} \frac{2^6\pi^3}{(6\pi)^{3/2}} \left(\frac{m}{kT_e}\right)^{\frac{1}{2}} \frac{e^6}{hm^2 c \nu^3} (1-\exp(-h\nu/kT_e))$$

Hence if the intensity and wavelength of the radiation are known, the temperature can be determined without requiring any atomic rate coefficient data (Harding et al [4] and references therein). However there are two limitations of this method: (i)the wavelength must be shorter than that of the plasma frequency and (ii) the size of the plasma must be sufficiently large so that it is optically thick at the position at which we require the temperature. Hence the method is not suitable for low- density high-temperature plasmas.

6.2 Visible, UV and Soft X-Ray Relative Continuum Intensity Measurements

In a plasma two processes are responsible for the emission of continuum radiation. One is radiative recombination, where a bound state captures a free electron and creates a photon whose energy equals the sum of the electron's kinetic and binding energies, and the other process is bremsstrahlung where the free electrons are scattered by positively charged ions.

The spectral distribution of bremsstrahlung and radiative recombination was given by Mandelshtam et al ([1] and references therein) as:

$$\varepsilon(\nu T_e) = \frac{B}{Z^2} Z^2 N_e N_T^Z (T_e)^{-\frac{1}{2}} \exp(-\frac{h\nu}{kT_e})$$

$$\{1+\sum_Z \frac{N^Z}{N_T^Z} \frac{1}{Z^2} (\frac{\chi^H}{kT_e}) \sum_n (\frac{\chi^{Z-1}(n,c)}{\chi^H})^2 \frac{\xi_n^{Z-1}}{n}$$

$$\cdot \exp(\frac{\chi^{Z-1}(n,c)}{kT_e})\} \qquad \text{ergs/sec/cm}^3\text{/Hz}$$

where B is defined in [1], N_T^Z is the total number density of ions of charge Z, N_T^Z is the number density of ions of charge labelled Z, χ^H is the ionisation potential of hydrogen, ξ_n^{Z-1} is the number of available states for recombination into shell n and $\chi^{Z-1}(n,c)$ is the ionisation potential of shell n of an ion of charge Z-1. From the above formula it can be seen that the slope of ln($\varepsilon(\nu)$), the electron temperature can be evaluated. The observed energy range must correspond to the electron temperature that is to be measured [4]. The method fails for very short wavelenghts due to intensity calibration problems. In order to overcome such problems, the method should not be applied for temperatures lower than $2.0\ 10^6$ ^oK for visible and

soft x-rays [4].The lower density limit obtained is arround $10^{16} cm^{-3}$ but more results are needed to give a correct and definite lower density applicability limit.

6.3 Line Intensity Measurements in LTE Plasmas

Experimentally speaking, line intensity measurements to predict T_e are the most convenient because all the energy of radiation is concentrated in a smaller wave band and is easiest separated from other sources of radiation [4]. However as mentioned previously, some of the atomic data coefficients are known with limited accuracy.

The lines preferred for these measurements are resonance lines of high principal quentum number in the H- and He- like ions sequence of medium Z elements. High n is required because (a) such levels require smaller n_e to have their populations in LTE with the next bound state or the next ionic stage (therefore the Boltzman and Saha relations can be used to determine the population densities of the excited levels in the plasma if n_e and T_e are known) and (b) resonance transitions from such high n states have lower A-values (and greater Stark widths) and hence lower opacity. For the intensity ratio to be a sensitive function of temperature [1] the two upper levels of the lines must be separated by an amount of the order of kT_e [4]. These requirements make this method most widely used in the high-density low-temperature region. Finally, a line to continuum intensity ratio can become a temperature diagnostic where one measures the intensity of a spectral line and that of the underlying continuum. Attention must be paid to ensure that the lines in question are optically thin.

6.4 Corona Model Measurements

It was seen in section 3 of this chapter that the following relation must hold for the coronal limit:

$$n_e n(z,gr)\ X(T_e,gr,p) = n(z,p) \sum_{q<p} A(p,q)$$

and therefore the intensity of an optically thin line in this density region becomes:

$$I(p,q) = \frac{1}{4\pi} \int n_e n(z,gr)\ X(T_e,gr,p) \frac{A(p,q)}{\sum_{r<q} A(p,r)}\ ds$$

From this formula it can be seen that the electron temperature of the plasma can be deduced from measurements of the intensity of a specific line through $X_e(T_e)$ [4].

a) Helium singlet to triplet method

This method was suggested by Cunningham [12] who observed that the excitation rates were different for the singlet and triplet lines in Helium. The values of these rates (obtained by Lees ([4] and references therein) were used by Cunningham to produce a curve giving the dependence of the $2^3P\text{-}4^3S/2^1P\text{-}4^1D$ ratio on T_e [4].

There are two limitations to this method. The first occurs when the density becomes such that the collisional processes compete with the radiative decay of level 4. The second is the neglect of the fact that the 4^1D and 4^3S levels can receive some of their electron population from the metastable 2^3S and 2^1S levels (since ground to metastable exciation rate is greater by an order of magnitude than that

from ground to 4^1D or 4^3S). This method is valid for low density plasmas.

b) He-like (CV) method

Kaufman and Williams [13] suggested another method of determining T_e based on measuring the intensity of the 2^3S-2^3P_2 transition in CV or BIV. They considered the intensity to be given by [4]:

$$I(z,2^3S\text{-}2^3P_2) = 0.4\,\pi\, a_o^2 \left(\frac{2kT_e}{\pi m}\right)^{\frac{1}{2}} n(z,gr)n_e \quad \text{ergs/cm}^3\text{/sec}$$

$$\cdot\, h\nu\left(1+\frac{\chi(z,2^3P_2)}{kT_e}\right) \exp\{-\chi(z,2^3P_2)\,/kT_e\}$$

Further they suggested that since the above formula is so strongly dependent on T_e, through the exponential factor the values of the electron temperature obtained with or without the inclusion in their calculations of the effects due to the 3^3S metastable level do not differ very much. This method is valid for every density of interest in LPP's but only for T_e between 10^5 and 10^6 ^oK (for Carbon).

c) Li-like method

The $2s\text{-}2p_{3/2}/2s3p_{1/2,3/2}$ intensity ratio of Li-like ions can become a very reliable temperature diagnostic. These excitations do not involve metastable statesand therefore in this case one does not have this added uncertainty. This line ratio was first calculated by Heroux [14] using collisional excitation rates given by Allen and more recently [4] by using the values of the excitation cross-sections given by Burke and Tait [4 and

references therein]. The results are shown in Fig.7 of [4]. As it can be seen from that figure the upper limit of the temperature to be diagnosed is given by the fact that at high T_e the curve becomes insensitive to temperature and the lower limit is given by the fact that the intensity ratio becomes too large to be observed. Further, the poirt where stepwise processes dominate gives the upper density limit.

7. Methods of Determining n_e

The plasma density can be determined by two ways: firstly by knowing the intensity (and the other plasma parameters) of optiaclly thin radiation and secondly by observing the broadening of a spectral line.

7.1 Line and Continuum Intensity Methods

Previously we saw that the intensity of radiation of a spectral line is given by:

$$I(i,j) = \frac{1}{4\pi} \int n(i)A(i,j)\ h\nu(i,j)\ ds$$

Therefore by knowing the intensity, the decay rate and the plasma volume, n(i,z) can be determined. Then if the plasma is in LTE, the Saha relation can be used and the product $n(i,z+1)n_e$ can be obtained. If the plasma is to be neutral then $n_e=n(i,z+1)$ for hydrogen. For other ions more lines are required to solve a system of n equations with n unknowns.

7.2 Stark Broadening Method

Lunney [2] has used the Stark broadening as a density diagnostic by matching the measured line profile to a

theoretical prediction. Empirically it was found [2] that the plasma parameters were related to the half width of a Stark broadened SiXIII L_α line (at $T_i=T_e=5.2\ 10^6\ ^oK$ and Z=9.3) as follows:

$$\Delta\lambda_{\frac{1}{2}} = 5.5\left(\frac{n_e}{10^{22}}\right)^{0.57 \pm 0.03}\ \text{mÅ}$$

and that $\Delta\lambda_{1/2} \propto T_e^{0.2}$ (for $T_e=5.2\ 10^6\ ^oK$, $n_e=1.5\ 10^{23}$), from where the weak dependence of the line on temperature and the strong dependence on density are obvious. Lunney [2] also states that the shapes of resonance lines of He-like and H-like silicon, aluminium and argon with $T_e=5.2\ 10^6\ ^oK$ and various values of n_e have been computed in order to compare them with the actual experimental spectra where we wish to determine the density. The computed spectrum takes account of Doppler broadening, self-absorption of radiation and the instrumental function. Lunney [2] also stated that several values of ρ and $R\rho$ (ρ = density and R= radius) can fit a particular spectrum. Lunney has plotted the electron density versus the ground state density of the resonance transition in question (n_1) (where n_1 is related to the optical depth by $\tau(\nu,l) \propto n_1 l$, where l is the line of sight of the plasma) for the best fit of $L_\alpha, L_\beta, L_\gamma$ and L_δ lines. For large values of n_e the optically thick region is approached. He found that these four lines of best fit intersected at a certain point which determines the value of n_e and n_1 which should be close to those found in the experiment.

8.Radiation Trapping

Radiation which is produced in a plasma will interact with the plasma for finite optical depths and as a consequence:

a) the populations of the excited states are modified by the absorption of radiation and b) the observed outgoing intensity is not just a summation of the intensities of the volume elements of the plasma [4].

8.1 C-R solutions

A few definitions will be listed below without which a clear approach to the radiation trapping problem is not possible [3]. The destruction probability P_d is "the average probability that a photon is destroyed when it next interacts with the material" [3]. Also:

$$P_d \propto X / (X + A_{ji})$$

where X and A_{ji} are the collisional and radiative rates from the upper level j to the lower levels i respectively.

Λ (the thermilisation depth) is the depth at which the radiation field reaches its equilibrium value.

$P_e(\tau)$ is defined as "the probability (of escape), averaged over a line that a photon emitted at optical depth τ escapes from the medium before being absorbed" [3]. It is clear that the following holds (for a two level atom):

$$P_e(\Lambda) = P_d$$

As mentioned in the beginning of this section radiation travelling in a plasma can be reabsorbed and therefore the opacity and consequently the population densities are different from what they would be in the optically thin case. The escape probability and the thermalisation depth depend on how the photons are redistributed over the line profile after being

emitted. If they are emitted coherently there is a great probability that those absorbed at the line centre will be re-emitted there (where the opacity is high) and will be trapped up to the shallowest layers of the plasma giving a compararively small thermalisation depth. In contrast, if the photons are completely redistributed over the line profile, then it is quite probable that after a few scatterings a photon which was absorbed at the line-centre will be emitted in the wing (where the opacity is low) and it will therefore escape from the plasma [3]. In this case the thermalisation depth is large compared to the coherent case. Also P_e and Λ depend on how much background continuum absorption there is in the plasma since the continuum sets the the maximum optical depth that a photon can travel to be unity (ie an upper limit on the depth from which a photon can escape at any frequency).

The escape factor approximation is a useful method which gives the change of the emergent radiation intensity and the change in excited level populations. g is the probability of a photon emitted (in the optically thick transition in question) escaping without being reabsorbed in the plasma. For a two-level atom the effect of reabsorption can be taken into account by reducing the decay rate A_{ji} to the value $(g\ A_{ji})$. Therefore the population ratio in the C-R region becomes:

$$\frac{N_j}{N_i} = \frac{n_e\ X}{g\ A_{ji} + n_e X} \quad .$$

The escape factor approximation gives results quite close to those obtained performing the proper radiation transfer calculations for an optically thick line (Bates et al [9] assumed g=0 for a C-R model Weisheit et al [15] assumed

$g(\tau_o) \neq 0$ again for a C-R model). In some cases $g(\tau_o)$ can be zero and therefore it can be concluded that the effective decay rate is zero, ie that the photons emitted are reabsorbed in the plasma. Usually $g(\tau_o) \neq 0$.

In a C-R plasma where stimulated emission has been neglected, the escape factor can take the form [4]:

$$g(\tau_o) = 1 - \frac{n_j\, g_j}{n_i\, g_i} \cdot \frac{c^2}{2h\, \nu_{ij}^{\,3}} \cdot \int_0^{\infty} I_\nu\, \phi_\nu\, d\nu$$

In the coronal density region the following inequality (modified with the escape factor) must hold:

$$g(\tau_o(j,gr))\, A_{jgr} > n_e\, X(T_e,j,gr)$$

and this equation a limit of applicability of the optically thick coronal model. If the spectrum of the plasma has more than one lines, then it may be the case that some are optically thin and that only the optically thick ones need the escape factor correction.

References for Chapter VIII

1. Key M.H. and Hutcheon R.J. Adv. in At. and Mole. Phys., 16, 202 (1980)
2. Lunney J.G. PhD thesis (Queen's Univerity, Belfast 1980)
3. "Stellar Atmosheres" by D.Mihalas (Freeman and Co. (1978)
4. McWhirter R.W.P. In "Plasma Diagnostic Techniques" (R.H.Hudelstone and L.Leonard eds.) Ch.5 (1965)
5. Burgess A. Astrophys. J., 139, 776 (1964)
6. Donaldson T.P. and Peacock N.J. J.Spectr.Rad.Trans., 16, 599 (1976)
7. Kilkenny J.D., Lee R.D., Key M.H. and Lunney J.G Phys. Rev.A. 22,2746 (1980)
8. Seely J.F. Phys.Rev.Lett. 42 1606 (1979)
9. Bates D.R., Kingston A.E. and McWhirter R.W.P. Proc. R. Soc. London , Ser.A, 267, 297 (1962)
10 McWhirter R.W.P. and Hearn A.G. Proc. Phys. Soc. London, 82, 641 (1963)
11. Cillie G. M.N.R.A.S. 92 820 (1932)
12. Cunningham S.P. USA Energ.Comm.Rep. No289 (1955) Wash.
13. Kauffman S. and Williams R.V. Natur.182557(1958)
14. Heroux L. Proc.Phys.Soc.(Lon) 83,121 (1964)
15. Weisheit J.C., Tarter C.B., Scofield J.H. and Richards L.M. J.Spectr.Rad.Trans., 16, 659 (1976)
16. Stavrakes T.A. and Lee R.W. J. Phys. B..15,1939 (1982)
17. Burgess D.D Culham Report CLM p567 (1979)
18. Lee R.W J.Q.S.R.T 27,87 (1982)

19. "Spectral Line Broadening by Plasmas" by H.R.Griem
(Academic Press 1974)

20. McWhirter R.W.P. "Plasma Physics and Nuclear Fusion
Research Eds.R.D.Gill (Academic Press1981)

21. Gabriel A.H. and Jordan C. In "Case Studies in Atomic
Collision Physics". Eds McDaniel and McIowell
(North Holland-Amstrdam 1971)

Chapter IX

Numerical Calculation of the Steady-State Ionisation Balance for Highly Ionised Silicon

This chapter discusses the radiative and collisional processes in a plasma and their effect on ionisation balance in a highly ionised plasma. The limits of LTE and coronal equilibria are discussed. The numerical solution of the steady-state rate equations are then considered. The results of previous work on steady state radiation balance in highly ionised Silicon are reviewed and a more complete model is discussed.

Introduction

The calculation of the ionisation balance is of interest because line ratios are used as a diagnostic of plasma parameters. In a recent paper Lunney and Seely [1] have proposed that the ratio:

$$\frac{N(2s2p^3P)\ A(2s2p^3P;1s2s^3S) + N(2p^{23}P)\ A(2p^{23}P;1s2p^3P)}{N(2p^{21}D_2)\ A(2p^{21}D_2;1s2p^1P_1)}$$

could be used as a density diagnostic for laser produced plasmas, while Vinogradov et al [2] have studied the dependence of the He-like resonance to intercombination line ratio:

$$\alpha = \frac{N(2^1P_1)\ A(2^1P_1;1^1S_0)}{N(2^3P_1)\ A(2^3P_1;1^1S_0)}$$

on plasma density. Uncertainties exist in these calculations for two pricipal reasons:

(i) firstly, uncertainties exist in the collisional rates which are employed and (ii) secondly, because of the restricted number of states and the restricted coupling between the states which are included in the calculations.

In this chapter the results of calculations of the ionisation balance in a Si plasma will be presented. These include higher-level hydrogenic and He-like states and a fuller modelling of the coupling between them than in previously reported results. Large discrepancies exist in the calculation of collision rates in the He-like ions. The effect of these differences on diagnostics has been investigated by performing calculations using three different models for the collision rates, due to Vinogradov et al [2], Mewe [3] and Sampson and Parks [4]. This chapter contains: section 2 where the collisional and radiative processes involved are described, section 3 where the three collisional models are discussed in some detail, section 4 where the solution of the rate equation is outlined, section 5 in which some of the previous work on SiXIII line intensity ratios is presented, section 6 which describes the model that was used. In sections 7 and 8 the results on the line ratio and on the satellite ratios are presented respectively and finally section 9 describes how the code can be extended to include Li-like states.

2.Radiative and Collisional Processes

We shall consider five types of processes: (a) bound-bound, (b) bound -free, (c) singly excited to doubly excited, (d) doubly excited to doubly excited and (e) doubly excited to the ground state of the next ionic stage.

(a) Bound-Bound

The radiative processes are: photoexcitation where a photon is absorbed by an atom leading to a transition of an electron from one bound state to another. The reverse processes are spontaneous de-excitation where the excited electron goes back to a lower state emitting a photon spontaneously and stimulated de-excitation where this process is induced by the radiation field.

The number of such transitions per unit time and per unit volume is respectively:

$$n_i \, B_{ik} \, J_{ik}$$

$$n_k \, B_{ki} \, J_{ik}$$

$$n_k \, A_{ki}$$

where n_i=population density of the lower lying state, n_k=population density of the higher lying state and the A's and B's are the Einstein coefficients related by:

$$A_{ki} = B_{ik} \, 2h \, \nu^3 / c^2$$

$$g_i \, B_{ik} = g_k \, B_{ki}$$

where: g_i=statistical weight of the lower state, g_k=statistical weight of the higher state and ν =frequency of the transition. The oscillator strength f is defined by the following formula:

$$f_{ik} = \frac{m \, c^3 \, h^2}{8 \, \pi^2 \, e^2 \, E_{ergs}^2} \, \frac{g_k}{g_i} \, A_{ki}$$

where m,e are respectively the mass and the charge of the

electron, c= velocity of light, h=Planck's constant and F_{ergs} is the energy difference in the transition (in units of ergs).

The f-values can follow the form [13]:

$$f = f_o + (1/Z)f_1 + \cdots$$

where f_o is the hydrogenic value and Z is the charge of the nucleus of the element. Using tabulated f-values for H and He we fit f against 1/Z using the first two terms of the above equation. In this way f-values for SiXIII for bound-bound transitions were obtained.

The collisional processes are: collisional excitation were an inelastic collision of an atom and another particle (usually an electron) leads to the excitation of a bound electron.The reverse process is collisional de- excitation. The number of such transitions per unit time and per unit volume is respectively:

$$n_k\ n_e\ C_{ki}$$

$$n_i\ n_e\ C_{ik}$$

where n_e is the electron number density and C_{ik} and C_{ki} are related by the detailed balance formula:

$$\frac{n_i}{n_k} = \frac{C_{ik}}{C_{ki}} = \frac{g_i}{g_k}\ \exp(\ E_i - E_k\ )/\ kT_e$$

A number of collisional formulae are compared in section 3 of the present chapter.

(b)Bound-Free

The radiative processes are photoionisation where a photon is absorbed by an atom and causes the atom to ionise. The reverse processes are spontaneous radiative recombination and stimulated radiative recombinations. These are analogous to the "bound-bound" processes. The number of transitions per unit time and per unit volume is respectively:

$$n_i \; B_{ic} \; J_{ic}$$

$$n_e \; n_+ \; A_{ci}$$

$$n_e \; n_+ \; B_{ci} \; J_{ic}$$

where n_i =population density of the excited state in the lower ionic stage and n_+ =population density of the ground state in the lower ionic stage. A_{ci} is obtained by integrating $\beta_i(v)$ (the cross-section for radiative recombination) over a Maxwellian velocity distribution:

$$A_{ci} = \int_0^\infty \beta_i(v) \; v \; f(v) \; dv$$

B_{ci} is calculated from:

$$B_{ci} \; \bar{J}_{ic} = \int_0^\infty \beta_i(v) \; v \; f(v) \; \frac{c^2}{2h\nu^3} \; J_\nu \; dv$$

where $h\nu = h\nu_{ic} + mv^2/2$ and finally B_{ic} is calculated from:

$$B_{ic} \; \bar{J}_{ic} = 4\pi \int_{\nu_{ic}}^\infty K_{ic}(\nu) \; J_\nu \; \frac{d\nu}{h\nu}$$

where $K_{ic}(\nu)$ is the cross-section for photoionisation from level i. For hydrogenic ions with charge Z [7]:

$$K_{ic}(\nu) = \frac{2^6 \pi^4 e^{10} m \; Z^4}{3\sqrt{3} \; ch^6 \; i^5} \; \frac{1}{\nu^3} \; g_{ic}(\nu)$$

So,

$$A_{ci} = \frac{2^9 \pi^5 e^{10} m Z^4}{3\sqrt{3}\, c^3 h^6} \frac{1}{i^5} \frac{h^3 e^{h\nu_{ic}/kT_e}}{g_+ \quad 2(2\pi m k T_e)^{3/2}} E_1(h\nu_{ic}/kT_e)$$

where E_1 is the exponential integral. When the field is Planckian then:

$$B_{ci} \bar{J}_{ic} = \frac{2^9 \pi^5 e^{10} Z^4}{3\sqrt{3}\, c^3 h^6} \frac{1}{i^5} \frac{h^3 e^{h\nu_{ic}/kT_e}}{2(2\pi m k T_e)^{3/2}} Q^*(h\nu_{ic}/kT_e)$$

where

$$Q^*(x) = \int_x^\infty \frac{e^{-x}\, dx}{x(e^x - 1)} \qquad I^*(x) = E_1(x) + Q^*(x)$$

and

$$I^*(x) = 1/x + \ln x /2 + 0.577 /2 - \ln \sqrt{2\pi} - \sum_{j=1}^{\infty} \frac{B_{2j}\, x^{2j-1}}{(2j-1)(2j)!}$$

where B_{2j} are the Bernoulli numbers.

The collisional processes are: electron impact ionisation where an electron collides with an atom and removes one electron and the reverse process, the three-body recombination, where two electrons and an ion collide and one electron is captured while the kinetic energy and momentum are shared between the atom and its other electron. The number of transitions per unit time and per unit volume is respectively:

$$n_i\, n_e\, C_{ic}$$

$$n_+\, n_e^2\, C_{ci}$$

By using the Saha equation we get for the three-body recombination:

$$C_{ic} = \frac{g_+}{g_i} \frac{2(2\pi m k T_e)^{3/2}}{h^3} e^{-h\nu_{ic}/kT_e} C_{ci}$$

In the computation described later the collisional ionisation rates were taken from [6].

(c) Singly Excited-Doubly Excited

Doubly excited states can be either above or below the ionisation potential. In the particular case that we considered they were above the ionisation potential so that for calculating the reverse process we could use the Saha equation.

The A-values we used were taken from Safronova [5] and the collisional rates from [3].

(d) Doubly Excited-Doubly Excited

In this kind of transitions the A-values were considered to be zero and the collisional rates were calculated by Sampson [9].

(e) Doubly Excited-Ground State of the Next Ionic Stage

Autoionisation is the process where a doubly excited state goes to the ground state of the next ionisation stage leaving a free electron. The reverse process is called electron capture.

The autoionisation values we used were given by Safronova [5] and the electron capture was calculated using the detailed balance argument by Jacobs and Davis [8].

3.Calculation of He-like Inter-Level Collision Rates

Although a large amount of effort has been put into

calculating bound-bound collisional rates, for a Maxwellian electron distribution, the results of some calculations exhibit large differences between each other. It is thus important to understand the effect of uncertainties in these rates on our results. To this end we have preformed calculations using the results of three independent collisional rate models, ie those of Mewe [3], Vinogradov et al [2] and Sampson and Parks [4]. Because of the importance of these models to this work we give the collision rates for each of Mewe, Vinogradov et al and Sampson and Parks respectively below:

For an i--> j transition between discrete levels, [3] gives:

$$C_{ij} = 1.70\ 10^{-3}\ T_e^{-\frac{1}{2}}\ E_{ij}^{-1}\ f_{ij}\ \bar{g}(y)\ 10^{-5040E_{ij}/T_e}$$

where f_{ij} is the absorption oscillator strength of the transition for allowed transitions and for the forbidden transitions it is the f-value of the allowed transition to the level with the same quantum number. This allows the same formula to be used for both allowed and forbidden transitions. E_{ij} is the excitation energy in eV, T_e is the elctron temperature in ^oK, $y = E_{ij}/kT_e$ and $\bar{g}(y)$ is the integrated gaunt factor given by:

$$\bar{g}(y) = A+(By-Cy^2+D)e^{y}E_1(y) + Cy$$

where

$$E_1(y) = \int_1^{\infty} t^{-1}e^{-yt}\ dt$$

Some of these parameters have been recently revised by the same author [11] but these revisions do not affect the result here.

Note that the prescription for forbidden transitions is dubious since it is based on allowed transition oscillator strengths. It will be shown below that these forbidden rates are not in agreement with other calculations. The values of the parameters A,B,C and D can be found in [3].

For a k--> l transitions between discrete levels reference [2] gives:

$$C_{kl} = 10^{-8} \left(\frac{E_l}{E_k} \frac{R_y}{\Delta E_{kl}} \right)^{3/2} e^{-\beta} \frac{B_{kl}}{g_k} \frac{1}{\beta + X_{kl}}$$

where E_k and E_l are the ionisation energies of levels k and l measured form the edge, $\Delta E = E_l - E_k$, g_k is the statistical weight of level k, B and X are parameters listed in [2]. R_y is the hydrogen ionisation energy and $\beta = \Delta E_{kl}/kT_e$.

for transitions without change in spin : $\phi(\beta) = \beta^{\frac{1}{2}} (\beta+1)$

for transitions with change in spin : $\phi(\beta) = \beta^{3/2}$

For a q--> q' transition between discrete levels reference [4] gives:

$$\frac{C(q \longrightarrow q')}{\pi a_o^2 N_e \bar{v}} = \frac{1}{\omega_q} \left(\frac{I_H}{kT_e} \right) \langle \Omega(q \longrightarrow q') \rangle$$

where ω_q is the statistical weight of level q, a_o is the first Bohr radius of the hydrogen atom. I_H is the hydrogen ionisation energy, T_e is the electron temperature, n_e is the electron number density, $\Omega(q \rightarrow q')$ is the collision strength for a q-->

q' transition, and $\bar{v}=(8kT_e/\pi\, m)^{1/2}$. $\langle \Omega(q \dashrightarrow q')\rangle$ is given by:

$$\Omega(q---q') = \int_y^{\infty} d(E/kT_e)\; e^{-E/kT_e} \langle \Omega(q \longrightarrow q')\rangle$$

where y is the ratio of the excitation energy E to kT_e. The collision strengths corresponding to the various transitions in which we are interested are given by [4].

The different dependencies of these rates on parameters such as the temperature is evident. Relevant differences between the values of the collisional rates from these three formulae include: the results given by Mewe [3] differ very greatly from those by Vinogradov et al [2] and Sampson and Parks [4] only for spin-forbidden transitions ($2^3P;1^1S$). Similar results have been found for all spin-forbidden transitions (indicating the incorrectness of Mewe's formulation). The spin allowed ($2^1P;1^1S$) values calculated from Sampson and Parks [4] and Vinogradov et al [2] can vary by as much as an order of magnitude at 100 eV and by a factor or two or more from some transitions at temperatures of 800 eV. In Figs.IX7 and 8 these trends are shown for one spin allowed and one spin forbidden transition. Since the calculation of Mewe [3] is actually suitable for allowed transitions the good agreement between the Mewe [3] and the Sampson and Parks [4] rates provides a verification of these two sets for the higher temperature region shown.

4.Solution of the Rate Equation

The equation for each state can be written in the form [14]:

$$-\sum_{i''<i} n_{i''i}(R_{i''i}+C_{i''i}) - \sum_{i'>i} n_{i'}(n_i/n_{i'})^{*}(R_{i'i}+C_{ii'})+$$

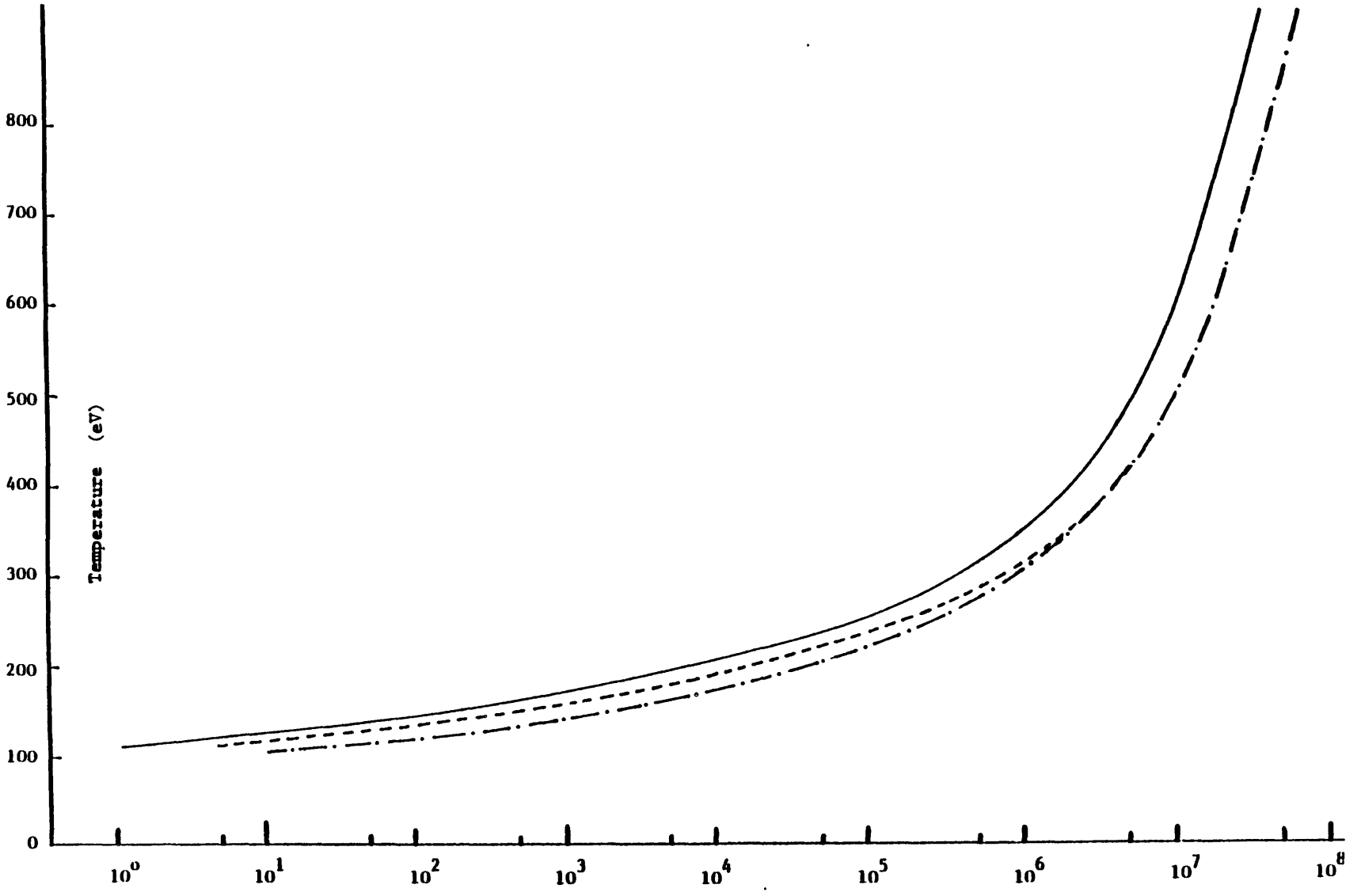

Fig.IX7 Temperature absissa and collision rates ordinate for $2^1P\text{-}1^1S$ using results from Mewe [3](------), Sampson and Parks [4](-.-.-.-) and Vinogradov et al [2](_____).

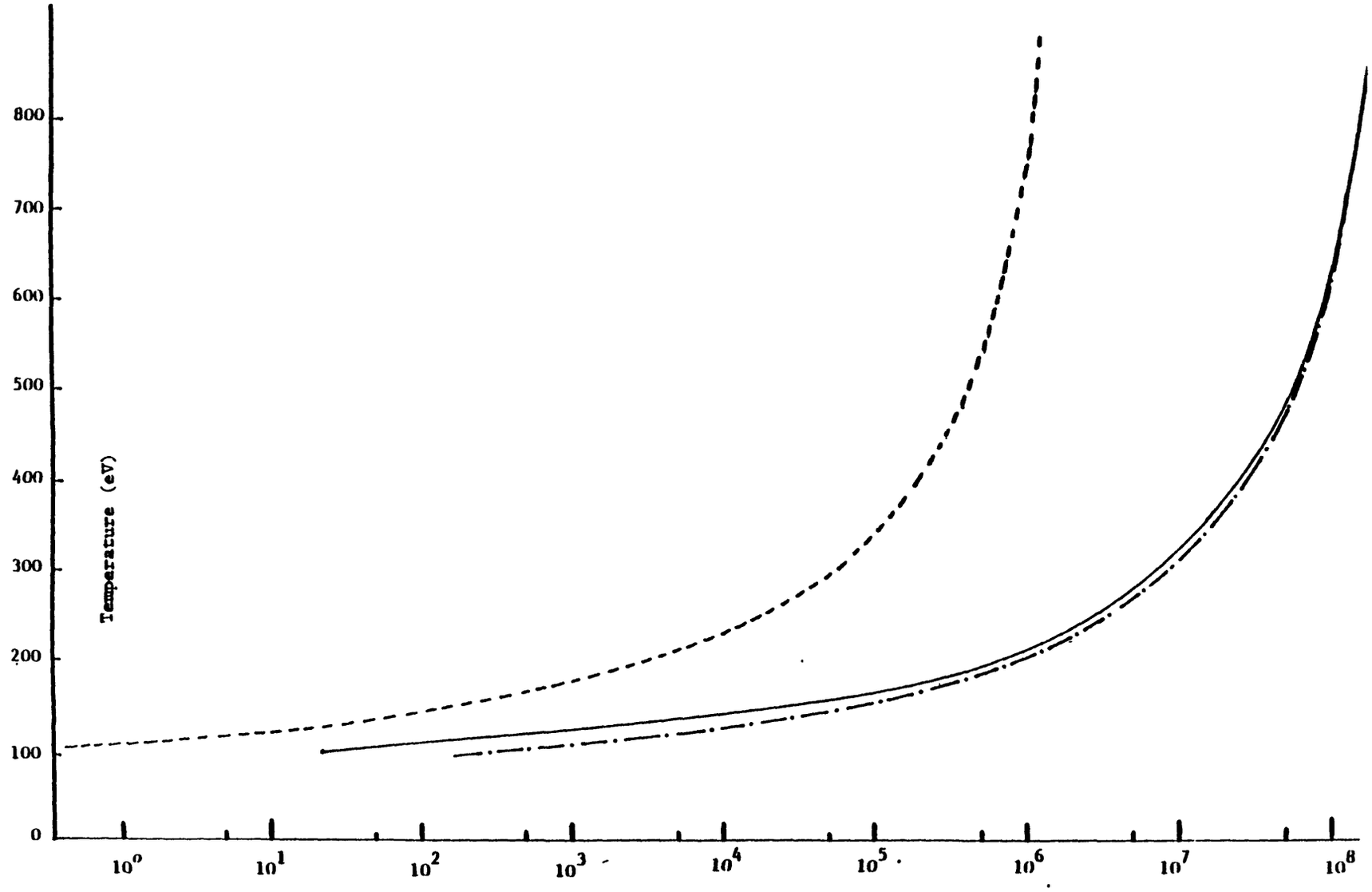

Fig.IX8 As Fig.IX7 but for the transition (2^3P-1^1S).

$$n_i \sum_{i''>i} (n_{i''}/n_i)^* (R_{ii''}+C_{i''i}) + \sum_{i'>i} (R_{ii'}+C_{ii'}) = 0 \qquad (IX.1)$$

where $R_{i''i}$(or $R_{ii'}$) and $C_{i''i}$(or $C_{ii'}$) are the radiative and collisional upward rates respectively and $R_{ii''}$(or $R_{ii'}$) the radiative downward rates. So if we have N states the above equation gives N homogeneous equations with N unknowns. We can either solve for the ratio of the populations to the population of one particular state or use an additional equation:

$$\sum_j j\, N_j = n_e$$

and i is the state, j is the ionisation stage and n_e is the electron density. If we want to be able to fix the total number density, then since the rates depend on n_e we must iterate.

5.Previous Work on SiXIII Line Intensity Ratios

In a recent paper [1] the use of dielectronic satellite ratio

$$\frac{N(2s2p\ ^3P)\ A(2s2p\ ^3P;1s2s\ ^3S) + N(2p^2\ ^3P)\ A(2p^2\ ^3P;1s2p\ ^3P)}{N(2p^2\ ^1D_2)\ A(2p^2\ ^1D_2;1s2p\ ^1P_1)}$$

has been proposed as a plasma density diagnostic and applied to results from laser imploded microballoons at the Rutherford Laboratory. In the model described in this chapter the collision de-excitation from doubly to singly excited states is not included and this may explain the inconsistency between the theoretically diagnosed densities and the actual experimental spectra that Lunney and Seely [1] found. The effect of including this process is discussed in the coming sections of this chapter.

Vinogradov et al [2] have described the use of the ratio

$$\alpha = \frac{N(2\ ^1P_1)\ A(2\ ^1P_1;1\ ^1S_0)}{N(2\ ^3P_1)\ A(2\ ^3P_1;1\ ^1S_0)}$$

as a density diagnostic. The dependence of this result on the choice of collision model will be discussd later.

6.Description of the Model

The ionisation balance in a Silicon plasma has been studied numerically. The states which were included were the ground states of SiI to SiXIV , bare nucleus, singly and doubly excited states of SiXIV (Fig.IX1). It has been found that the neglect of higher states is justfiable by performing calculations in which the occupation of the highest states which were included was always small. The errors due to the neglect of higher- energy states were assessed by performing calculations with and without the n=5 singly excited He-like state. This resulted in the fractional changes of the order 10^{-3} in the populations of the states of interest which were the n=2 states and the ground state.

The collisional and radiative rates which were used have been described in section 2 of this chapter and are of the form of equation IX1. If we choose to calculate the ratios of the populations to that of the ground state of SiXI then we can solve for the ground state of SiI to SiX and then for the others. The equations for the ground states of SiI to SiX are of the form:

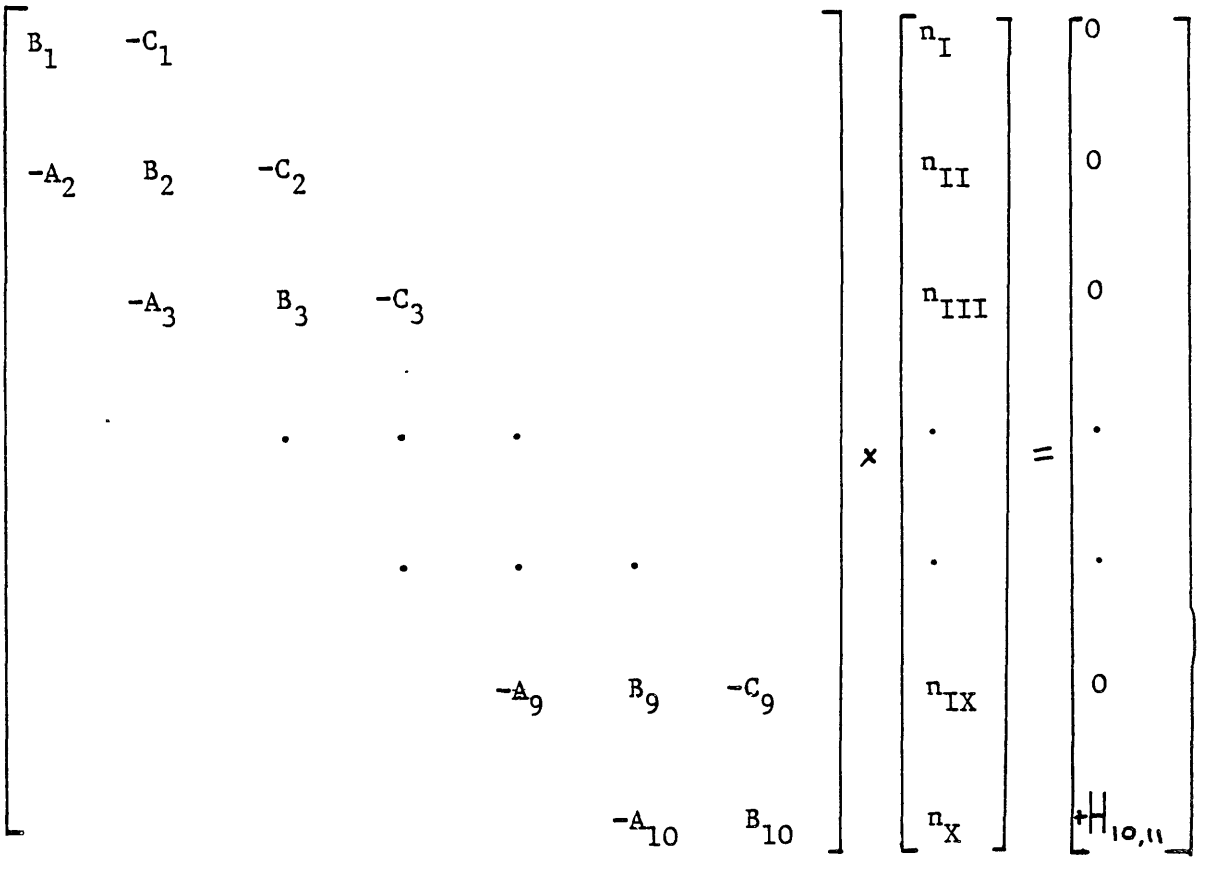

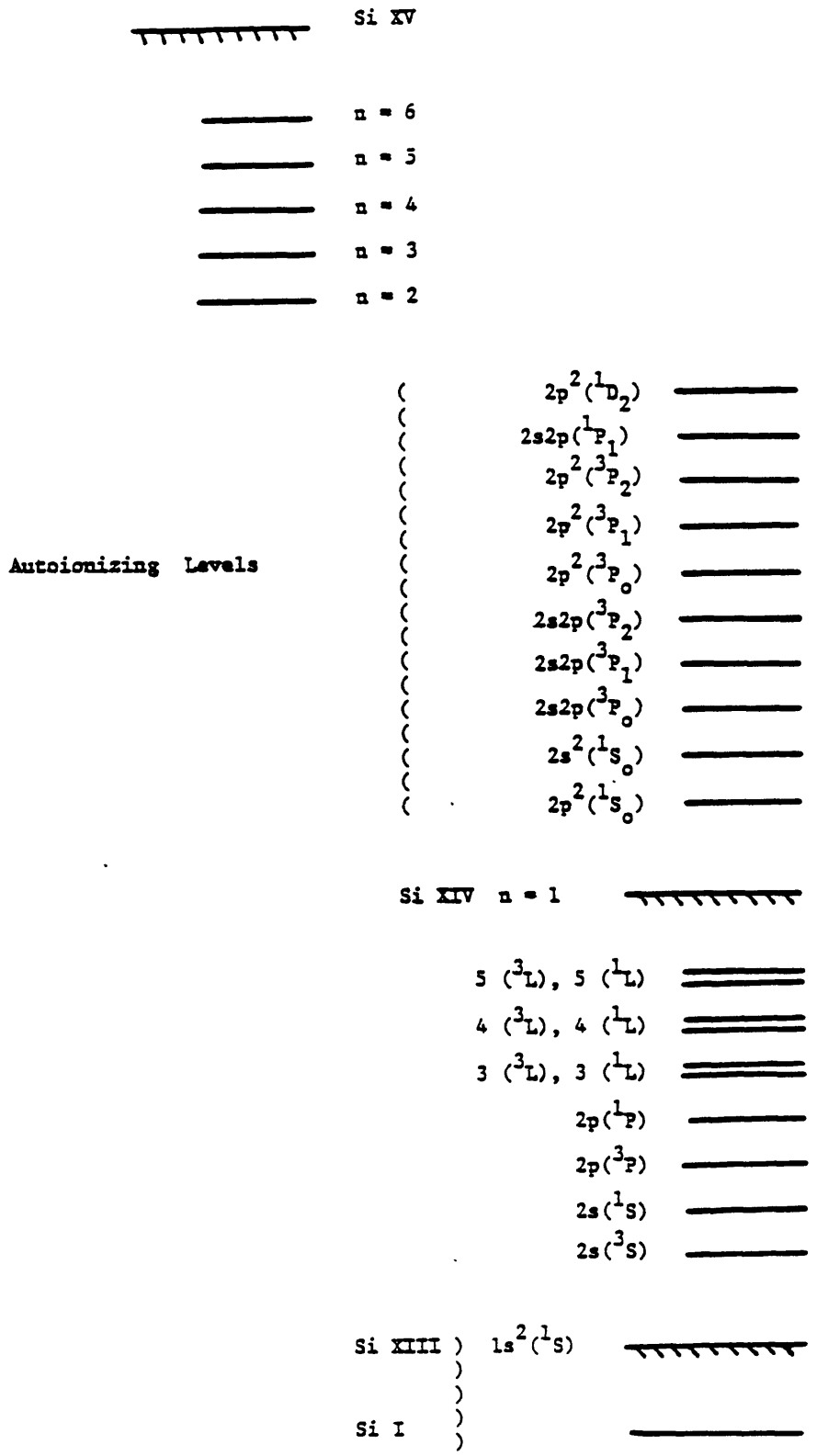

Fig.IX1 The ionisation stages of Silicon which were used in the calculations.

This tridiagonal system may be solved using a triangular solving routine. The equation for the remaining states is of the form:

$$A * n = B$$

where A is a sparce symmetric matrix with positive diagonals and negative off-diagonals and n and B are vectors.

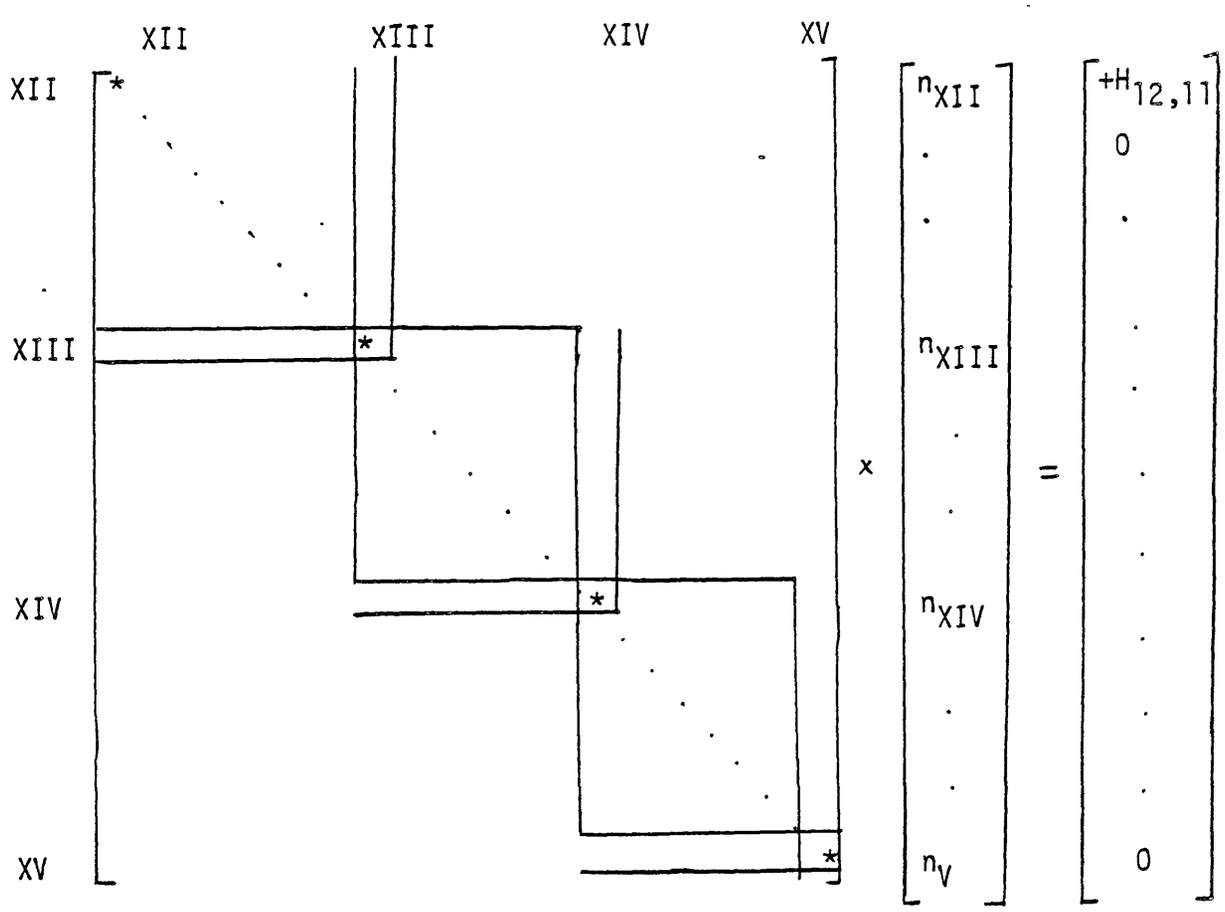

The non-zero element of B represents the coupling of SiXI to the ground state.The solution of this large set of sparce linear equations is obtained using the method described by Duff [10].

This method gives an efficient and very accurate solution, but has the disadvantage of requiring large storage space.

7.Results on the Line Ratio

The line ratio

$$\alpha = \frac{N(2^1P_1)\ A(2^1P_1;1^1S_0)}{N(2^3P_1)\ A(2^3P_1;1^1S_0)}$$

has been calculated using the model described in the previous section and each of the three collisional formulae for the collisional bound-bound exciation rates for He-like Silicon. Figs.IX2,3 and 4 show the line ratio as a function of n for temperatures of 100, 400 and 800 eV respectively and with no radiation field. A good agreement between results from different collisional models is found only for electron densities $\gtrsim 10^{23}$ cm^{-3}. At these densities for the temperatures considered the populations of the states are in LTE. So at these densities the line ratio depends only on temperature and is not useful for finding the density. At intermediate densities (10^{20}- 10^{22} cm^{-3}) the results from using the three different collisional models vary considerably. At lower densities they approach the low-density limit which is given by the ratio of the excitation rates of the 2^1P and 2^3P levels by electron impact from the ground state. The range of electron densities of interest for laser imploded microballoons is 10^{22} to 10^{24} cm^{-3}. In this range the difference between collisional models can lead to order of magnitude or more errors in determining the density. The use of the set of rates by Sampson and Parks [4] which is valid for both allowed and forbidden transitions should be seen as preferable.

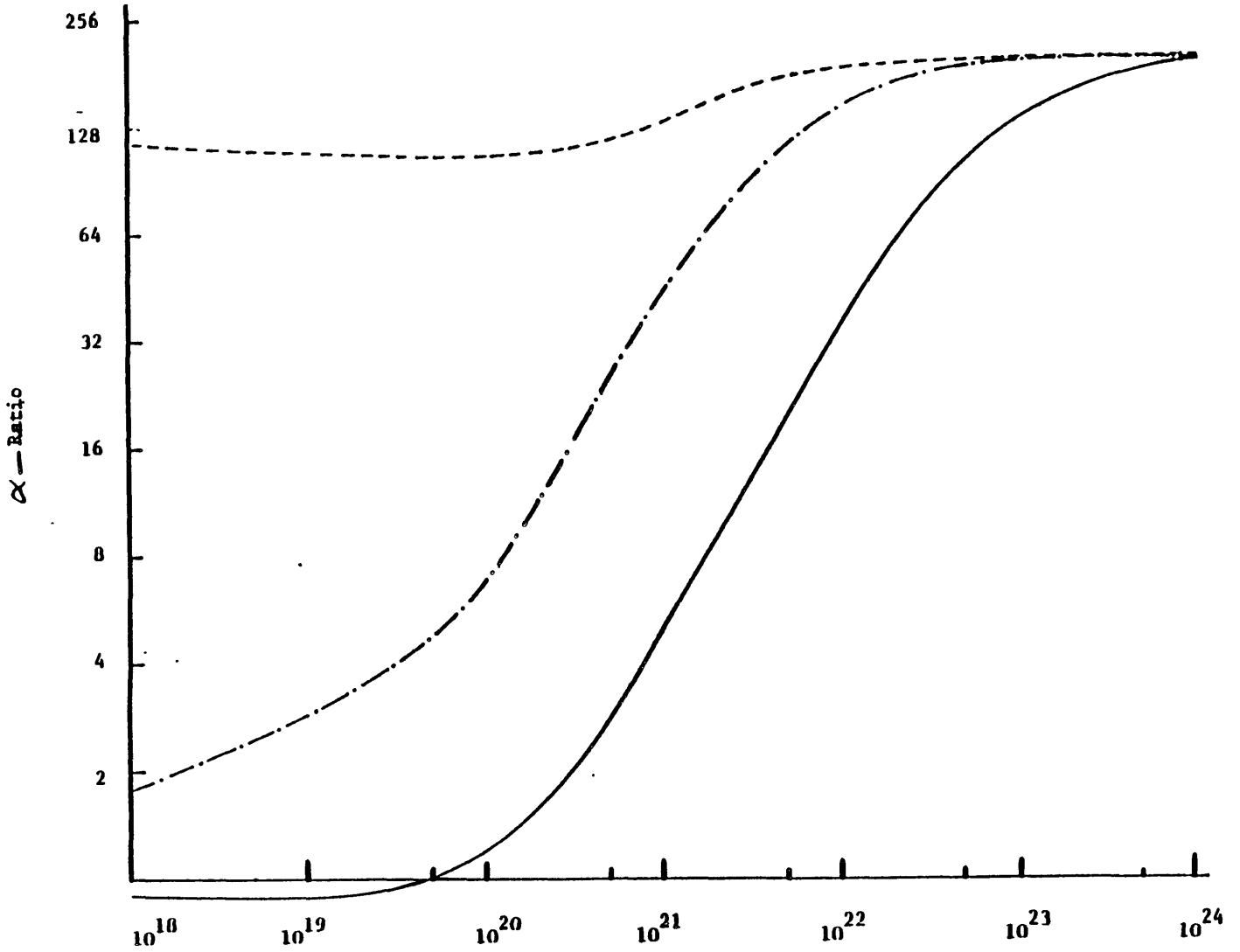

Fig.IX2 The value of the ratio "α" as a function of density for a temprerature of 100eV using collision rates from Mewe [3](------), Sampson and Parks [4](-.-.-.-.) and Virogradov et al [2](_____).

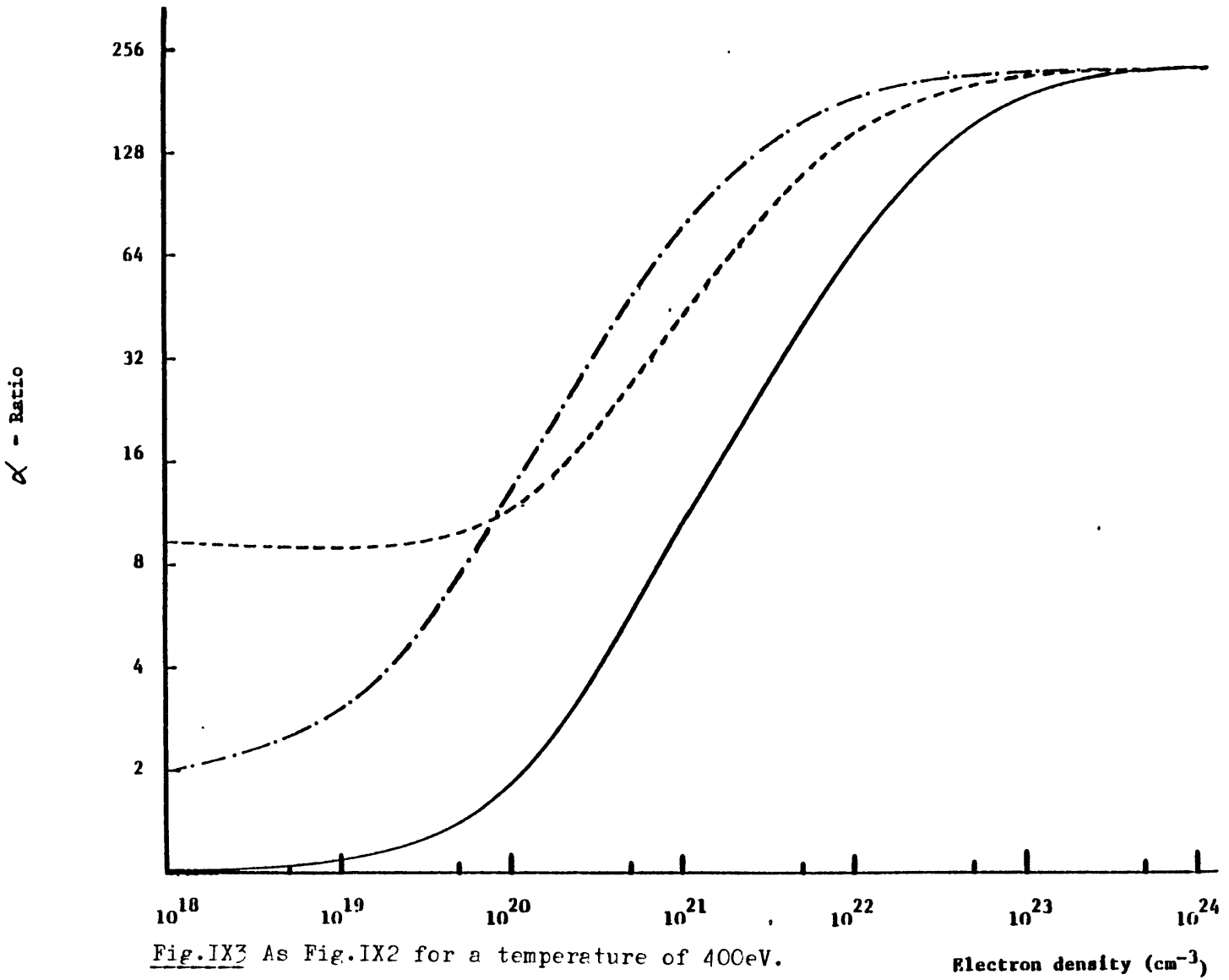

Fig.IX3 As Fig.IX2 for a temperature of 400eV.

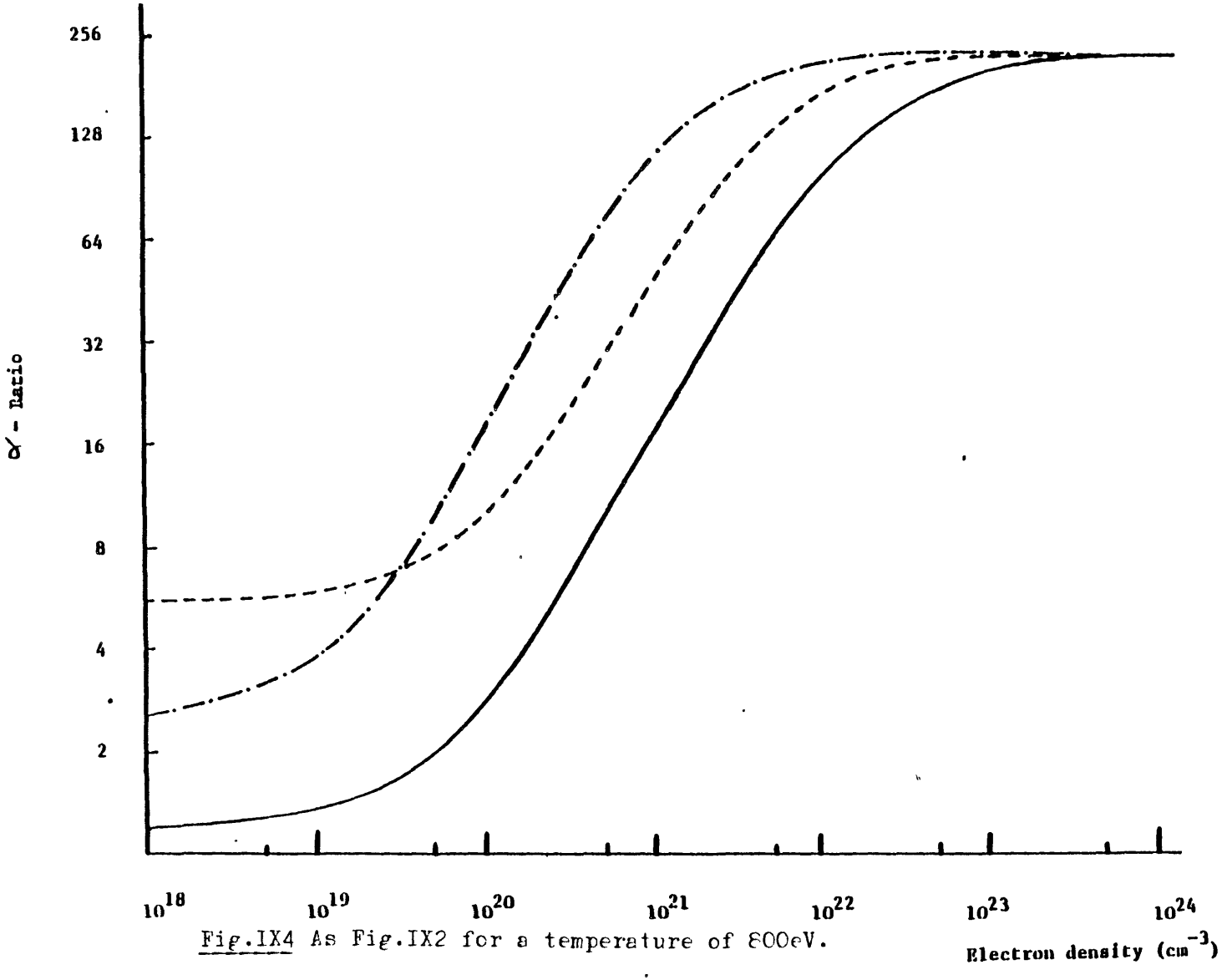

Fig.IX4 As Fig.IX2 for a temperature of 800eV.

8.Results on Satellite Ratios

The use of dielectronic satellite intensity ratios for diagnosing hot, dense, laser compressed plasmas has certain advantages. They are less susceptible to opacity effects than resonance lines. The satellite line emission is also more characteristic of the hot, dense, core region as it has been observed that it is only emitted briefly from the hottest plasma region.

The calculation of the dielectronic satellite ratios by Lunney and Seely [1] did not include collisional de-excitation from doubly to singly excited He-like states. These rates are comparable to the radiative de- excitation rates for electron densities greater than 10^{22} cm^{-3}. Figs.IX5 and 6 show the dielectronic satellite ratio as a function of density for electron temperatures of 100 and 400 eV respectively, calculated with and without collisional de-excitation from doubly to singly excited levels. From these results it can be seen that the neglect of these rates can lead to overestimates of order 20 to 30% in the inferred density from the neglect of these rates. At temperatures above a few times 10^{24} cm^{-3} the satellite ratio is given by LTE. At low densities the collisional downward rate is negligible compared with the radiative rate and the intensities depend only on the collisional upward rates.

9.Extension of the Code for Li-Like States

The work described so far in this chapter was extended to include Li-like states. The states which were used are shown in Fig.IV9.

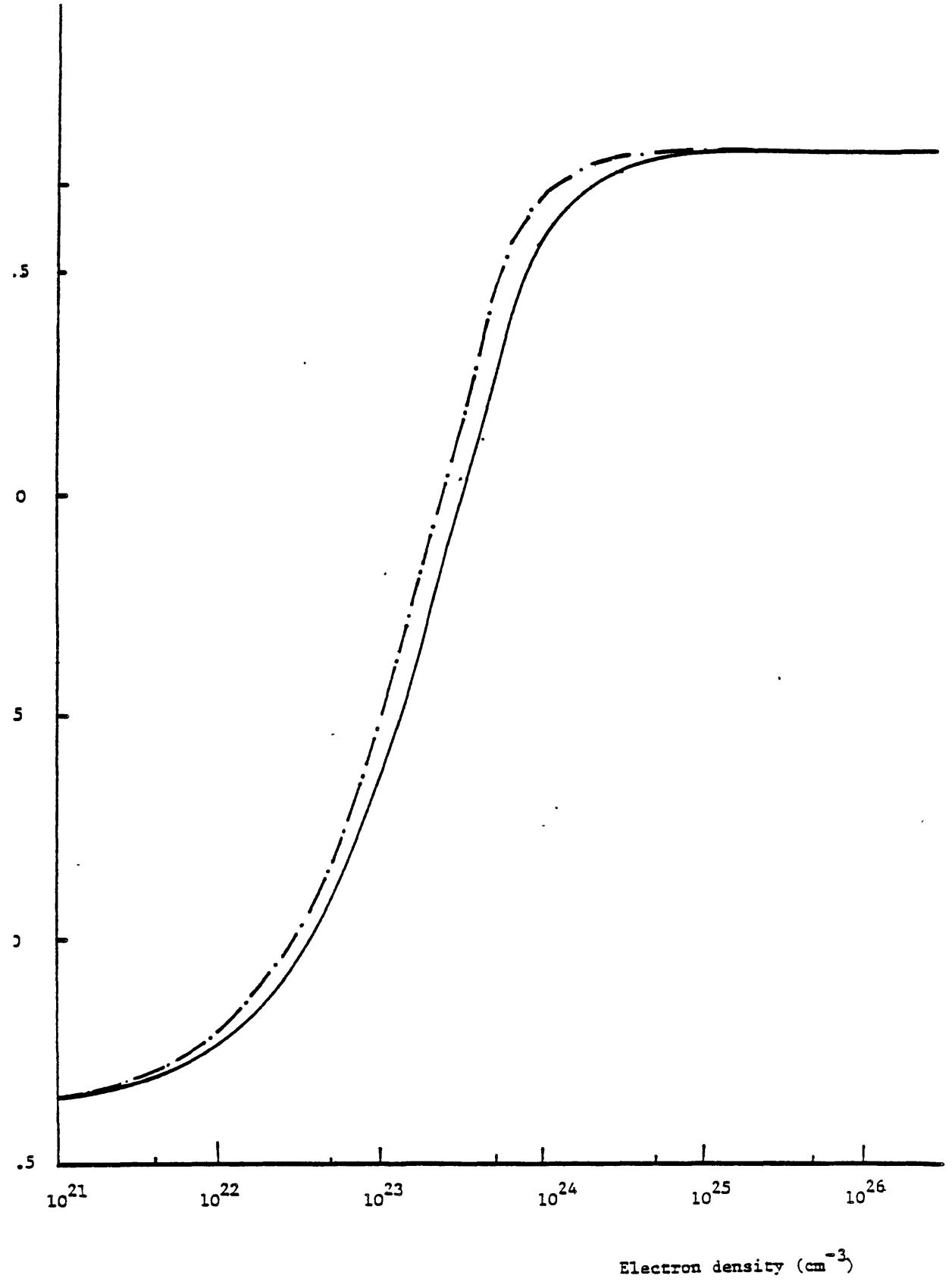

Fig.IX5 The satellite line intensity ratio as a function of density for a temperature of 1COeV excluding (_____) and including (-.-.-.-) collisional de-excitation from doubly to singly excited He-like states.

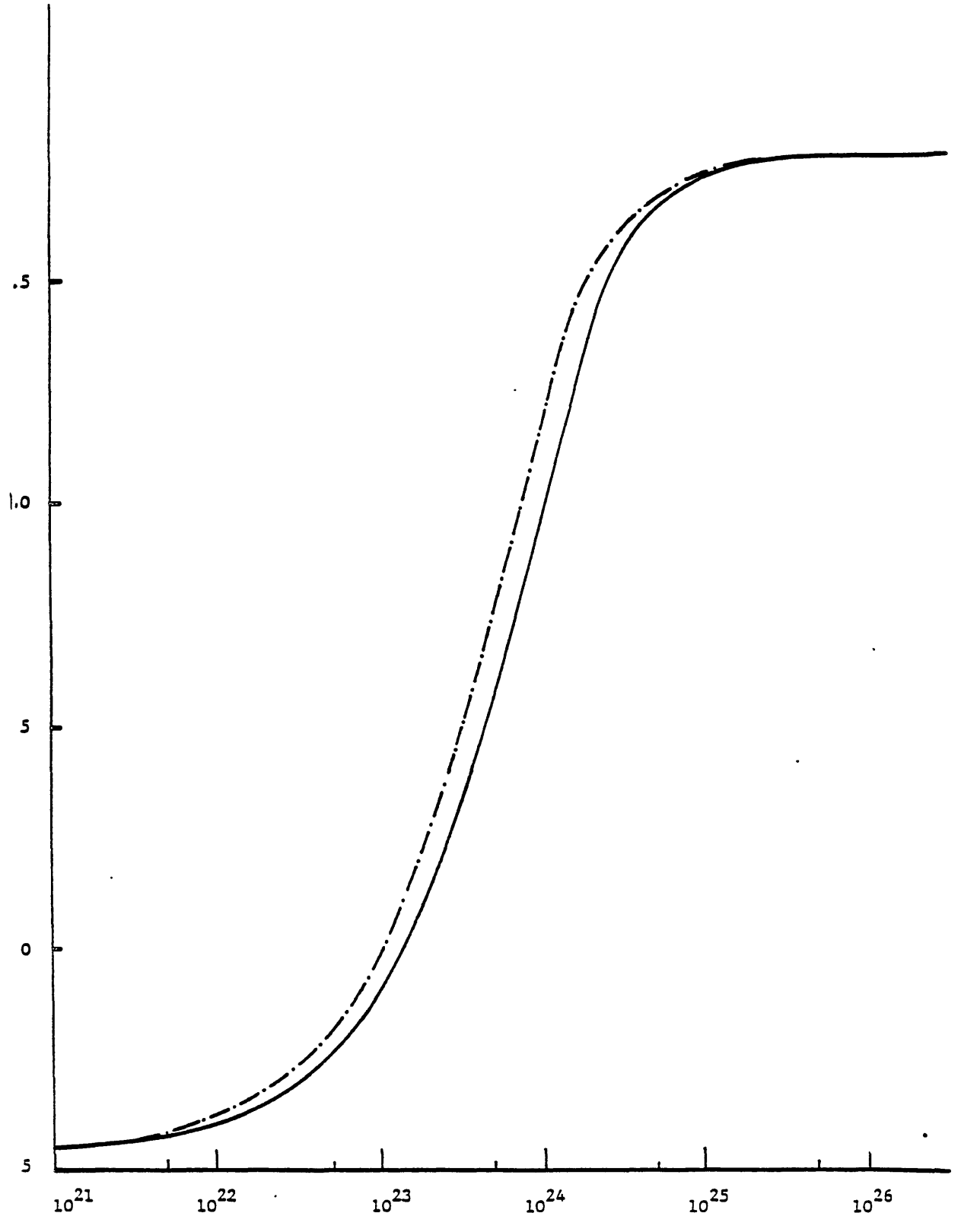

Fig.IX6 As Fig.IX5 for a temperature of 400eV.

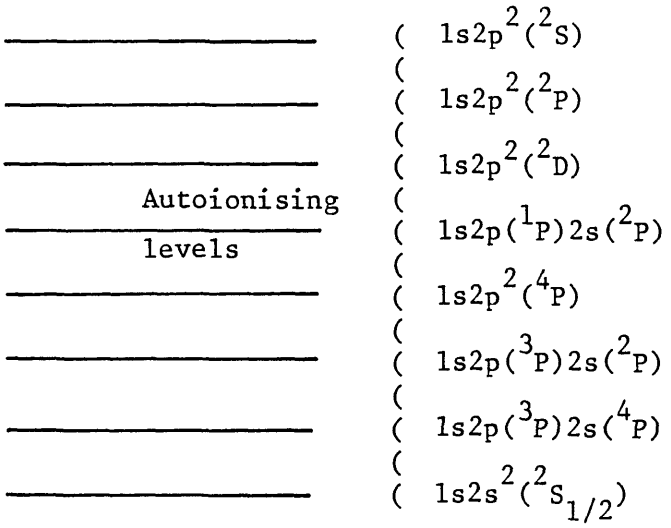

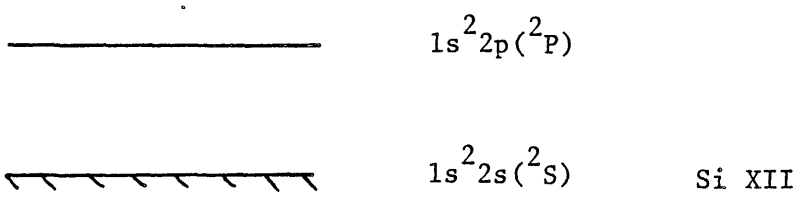

Fig.IX9

The added levels (to the ones previously shown) for Li-like calculations.

The radiative and the autoionising rates are taken from Safronova [5]. The calculation of collision rates was based on the collision strength data given by Jacobs and Blaha [15]. The collision cross-section Q can be expressed in terms of the collision strength Ω as:

$$Q(aLS \rightarrow a'L'S') = \frac{\Omega(aLS \quad a'L'S') \quad \pi a_o^2}{E(2L+1)(2S+1)} * 13.6$$

where E is the incident electron energy in eV. The collision rates are obtained by integrating over a Maxwellian velocity distribution:

$$C_{ij} = \int_{v_o}^{\infty} f(v)\ v\ Q(v)\ dv$$

which reduces to:

$$C_{ij} = \int_{v_o}^{\infty} \frac{f(v)\ v\ \ \Omega(v)\ \pi a_o^2\ 13.6}{E(2L+1)(2S+1)}$$

In calculating these integrals we use linear interpolation between the tabulated values given by Jacobs and Blaha [13]. The calculation of collision rates for very high temperatures (over 1KeV) requires collision strengths outside the range which was tabulated and for these we assume that the collision strength remains constant. The integration has been tested by comparison with the collisional excitation rate coefficients plotted by Jacobs and Blaha [15] for Al XI.

Satellite spectra for temperatures of 400 and 800 eV and densities of 10^{20}, 10^{22} and 10^{23} cm^{-3} have been calculated.

10.Conclusions

A large computer program has been developed to study the ionisation balance for highly ionised Silicon. A more complete description in both the number of states included and the coupling between them has been included. We have used a recently developed sparce linear equation solving routine to calculate the ratio of the populations.

Results form this program so far are:

(1) a study of the effect of using different collisional formulae for bound-bound transitions, and

(2) finding a correction to the results published by Lunney and Seely in 1981 [1]. In a very recent (1983) publication Lunney [12] has included this correction is his calculations.

References for Chapter IX

1. Lunney J.G. and Seely J. Phys. Rev. Lett., 46, 342 (1981)
2. Vinogradov A., Skobelev T. and Yukov E. Sov. J. Quant. Electr., 5, 630 (1975)
3. Mewe R. Atron. and Astrophys., 20, 215 (1972)
4. Sampson D. and Parks A. Astrophys. J. Supll., 28, 323 (1974)
5. Veinshtein L. and Safronova V. Atomic Data and Nuclear Data Tables, 21, 49 (1970)
6. Seaton M.J. Phys. Soc., 79, 1106 (1962)
7. Ivanov V. "Transfer of Spectral Lines" NBS Special Publ., 385 (1973)
8. Jacobs V. and Davis J. NRL Mem. Rep., 3641 (1978)
9. Sampson D. (Private Communication)
10. Duff I. A.E.R.E. Report R.8730 (1976)
11. Mewe R., Schrijver J. and Sylwester J. Astron. and Astrophys. 87, 55 (1980)
15. Davis J.,Kepple P.C. and Blaha M. J.Q.S.R.T. 18,535(1977) Jacobs V.L. and Blaha M. Phys.Rev.A. 21,525(1980)
14. "Stellar Atmospheres" by D.Mihalas (Freeman and Co. 1978)
12. Lunney J.G. J. Phys. B., 16, L83 (1983)
13. Wiese W.L., Smith H.W. and Miles B.M. Atomic Transition Probabilities NSRDS-NBS22 Vol.2 (Washington 1969)

Appendix AIV

In this appendix various experimental and theoretical methods (other than the magneto-optical) commonly used to measure and calculate transition probabilities and lifetimes will be described. The discussion however will be limited to well established techniques and only a brief outline of each will be given. In section 1 theoretical methods of deriving spontaneous transition probabilities will be discussed. In sections 2 and 3 respectively emission and absorption techniques will be discribed and finally in section 4 some lifetime measurement techniques will be presented.

1.Transition Probability Calculations

In this section an outline of calculating transition probabilities will be given. In section 1a the Einstein coefficients will be derived and the relations between them presented. In section 1b the absorption coefficient B_{ij} will be calculated by assuming that we are dealing with a classical atom in an electro-magnetic field. The value of the absorption coefficient derived is quite accurate for strong lines whereas wrong by orders of magnitude for weak lines. In section 1c we will be considering a quantum mechanical atom in a classical electromagnetic field and calculate the absorption coefficient. The spontaneous emission coefficient A_{ji} does not come into these calculations but can be related to B_{ij} through the Einstein coefficient relations. However, the most rigorous method of calcualtion is to consider a quantum mechanical atom in a quantised electromagnetic field, where the correct results

are obtained immediatelly for all three coefficients but a discussion of this may be found in (Merzbacher [2] or Sakurai [3]). Following these, in section 1d the Hartree-Fock and Coulomb approximation methods for determining transition probabilities for light elements will be briefly discussed as a more detailed discussion will follow in Chapter VII.

1a.The Einstein Relations for Bound-Bound Transitions

Let us consider the absorption and emission of radiation [4] by an atom in a transition between two bound states -a lower state i which has statistical weight g_i and an upper state j which has statistical weight g_j. Their populations are n_i and n_j respectively. Only three processes are likely to occur:

(1) The first process is absorption of radiation and the rate at which energy is removed from an incident beam of radiation I in terms of the absorption Einstein coefficient B_{ij} and the absorption coefficient α_ν ,can be expressed as:

$$\alpha_\nu I_\nu = n_i \frac{B_{ij}\, h\nu_{ij}}{4\pi} I_\nu$$

(2) The second process is a spontaneous transition with the emission of a photon. The Einstein coefficient related to spontaneous emission per unit time is A_{ji} and the rate of emission of energy is:

$$n_\nu(\text{spont}) = n_j \frac{A_{ji}\, h\nu_{ij}}{4\pi}$$

(3) Finally, the third process is a transition induced by the radiation field (stimulated emission). The rate of energy emitted is given in terms of the Einstein coefficient related to stimulated emission, by the following expression (which asssumes

the rate of emission to be proportional to I_ν):

$$n_\nu(\text{induced}) = n_j \frac{B_{ji}\, h\nu_{ij}}{4} I_\nu$$

In thermodynamic equilibrium A_{ji}, B_{ji} and B_{ij} are related by the following expressions:

$$A_{ji} = 2h\nu^3 / c^2 B_{ji} \qquad \text{and} \qquad g_i B_{ji} = g_j B_{ij}$$

bearing in mind that the occupation numbers of levels i and j are related by the Boltzman law and that $I_\nu \equiv B_\nu$ (the Planck function). The Einstein coefficients are properties of the atom only and are independent of the radiation field.

1b.The Classical Oscillator Model

The equation of motion (for a classically oscillating) electron of mass m and charge e driven by an oscillating electric field $E_{t,r}=E_{o,o}e^{i\omega\,(t-r/v)}$, is given by [5]:

$$m(\ddot{x} + \gamma\dot{x} + \omega_o{}^2 x) = -eE_{o,r}\, e^{i\omega t} \qquad \text{(AIV 1)}$$

where ω_o is the resonant angular frequency and γ takes into account all forms of damping. Further, the phase velocity v of the electric vector E is given by:

$$v = c/n'$$

where n' is the complex refractive index (n'=n+ik). Therefore $E_{t,r}$ becomes:

$$\vec{E}_{t,r} = E_{o,o}\, e^{-\omega k r/c}\, e^{i\omega(t-rn/c)} \qquad \text{(AIV2)}$$

The solution of equation AIV1 then becomes (for a fixed value of r where $E_{t,r}=F_{o,r}e^{i\omega t}$):

$$x_{t,r} = \frac{-(e/m)\, E_{o,r}}{(\omega_o^2 - \omega^2) + i\omega\gamma}\, e^{i\omega t}$$

For $\mathcal{N}$ electron oscillators per unit volume the polarisation is defined as:

$$P_{t,r} = -\mathcal{N} e x_{t,r} = -\mathcal{N} e x_{o,r}\, e^{i\omega t}$$

The susceptibility (polarisation per unit field) is $\chi=P/E$

$$\chi = \frac{\mathcal{N} e^2 m}{(\omega_o^2 - \omega^2) + i\omega\gamma}$$

But the susceptibility is related to the complex refractive index n' through the permitivity ε as follows: $1+\chi/\varepsilon_o=\varepsilon/\varepsilon_o=(n')^2=1+e^2\mathcal{N}/(2\pi m\nu_o((\nu-\nu_o)+i\gamma/4\pi))$. Using equation AIV2 and separating real from imaginary parts, and using the relationship $\mathcal{N}=N_j f$ (where N_j is the number of atoms and f is the oscillator strength, which relates the quantum mechanical and classical models of absorption), we obtain the following [5].

$$n_\nu = 1 + \frac{e^2 N f}{4\pi m \nu_o} \frac{(\nu_o - \nu)}{(\nu_o - \nu)^2 + (\gamma/4\pi)^2}$$

$$a_\nu = \frac{\pi e^2 N f}{mc} \frac{\gamma/4\pi^2}{(\nu_o - \nu)^2 + (\gamma/4\pi)^2}$$

From section 1a of the present appendix we had that the rate at which energy is removed form an incident beam of radiation I_ν to be $a_\nu I_\nu = N_i B_{ij} I_\nu \phi_\nu h\nu_{ij}/4\pi$. Integrating over the line profile we obtain:

$$I_\nu \int_{-\infty}^{+\infty} a_\nu \, d\nu = N_i B_{ij} \frac{h\nu_{ij}}{4\pi} I_\nu \int_{-\infty}^{+\infty} \phi_\nu d\nu = N_i B_{ij} \frac{h\nu_{ij}}{4\pi} I_\nu \qquad \text{(AIV 3)}$$

where ϕ_ν is the absorption profile. From above, integrating the absorption coefficient over the line profile we obtain:

$$\int a_\nu \, d\nu = \frac{\pi e^2}{mc} N_i f_i \qquad \text{(AIV 4)}$$

Combining equations AIV3 and 4 we get

$$f_i = \frac{mhc}{4\pi^2 e^2} \nu_{ij} B_{ij}$$

f may therefore be related to A_{ji} and B_{ji} as well.

1c.The Quantum-Mechanical Model

We will now calculate B_{ij} for a quantum-mechanical atom in a classical electromagnetic field [10, 4].

Suppose that the structure of the atom in a stationary state j can be described by a wavefuncion of the form $\psi_j(r,t)$ which is also a solution of Schrodinger's equation:

$$H_A \psi = i\hbar \frac{\partial \psi}{\partial t} = E_j \psi_j \qquad \text{(AIV 5)}$$

where E_j is the energy of state j and H is the Hamiltonian operator. The solution to the above equation is $\psi_j(t) = \psi_j(0)e^{-iE_jt/h}$ and with spacial dependence it takes the slightly more general form of $\phi_j(r,t) = \phi_j(r)e^{-iF_jt/h}$. The time-independent eigenstates ϕ_j are orthogonal and satisfy the equation

$H_A \phi_j = E_j \phi_j$. At t=0 a general solution has the form $\phi = \sum_j a_j \phi_j$ while at any time t it takes the form of:

$$\psi(t) = \sum_i a_j(t)\, \psi_j(t) = \sum_j a_j(t)\, \psi_j(r) e^{-iE_j t/h} \qquad \text{(AIV 6)}$$

where a_j is such that at t=0, $\psi(0) = \sum_j a_j \phi_j$ and the probability of finding the system in a specific state j is $a_j^* a_j = |a_j|^2$.

If $H=H_A$ the atom is not perturbed and the a_j's are constant. If the atom is perturbed by some potential V (eg if the atom is assumed to be inside an electromagnetic field $\underline{E}=E_o \cos\omega t \hat{\underline{i}}$), then the a's will change with time and the atom will undergo transitions from one state to another. So,

$$V = \underline{E}.\underline{d} = (E_o \cos\omega t)\ (\hat{\underline{i}}.\underline{d})$$

where $\underline{d}$ is the dipole moment of the atom. Therefore Schrodinger's equation now becomes:

$$(H_A + V)\psi = i\hbar \frac{\partial \psi}{\partial t} \qquad \text{(AIV 7)}$$

Substituting equation AIV6 in equation AIV7 and using equation AIV5 we get:

$$\sum_n a_n V \psi_n = ih \sum_n \dot{a}_n \psi_n \qquad \text{(AIV 8)}$$

Multiplying equation AIV8 by ψ_m^*, integrating over space and defining $\omega_{mn} = (E_m - E_n)/\hbar$ and $V_n = \langle \phi_m^* / V / \phi_n \rangle$ we get:

$$\dot{a}_m(t) = \frac{1}{i\hbar} \sum_n a_n(t)\, V_{mn}\, e^{i\omega_{mn} t} \qquad \text{(AIV 9)}$$

But also since $V_{mn} = (E_o \cos\omega t)\ \hat{\underline{i}} \cdot \langle \phi_m^* / \underline{d} / \phi_n \rangle = (E_o \cos\omega t)\ (\hat{\underline{i}}.\underline{d}_{mn}) =$

$$= 2h_{mn} \cos\omega t = h_{mn} (e^{i\omega t} + e^{i\omega t})$$

equation AIV9 becomes:

$$\dot{a}_m(t) = \frac{1}{i\hbar} \sum_n a_n(t)\, h_{mn}\, e^{i\omega_{mn}t} \left(e^{i\omega t} + e^{i\omega t}\right)$$

Further by assuming that:(a) at t=0 the atom is in definite eigenstate k, (b) at t=T (T very small) eigenstate k is not depopulated and (c) $a_k(t)=1$ for $t< T$ and integrating with respect to time, we get:

$$a_m(t) = \frac{h_{mk}}{i\hbar} \left\{ \frac{\exp(i(\omega_{mk} - \omega)t) - 1}{(\omega_{mk} - \omega)} + \frac{\exp(i(\omega_{mk} + \omega)t) - 1}{(\omega_{mk} - \omega)} \right\}$$

(AIV10)

For absorption processes ($\omega_{mn} > 0$)), the dominant contribution to $a_m(t)$ comes when $\omega_{mn} \doteq \omega$. Then integrating $/a_m(t)/^2$ over all frequencies that can contribute to the k->m transitions and substituting $x=(\omega - \omega_{mk})$, $u=xt/2$ and $d\nu = d\omega/2\pi = dx/2\pi$ we obtain (assuming that the line profile goes to 0 at frequencies + and - ∞)

$$\mathcal{N}_{km} = \frac{E_o^2}{4\pi\hbar^2} \, /\hat{i}.\underline{d}_{mk}/^2 \, t \int u^{-2} \sin^2 u \, du = \frac{8\pi^2}{\hbar^2 c} \, /\hat{i}.\underline{d}_{mk}/^2 \, \bar{J}_\nu \, t$$

where d_{mn} are the dipole moment matrix elements and J_ν is the mean intensity of radiation ($J_\nu = c/4\pi \cdot E_o^2/8\pi$). Since the Einstein emission coefficient is defined as:

$$\mathcal{N}_{km} = B_{km} \bar{J}_\nu \, t$$

then

$$B_{km} = \frac{8\pi^2}{\hbar^2 c^2} /\hat{i}\cdot\underline{d}_{mk}/^2 = \frac{8\pi^2 d_{mk}^2}{3\hbar^2 c}$$

The other two coefficients can be easily obtained. Summing over all substates k (of the lower level i) and all substates m (of the upper level j), we define the strength of the line to be:

$$S(ij) = \int_{mk} d_{mk}^2$$

1d.Transition Probabilities for Light Elements

When the atom has more than one electron, the Hamiltonian for N electrons becomes:

$$H = -\frac{\hbar^2}{2m}\sum_{i=1}^{N}\nabla_i^2 - \sum_{i=1}^{N} Ze^2/r_i + \sum_{\substack{\text{all}\\ \text{pairs}\\ (i,j)}} \frac{e^2}{/r_i - r_j/}$$

The first term represents the kinetic energy of the electrons. The second term their electrostatic attraction to the nucleus (which has charge Z) and the third term represents the Coulomb repulsion between all pairs of electrons. In Hartree's self-consistent field method, the rapidly changing field due to other electrons (for a given electron) is approximated by a static mean spherically symmetric field. In this way, the angular factors in the Schrodinger equation can be separated out exactly like for the hydrogenic case. There is only an iterative solution to determine the electronic wavefuncions (see any standard textbook eg [4] or [9]): we start with an approximate set of functions, compute the effective nuclear charge Z_{eff} (seen by an electron considering the effect of the others), solve for the radial function, recompute Z_{eff} and iterate until the procedure converges. The line strength can be obtained form

the following expression assuming that only one electron undergoes a transition:

$$S(n',L',S';n,L,S) = a_0^2\, e^2\, (4l^2-1)^{-1} \int_0^\infty \left(P_{n'l'}\, P_{nl}\, r\, dr \right)^2 J(M)J(L)$$

where J(M) is the line strength of the multiplet and J(L) is the strength of the line and their values are tabulated [6].

Bates and Damgaard [7] have shown that the cumbersome evaluation of $\int_0^\infty P_{nl}P_{n'l'}dr$ can be simplified when the largest contribution to that integral comes from large values of r where the electron moves in a nearly Coulomb potential. In this case, the integral is approximated to hydrogenic values. For cases where this approximation cannot be made, Hartree-Fock calculations are useful and for those where the independent particle model itself breaks down, new theoretical techniques have been developed in recent years [1] which take into account electron-electron correlation effects. The main ones are the following: (i) the many body perturbation theory (MBPT) based on the work of Brueckner and Goldston and first applied to atoms by Kelly which includes all the correlation diagrams (ie all the terms of perturbation theory)to a given finite order, (ii) the random phase approximation expansion with exchange (RPAE) developed by Amusia and Wendin which includes some diagrams to all orders of perturbation but does not include all the diagrams. (iii) The g-Hartree method developed by Dietz et al which includes all the diagrams to second order in an optimised basis (rather than in the somewhat arbitrary basis of perturbation theory) so that the mean field is correct to all orders and finally (iv) the hyperspherical method developed by Macek and Fano which considers only two electron correlations

but solves the Schrodinger equation directly.

Multi-configurational Hartree-Fock is a less sophisticated alternative to the many body approaches above, but also produces a significant improvement in agreement between theory and beam-foil data for many transitions. In Chapter VII some resonance line transition probabilities for MgI that the author of this thesis calculated, will be given in greater detail using the multi- configurational Hartree-Fock (MCHF) model (Fischer and Saxena [8] and references therein).

Another useful new idea was the establishment of rigorous upper and lower error bounds to the theoretical data (Wiese [1] and references therein). This approach allows a theoretical assessment of the experimental results obtained. However, this scheme is limited only to the He-, Li- and Be-sequence where the wavefunctions can be obtained with a reasonably high accuracy.

Relativistic effects in transition probabilities must be taken into account for elements with high Z along an isoelectronic sequence, since the remaining bound electrons of a highly stripped ion (which move in the field of a large nuclear charge) approach relativistic speads. This starts happening for Z between 15 and 40 depending on the transition [1].

2.Emission Measurements

So far, the emission technique [5] has been the most basic source of experimental transition probability data but not necessarily the most accurate. In recent years, attempts have been made to improve the experimental conditions in order to obtain a homogeneous, stable, optically thin and well analysed plasma.

The underlying idea behind the emission measurements is that the energy emitted in all directions per unit solid angle, per second per unit area accross a layer of thickness l is $I_{21}=1/4\ N_2A_{21}lh\ \nu_{21(0)}$.

For absolute measurements A_{21} can be obtained by determining I_{21} and N_2. However such measurements are extremelly difficult to perform accurately. Normally, the intensity would be compared with that of a standard source. The second important problem to be tackled is the correct calculation of N_2. If the experimental conditions are chosen such that the gas is in the state of local thermodynamic equilibrium (LTE), then N_2 can be related to the total number density of a species a according to the Boltzman relation:

$$N_{ka} = N_a \frac{g_k}{U(T)}\ e^{-E_k/k_BT}$$

where a represents the ionisation stage, k the excitation level k, E_k is the excitation energy for level k and $U(T)$ ($= \sum_k g_k e^{-E_k/k_BT}$) is the partition function (the temperature T can be measured). True thermodynamic equilibrium cannot hold in a source such like an arc, as energy is fed in constantly in as electrical power and comes out as radiation. For LTF conditions the temperature T and the total number density N_a are related by a set of conservation and equilibrium equations ($N_a = \sum_k N_{ka}$ and the Boltzman relation). For one-element arcs these equations enable us to determine the state of the plasma just by knowing either N_a or T. But for two-element arcs considerable errors arise due to de-mixing effects ("the various components of the arc plasma tend to separate out, with the more highly excited atoms apparently congregating in the hottest bit of the arc."[

5]) and two independent measurements have to be made.

A third difficulty that has to be overcome in emission measurements is the correction for optical thickness effects. Most sources usually have cylindrical geometry and symmetry and when the line is viewed end-on it tends to be optically thick and there might also be a radial temperature gradient. Corrections to radiation trapping can be made although ideally they should not be needed. Some of these problems seem not to exist in wall-stabilised arcs recently developed [1]. In this case, the arc is very stable and enables us to vary its physical conditions over a wide range of densities and temperatures for the maximum desirable amount of obtainable data. The arc source can be any neutral or singly ionised gaseous element and also the plasma is homogeneous along the line of sight (for side-on observations of a cylindrical plasma the Abel inversion process may be applied).

A final uncertainty may arise if there is some continuum radiation arround and therefore shifts the base line from its true position. Furthermore if the measurement is made at high pressures then inevitably there will be a Lorentzian component in the line profile. In cutting off 5 FWHM from the line centre would produce an error of 7% for the Lorentzian line whereas a negligible one if the line was purely Doppler. This last effect may explain the 20% discrepancy between observed and calculated transition probabilities in the late sixties when calculations had been extended only to 1 FWHM on either side of the line centre [1].

When the determination of N_a becomes very difficult (especially in the case of arc plasmas with several elements)

then it must be treated as an unknown and transition probability data has to be measured on a common relative scale. Absolute values can be obtained if the life-time of one of the lines was measured with any of the recently developed atomic life- time techniques. If one is dealing with excited states, a lower electron density is required to obtain "partial" LTE than for the ground state. The transition probability ratios (with an arbitrarily chosen reference line r) are as follows [1]:

$$A_x / A_r = \frac{\lambda_x g_x I_x}{\lambda_r g_r I_r} e^{-(E_x - E_r)/kT}$$

Since $/E_x-E_r/$ is equal to a few times kT, the ratio A_x/A_r is not very sensitive to temperature uncertainties. From the above statements it is obvious that relative A-value measurements are much more accurate than absolute ones.

Another very usefull emission technique is the branching ratio technique in conjunction with life-time measurements. Emission lines, originating from a common atomic level are defined as branches and if we introduce the definition of photon density being $\Gamma_{ik}=I_{ik}/h\,\nu_{ik}$ we obtain [1]:

$$D_{k1} : D_{k2} : D_{k3} : \ldots = A_{k1} : A_{k2} : A_{k3} : \ldots$$

Also we know that:

$$\tau_k = \frac{1}{\sum_i A_{ki}} = \frac{1}{A_{kj} \sum_i (A_{ki}/A_{kj})}$$

Consequently:

$$A_{kj} = \frac{1}{\tau_k} \frac{A_{kj}}{\sum_i A_{ki}} \quad \frac{1}{\tau_k} \frac{D_{kj}}{\sum_i D_{ki}}$$

In this method, emission spectra were generated in special hollow cathode sources (the metal under study was usually what the cylindrical cathode was made from). The total line intensity measurements were quite accurate (a few %) under normal conditions and relative photon intensities of all the branch lines were measured for a number of atomic levels. The lifetimes of these levels were measured by the beam-foil technique which is explained later in this appendix. Therefore in the branching ratio technique each group of emission lines originating from a given atomic level must be normalised individually unlike the relative measurements where only one lifetime is needed to normalise all the relative emission data for one type of gas [1].

Furnaces may also be used for emission work but they are usually not hot enough ($3000^{\circ}K$) and sometimes are not optically thin, although they have a uniform and well defined T and the contained gas is in equilibrium. Shock tubes could be used instead, if the temperature could be always measured accurately. The wall-stabilised arc desribed above has proved to be the most suitable emission measurement source [5].

3.Absorption Measurements

3a.Integrated Absorption

When light radiation of intersity $I_{\nu}(0)$ is incident on a column of absorbing medium of thickness 1, the emerging intensity is equal to:

$$I_{\nu}(1) = I_{\nu}(0) \exp\left(- \int_0^1 a_{\nu} \, dx \right) = I_{\nu}(0) \, e^{-a_{\nu} 1} \qquad \text{(AIV 11)}$$

if the medium is homogeneous so that a_ν is independent of x. The absorption coefficient can be written as:

$$a_\nu = \frac{1}{l} \ln \frac{I_\nu(0)}{I_\nu(l)} \qquad \text{(AIV 12)}$$

For convenience, equation AIV4 will be restated:

$$\int a_\nu \, d\nu = \frac{e^2}{4\varepsilon_o \, mc} \, N_l \, f$$

The absorption coefficient has to be obtained from equation AIV12 as it cannot be measured directly, and the integrated absorption is the area under the curve when a_ν is plotted versus ν.

Therefore, knowing the area under $\int a_\nu \, d\nu$, l and N_1 would allow us to determine f [1,5]. The first difficulty of the method is the determination of N_1. If the relevant transition levels are in LTE then N_1 is related to the total number density N_a of species a and the temperature T, through the Boltzman relation. T can be measured fairly accurately using optical pyrometry or thermocouples. If we are interested in relative oscillator strengths, then N_a need not be measured. If all the transitions start from the same lower state then knowledge of T is not necessary for relative measurements. For a transition starting from the ground state (where we can say that $N_{gr} \cong N_a$), N_{gr} can be easily found from the equation of state for a gas if we know the vapour pressure and temperature ($P/k_B T = N_a$) [1].

The second difficulty of the method is that of using an instrument of high resolution to obtain a realistic line profile. The instrumental width should be much less than the line width. If that is not so, then the instrument smooths too

much the line profile, the curve is flattened out and the value for the area is found to be too low. To avoid this difficulty it is common to pressure-broaden the line [5]. Finally, the path l must be defined accurately.

3b. Equivalent Width Method

The equivalent width W_ν of a line is given by the following formula:

$$W(\nu) = \int_{\text{line}} \frac{I_\nu(0) - I_\nu(l)}{I_\nu(0)} \, d\nu \qquad \text{(AIV 13)}$$

and measures the total energy extracted from the incident radiation beam and is almost independent of the instrumental resolution. Equation AIV13 can be rewritten as follows in terms of equation AIV11:

$$W_\nu = \int_{\text{line}} (1 - e^{-a_\nu l}) d\nu \qquad \text{(AIV 14)}$$

and for the opically thin case $k_\nu l \ll 1$ the above reduces to:

$$W_\nu = \int a_\nu \, l \, d\nu = l \int a_\nu \, d\nu = \frac{e^2}{4\varepsilon_o \, mc} \, N_l \, fl \qquad \text{(AIV 15)}$$

Therefore by plotting $\log(W_\nu / \delta\nu_D)$ versus $\log(Nfl/ \delta\nu_D)$ for the optically thin case (where $\delta\nu_D$ is the half value width) we should get a straight line. As the optical depth increases, W_ν rises much less quickly as a function of Nfl compared to the thin case and for a pure Doppler line W_ν saturates to a certain value since all the radiation that can be absorbed is. But, however it does not completely saturate for a Lorentzian line, where the wings are much more important, since radiation can still be absorbed from the line wings even if the line centre

has reached its saturation point. Such typical curves of growth ($\log W_\nu / \delta\nu_D$) versus $\log(Nfl/\delta\nu_D)$ are shown in Fig.9.9 of [5].

For the optically thin case the straight part of the curve may be used to determine f from equation AIV15, W_ν and l can be measured with a high accuracy. The determination of N_1 was described above. However, the curve of growth could be used to measure f-values of optically thick lines as follows: theoretical curves of growth are computed for several values of a ($a=\ln 2\ \delta\lambda_L/\ \delta\nu_D$). W_ν is then measured as a function of Nfl. When the experimental plot of $\log W_\nu$ versus $\log Nfl$ is slit horizontally over the the theoretical curves and coincides with one of them, the absolute value of Nf can be found [5].

There are two main sources of error in absorption measurements. One is the absorption of radiation from the wings of the line which is hard to measure very accurately and the other is the fact that inevitable scattered light reduces the absorption.

3c.The Dispersion Technique

In section 1a of the present appendix the expression for the refractive index n_ν in the region of an isolated absorption line of wavelength λ_o was derived and found to be equal to:

$$n_\nu - 1 = \frac{e^2 Nf}{4\pi m\nu_o} \frac{\nu_o - \nu}{(\nu_o-\nu)^2 + (\gamma/4\pi)^2} \qquad \text{(AIV16)}$$

In the region away from ν_o($\nu_o-\nu >> \gamma/4\pi$), the above reduces to:

$$n_\nu - 1 = \frac{e^2}{16\pi^2 \varepsilon_o mc} \frac{Nf\ \lambda_o^3}{\lambda - \lambda_o}$$

In this technique the relation between n_ν and the f-value near λ_o will be applied and is called the "Hook" technique invented by Rozhdestvenskii [1,5].

The experimental set-up consists of a Mach-Zehnder interferometer which is illuminated by a continuous source. The optical path lengths of the two interferometer arms are equal and the fringes which are formed on the slit of the spectrograph are nearly horizontal. By placing a dispersive medium of length l and refractive index n with an absorption line at λ_o in one arm of the interferometer, the fringes become distorted due to the rapid change of the refractive index (actually they follow the known n-1 curve behaviour). A compensating plate of length l' and refractive index n' is inserted in the other arm and a very large path difference (order 10^6) occurs between the two rays. Two characteristic hooks symmetric to the centre of the line are formed and their separation can be related to the oscillator strength of the transition. Also, because of the large path difference, the fringes away from λ_o slope diagonally accross the spectrum. Therefore, the fringe equation becomes:

$$by + (n-1)l + (n'-1)l' = pl$$

where p is a large integer, y is the distance up the spectrograph slit and b is equal to $h\alpha/f$ where f is the focal length of the lens used to image the source on the spectrograph, α is the angle through which the first beamsplitter and mirror are rotated about an axis perpendicular to the plane of the optical axes and finally, h is the distance between the first beamsplitter and the first mirror.

The position of the hooks is given by $dy/d\lambda = C$. Also it can be said that the refractive index of the compensating plate remains almost constant with wavelength changes: ie $dn'/d\lambda = 0.$, From equation AIV16 we obtain:

$$-1 \frac{e^2}{16\pi^2 \varepsilon_o m c} \frac{Nf \lambda_o^3}{(\lambda_H - \lambda_o)^2} = p$$

where λ_H is the hook wavelength. Therefore if $2/\lambda_H - \lambda_o/ = \Delta$, then $-p\Delta^2 = e^2 \lambda_o^3 N_1 fl/(4\pi^2 \varepsilon_o mc)$ So, $N_1 f$ can be determined for relative values by the hook distance Δ, which can be measured to a good accuracy. Uncertainties in the interferometer constant are negligible. If absolute f-values are to be obtained, then N_1 can be obtained by the methods described in the previous sections.

The hook method has some very basic adventages compared to the emission and absorption intensity measurements.

(a) Wavelength distance is easier to measure than intensity.

(b) There is no radiation trapping, and

(c) There is no need for intensity calibrations.

However, the hook technique has two limitations and cannot be successfully applied a) if the lines are weak (the hooks are not very clear) and b) if the lines overlap with each other (the hooks are not very well separated).

4 Lifetime Measurements

If $A_{21}N_2$ is the number of spontaneous emissions per unit time from level 2 to level 1 and there is no absorption or stimulated emission then state 2 decays as $dN_2/dt = -N_2 \sum_i A_{2i}$.

This means that:

$$N_2(t) = N_{2,0} \exp(-(\sum_i A_{2i})\, t)$$

where the mean lifetime τ_2 is the time taken for $N_2(t)$ to decay to 1/e of its original value. Therefore,

$$\tau_2 = 1 \,/\, \sum_i A_{2i}$$

The basic reason for requiring to measure the lifetime of excited stomic states [1,5] is that they are related to transition probabilities, through $\tau_k = 1/\sum_i A_{ki}$. If in low-lying atomic states only one radiative transition k-->i exists or dominates, then the lifetime can determine immediately the transition probability through $\tau_k = 1/A_{ki}$. However, in most cases, a wide range of transitions takes place and from all the methods of measuring transition probabilities in this appendix it was shown that only relative f-values can be obtained. The measurement of only one lifetime can allow us to normalise all the relative transition probability data for a given species. However, for the branching ratio technique each group of emission lines for a given atomic level had to be normalised separately (see section 2 of present appendix).

There are three main techniques for measuring lifetimes: the delay time, beam-foil spectroscopy and the Hanle effect. None of these methods (in contrast to absorption and emission measurements) requires knowing the temperature, density and the level population of the relevent level or making assumptions of LTE, thus avoiding serious sources of error.

4a.Beam-Foil Method

A beam of ions of various degrees of ionisation (accelerated in a Van der Graaf accelerator) passes through a thin foil [5]. The interaction of the beam with the atoms of the foil has as a result that the beam emerges in different states of excitation. By knowing the velocity of the beam and by measuring the intensity decay as a function of distance from the foil, atomic mean lifetimes can be obtained. For these measurements it is preferable to keep the spectrometer fixed and measure the intensity of the lines in which we are interested by moving the foil upstream. This method is very widely used because of the simple experimental set-up. Also, the recent progresses in high energy accelerator technology, have made it possible to use very highly charged states of heavy elements. In this case, the lifetimes are very short and very accurate measurements are necessary as well as having the slit very close to the foil.

Apart from the advantages of this method, there are some problems associated with it. The major is the repopulation of the upper level (of the transition in question) by radiative cascading from higher lying atomic states. Other similar problems are radiation trapping and de- and re-population of this level collisionally. Low light intensity may also create difficulites. Finally, the finite acceptance angle (say 2θ) of the spectrometer has as a result to accept velocities $v\sin^2\theta$ on either side of the direction perpendicular to the beam. Doppler shifts will cause the line to appear broadened.

So, if the beam intensity is low, the cascading problems can be overcome, but a wider apperture will be needed and the Doppler broadening problem will be enhanced. This is the only

lifetime measurement method applicable to ionic spectra.

4b.Delay Methods

The gas which is contained in the vessel shown in Fig.AIV1 is excited by a pused electron beam [5]. At the same time a time-to-pulse height converter is switched on. When the emitted radiation passes through a monochromator and a photomultiplier, the converter is stopped and therefore the height of the pulse is proportional to the time the excited level in question took to decay from the moment it was excited. Statistics for dN/dt as a function of t, show that N decays exponentially with time constant τ.

Alternatively, we could use a coincidence counter instead of a time- to-pulse height converter. In this way we would record the coincidences between the electron pulse that excites the atoms and the emitted radiation as a function of a delay time t. This delay time is introduced to the signal from the electron pulse [5].

4c.The Hanle Effect

In this technique, polarised resonance radiation excites atoms in the presence of known magnetic fields. The field causes the electrons of the atoms to precess about its direction. The radiation that is re-emitted involves the field and the atomic lifetime, which therefore may be calculated. The Hanle effect is shown schematically in Fig.AIV2 [5].

Plane polarised light in the x-direction and travelling in the y- direction leaves the source and ther enters the resonance vessel where it is absorbed and then re-emitted. The photomultiplier on the x-axis does not record a signal since the

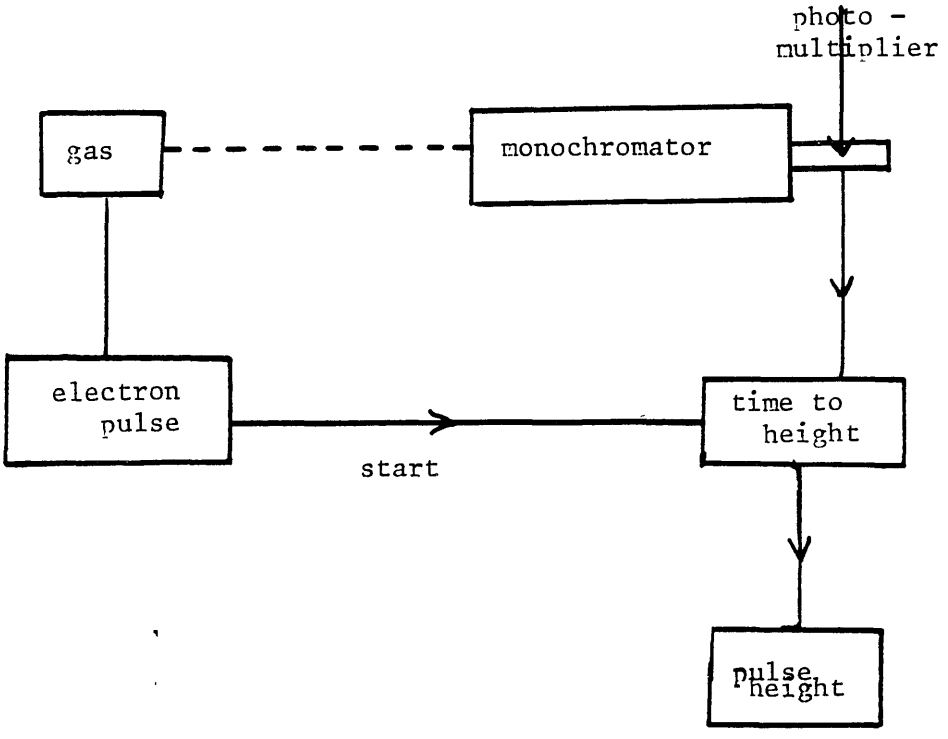

Fig.AIV1 Schematic representation of the delayed coincidence experiment to measure atomic lifetimes.

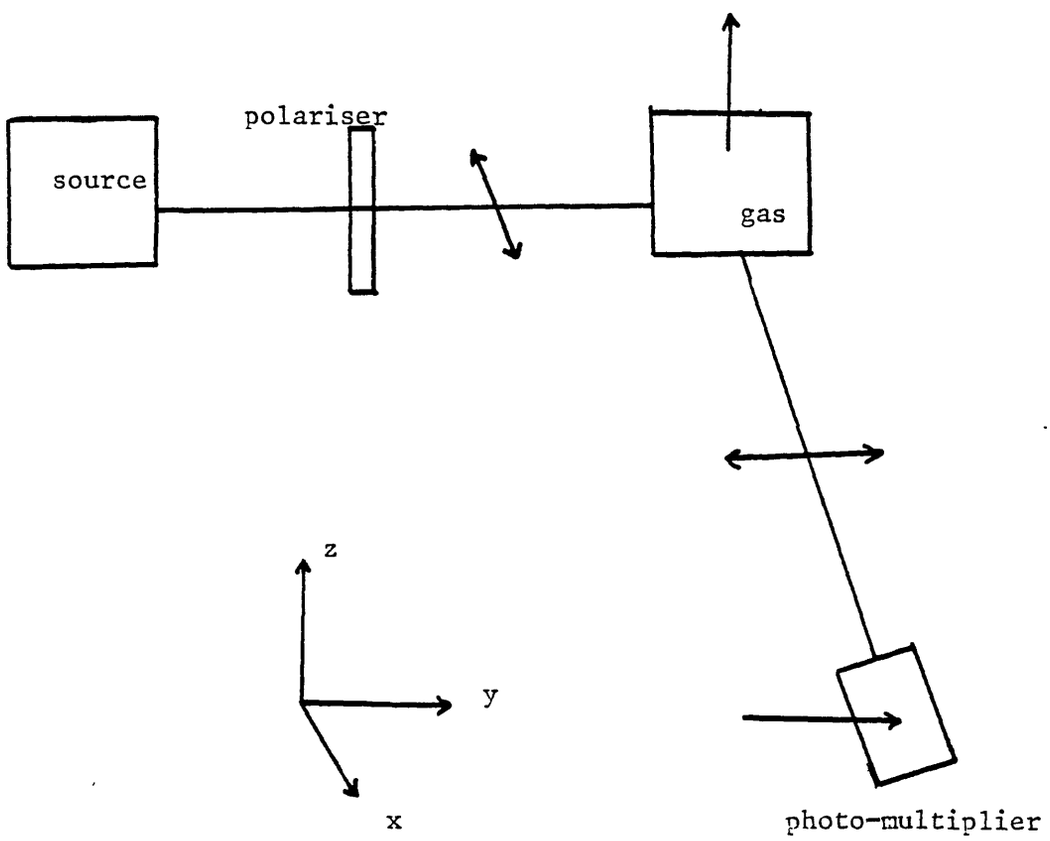

Fig.AIV2 Schematic representation of the Hanle effect.

emitted radiation has the same polarisation as the exciting radition. When a magnetic field B is applied in the z-direction the photomuliplier records a signal because the resonance radiation is partly de-polarised. The electrons that initially oscillated in the x-direction now precess about the z-direction. If some atoms decay before the precessional cycle ends the intensity of the y-direction will be less than that of the x-component originally. The above statement can be expressed mathematically as follows:

$$I \propto 1 - \frac{\gamma^2}{\gamma^2 + 4\,\omega_B^2}$$

where I is the intensity of the signal recorded, γ is the damping constant ($\gamma = 1/\tau$) and μ_B is the precessional frequency ($\omega_B = g_J\,\mu_B B/\hbar$ where g_J is the Lande g-factor and g_J is the Bohr magneton). From the FWHM of the signal we get:

$$\tau = \frac{\hbar}{g_J^{\,2}\,\mu_B\,B_{\frac{1}{2}}}$$

where $B_{+-1/2}$ is the value of the B-field corresponding to half maximum intensity points. Therefore if g_J is known, τ can be determined from the half width of the signal intensity plotted against the applied magnetic field.

References for Appendix AIV

1. Wiese W.L. Progress in At. Spectroscopy Part B, 1101 (1979) (Eds. Hanle W. and Kleinpoppeutt Plenum Publ. Corp. 1979)

2. "Quantum Mechanics" by E. Merzbacher (John Wiley 1970)

3. "Advanced Quantum Mechanics" by J.J.Sakurai (Addison-Wesley 1967)

4. "Stellar Atmospheres" by D. Mihalas (W.H. Freeman and Co. 1978)

5. Spectrophysics" by A.P. Thorne (Chapman and Hall 1974)

6. "The Atmospheres of the Sun and Stars" by L. Aller (Ronald Press 1963)

7. Bates D. and Damgaard A. Phil. Trans. Roy. Soc. London 242A, 101 (1949)

8. Fischer C. and Saxena K.M.S. Comput. Phys. Communicat., 9, 381 (1975)

9. "Atoms and Molecules" by M. Weissbluth (Academic Press 1978)

10. "Introduction to Atomic Physics" by H.A. Enge, M.R. Wehr and J.A. Richards (Addison-Wesley 1972)

Appendix AV

Second Order Magnetic Field Effects

This appendix will be devoted to a brief discussion of second order magnetic field effects. The second order Zeeman and diamagnetic effects are discussed and the fact that these two effects never occur simultaneously is demonstrated . Following this, some basic features of the alkali and the alkaline earth spectra with principal quantum numbers between 6 and 40 will be presented [1,2] and a brief qualitative [2] and quantitative [3] discussion of these effects will be given. Finally, the work on these aspects performed by King [4] will be outlined briefly as well as some of the results of his calculations.

Extending (to higher orders) the formula which gives the energies of the 2j+1 components of a line after the application of a magnetic field, we get [5]:

$$\Delta E_m = \hbar\beta m g \underline{B} + \frac{\hbar^2\beta^2 \underline{B}^2}{-\zeta \pm 2(j+1)\zeta} f(j,m) + \ldots \qquad \text{(AV 1)}$$

where

$$f(j,m) = \sqrt{\frac{(J+L+S+2)(-J+S+L)(J+S-L+1)(J+L-S+1)(J+M+1)(J-M+1)}{4(J+1)^2(2J+1)(2J+3)}}$$

and where $\beta = e/2\mu c$ is the Bohr magneton. To first order approximation for low P's, J precesses about itself much faster than J about P. For higher P's equation AV1 is a good approximation. This second order term in P^2 can also be seen as due to a component of $\underline{\mu}$ perpendicular to $\underline{J}$ and is important

when the spin-orbit and magnetic interactions are of comparable size. This case produces the Zeeman pattern asymmetries (partial Paschen -Back effect).

A second type of a spectral line shift in the vicinity of a B-field arises from the intrinsic universal atomic diamagnetism which all atoms possess. Garton and Tomkins [1] and Van Vleck [5] have calculated this shift (by considering an electron of an atomic core of charge Z to move with velocity v at a distance r from the nucleus and influenced by the magnetic field B) and found that:

$$\Delta E = \frac{e^2 B^2 r_B^2}{8 m c^2} \qquad \text{(AV 2)}$$

where r_B is the projection of r perpendicular to B. But a more thorough quantum mechanical approach by Van Vleck [5] has shown the shift to be:

$$\Delta\nu_Q = \frac{e^2 B^2}{8mh c^3} a_o (n^*)^4 (1+m_1)^2 \qquad \text{(AV 3)}$$

where a_o is the Bohr radius and n* is the effective quantum number.

When the principal quantum number is large, then the spin-orbit coupling coupling is very weak (the spins of the core and the atomic electrons are almost uncoupled). Therefore the diamagnetic term (equation AV2) must be added to the Pachen-Back formula ($\Delta E_m = h\beta P \sum_i m_{1i} + 2m_{si}$) rather than to the one that corresponds to lower magnetic fields (ie equation AV1). This means that the two types of quadratic shifs are never simultaneously of great importance. The second order term of equation AV1 is proportional to $1/\zeta$ (and the spin-orbit

coupling constant ζ is proportional to n^{-3}). Therefore we could say that the diamagnetic term varies as n^4B^2 whereas the Lande term as n^3B^2. At low values of n (where the LS coupling is still valid) the two quadratic effects are comparable and none of them should be neglected. As n* increases, the Lande factor increases as $(n^*)^3$ and at some point where the LS coupling breaks down it becomes negligible whereas the diamagnetic term increases constantly as $(n^*)^4$ since it does not depend at all on the coupling conditions [4].

King [4] has measured quadratic effects for SrI and BaI. For Ba he shows that for low n-members the two shifs are comparable whereas for n in the region ($16< n <21$) the diamagnetic shifts dominate (since Lande shift/diamagnetic = $1/n^*$). A small discrepancy of the measured shifs with calculated ones (the latter lying above the former) was explained [4] by the fact that the matrix elements $\langle nl'm' \; /\overline{r^2}/ nlm \; \rangle$ were overestimated since hydrogenic wavefunctions were used instead of more realistic ones taking into account the core and screening effects. For the higher members n> 27 the LS coupling breaks down and therefore the only shifs present are the diamagnetic ones. However for these members King noticed that the observed shifts lied above the calculated diamagnetic ones. At even higher n's the observed points go back to being below the calculated ones. The theory that would explain these higher n trends has not yet been developed. The results that King [4] gives for Sr are similar to those of Ba, show good linearity with B^2 and $(n^*)^4$ and the observed plots are lying below the calculated pure diamagnetic ones. For n< 27 in Sr, the quadratic shifts that King [4] gives are by an order of magnitude smaller

than the inter-n separation. Therefore at arround n=27 (at which point our calculations stop) we can be sure that the quadratic diamagnetic effect plays no significant role in the spectrum.

Next in the discussion of this section, comes the problem of mixing of configurations in atomic spectra. Experiments were carried out in the 1930's by Jenkins and Segre [2] using a magnetic field of 2.7 Tesla and observing the n=10 to n=35 lines of Sodium and Potassium. At the same time Schiff and Snyder [3] presented some very enlightening theoretical explanations.

In these two papers, the whole spectral region they dealt with was devided into smaller ones depending on the features they exhibited.

(a) For n<6 the ^2P separation was larger than the magnetic splitting.

(b) For n<12 the magnetic splitting begins to increase at the expence of the ^2P separation. Further spin and orbital angular momenta become uncoupled as n increased and finally the Paschen-Back regime was approached.

(c) For 12<n<20 the components were displaced towards the shorter wavelengths by $(n^*)^4B^2$ (as was dictated by the diamagnetic shift discussed previously in this chapter). The shift of the centre of the two σ -components was twice as much as that of the π -component.

(d) Above n=20 the experimental results start not to agree very well with the pure diamagnetic $(n^*)^4$ theory. In fact the shift goes as $(n^*)^{11}$ as Schiff and Snyder [3] predict, towards the same direction (shorter wavelengths). Jenkins and Segre [2]

observed a broadening of the lines in this region ($20<n<28$) as well. They found that the long wavelength component of the σ - components was stronger, by being enhanced by the wing of an adjacent line. The observed shift differed from the expected value considerably and this difference could not be attributed to measurement errors. This was explained as follows:

The pure diamagnetic theory assumes that a certain P level is isolated from states with different L's. However a magnetic perturbation causes two states with different L's to mix and produce what is called configuration mixing effects. Parity restrictions allow only mixing between states of L=0,+2,... and since only the L=1 of the p-states of an s-p configuration can radiate where will only be mixing between the P,F,H....states. When the magnetic energy starts being smaller compared to the P-F separation then two things happen:(i) To a first approximation the eigenfunctions of the P states mix with those of the F states. This P and F repulsion causes a displacement of the P level towards the shorter wavelengths.(ii) To a higher approximation the eigenfunctions of the P states mix with those of H,K,... states and this causes S--→ F, S--→ H etc transitions (on the longer wavelength side of the line) which under normal circumstances would be forbidden. The proof of the existence of such forbidden transitions in the spectra is the line broadening (since the poor resolution of the instrument that Jenkins and Segre [2] used showed only one broadened line).

(e) For $n>30$ the magnetic energy becomes comparable to the n-separation energy and thus terms with different n, as well as different l, begin to mix. Now the broadening is symmetric (and the intensity of these lines decreases constantly) until the

lines are no longer distinguishable at arround n=40.

At this point it would be useful to state some of the theoretical explanations of the above facts treated very well in the paper of Schiff and Snyder [3]. The diamagnetic term in the Hamiltonian stops n and l being exact quantum numbers for the terms in question. The real eigenfunctions radiate only due to the l=1 contribution. In order to obtain the eigenvalues of the terms we are interested in, a diamagnetic matrix was formed with non-zero elements only between states with L=0,+2... The matrix elements were given by [5]:

$$\langle nl'm/r^2\sin^2\theta\ /nlm\rangle = \langle /\bar{r}^{-2}/\rangle \left(\frac{2(l^2-l-1+m_l^{\ 2})}{(2l-1)\ (2l-3)} \right)$$

Schiff and Snyder [3] used hydrogenic wavefunctions to evaluate the radial functions and assumed that for l=1, n*=n-0.85 while for l=3,5... n*=N. The diagonal and off-diagonal elements (for m=+1) of the diamagnetic matrix were given by the following expressions:

$$V_{ll}(n,\pm l) = \frac{\hbar^4\ H^2}{8m^3\ c^2\ e^2}\ \frac{n^2(\ 5n^2+\ 1\ -3l(l+1))\ l(l+1)}{(2l+3)\ (2l-1)}$$

$$V_{l,l-2}(n,\pm l) = -\frac{\hbar^4\ H^2}{8m^3\ c^2\ e^2}\ \frac{5n^2}{2(2l-1)}$$

$$\cdot\left\{\frac{(n^2-l^2)(n^2-(l-1)^2)(l+1)l(l-1)(l-2)}{(2l\ +1)\ (2l-3)}\right\}^{1/2}$$

At the time when the above work was carried out calculations had to be done analytically. However the breadths of the lines as well as the centres of gravity of the broadened lines were found easily. The matrix was diagonalised by a real, normalised and orthogonal matrix S (where $\sum_{kl} S_{ik} H_{kl} S_{jl} = E_i \delta_{il}$). The position of the centre of gravity of the lines as well as their breadth were given by:

$$\bar{E}(n,\pm 1) = -\frac{m e^4}{2\hbar^2 (n^*)^2} \pm \frac{e\hbar H}{2mc} + \frac{\hbar^4 H^2 (n^*)^4}{4m^3 c^2 e^2}$$

$$\Delta E(n,\pm 1) = \tfrac{1}{2}\sqrt{2/7}\ \frac{\hbar^4 H^2 (n^*)^4}{4m^3 c^2 e^2}$$

Second order perturbation calculations gave the eigenvalue of the peak E_p of each line as higher order of $(n^*)^4$ as mentioned earlier in this section:

$$E_p(n,\pm 1) = \bar{E}(n,\pm 1) + \frac{h^{10} H^4 (n^*)^{11}}{224\, m^7 c^4 e^8 D}$$

However, since for $28<n<35$ for the case of K or Na mentioned by Jenkins and Segre [2], the line broadening becomes symmetric, E_p and E begin to have an identical meaning. For $n> 35$ the above approximations become invalid.

King [4] used a large computer for his calculations, set up the matrix and solved for the eigenvalues and the intensities of the lines in question. He also noted that for $n< 15$ the lifting of the degeneracy was more pronounced as the electrons were closer to the core. Therefore a hydrogenic wavefuncion was

not the best choice for this region. On the other hand n should not be so high that n-mixing would prevail. So there is a certain n region for which the previous treatment should not be applied. King [4] also obtained some experimental spectra on Sr and Ba. He found that his Sr spectra (with 12<n<25) did not exhibit any inter-l mixing even at very high fields which is a reasuring point for our f-value calculations with the MQV method, since we suspected l-mixing above n=25, but ignored it up to that n value. For the lower members of Ba, King [4] found that arround n=19 some very faint l-mixing lines were present. However they were so faint that actually only the first and second inter-l lines could be observed. The experimental predictions of the positions of these lines were very slightly higher than the observed ones. For the higher members of Ba, similar behaviour was observed. He also found that experimental results lied much closer to the ones calculated from the l-mixing matrix rather than the pure diamagnetic theoretical ones. Of cource results from l-mixing calculations match with the experimental data only in the region where n-mixing is insignificant. King [4] also found that as n increases, the l-spacings become smaller and so n-mixing dominates as one would expect.

Finally, in an important paper Garton and Tomkins [1] present spectra for Ba up to quite high n-values (n=75) and have actually experimentally observed what Jenkins and Segre [2] predicted. A significant advance in this last paper [1] was the considerable improvement of the experimental set-up which enabled them to get very accurate spectra which showed explicitly the l-mixing effect.

Garton and Tomkins [1] and also King [4] found that on their Barium plates there was a number of equally spaced lines beyond the field-free ionisation limit. Subsequenlty, King [4] also found that after the l- and n- mixing spectral regions (ie after n=40 for Ba) there were regularly spaced lines by $1/2\hbar w$ (where $w=eB/mc$). He noted that there was a region where there were a few broad lines separated by hw and afterwards there were lines separated by $1/2\hbar w$ again. He explained this $1/2\hbar w$ separation "as due to the separation of the M=+1 and M=-1 spectral lines with a relative shift of hw". Finally he also observed spectral lines separated by $3/2\hbar w$ below and above the field-free ionisation limit. These spacings of the lines were called "quasi-Landau levels" [4] because they reminded us of the hw line separations that Landau attributed to a free electron gas in a magnetic field.

In the presence of an externally applied magnetic field and under the influence of its nucleus (although far away form it) an electron obeys the following equations of motion [4]:

$$m_{reduc}\ddot{x} = -\frac{e^2}{r^3}x + \frac{e}{c}B_z y \qquad m_{reduc}\ddot{y} = -\frac{e^2}{r^3}y + \frac{e}{c}B_z x$$

$$m_{reduc}\ddot{z} = -\frac{e^2}{r^3}z$$

When the electron moves along the z-direction and the Coulomb potential dominates over the other potentials, then it will have a frequency ($\alpha\eta^3$) which will be much smaller than w and then the adiabatic approximation will hold [4 and references

therein].Edmonds [6] developed a semi-classical model to study these line separations (3/2hw) near the field-free series limit of Barium. Very near the origin (which is the region of importance for radiative transitions) at $z \cong 0$, the above equations of motion become invalid and the adiabatic approximation failed. By applying the Bohr-Sommerfield condition and assuming that $z \cong 0$ (therefore the electron was almost entirely in the x-y plane) the equation of motion was given by [6]:

$$\sqrt{2} \int_{\rho_0}^{\rho} \{ E + \frac{e^2}{(\rho + z^2)^{\frac{1}{2}}} - \frac{1}{2\rho^2}(m_1 + \frac{m_{reduc}\ \omega}{2\hbar} \rho^2)\}^{\frac{1}{2}} d\rho = \pi\hbar(N + \frac{1}{2})$$

After the integration was performed, the correct values of E were chosen so that N would be an integer [6]. For $z \cong 0$ and $E \cong 0$ the spacing of the lines was found to be almost $3/2\hbar w$ (not exactly because of the effect of the electrostatic potential).

Now, we will try to find an explanation for what happens above the series limit. The total energy of an atomic electron in a magnetic field is given by [4]:

$$E = E' + \frac{\omega L_z}{2} = \frac{m_{reduc}\ \rho^2\ \omega^2}{8} + \frac{p^2}{2\ m_{reduc}} - \frac{e^2}{(\rho^2 + z^2)^{\frac{1}{2}}} + \frac{\omega L_z}{2}$$

For $p^2/2m_{reduc}=0$ we have that $E'=m_{reduc}\ \omega^2\ \rho^2/8-(e^2/(\rho^2+z^2)^{1/2})$. .For $E'<0$ the Coulomb attraction dominates the magnetic interaction and in particular if $E'<<0$ then the electron will follow the Bohr orbit while if the electron is less strongly bound to the nucleus it will perform an elliptical one. For $E'>0$

the electron trajectory will follow the asymptotic $\rho = \rho^*$ line as $z \rightarrow \infty$ (where $\rho^* = (8E'/m_{reduc}\ \omega^2)^{1/2}$. If $E' > 0$ and $(p^2/2m_{reduc}) - (e^2/(\rho^2 + z^2))^{1/2} < 0$ then the electron will be conditionally bound and its energy will be quantised [4], ie:

$$\frac{m_{reduc}\ \rho^2\ \omega^2}{8} = E_M(N) = \hbar\omega(N + \frac{1}{2})$$

If the electron's electrostatic energy increases until $E' > m_{reduc}\ \omega^2\ \rho^2/8$ then it will be unbound and its energy will be unquantised.

The above arguments [11, 9] attempt to explain very briefly and semi-classically the band periodic structure in the region of the field-free series limit in terms of bound states of the electronic motion (if certain requirements are met, ie $E' < m_{reduc}\ \omega^2\ \rho^2/8$). Below the field-free series limit, the states are always bound and therefore the same arguments apply straight away.

References for Appendix AV

1. Garton W.R.S. and Tomkins F.S. Astrophys. J., 158, 839 (1969)

2. Jenkins F.A. and Segre E. Phys. Rev., 55, 52 (1939)

3. Schiff L.I. and Snyder H. Phys. Rev., 55, 59 (1939)

4. King P.W. PhD Thesis (University of London 1972)

5. "The Theory of Electric and Magnetic Susceptibilities by J.H. Van Vleck (Oxford 1932)

6. Edmonds A.R. Tour de Physique, 31 C4-71 (1970)

Appendix AVII

The s-p Hamiltonian Matrix and the Pachen-Back Effect.

In this appendix the total Hamiltonian matrix for an s-p configuration will be derived. After the appropriate transformations it is possible to derive the eigenvalues and the coefficients of the eigenvectors of the states involved. This will erable us to verify quantitatively that it is often the case that a ^3P level is admixed with a $^1P_1$ level, in which case the resulting M-O pattern could be calculated with the overlapping lines technique described in section 1 of Chapter V.

Suppose now that we have a state:

$$\Psi = \sum_{n=1}^{N} a_n u_n \qquad \text{(AVII1)}$$

where the functions u_n can be any orthonormal set and where the coefficients a_n are the unknowns. Inserting the above equation in Schrodinger's equation we get:

$$\sum_{n=1}^{N} a_n H u_n = E \sum_{n=1}^{N} a_n u_n \qquad \text{(AVII2)}$$

Multiplying equation AVII2 by u^*_k we get:

$$\sum_{n=1}^{N} a_n H_{kn} = E a_k \qquad \text{(AVII3)}$$

where the matrix element is defined as:

$$H_{kn} = \langle u_k \,/H/\, u_n \rangle \qquad \text{(AVII4)}$$

Equation AVII3 can be rewritten as:

$$\begin{aligned} a_1(H_{11}-E) + a_2H_{12} + \quad &\ldots + a_NH_{1N} = 0 \\ \vdots \qquad\qquad\quad &\vdots \qquad\qquad \vdots \\ a_1H_{1N} + a_2H_{N2} + \quad &\ldots + a_N(H_{NN}-E) = 0 \end{aligned}$$

Such a set of homogeneous equations can only be solved if:

$$\begin{vmatrix} (H_{11}-E) & H_{12} & \ldots & H_{1N} \\ H_{21} & (H_{22}-E) & \ldots & H_{2N} \\ \vdots & & \vdots & \vdots \\ H_{N1} & H_{N2} & & (H_{NN}-E) \end{vmatrix} = 0$$

The above matrix (known as the secular equation) can be diagonalised by applying the appropriate transformation. Then since $H^*_{kn}=0$ unless $n=k$, the functions $u_{n=k}$ become eigenfunctions to the Hamiltonian H and H_{kk} are the actual eigenvalues.

The total interaction Hamiltonian matrix H [1] can be considered to consist of three basic contributions: the electrostatic, the spin-orbit and the external magnetic field

interactions. It is also convenient to show at this stage (table AVII1) all the allowed basis states for an s-p configuration (table 3.b of [1]), although ideally we should use infinite complete sets of functions.

(i) The electostatic contribution to H

The electrostatic contribution to the Hamiltonian is equal to:

$$H = \sum_i f_i - \sum_{i,j} g_{ij}$$

where the one electron operator is equal to:

$$f_i = (-\nabla_i^2 - \frac{2Ze^2}{r_i})$$

and where the two electron operator is equal to:

$$g_{ij} = \frac{2e^2}{r_{ij}}$$

At this stage spin-orbit and magnetic interactions are ignored (the z-components of the orbital and spin angular momenta, M_L and M_S respectively, are quantised and constant). Therefore the Hamiltonian has no matrix elements between two states which do not have the same values of M_L and M_S [1].

1. The diagonal matrix elements for the one-electron operators f_i are [2]:

$$I(nl) = \langle k/f_i/k \rangle = \int_0^\infty (r^{2l+2} \frac{d}{dr}(\frac{R_{nl}^*}{r^l}) \frac{d}{dr}(\frac{R_{nl}}{r^l}) 2ZrR_{nl}^* R_{nl}) dr \qquad \text{(AVII5)}$$

Zero Ord. Function	$m_l(1)$	$m_l(2)$	$m_s(1)$	$m_s(2)$	M_L	M_S	M_J
U_1	0	1	$\frac{1}{2}$	$\frac{1}{2}$	1	1	2
U_2	0	1	$\frac{1}{2}$	$-\frac{1}{2}$	1	0	1
U_3	0	1	$-\frac{1}{2}$	$\frac{1}{2}$	1	0	1
U_4	0	1	$-\frac{1}{2}$	$\frac{1}{2}$	1	0	1
U_5	0	0	$\frac{1}{2}$	$\frac{1}{2}$	0	1	1
U_6	0	0	$\frac{1}{2}$	$-\frac{1}{2}$	0	0	0
U_7	0	0	$-\frac{1}{2}$	$\frac{1}{2}$	0	0	0
U_8	0	0	$-\frac{1}{2}$	$-\frac{1}{2}$	0	-1	-1
U_9	0	-1	$\frac{1}{2}$	$+\frac{1}{2}$	-1	1	0
U_{10}	0	-1	$\frac{1}{2}$	$-\frac{1}{2}$	-1	0	-1
U_{11}	0	-1	$-\frac{1}{2}$	$\frac{1}{2}$	-1	0	-1
U_{12}	0	-1	$-\frac{1}{2}$	$-\frac{1}{2}$	-1	-1	-2

Table AVII1 The basis set for an s-p configuration.

2. The diagonal matrix elements for the two electron operators g_{ij} are given by the following two expressions for the Coulomb and Exchange parts [2]:

$$\langle ij\ /g/\ ij\rangle = \sum_{k=0}^{\infty} a^k(l_i m_{l_i}; l_j m_{l_j})\ F^k(n_i l_i; n_j l_j)$$

(AVII6)

for the Coulomb integral where i and j represent two states, u_i and u_j respectively and where:

$$a^k(l_i m_{l_i}; l_j m_{l_j}) = c^k(l_i m_{l_i}; l_i m_{l_i})\ c^k(l_j m_{l_j}; l_j m_{l_j})$$

(AVII7)

and

$$F^k(n_i l_i; n_j l_j) = R^k(ij;ij) =$$

(AVII8)

$$= \iint R^*_{n_i l_i}(r_1) R^*_{n_j l_j}(r_2) R_{n_i l_i}(r_1) R_{n_j l_j}(r_2)\ \frac{2r(a)^k\ r_1^2 r_2^2}{r(b)^{k+1}}\ dr_1\ dr_2$$

and for the Exchange integral we write:

$$\langle ij\ /g_{ij}/\ ji\rangle = \delta(m_{s_i}, m_{s_j}) \sum_{k=0}^{\infty} b^k(l_i m_{l_i}; l_j m_{l_j})\ G^k(n_i l_i; n_j l_j)$$

(AVII9)

where

$$b^k(l_i m_{l_i}; l_j m_{l_j}) = (c^2(l_i m_{l_i}; l_j m_{l_j}))^2 \qquad \text{(AVIII10)}$$

and
$$G^k(n_i l_i; n_j l_j) = R^k(ij;ji) \qquad \text{(AVIII11)}$$

$$= \iint F^*_{n_i l_i}(r_1)\, R^*_{n_j l_j}(r_2)\, F_{n_j l_j}(r_1)\, R_{n_i l_i}(r_2)\, \frac{2r(a)^k}{r(b)^{k+1}}\, r_1^2\, r_2^2\, dr_1 dr_2$$

If the M_L, M_S criterion is satisfied (ie for non-zero off diagonal elements must have $\Delta M_L = 0$ and $\Delta M_S = 0$) then there will exist such elements and it is therefore useful to state the general expression for the <ij/g/rt> integral:

$$\langle ij\ /g/\ rt \rangle = \sum_{k=0}^{\infty} \sum_{m=-k}^{\infty} \frac{(k-/m/)}{(k+/m/)}\, \delta(m_{s_i}, m_{s_r})\, \delta(m_{s_j}, m_{s_t})$$

$$* (-1)^{(m_{l_i} + /m_{l_i}/ + m_{l_j} + /m_{l_j}/ + m_{l_r} + /m_{l_r}/ + m_{l_t} + /m_{l_t}/)^2}$$

$$* \sqrt{\frac{(2l_i+1)\ (l_i - /m_{l_i}/)}{(l_i + /m_{l_i}/)}}\ \sqrt{\frac{(2l_j+1)\ (l_j - /m_{l_j}/)}{(l_j + /m_{l_j}/)}}$$

$$* \sqrt{\frac{(2l_r+1)\ (l_r - /m_{l_r}/)}{(l_r + /m_{l_r}/)}}\ \sqrt{\frac{(2l_t+1)\ (l_t - /m_{l_t}/)}{(l_t + /m_{l_t}/)}} \qquad \text{(AVIII12)}$$

$$* \int_0^\infty \int_0^\infty R^*_{n_i l_i}(r_1) R^*_{n_j l_j}(r_2) R_{n_r l_r}(r_1) R_{n_t l_t}(r_2)\, \frac{2r(a)^k}{r(b)^{k+1}}\, r_1^2\, r_2^2\, dr_1\, dr_2$$

$$* \int_0^\pi P_{l_i}^{/m_{l_i}/}(\cos\theta_1)\, P_{l_r}^{/m_{l_r}/}(\cos\theta_1)\, P_k^{/m/}(\cos\theta_1)\, \sin\theta_1\, d\theta_1 /2\pi$$

$$* \int_0^\pi P_{l_j}^{/m_{l_j}/}(\cos\theta_2)\, P_{l_t}^{/m_{l_t}/}(\cos\theta_2)\, P_k^{/m/}(\cos\theta_2)\, \sin\theta_2\, d\theta_2 /2\pi$$

$$* \int_0^{2\pi} \exp(i(-m_{l_i} + m_{l_r} + m)\phi_1)\, d\phi_1 /2 \int_0^{2\pi} \exp(i(-m_{l_j} + m_{l_t} - m)\phi_2)\, d\phi_2 /2\pi$$

Using the basis functions of table AVII1 it is obvious that the resulting matrix will possess non-zero diagonal elements where $\Delta M_L=0$ and $\Delta M_S=0$, ie for states u_2 and u_3, u_6 and u_7 and u_{10} and u_{11}.

Equation AVII5 gives us that all diagonal elements contain a term equal to I(ns)+I(np) since the Hamiltonian involves Σf_i. which is a summation over an (ns) and an (sp) electron of our (sp) configuration. Equation AVII6 gives us an F^0(ns,np) term for all the diagonal elements. Equation AVII9 involves the term $\delta(m_{si},m_{sj})$ which is zero for some functions, ie the elements H_{22}, H_{33}, H_{66}, H_{77}, H_{1010} and H_{1111} have $m_{si}=-m_{sj}$ and therefore do not have a non-zero exchange integral. Finally equation AVII12 can be used to evaluate the direct ($\langle ij/g/rt\rangle$) or exchange ($\langle ij/g/tr\rangle$) integrals for the states which possess non-zero off-diagonal elements. Since the formlula contains temrs like $\delta(m_{si},m_{st})$and $\delta(m_{sj},m_{sr})$ for the direct case and $\delta(m_{si}, m_{sr})$ and $\delta(m_{sj},m_{st})$ for the exchange case, then considering the basis functions it is obvious that $H_{23}=H_{32}=H_{67}=H_{76}=H_{1011}=H_{1110}$ = C. The values of the coefficients a^k and c^k can be found in tables and for this s-p configuration case we have that:

$\langle k/f_i/k\rangle = I^0(ns) + I^0(np)$ always

$\langle ij/g/ij\rangle = F^0(ns,np)$ always

$\langle ij/g/ji\rangle = -G_1/3$

or $= 0$ if $m_{s_1} \neq m_{s_j}$

$\langle ij/g/rt\rangle = 0$ (for $i\neq r$ and $j\neq t$) always since

always since we must satisfy the requirement that $\Delta M_S=0$ which would mean that according to Pauli's principle we could not have $m_{si}=m_{sr}$ and $m_{sj}=m_{st}$ therefore $m_{si}=-m_{sr}$ and $m_{sj}=-m_{st}$ so $\delta(m_{si},m_{sr})=\delta(m_{sj},m_{st})=0$ and finally, $\langle ij/g/tr\rangle = -G_1/3$ for the reverse reasoning given above.

The matrix of the electrostatic interaction of the basis set given in table AVII1 is shown in table AVII2 [1]. From the above it can be seen that all the diagonal elements without any corresponding off- diagonals are triplet states with $M_S=+-1$. The energy of a triplet state is given by:

$$E(^3P) = I(ns) + I(np) + F^0(ns,np) - G_1/3$$

for the case where $M_S=0$ and $M_L=0,+-1$ we must solve the following:

$$\begin{vmatrix} I(ns)+I(np)+F^0(ns,np) & -G_1/3 \\ -G_1/3 & I(ns)+I(np)+F^0(ns,np) \end{vmatrix} = 0$$

Therefore the energy of the singlet is:

$$E(^1P) = I(ns) + I(np) + F^0(ns,np) + G_1/3$$

since the $-G_1/3$ term corresponded to the triplet case.

(ii) The magnetic contribution to H

	U_1	U_2	U_3	U_4	U_5	U_6	U_7	U_8	U_9	U_{10}	U_{11}	U_{12}
U_1	$E_o - \frac{G_1}{3}$;											
U_2		E_o;	$-\frac{G_1}{3}$;									
U_3		$-\frac{G_1}{3}$;	E_o;									
U_4				$E_o - \frac{G_1}{3}$;								
U_5					$E_o - \frac{G_1}{3}$;							
U_6						E_o;	$-\frac{G_1}{3}$					
U_7						$-\frac{G_1}{3}$;	E_o;					
U_8								$E_o - \frac{G_1}{3}$;				
U_9									$E_o - \frac{G_1}{3}$;			
U_{10}										E_o;	$-\frac{G_1}{3}$	
U_{11}										$-\frac{G_1}{3}$;	E_o;	
U_{12}												$E_o - \frac{G_1}{3}$;

Table AVII2 The electrostatic interaction matrix with respect to the functions of Table AVII1.

The Hamiltonian for an external magnetic interaction is given by:

$$\alpha^2(\underline{L} + 2\underline{S}) \cdot \underline{B}\, u_{nlm} = \alpha^2(M_L + 2M_S)\ B\, u_{nlm}$$

(AVII13)

where α = fine structure constant. Using the values of M_L and M_S of the basis states (table AVII1) we obtain table AVII3 [1] which contains only diagonal elements.

(iii) The spin-orbit contribution to H

Some fundamental relations of the individual angular momenta of an unfilled shell will now be given [2]:

$$l_x u_{nl,m_l} = \tfrac{1}{2}\sqrt{(l-m_l)(l+m_l+1)}\ u_{nl,m_l+1}$$

$$l_y u_{nl,m_l} = -1/i\ \tfrac{1}{2}\sqrt{(l-m_l)(l+m_l+1)}\ u_{nl,m_l+1}$$

$$l_z u_{nl,m_l} = m_l u_{nl,m_l}$$

(AVII14)

and similarly for the spin angular momenta:

$$s_x u_{nl,\underline{m_l}\atop m_s} = \tfrac{1}{2}\sqrt{(\tfrac{1}{2}-m_s)(\tfrac{1}{2}+m_s+1)}\ u_{nlm_l,m_s+1}$$

$$s_y u_{nl,\underline{m_l}\atop m_s} = -1/i\ \tfrac{1}{2}\sqrt{(\tfrac{1}{2}-m_s)(\tfrac{1}{2}+m_s+1)}\ u_{nlm_l,m_s+1}$$

$$s_z u_{nlm_l,m_s} = m_s u_{nlm_l,m_s}$$

(AVII15)

	U_1	U_2	U_3	U_5	U_4	U_6	U_7	U_9	U_8	U_{10}	U_{11}	U_{12}
		M=+2										
U_1	$3\alpha^2B$;	M = +1										
U_2		α^2B;										
U_3			α^2B;									
U_5				$2\alpha^2B$;	M = 0							
U_4					$-\alpha^2B$;							
U_6						0;						
U_7							0;					
U_9								α^2B	M = -1			
U_8									$-2\alpha^2B$			
U_{10}										$-\alpha^2B$		
U_{11}											$-\alpha^2B$	M = -2
U_{12}												$-3\alpha^2B$

Table AVII2 The magnetic interaction matrix with respect to the functions of Table AVII1.

For the two electrons (s-p) the total spin-orbit contribution to the Hamiltonian is [1]:

$$\zeta(\underline{l}_1\cdot\underline{s}_1+\underline{l}_2\cdot\underline{s}_2) =$$

$$\zeta(l_x s_x+l_y s_y+l_z s_z)^{(1)}+\zeta(l_x s_x+l_y s_y\} l_z s_z)^{(2)}$$

Since l_x, l_y, s_x and s_y involve changes in m_l and m_s ($m_l'=m_l+-1$, $m_s'=m_s+-1$) then the diagonal elements will involve only the $l_z s_z$ terms, ie:

$$\langle u_k^*/(l_z s_z)^{(1)}_{+}(l_z s_z)^{(2)}/u_k\rangle$$

For the s-electron $m_l^{(1)}=0$ and for states u_5, u_6, u_7 and u_8 $m_l^{(2)}=0$, therefore these states will have a zero diagonal element. The remaining ones will have a $+-\zeta/2$ depending on the sign of the product $m_l^{(2)} m_s^{(2)}$.

The off-diagonal elements will not contain the l_z and s_z operators (equations VII14c and 15c). The empirical magnetic selection rule must also be satisfied ie that $M_J=M_L+M_S$ is never crossed. Therefore there are non-zero off-diagonal elements if:

$M=M'$ and $m_l'^{(1)}= m_l^{(1)}\pm 1$ ____ $m_s'^{(1)}= m_s^{(1)}\pm 1$

$m_l'^{(2)}= m_l^{(2)}\pm 1$ ____ $m_s'^{(2)}= m_s^{(2)}\pm 1$

	U_1	U_2	U_3	U_5	U_4	U_6	U_7	U_9	U_8	U_{10}	U_{11}	U_{12}
	M=+											
U_1	$\frac{\zeta}{2}$;	M = + 1										
U_2		$-\frac{\zeta}{2}$;		$\frac{\zeta}{2}$;								
U_3			$\frac{\zeta}{2}$;									
U_5		$\frac{\zeta}{2}$;		0;		M = 0						
U_4					$-\frac{\zeta}{2}$;		$\frac{\zeta}{2}$;					
U_6						0;		$\frac{\zeta}{2}$;				
U_7					$\frac{\zeta}{2}$;		0;					
U_9						$\frac{\zeta}{2}$;		$-\frac{\zeta}{2}$;		M = -1		
U_8									0;		$-\frac{\zeta}{2}$	
U_{10}										$\frac{\zeta}{2}$		
U_{11}									$\frac{\zeta}{2}$;		$-\frac{\zeta}{2}$	M 1.2
U_{12}												$\frac{\zeta}{2}$

Table AVII4 The spin-orbit interaction matrix with respect to the functions of Table AVII1.

		U_2	U_3	U_5
M=+1	U_2	$E_o-\frac{\zeta}{2}+\alpha^2B$	$-G_1/3$	$-\zeta/2$
	U_3	$-G_1/3$	$E_o+\zeta/2+\alpha^2B$	0
	U_5	$-\zeta/2$	0	$E_o-G_1/3-2\alpha^2B$

		U_8	U_{10}	U_{11}
M=-1	U_8	$E_o-G_1/3-2\alpha^2B$	0	$\zeta/2$
	U_{10}	0	$E_o-\zeta/2-\alpha^2B$	$-G_1/3$
	U_{11}	$\zeta/2$	$-G_1/3$	$E_o-\zeta/2-\alpha^2B$

Table AVII5 The sub-matrices of the total interaction matrix with respect to the functions of Table AVII1 for M=+-1.

Considering all the above facts and interchanging states u_4 and u_8 with u_5 and u_9 for convenience) we obtain table AVII4 [1]. The total Hamiltonian is given by:

$$H_{tot}= \sum_i (-\nabla_i^2-2Ze^2/r_i)+\sum_{ij} 2e^2/r_{ij}+\sum_i \zeta\ l_i.s_i+\ \alpha^2(L+2S).B$$

and each element (x,y) of the total matrix is just the summation of each (x,y) element of the electrostatic, spin-orbit and magnetic interaction matrices respectively. This total Hamiltonian is given in table AVII5 [1]. When all the elements of the above matrix and the interactions between them are considered, the solution to this matrix will give us all the eigenvalues of the basis states involved The calculations however are cumbersome and a computer is necessary.

If the spin-orbit and the magnetic interactions are small compared to the electrostatic interactions then the matrix is mainly diagonal and J and M_J are good quantum numbers. However, an (s-p) configuration involves ^1P and ^3P states and so the initial scheme is inappropriate [1] and the matrix must be transposed into a (M_L,M_S) scheme. At this point it is useful to state all the possible combinations of an (s-p) configuration [2]:

$^3P^o$:	M_L= 1,	M_S=1:	(0+1+)
		M_S=0:	(2)-½ (0+1) + (0-1+)
		M_S=-1:	(0-1-)
	M_L=0,	M_S=1:	(0+0+)
		M_S=0:	(2)-½ (0+0-) + (0-0+)
		M_S=-1:	(0-0-)
	M_L= -1,	M_S=1:	(0+-1+)
		M_S=0:	(2)-½ (0+-1) + (0-1+)
		M_S=-1:	(0- -1-)

and

$^1P^o$: $M_L=1$, $M_S=0$: $(2)^{-\frac{1}{2}}$ (0+1-) - (0-1+)

$M_L=0$, $M_S=0$: $(2)^{-\frac{1}{2}}$ (0+0-) - (0-0+)

$M_L=-1$, $M_S=0$: $(2)^{-\frac{1}{2}}$ (0+ -1-) - (0- - 1+)

The ^3P and ^1P functions that we are interested in are the ones with $M=M_L+M_S = +-1$ since we only have matrix blocks for $M=+-1$ which we require to be transposed. They are the following states [1]:

$M=+1$ $\quad {}^3P_{1,0}=(u_2+u_3)/\sqrt{2}$

$\quad {}^3P_{0,1}=u_5$

$\quad {}^1P_{1,0}=(u_2-u_3)/\sqrt{2}$

and $M=-1$ $\quad {}^3P_{-1,0}=(u_{10}+u_{11})/\sqrt{2}$

$\quad {}^3P_{0,-1}= u_8$

$\quad {}^1P_{-1,0}=(u_{10}-u_{11})/\sqrt{2}$

Table AVII6 The s-p eigenfunctions in (M_L,M_S) representation for $M=+-1$.

In order to diagonalise the total Hamiltonian matrix, it must be trasposed into a (J,M_J) scheme and $u_{J,M}$ can be written

as a linear combination of the old $u_{ML,MS}$ functions, ie

$$u_{J,M} = \sum_{M_L M_S} C_{\substack{(M_L,M_S)\\(J,M_J)}} u_{M_L,M_S}$$

where the Clebsh-Gordon coefficients $C_{(ML,MS)(J,MJ)}$ are non-zero and given in tables [2] if the (J,M_J) functions satisfy the condition $M=M_L+M_S$. The new (J,M_J) functions are given in table AVII7 [1].

For M = + 1:

$$^3P_2 = (^3P_{1,0}+{}^3P_{0,1}) / \sqrt{2} = (U_2 + U_3)/2 + U_5/\sqrt{2} \quad (a)$$

$$^3P_1 = (^3P_{1,0} - {}^3P_{0,1}) \sqrt{2} = (U_2 + U3)/2 - U_5/\sqrt{2} \quad (b)$$

$$^1P_1 = (^1P_{1},o) = (U_2 - U_3)/\sqrt{2} \quad (c)$$

and for M= -1:

and

$$^3P_2 = (^3P_{0,1}+{}^3P_{-1,0})/\sqrt{2} = U_8/\sqrt{2} + (U_{10} + U_{11})/2 \quad (a)$$

$$^3P_1 = (^3P_{0,-1}-{}^3P_{-1,0})/\sqrt{2} = U_8/\sqrt{2} - (U_{10}+ U_{11})/2 \quad (b)$$

$$^1P_1 = (^1P_{-1,0}) = (U_{10} - U_{11})/\sqrt{2} \quad (c)$$

Table AVII7 The s-p eigenfunctions in the (J,M_J) representation for M=+-1.

The above table would for example give [1]:

$$H\, u(^3P_2) = \tfrac{1}{2}H\, u_2 + \tfrac{1}{2}H\, u_3 + 1/\sqrt{2}H\, u_5$$

But also from table AVII5:

$$H\,u_2 = \tfrac{1}{2}(E+\zeta/2+\alpha^2 B)\,u_2+\tfrac{1}{2}(-G_1/3)\,u_3+\zeta/2\,u_5$$

and similarly for the other (J,M_J) and basis functions. After algebraic manipulations, we obtain the M_J=+-1 sub-matrices in the (J,M_J) representation:

	$^1P_1$	$^3P_2$	$^3P_1$
$^1P_1$	$E_o+G_1\pm\alpha^2\underline{B}$	0	$-\zeta/2$
$^3P_2$	0	$E_o-G_1+\tfrac{1}{2}\zeta\pm\tfrac{3}{2}\alpha^2\underline{B}$:	$-\tfrac{1}{2}\alpha^2 B$
$^3P_1$	$\zeta/2$	$-\tfrac{1}{2}\alpha^2 B$	$E_o-G_1-\tfrac{1}{2}\pm\tfrac{3}{2}\alpha^2\underline{B}$

Table AVII8 The total interaction M_J=+-1 sub-matrices in the (J,M_J) scheme.

The (J,M_J) must be transposed again to become diagonal. Then these diagonal elements will be the eigenvalues per se. King [1] has written and modified two programs respectively -one called "Pasbac" which sets up the (J,M_J) matrix and the other called "Figen" (originally an IBM routine) which diagonalises the matrix- and has therefore calculated the energy levels of SrI, PaI and HgI. Values of the magnetic field, and G_1 must be inserted as data into the codes. He used the code for fields from 3.0T to 1.7 10^5 T thus covering the range from a very weak field to the complete Paschen-Back effect.

References for Appendix AVII

1. King P.W. PhD Thesis (Univerisity of London 1972)

2. "Quantum Theory of Atomic Structure" by J.C.Slater
Vols.I and II (McGrawhill 1963)

Appendix EVII

Qualitative Discussion on the f-Value Dependence on the Externally Applied Magnetic Field

It was mentioned in the introduction of this chapter that an attempt will ba made to study the dependence of the f-values on the B-field. Several authors in various fields of physics have dealt with the problem of studying the B-field dependence of the energy levels but not many have dealt with the B-field dependence of the atomic transition probabilities. Most of the published work on this problem is conserned with fields $\gtrsim 10^4$ which are unatainable experimentally, for instance Brandi et al [1] for $B=10^3 \sim 10^4$T, Santos and Brandi [2] and Simota and Virtamo [3] for $B>10^6$T.

The most complete calculations at medium fields are those of Brandi [4] who has a basis of unpertubed atomic hydrogen and then diagonalises the appropriate Hamiltonian and finds the energy levels of the fourteen lowest lying states for $B \sim 10^3$, 10^4T. He considers the Hamiltonian for a H atom in a uniform magnetic field to be:

$$H_0 = p^2/2\mu \quad -e^2/r + \hbar\, \omega_m L_z + \tfrac{1}{2}\mu\, \omega_L{}^2 r^2 \sin^2\theta$$

where $\omega_L = eB/2\,\mu c$ is the Larmor frequency, the interaction Hamiltonian to be:

$$H_I = e/\,\mu c\; \underline{A}\cdot(\underline{p} + \mu\omega_L \underline{z} \wedge \underline{r})$$

where A is the vector potertial.The eigenvectors are of the

form:

$$\Psi(\underline{r}) = \sum_i c_i \phi_i(r) = \sum_i c_i N_{n_i l_i} F_{n_i l_i}(X)\, Y_{l_i}^{m_i}(\theta,\phi)$$

where

$$X=2r/n, \quad N_{nl}=2/n^2 \left(\frac{(n-l-1)!}{(n+l)!^3}\right)^{\frac{1}{2}} \text{ and } F_{nl}(X)=X^l e^{-X/2} L_{n-l-1}^{X+l}(X)$$

and where $L^{2l+1}_{n-l-1}(X)$ are the Laguerre polynomials.

The atomic transition probability $A_{\nu\nu'}$, , into solid angle $d\Omega$ is:

$$A_{\nu\nu'}\, d\Omega = e^2\hbar/(2\pi\mu^2c^2)\, \omega_{\nu\nu'}\, /\langle\nu'(\nabla + i\,\frac{\mu}{h}\,\omega_L \underline{z}\wedge\underline{r}).e_q^*/\,\nu/\!\!\!\!\!\!\int^2 d\Omega$$

(where $e_{+-1}=-+(x+-iy)\sqrt{2}$, $e_o=z$) was then calculated by these authors who give tables of their results for $B=10^3$-10^4T in their paper [1, 4]. Although we are not interested in the magnetic field range they covered (Figs.1 and 2 of [1]) it is useful to point out that f-values depend on the field in an unpredictable way. That is, unless one solves the matrix and then the A-value formula properly, one cannot anticipate the trend of the graph.

At fields $10^2 \sim 10^5$T [4and 5 and references therein] Praddude found that he could not use spherically symmetric atomic H basis and therefore used cylindrical coordinates and associated Laguerre polynomials. Kara and McDowell [5] used a basis of simple separable functions of cylindrical symmetry which was also chosen so that the photoionisation cross-section

could be easily calculated. Although Kara and McDowell's paper produced similar results for most of the field range to those of Praddude, the former was much simpler to use. According to Kara and McDowell [5], the Hamiltonian in cylindrical coordinates in the presence of a magnetic field and ignoring spin effect is given by:

$$H = - \partial^2/\partial\rho^2 - 1/\rho\ \partial/\partial\rho - 1/\rho^2\ \partial^2/\partial\phi^2 - \partial^2/\partial z^2 + \gamma L_z + \gamma^2\rho^2/4 - 2/r$$

where $r^2 = \rho^2 + z^2$, $\gamma = \mu_B B/Ryd = h\omega_c/Ryd$ and ω_c = cyclotron freq. frequency

They [5] consider the eigenvectors to be of the form:

$$\Psi_j = \sum_{\alpha,\beta,\delta} c^{(j)}_{\alpha\beta\delta}\ \chi_{\alpha\beta\delta}(r)$$

where:

$$\chi_{\alpha\beta\delta}(r) = z^{\alpha}\rho^{\beta}\ e^{-\delta r^2} e^{im\phi}$$

The form of the A-value expression that they use agrees well with the one that Prandi et al [1] used and which was mentioned above, ie

$$A_{pq}\ d\Omega = e^2/2\pi c^3\hbar\ (E_p - E_q)^3 \sum_{\mu=-1}^{1} |\langle p/r_\mu/q\rangle|^2 \sin^2\theta\ d\Omega$$

with

$$r_0 = z \text{ and } r_{\pm 1} = \mp (x \pm iy)/\sqrt{2}$$

The following selection rules had also to be obeyed:

$$\underline{E} \;//\; \underline{B} \qquad \Delta m = 0 \qquad \Delta\pi = +-1$$

$$\underline{E} \;\_/\; \underline{B} \qquad \Delta m = +-1 \qquad \Delta\pi = 0$$

From the above the transition probabilities were calculated. For some transitions (especially for strong ones) the Kara and McDowell [5] results disagree with those of Prandi et al [1] in less than 4% while for others there is more disagreement (up to orders of magnitude) between these two sets of results and also in those of Smith et al [6]. Therefore it can be said that the variation of the A-values with increasing magnetic field depends on two things: (i) the energy difference and (ii) the dipole matrix element and so it is not always a monotonic function.

For a better understanding and interpretation of our MgI results (section 3b of Chapter VI) ideally we would require an extension of Clark and Taylor's theory (see next section) to atoms heavier than hydrogen (Mg) - a presently unresolved problem. Calculation should cover the MgI principal series for n=7 to n=14 and for various fields so that a direct comparison could be made with our experimental spectra. However at present, as we have seen from the other papers mentioned in this section, it is only known that the f-values do not vary monotonically with field strength and therefore we can say that our MCV results are plausible. It will be a very interesting problem to

obtain M-C spectra for the alkaline earths both with increasing and decreasing fields (to eliminate any errors associated with that, then calculate f-values with the MCV method and then compare the behaviour of f-values versus field with the ones that Clark and Taylor's method would predict, assuming that the latter can be more readily extended to alkaline earth spectra (using some form of quantum defect theory) than to the two electron spectra considered here.

References for Appendix PVII

1. Brandi H.S., Santos R.R and Miranda L.C.M. Lett. Nouvo Cim., 16, 187 (1976)
2. Santos R.R. and Brandi H.S. Phys. Rev. A, 13, 1970 (1976)
3. Simola J. and Virtamo J. J. Phys. B., 11, 3309 (1978)
4. Brandi H.S. Phys. Rev. A., 11, 1835 (1975)
5. Kara S.M. and McDowell M.R.C. J. Phys. B., 13, 1337 (1980)
6. Smith E.R. et al Astrophys. J., 179, 659 (1973) and 182, 651 (1975)

List of Figures

Chapter I

Fig.I13 The computed refractive index and absorption coefficient to be used in the magneto-optical calculations.

Chapter II

Fig.II1 The experimental set-up for the magneto-optical studies in the Physikalisches Institute in Bonn.

Fig.II2a An experimental magneto-optical spectrum (for n=11 in SrI).

Fig.II2b A theoretical magneto-optical spectrum (for n=11 in SrI).

Fig.II3 The middle part of a computed magneto-optical spectrum (n=11 in SrI). Part of a magneto-optical cycle is demonstrated.

Chapter III

Fig.III1 SrI n=11 pattern calculated with the FCV method at T=700°C and B=4.2T. The polarisation efficiency of the grating was assumed to be 85%, the asymmetry of the two Lorentx components was k=.15 and the half width of the apparatus function was =8.5 10^{10} Hz.

Fig.III1a SrI n=11 experimental pattern obtained in Bonn.

Figs.III2 and 3 SrI n=11 computed spectra. All the parameters used were identical to those of Fig.III1 except T which was 600°C and 1000°C respectively.

Figs.III4 and 5 SrI n=11 computed spectra. All the parameters used were identical to those of Fig.III1 except that B=4.0T for both figures and Nfz=9.67 10^{14} and 9.63 10^{14} respectively.

Figs.III6 and 7 SrI n=11 computed spectra. T=700°C, B=4.2T and Nfz=9.67 10^{14} for both figures. The pattern was assumed to have identical Lorentz components and also to have 100% and 85% polarisation efficiency respectively.

Figs.III8 and 9 SrI n=11 computed spectra. All parameters used were identical to those of Fig.III6 and 7 except that P=40%

respectively.

Fig.III10 SrI n=11 computed spectrum. The temperature, F-field and Nfz values were identical to those of Fig.III1. The pattern was calcualted with k=.15 and P=100%.

Figs.III11 and 12 SrI n=11 computed spectra. All parameters used were identical to those of Fig.III10 except that P=40% and 0% respectively.

Figs.III13 and 14 SrI n=11 computed spectra. All paramters used were identical to those of Fig.III1 except that k=.35 and P=100% and 85% respectively.

Figs.III15 and 16 SrI n=11 computed spectra. All parameters used were identical to those of Figs.III13 and 14 except that P=40% and 0% respectively.

Figs.III17 and 18 SrI n=11 computed spectra. All parameters used were identical to those of Fig.III1 except that k=.15 for both figures and P=80% figures and 90% respectively.

Figs.III19 and 20 SrI n=11 computed spectra. All parameters used were identical to those of Figs.III17 and 18 except that P=85% for both and figures and k=.10 and .20 respectively.

Fig.III21 A magneto-optival pattern (and in an expanded form) of the n=11 SrI line without apparatus smoothing. The parameters used were identical to those of Fig.III1.

Fig.III22 This figure is identical to Fig.III1, but is repeated here for reasons of convenience.

Figs.III23 and 24 SrI n=11 computed spectra. All parameters used were identical to those of Fig.III1 except that the apparatus width was $4.0\ 10^{10}$ and $6.0\ 10^{10}$ respectively.

Figs.III26 and 27 SrI n=11 computed spectra. All parameters used were identical to those of Fig.III1 except that the apparatus width was $11.0\ 10^{10}$ and $15.0\ 10^{10}$ respectively.

Figs.III25 and 28 SrI n=11 computed spectra. All parameters used were identical to those of Fig.III1 except that the apparatus width was $9.5\ 10^{10}$ and Nfz=$9.68\ 10^{14}$ and $9.655\ 10^{14}$ respectively.

Figs.III29 and 30 SrI n=11 computed spectra. All parameters used were identical to those of Fig.III1 except that the number of steps between two successive freqeuncy points was 21 and 51 respectively as opposed to the 101 of Fig.III1.

Figs.III31 and 32 SrI n=11 computed spectra. All parameters used were identical to those of Fig.III1 except that the number of steps between two successive frequency points was 81 and 161.

Fig.III33SrI n=11 computed spectrum with a Gaussian apparatus profile. All other parameters used were identical to those of Fig.III1.

Figs.III34 and 35 SrI n=11 computed spectra with (a) a Gaussian (dashed line) and a Lorentzian (solid line) and (b) a triangular (dashed line) an a Lorertzian (solid lire) apparatus functior. All parameters used were identical to those of Fig.III1.

Fig.III36SrI n=11 computed spectrum with a Lorentzian apparatus smoothing (solid line) and with no smoothing (dashed line). All the parameters used were identical to those of Fig.III1.

Fig.III37MOV cycles for n=11,16,24 and 18 for SrI. The sensitivity of the cycle structure to changes in Nfz decreases as n increases under otherwise identical experimental conditions.

Fig.III38SrI n=11 MOV cycle. The sensitive dependence of the middle part on the product Nfz is obvious.

Figs.III39 and 40 SrI n=11,15,20 and 25 spectra theoretical and experimental in quite good agreement.

Chapter V

Fig.V1 Overlapping patterns for BaI and SrI at T=775°C and (a) B=2.0T, (b) B=2.5T and (c) B=3.0T.

Fig.V2 Overlapping patterns for BaI and SrI at T=900°C and (a) B=3.0T, (b) B=3.5T and (c) B=4.3T.

Fig.V3 ($^1S - {}^3P$) computed magneto-optical spectrum for n=1 ^{1}SrI, polarisation efficiency=85%, asymmetry constant=.15 and Nfz=9.68 10^{14}.

Fig.V4 Computed refractive index and absorption coefficient curves for a ($^1S - {}^1P$) transition.

Fig.V5 Computed magneto-optical spectrum including the effect of hyper- fine structure for n=11 SrI, polarisation efficiency=85%, asymmetry constant=.15 and $Nfz=9.68\ 10^{14}$.

Fig.V6 Schematic representation of the $^1P(M_J=+1)$ levels with hyperfine structure.

Fig.V7 Computed refractive index and absorption coefficient curves when hyperfine structure is included in the calculations.

Fig.V8 Computed refractive index and absorption coefficient curves when only fine structure is included in the calculations.

Chapter VI

Fig.VI1 Quantum defect theory oscillator plot for SrI (for n=11 to 28). The f-values were calculated with the MOV method.

Fig.VI2 Comparison between (a) present calculations, (b) the experimental magneto-optical spectrum and (c) Connerade's (reference [4] of Chapter VI) (all patterns were for n=11 of SrI).

Fig.VI3 Quantum defect theory f-value plot for MgI for B=2.5,3.7 and 4.5T calculated with the MOV method. All results were normalised to the n=7 value of Mitchell (reference [5] of Chapter VI).

Fig.VI4 Quantum defect theory f-value plot for MgI for B=2.5,3.7 and 4.5T calculated with the MOV method. All results were normalised to the n=8 value of Mithcell (reference [5] of Chapter VI).

Fig.VI5 Overlapping patterns for BaI and SrI at T=775°C and (a) B=2.0T, (b) B=2.5T and (c) B=3.0T.

Fig.VI6 Overlapping patterns for BaI and SrI at T=900°C and (a) B=3.0T, (b) B=3.5T and (c) B=4.3T.

Fig.VI7 The ratio R of the f-values (defined in the text of Chapter VI) plotted as a function of the wavelength interval spanned by the impurity line, showing that R is very nearly independent of the overlap.

Fig.VI8 The computed MCV CaI impurity pattern next to the n=17 line of SrI.

Chapter VII

Fig.VII1 Results using Clark's and Taylor's code for hydrogenic f- values against energy for B=2.5 Tesla.

Fig.VII2 As Fig.VII1 but for B=7.5 Tesla.

Fig.VII3 As Fig.VII1 but for B=19.5 Tesla.

Figs.VII4 and 5 Computed radial wavefunction for the $3s^2 3p$ configuration for MgI on the logarithmic mesh given by [16] and on the "linear 5" mesh (see text), both for 320 points.

Figs.VII6 and 7 As Figs.VII4 and 5 but for "linear 10" and "linear 20" radial grids respectively (both for 620 points accross).

Figs.VII8 and 9 As Figs.VII4 and 5 but on the logarithmic radial mesh suggested by [16] and on the "1/2" logarithmic radial mesh suggested by the present calculations (see text), both for 620 points accross.

Fig.VII10 The computed radial functions of the inner electrons ($3s^2 s$-$3s^2 p$).

Figs.VII11 and 12 Computed zero field f-values with present calculations versus energy and n-value respectively for the principal series of MgI (with $7<n<27$).

Figs.VII13 and 14 The P-field dependence of the f-values ($3s^2 s$-$3s^1 p$ transition for MgI) according to the present calculations of the $/^1P_1^*>$, $/^3P_2^*>$ and $/^3P_1^*>$ states for M=+1 and M=-1 respectively (see text for $/^1P^*>$ notation).

Fig.VII15 The same information as in Figs.VII13 and 14 but grouped differently.

Figs.VII16,17 and 18 As Figs.VII13 and 14 but for different n's in the range 7 to 27.

Chapter IX

Fig.IX1 The ionisation stages of Silicon which were used in the calculations.

Fig.IX2 The value of the ratio "a" as a function of density for a temprerature of 1CCeV using collision rates from Mewe [3](-----), Sampson and Parks [4](-.-.-.-.) and Vinogradov et al [2](_____).

Fig.IX3 As Fig.IX2 for a temperature of 4OCeV.

Fig.IX4 As Fig.IX2 for a temperature of 8CCeV.

Fig.IX5 The satellite line intensity ratio as a function of density for a temperature of 1OCeV excluding (_____) and including (-.-.-.-) collisional de-excitation from doubly to singly excited He-like states.

Fig.IX6 As Fig.IX5 for a temperature of 4OCeV.

Fig.IX7 Temperature absissa and collision rates ordinate for $2^1P\text{-}1^1S$ using results from Mewe [3](------), Sampson and Parks [4](-.-.-.-) and Vinogradov et al [2](_____).

Fig.IX8 As Fig.IX7 but for the transition ($2^3P\text{-}1^1S$).

Fig.IX9 The added levels (to the ones previously shown for Li-like calculations.

Appendix AIV

Fig.AIV1 Schematic representation of the delayed coincidence experiment to measure atomic lifetimes.

Fig.AIV2 Schematic representation of the Hanle effect.

List of Tables

Chapter VI

Chapter VII

Appendix AVII

Table AVII6 The s-p eigenfunctions in (M_L, M_S) representation for $M=+-1$.

Table AVII7 The s-p eigenfunctions in the (J, M_J) representation for $M=+-1$.

Table AVII8 The total interaction $M_J=+-1$ sub-matrices in the (J, M_J) scheme.

Contents

Chapter VII

Calculation of f-Values and their B-Field Dependence

1. Discussion on the Results of Appendix AVII and their Application to the MQV Method
2. A Brief Outline on the Work of C.W.Clark and K.T.Taylor Relevant to the Quadratic Effect in High Rydberg Hydrogenic States.
3. An Approximate Theoretical Method to calculate f-Values in the Presence of an External Magnetic Field
4. A Brief Discussion on Hartree-Fock Calculations
5. Solution of the Radial Equations for High-n States
6. The calculational and Computational Aspects of Evaluating f-values
7. Results
8. References

Chapter VIII

A Brief Theoretical Background to Plasma Diagnostic Techniques

1. Brief Introduction
2. Local Thermodynamic Equilibrium Model (TLE)
3. Coronal Model
4. Collisional Radiative Model
5. Dielectronic Satellites
6. Methods of Diagnosing T_e :
   - 6.1 I R Measurements
   - 6.2 Visible, UV and Soft X-Ray Relative Continuum Intensity Measurements
   - 6.3 Line Intensity Measurements in LTE Plasmas
   - 6.4 Corona Model Measurements
7. Methods of Diagnosing n_e :

J. Phys. B: At. Mol. Phys. **15** (1982) 1939–1948. Printed in Great Britain

Model dependence of the calculated line intensity ratios for a highly ionised silicon plasma

T A Stavrakas and R W Lee

Blackett Laboratory, Imperial College of Science and Technology, London SW7 2BZ, England

Received 5 November 1981, in final form 19 January 1982

Abstract. The results of calculations of the steady-state ionisation balance in a silicon plasma are presented. The effect of collisional de-excitation on the dielectronic satellite ratios is shown to be important for electron densities in the range 10^{19} to 10^{24} cm^{-3} and temperatures greater than 100 eV. This is the regime of interest for laser-produced and laser-compressed plasmas and for which the dielectronic satellite ratios have been proposed as a useful density diagnostic

The sensitivity of the He-like resonance to intercombination line ratio

$$\alpha = N(2^1P_1)A(2^1P_1, 1^1S_0)/N(2^3P_1)A(2^3P_1; 1^1S_0)$$

to the model used for the collision rates between singly bound He-like silicon levels has been investigated. Large differences in the calculated value of this ratio result from the use of different collisional models and so it may be possible to compare the results of different theoretical predictions with experiment.

1. Introduction

The calculation of the ionisation balance is of interest because line ratios are used as a diagnostic of plasma parameters. In a recent paper, Lunney and Seely (1981) have proposed that the ratio $N(2s2p\ ^3P)A(2s2p\ ^3P; 1s2s\ ^3S) + N(2p^2\ ^3P)A(2p^2\ ^3P: 1s2p\ ^3P)/N(2p^2\ ^1D_2)A(2p^2\ ^1D_2; 1s2s\ ^1P_1)$ could be used as a density diagnostic for laser-produced plasmas, while Vinogradov *et al* (1975) have studied the dependence of the He-like resonance to intercombination line ratio

$$\alpha = N(2^1P_1)A(2^1P_1; 1^1S_0)/N(2^3P_1)A(2^3P_1; 1^1S_0)$$

on plasma density. However, as Weisheit *et al* (1976) point out the analysis of the line ratios should still be corrected for opacity effects before experimental data is compared with theory. Uncertainties exist in these calculations for two principal reasons. Firstly, uncertainties exist in the collisional rates which are employed and, secondly, because of the restricted number of states and the restricted coupling between the states which are included in these calculations.

In this paper the results of calculations of the ionisation balance in a Si plasma are presented. These include higher-level hydrogenic- and He-like states and a fuller modelling of the coupling between them than in previously reported results. Large

0022-3700/82/121939+10$02.00

discrepancies exist in the calculation of the collision rates in the He-like ions. We investigate the effect of these differences on diagnostics by performing calculations using three different models for the collision rates, due to Vinogradov *et al* (1975), Mewe (1972) and Sampson and Park (1974). The work by Weisheit *et al* (1976) implied that the rates by Vinogradov *et al* (1975) and Aglitski *et al* (1974) are essentially the same as those of Sampson and Park (1974). This is not correct.

An outline of this paper is: § 2 describes in detail the rate model; the states involved, the coupling between them and the solution of the resulting algebraic equations. Section 3 describes the collisional models which are used. Section 4 describes the results of the calculations of the $N(2^1P_1)A(2^1P_1; 1^1S_0)/N(2^3P_1)A(2^3P_1; 1^1S_0)$ line ratio, and the results for the dielectronic satellite lines and interprets the difference between these and previously reported results (Lunney and Seely 1981).

2. The rate model

The states which are being used in these calculations are shown in figure 1. The errors due to the neglect of higher-energy states were assessed by performing calculations with and without the $n = 5$ singly excited He-like state. This resulted in the fractional changes of order 10^{-3} in the populations of the states of interest which were the $n = 2$ state and the ground state. The autoionising rates and the energies of doubly excited states were taken from Vainshtein and Safronova (1978), as were the radiative rates of the transitions of autoionising states to singly excited states.

The processes included are

(i) For 'bound–bound' transitions the radiative decay values which were not tabulated were obtained from the oscillator strength. The f values can be expressed (Wiese *et al* 1969) as

$$f = f_0 + Z^{-1}f_1 + Z^{-2}f_2 + \ldots \tag{1}$$

where f_0 is the hydrogenic value and Z is the charge of the nucleus of the element. Using tabulated f values for He and H we fit f against $1/Z$ using the first two terms in the power series in equation (1). We thus obtained values for Si XIII f values for bound–bound transitions.

A number of models have been used for 'bound–bound' collision excitation rates; discussion of these has been deferred to the next section. The collision de-excitation rates are derived by employing the principle of detailed balance.

(ii) For 'bound–free' transitions the collisional ionisation rates are taken from Seaton (1962) and the three-body recombination is calculated by the principle of detailed balance. The radiative recombination rates may be calculated from the photoionisation rates given by Ivanov (1973) in an analogous manner.

(iii) For the case of transitions from the doubly excited levels to the next ionic ground state the rates, i.e. autoionisations, are taken from Vainshtein and Safronova (1978) and the reverse process, electron capture, is again calculated using detailed balance (Jacobs and Davis 1978).

(iv) Finally, for transitions between doubly excited states the radiative decay values are considered negligible and the collisional rates have been calculated by Sampson (1980).

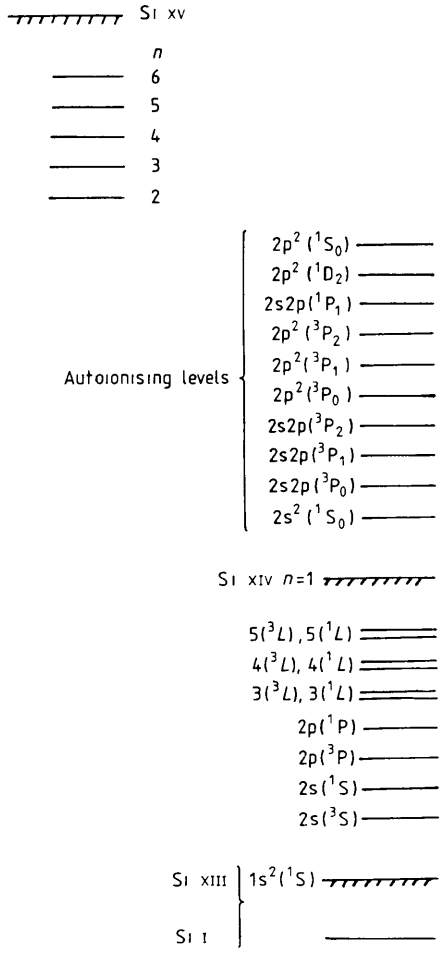

Figure 1. The ionisation stages and states of silicon which are used in the calculations

The rate equation of each state has the following form

$$-\sum_{i''<i} n_{i''}(R_{i''i}+C_{i''i})+n_i\left\{\sum_{i''<i}\left[R_{ii''}+\left(\frac{n_{i''}}{n_i}\right)^* C_{i''i}\right]+\sum_{i'>i}(R_{ii'}+C_{ii'})\right\}$$

$$-n_{i'}\sum_{i'>i}\left[R_{i'i}+\left(\frac{n_i}{n_{i'}}\right)^* C_{ii'}\right]=0$$

where R_{jk} and C_{jk} are the radiative and collisional rates from state j to state k, respectively, and an asterisk denotes the local thermodynamic equilibrium value.

The rate equation for the states shown in figure 1 constitutes a homogeneous set of n algebraic equations. We choose to solve for the ratio of each of the populations to the population of the Li-like ground state. The equations then reduce to an inhomogeneous set of $n-1$ equations. The solution of this large set of sparse linear equations is obtained using the method described by Duff (1976). This method gives an efficient and very accurate solution, but has the disadvantage of requiring large storage.

3. Calculation of the He-like interlevel collision rates

Although much effort has been put into calculating bound–bound collisional rates, for a Maxwellian electron distribution, the results of some calculations exhibit large differences between each other. It is thus important to understand the effect of the uncertainties in these rates on our results. To this end we have performed calculations using the results of three independent collisional rate models, i.e. those of Mewe (1972), Vinogradov *et al* (1975) and Sampson and Park (1974). Because of the importance of these models to this work we give the collision rates from each below.

For an $i \rightarrow j$ transition between discrete levels Mewe (1972) gives

$$C_{ij} = 1.7 \times 10^{-3} T_e^{-1/2} E_{ij}^{-1} f_{ij} \bar{g}(y) 10^{-5040 E_{ij}/T_e}$$

where f_{ij} is the absorption oscillator strength of the transition for allowed transitions, and for forbidden transitions we assume the f value of the allowed transition to the level with the same quantum number. This allows the same formula to be used for both allowed and forbidden transitions. E_{ij} is the excitation energy in electron volts, T_e is the electron temperature in Kelvin, $y = E_{ij}/kT_e$ and $\bar{g}(y)$ is the integrated gaunt factor given by Mewe (1972) and has the following form

$$\bar{g}(y) = A + (By - Cy^2 + D) \exp(y) E_1(y) + Cy$$

where

$$E_1(y) = \int_1^\infty t^{-1} \exp(-yt)\, dt.$$

The values of the parameters A, B, C and D are given by Mewe (1972). Some of these parameters have been recently revised by the same author (Mewe *et al* 1980), but these revisions do not affect the results here. Note that the use of the prescription for forbidden transitions is dubious since it is based on allowed transition oscillator strengths. We find below that these forbidden rates are not in agreement with other calculations.

For an $i \rightarrow j$ transition between discrete levels Vinogradov *et al* (1975) give

$$C_{ij} = 10^{-8} \left(\frac{E_j R_y}{E_i \Delta E_{ij}} \right)^{3/2} \exp(-\beta) \frac{B_{ij} \phi(\beta)}{g_i (\beta + X_{ij})}$$

where E_i and E_j are the ionisation energies of levels i and j measured from the edge, $\Delta E_{ij} = E_j - E_i$, g_i is the statistical weight of level i, B and X are fitted parameters given in Vinogradov *et al* (1975). R_y is the hydrogen ionisation energy and $\beta = \Delta E_{ij}/kT_e$

$$\phi(\beta) = \beta^{1/2}(\beta + 1) \qquad \text{for transitions without change in spin}$$

$$\phi(\beta) = \beta^{3/2} \qquad \text{for transitions with change in spin.}$$

For a $i \rightarrow j$ transition between discrete levels Sampson and Park (1974) give

$$\frac{C_{ij}}{\pi a_0^2 N_e \bar{v}} = \frac{1}{\omega_i} \left(\frac{I_H}{kT_e} \right) \langle \Omega(i \rightarrow j) \rangle$$

where ω_i is the statistical weight of level i, a_0 is the first Bohr radius of the hydrogen atom, I_H is the hydrogen ionisation energy, T_e is the electron temperature, N_e is the electron number density, $\Omega(i \rightarrow j)$ is the collision strength for an $i \rightarrow j$ transition, and

$\bar{v} = (8kT_e/\pi m)^{1/2}$. $\langle\Omega(i \to j)\rangle$ is given by

$$\langle\Omega(i \to j)\rangle \equiv \int_y^\infty \mathrm{d}\left(\frac{E}{kT_e}\right) \exp(-E/kT_e)\Omega(i \to j)$$

where y is the ratio of the excitation energy E to kT_e. The collision strengths corresponding to the various transitions in which we are interested are given by Sampson and Park (1974).

The different dependencies of these rates on parameters such as the temperature is evident. Some important differences between the results of the three collision formulae are illustrated by figures 7 and 8. Figure 8 shows the large difference between the results of Mewe (1972) and those of Vinogradov *et al* (1975) and Sampson and Park (1974) for the spin-forbidden transition (2^3P; 1^1S). Similar results have been found for all spin-forbidden transitions (indicating the incorrectness of Mewe's formulation). Figure 7, which gives collision rates for the spin-allowed transition (2^1P: 1^1S), shows that the collision rates calculated from Sampson and Park (1974) and Vinogradov *et al* (1975) can vary by as much as an order of magnitude at 100 eV and by a factor of two or more at temperatures of 800 eV. Since the calculation of Mewe (1972) is actually appropriate for allowed transitions the close agreement between the Mewe rates and the Sampson rates provides a verification of these two sets for the higher temperature region shown.

4. Results

4.1. Effect of different collision rates on the $N(2^1P_1)A(2^1P_1; 1^1S_0)/N(2^3P_1)A(2^3P_1; 1^1S_0)$ ratio

Calculations of the He-like resonance to intercombination line ratio, i.e.

$$\alpha = N(2^1\mathrm{P}_1)A(2^1\mathrm{P}_1; 1^1\mathrm{S}_0)/N(2^3\mathrm{P}_1)A(2^3\mathrm{P}_1; 1^1\mathrm{S}_0)$$

have been performed using the model described in § 2 and using each of the three collision rate formulae described in § 3, for the collisional rates for 'bound–bound' transitions.

Figures 2, 3 and 4 show the line ratios as a function of density for electron temperatures 100, 400 and 800 eV respectively. Good agreement between results from different collisional models is found only for electron densities greater than about 10^{23} cm^{-3}, where the limit of LTE is approached. At low densities the ratio of intensities is independent of the density and equal to the ratio of the excitation rates of the 2^1P and 2^3P levels by electron impact from the ground state. The relevant collision rates are those shown in figures 5 and 6.

The density range of interest for 'laser-imploded microballoons' (see e.g. Lunney and Seely 1981) is 10^{22} to 10^{24} cm^{-3}. In this range of densities the use of different collisional models can lead to order of magnitude errors in determining the density. The use of the set of rates by Sampson which is valid for both the allowed and forbidden rates should be seen as preferable.

4.2. Effect of level scheme on dielectronic satellite ratios

The use of dielectronic satellite intensity ratios for diagnosing hot, dense, laser-compressed plasmas has certain advantages. They are less susceptible to opacity

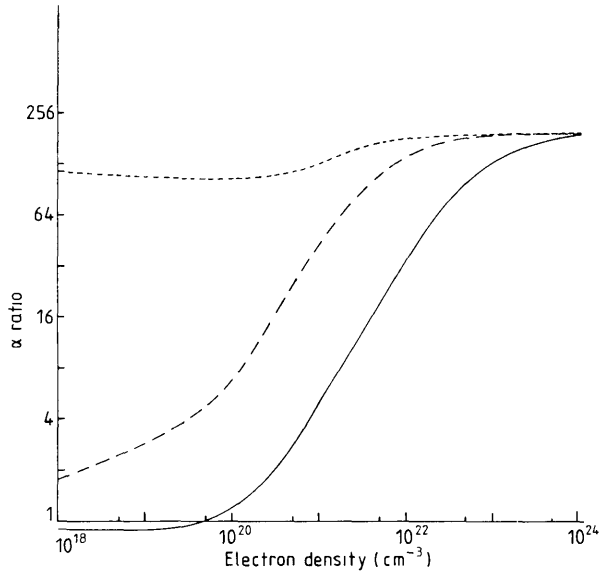

Figure 2. The value of the ratio α as a function of density for a temperature of 100 eV using collision rates from full curve, Mewe (1972), chain curve, Sampson and Park (1974) and broken curve, Vinogradov *et al* (1975).

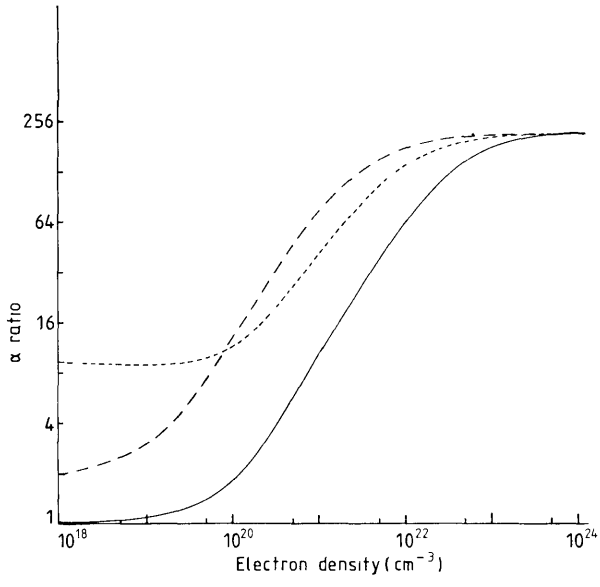

Figure 3. Same caption as for figure 2 for a temperature of 400 eV

effects than resonance lines. The satellite line emission is also more characteristic of the hot, dense, core region as it has been observed that it is only emitted briefly from the hottest plasma region.

The calculation of dielectronic satellite ratios given by Lunney and Seely (1981) excludes collisional de-excitation from the doubly to singly excited states. These rates are comparable with the radiative rates for electron densities greater than 10^{22} cm^{-3}.

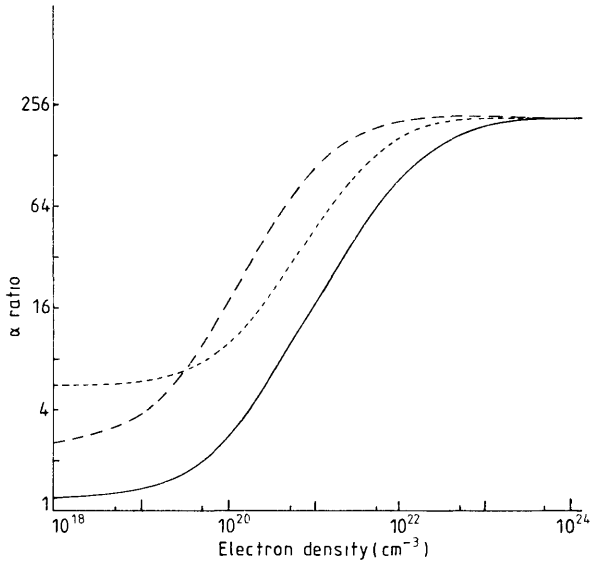

Figure 4. Same caption as for figure 2 for a temperature of 800 eV.

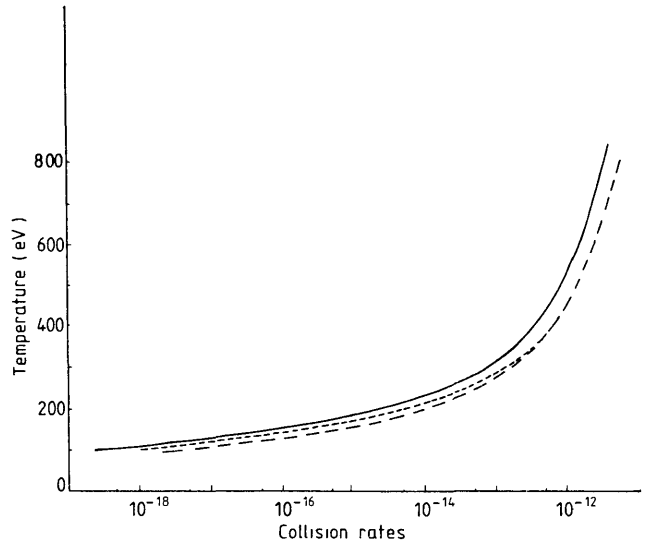

Figure 5. Temperature abscissa and collision rates ordinate for 2^1P–1^1S transition using results from full curve, Mewe (1972), chain curve, Sampson (1974) and broken curve, Vinogradov *et al* (1975)

Figures 7 and 8 show the dielectronic satellite ratio as a function of density, for electron temperatures of 100 and 400 eV respectively, calculated with and without collisional de-excitation from doubly to singly excited levels. From this it can be seen that errors can lead to overestimates of order 20 to 30% in the inferred density from the neglect of these rates.

At high densities the states are in LTE and the ratio is only dependent on temperature. At low densities the collisional downward rate is negligible compared with the radiative rate and the intensities depend only on the collisional upward rates.

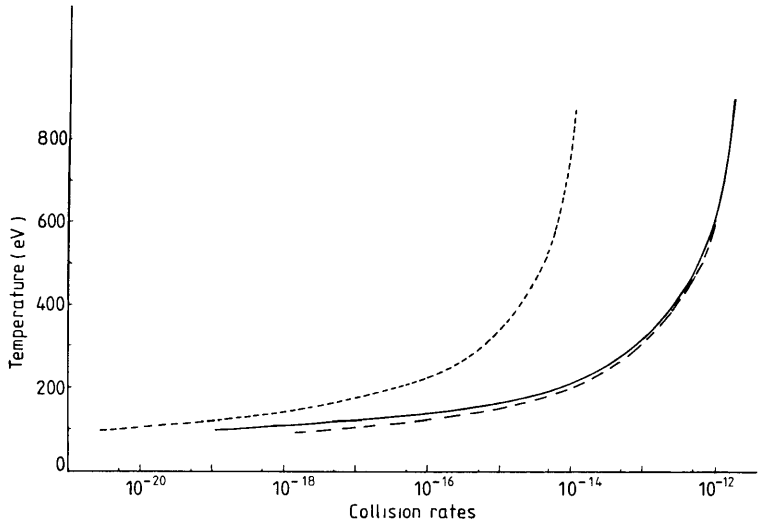

Figure 6. Same caption as for figure 5 but for the 2^3P–1^1S transition

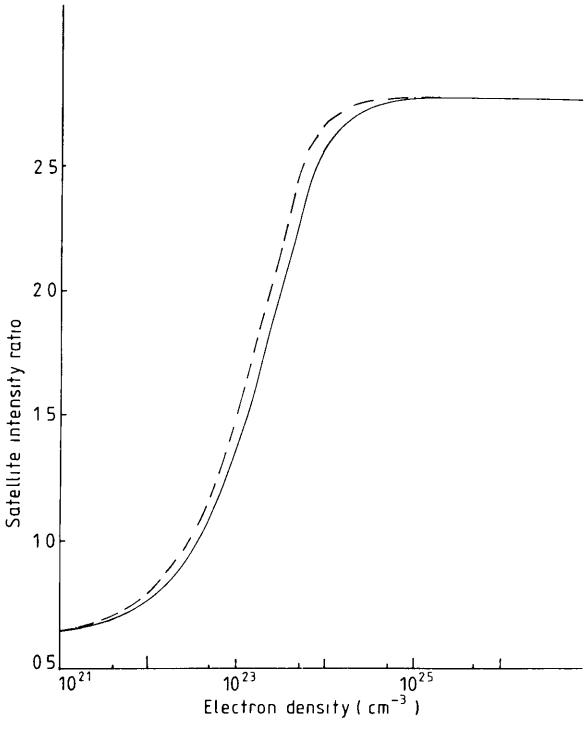

Figure 7. The satellite line intensity ratio as a function of density for a temperature of 100 eV excluding (full curve) and including (chain curve) collisional de-excitation from doubly to singly excited He-like states

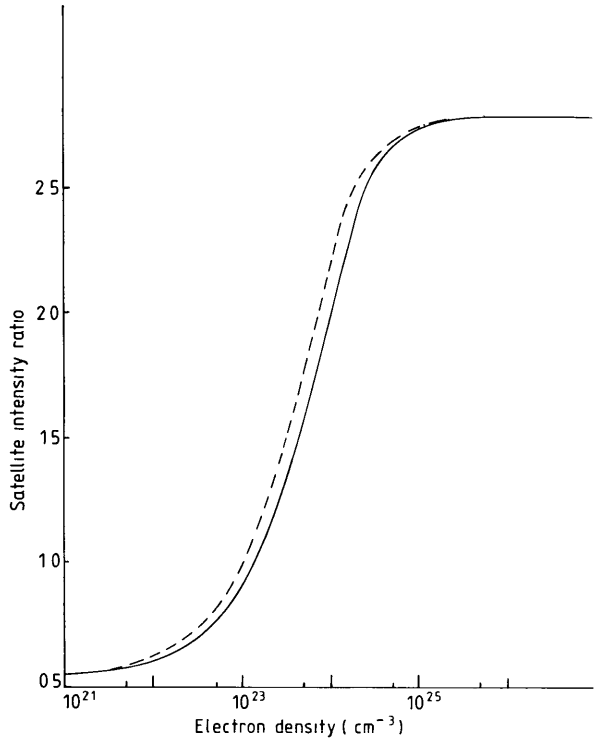

Figure 8. Same caption as for figure 7 for a temperature of 400 eV

5. Conclusions

Calculations using a rate equation model applicable to the study of high-density $n_e \geqslant 10^{19}\,\mathrm{cm}^{-3}$, and high-temperature, $T_e \geqslant 100\,\mathrm{eV}$, plasmas have been used to examine the effects of different collision rates and of incomplete coupling between the levels which are used.

In the case of the dielectronic satellite ratio the neglect of the collisional de-excitation from autoionising to singly excited He-like levels has been shown to result in a significant error in the line ratio. This can explain the inconsistency between the diagnosed densities and experimental data which Lunney and Seely (1981) explained by increased electron capture from the first excited state of the hydrogenic ion. However, it should be noted that the original diagnostic predicts electron densities which are accurate to 30%.

The effect of using different models for collision rates was investigated by calculating the line ratio $(2^1P_1; 1^1S_0)/(2^3P_1; 1^1S_0)$ using the results of Mewe (1972), Vinogradov *et al* (1975) and Sampson and Park (1974) for collision rates between singly excited He-like states. This shows that large differences in the line ratio result from using different collisional models, and emphasises the importance of accurate calculation of collision rates if meaningful spectroscopic diagnosis of plasmas is to be performed. As pointed out by Weisheit (1976) the analysis of line ratios involving resonance lines has to include the effect of opacity. This does not alter the importance of accurate calculations of collision rates in the theoretical determination of line ratios.

Acknowledgments

We would like to thank the referees for their useful comments. One of us (TAS) was supported by an agreement with the Rutherford and Appleton Laboratories.

References

Aglitski E, Boilko V, Vinogradov A and Yukov E 1974 *Sov J Quantum Electron* **4** 322
Duff I 1976 *AERE Report* R8730
Ivanov V 1973 *NBS Special Publication* 385
Jacobs V and Davis J 1978 *NRL Mem Rep* 3641
Lunney J and Seely J 1981 *Phys Rev Lett* **46** 342
Mewe R 1972 *Astron. Astrophys* **20** 215
Mewe R, Schrijver J and Sylwester J 1980 *Astron Astrophys.* **87** 55
Sampson D 1980 *private communication*
Sampson D and Park A 1974 *Astrophys J Suppl* **28** 323
Seaton M J 1962 *Proc Phys Soc* **79** 1106
Vainshtein L and Safronova U 1978 *At Data Nucl. Data Tables* **21** 49
Vinogradov A, Skobelev I and Yukov E 1975 *Sov. J Quantum Electron* **5** 630
Weisheit J, Tarter C, Scofield J and Richards L 1976 *J. Quant Spectrosc. Radiat Transfer* **16** 659
Wiese W L, Smith H W and Miles B M 1969 *Atomic Transition Probabilities* NSRDS–NBS22, vol 2 (Washington, DC: US Govt Printing Office)

JOURNAL DE PHYSIQUE

Colloque C2, supplément au n°11, Tome 43, novembre 1982 *page* C2-317

MAGNETIC ROTATION SPECTROSCOPY WITH SYNCHROTRON RADIATION

J.P. Connerade*, W.R.S. Garton*, M.A. Baig, J. Hormes, T.A. Stavrakas* and B. Alexa

**Blackett Laboratory, Imperial College, London SW7 2AZ, U.K.*

Physikalisches Institut, Universitat Bonn, 53 Bonn, F.R.G.

Résumé: Nous décrivons des expériences récentes où la polarisation linéaire du rayonnement synchrotron dans le plan de l'orbite a été exploitée pour étudier les effets combinés de la biréfringence magnétique circulaire (effet Faraday) et du dichroisme magnétique circulaire (MCD) dans l'ultraviolet. A l'heure actuelle, nos études portent sur les séries principales des alcalino-terreux dans des champs magnétiques allant jusqu'à 4,6 Tesla. Nous avons pu observer des oscillations d'intensité dues à l'effet Faraday jusqu'à n=28 environ. Au-dessus de cette valeur, les structures supplémentaires dues au mélange de l en champ intense compliquent l'interprétation du phénomène. A partir de nos mesures, nous avons pu, par une méthode nouvelle, déduire les forces d'oscillateur relatives des transitions atomiques avec une précision qui va jusqu'a + - 0,25%, et qui dépasse donc largement celle des meilleures déterminations antérieures. Notre méthode offre aussi, du moins en principe, l'avantage de permettre l'étude des perturbations de la force d'oscillateur en présence d'un champ magnétique intense. Enfin, elle ne nécessite qu'une optique réfléchissante et peut donc être utilisée dans l'ultraviolet lointain.

Abstract: We describe recent experiments in which the linear polarisation of synchrotron radiation in the orbital plane has been exploited to study the combined effects of magnetic circular birefringence (Faraday rotation) and magnetic circular dichroism (MCD) in the ultraviolet. To date, our experiments have concentrated on the principal series of alkaline-earths in magnetic fields of up to 4.6 Tesla. We have observed intensity oscillations due to Faraday rotation up to about n=28. Above this value, additional structures due to l-mixing in high fields complicate the interpretation of the patterns. From our measurements, we have been able to deduce relative oscillator strengths of atomic transitions by a novel technique. The precision of these determinations can be as high as + - 0.25% in favourable cases, and is thus considerably higher than in earlier measurements using different techniques. Also, the present method has the advantage that, in principle, one could investigate perturbations of the f-value by intense magnetic fields. Finally, it requires only reflecting optics and can therefore be used in the vacuum ultraviolet.

Introduction. - The present paper is a report on experiments recently performed at the 500 MeV electron synchrotron of the Physikalisches Institut in Bonn, where a laboratory specialised in high resolution vacuum ultraviolet spectroscopy has been set up in collaboration with the Blackett Laboratory, Imperial College. An example of investigations carried out in Bonn using the same source and spectrographic apparatus as the present work is given by Connerade Baig Garton & McGlynn (1980).

In the experiment described below, the high degree of linear polarisation of synchrotron radiation in the orbital plane of the accelerator has been exploited to study the combined effects of magnetic circular birefringence (Faraday rotation) and magnetic circular dichroism from 2300 to about 1600 angstroms.

Although dichroism and rotation generally can occur together, most experiments are designed to isolate one or the other of the two effects. Thus, the present combination is believed to be novel and, as will be shown, possesses some special advantages. It does, however, require a new approach for the interpretation of the data, and this will be described in some detail.

Experimental. - The basic experimental arrangement is shown in Fig.1: radiation from the 500 MeV accelerator is collected by a cylindrical mirror which focusses only in the horizontal plane, and therefore minimises any admixture of out-of-plane elliptically polarised light. The light is thus concentrated on the vertical entrance slit of a 3-metre vacuum spectrograph designed and constructed at Imperial College (Learner 1965).

The spectrograph is equipped with a 5000 line per mm holographic grating manufactured to special order by Jobin-Yvon SA (France). The resolving power of this combination is believed to be the highest currently available on a synchrotron radiation source. We are applying this experimental advantage to the study of a number of atomic and molecular spectra which are outside the scope of the present paper (see eg Baig Connerade and Hormes 1982 and references therein). In the work described here, the optimum spectrographic resolving power (about 300 000) was not achieved, because the apparatus function was affected by factors independent of the spectrograph (see below). Nevertheless, it was important to use a high density ruling, because the large tilt (38 degrees at 2500 angstroms) made the optical system very sensitive to the angle between the plane of polarisation of the incident radiation and the rulings on the grating surface. Also, the high dispersion enabled intensity oscillations much sharper than the actual linewidth to be observed.

The optical system was set up with the grating rulings vertical. Thus, in effect, the polariser (or electron accelerator) and analyser (or spectrograph) were crossed, as in the standard configuration for observing the Faraday effect.

Of course, a grating is not an ideal polarising element: its behaviour was investigated by a simple experiment in which a wedge of crystalline quartz with the optic axis running towards the apex, a nominal thickness of 5 mm at the centre and an angle between the faces of about 1 minute of arc was mounted just in front of the spectrograph slit with the axis at 45 degrees to the vertical. The difference between n_+ and n_-, the refractive indices for right- and left-hand circularly polarised radiation in crystalline quartz is roughly constant as a function of wavelength between 2500 and 2000 angstroms. Therefore, the optical path difference between + and - light expressed in units of wavelengtn varies as the reciprocal wavelength. If t is the thickness of the crystal, we have

$$t\,(n_+ - n_-) = (n + 1/2)\,\lambda$$

where n is an integer (274 at 2190 angstroms), as the condition for rotating the plane of polarisation through $\pi/2$. Since, in fact, we used a wedge, we observed a succession of sloping fringes, spaced more closely towards short wavelengths. They are illustrated in Fig 2. From these and other data, we estimate that the polarising efficiency of the grating is about 75%.

Between the synchrotron and the cylindrical mirror, we placed a superconducting magnet capable of producing field strengths of up to 4.7 Tesla over a length of 50 cm. A simple wire-wound furnace was used as the absorption cell in the warm bore of the magnet. For the initial experiments reported here, we have investigated the vapours of Sr I and Mg I at temperatures corresponding to measured particle densities of about 10 to the 16 cm^{-3}. Further experiments are in hand on elements which possess singlet principal series and therefore exhibit simple Zeeman structures.

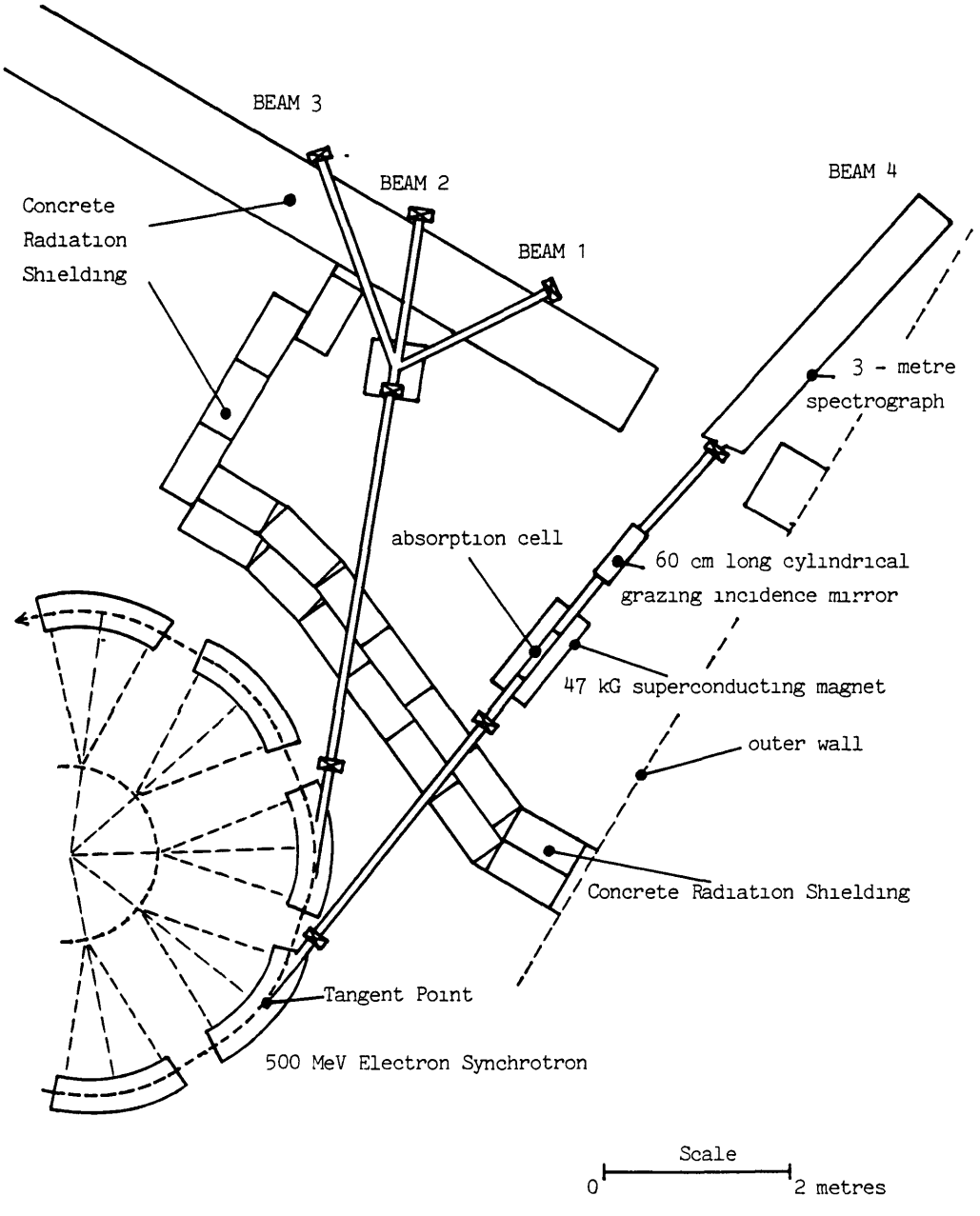

Fig 1

Experimental Layout for Magneto-optical studies at the Bonn 500 MeV electron-synchrotron. For clarity, the experiments on beam lines 1,2 & 3 are not shown.

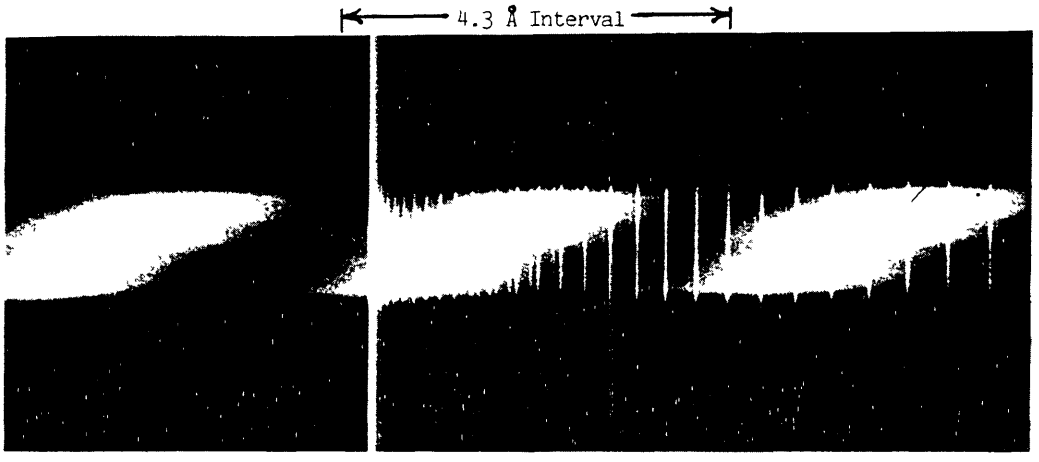

Fig2
Showing the sloping fringes observed when a crystalline quartz wedge is interposed between the cylindrical mirror and the entrance slit of the spectrograph (see text). Emission lines of CO^+ from a hollow cathode source were superposed as wavelength markers.

Results and Discussion. - A typical magneto-rotation pattern recorded in the present experiments is shown in Fig 3. The Zeeman structure, which consists of a Lorentz doublet, can be seen towards the centre of the pattern. It is surrounded by intensity oscillations which are symmetrical about the field-free resonance wavelength and which I shall refer to as 'magneto-optical beats'. The physical origin of these beats is as follows: as noted above, the polariser and analyser in our experiments were crossed. Also, with the combination of high magnetic field, long path length and high vapour density we used, typical atomic f-values resulted in Faraday rotations of many turns towards the centre of absorption lines. Thus, as the profile of a line is scanned in frequency, with the fast change in rotation angle as the line is traversed, the emerging light can have its plane of polarisation rotated through different integral multiples of $\pi/2$ at different points on the profile, and the intensity therefore oscillates between these points. In other words, the electric vector of the light describes a helix with many turns, and the actual number of turns varies as the profile is scanned.

In our experiments, magneto-optical patterns have been recorded over a wide range of n-values and magnetic field strengths. For example, in Sr I, we have recorded patterns from $n = 11$ to $n = 28$ in fields of 2.5, 3.0, 3.5, 4.0 and 4.6 Tesla. Since the spectra were recorded photographically for optimum wavelength resolution, the patterns for different n-values are all recorded simultaneously. This has the following advantages: over the duration of the exposure, some of the parameters of the experiment (eg the magnetic field strength or the density of absorbers in the furnace) could drift or fluctuate. The variations will, however, be identical for all the transitions recorded on the same plate. Since, as will be explained below, we are primarily concerned with the determination of relative f-values from the product NflB (where N is the number density of absorbers, f is the oscillator strength, l is the length of the furnace and B the magnetic field strength), this simple expedient obviates any need to measure N, l or B accurately, although an approximate value of B is in fact necessary to calculate the Zeeman structure at the centre. Thus, all that is required is to hold these quantities sufficiently constant for the magneto-optical beats to be recorded with good contrast. Small fluctuations in any of them are, in fact, accounted for in the analysis by the introduction of an apparatus function, as will be explained below.

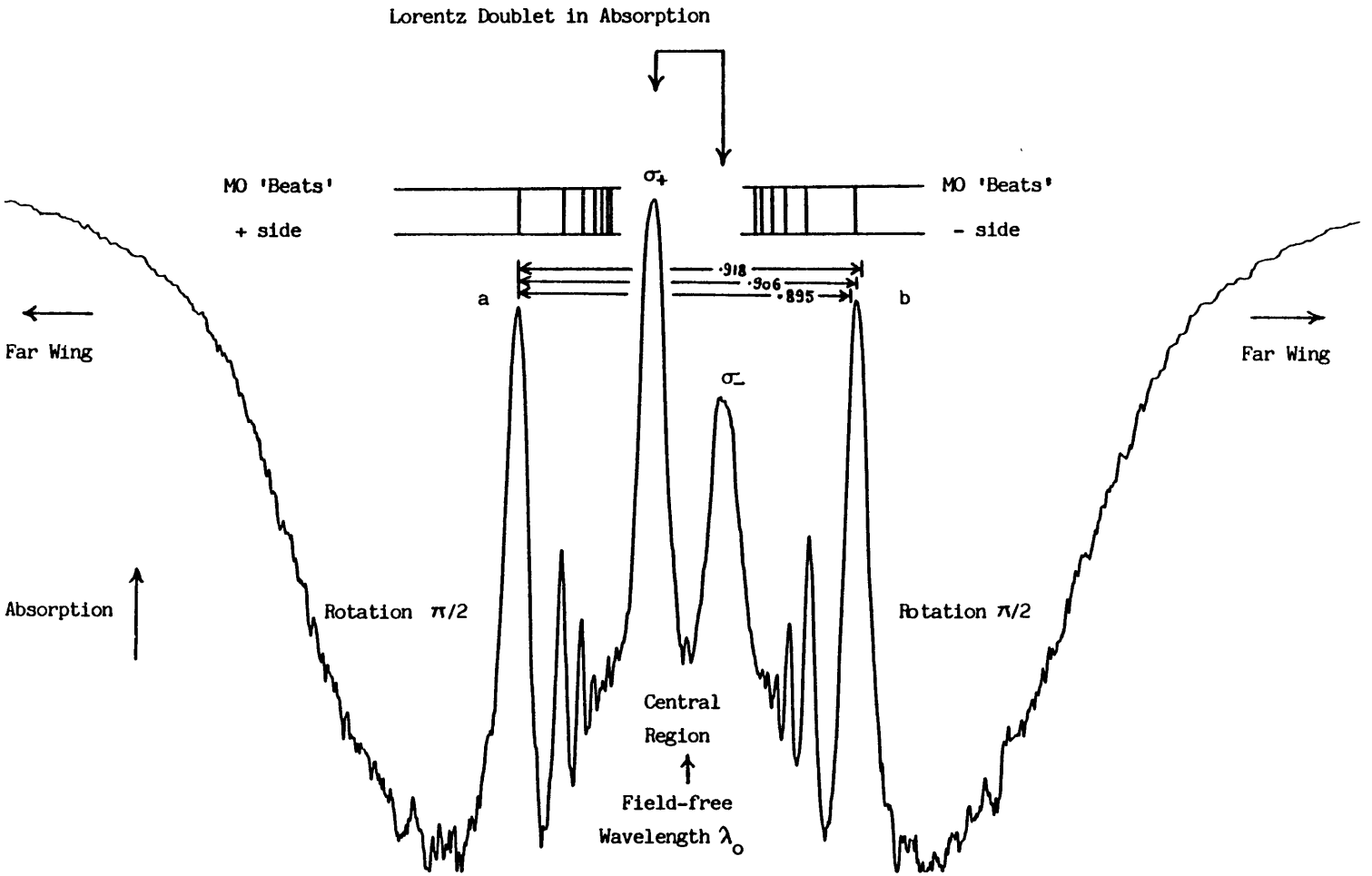

Fig. 3 A typical well-resolved magneto-optical pattern (for n = 11 in Sr I).

In Fig 3, we have given names to various parts of the pattern which will facilitate the following discussion. Several approaches are helpful in the interpretation of the patterns, and they can be applied in steps of progressively increasing accuracy:

1. Estimates of Nf1B are readily obtained from well-resolved patterns such as the one in Fig. 3 by applying the far-wing approximation of Mitchell and Zemansky (1971), which gives the rotation angle φ as a function of the detuning $\nu-\nu_0$ from the field-free line centre :

$$\varphi = \frac{N f_3 B e^3}{8\pi m^2 c^2} \frac{1}{(\nu-\nu_0)^2}$$

Clearly, as the detuning increases, the rotation will tend to zero. Conversely, moving in towards the line core, the rotation increases until, at $\pi/2$, the transmission through the crossed polarisers is maximum. When the detuning is reduced still further, we obtain the magneto-optical beats for angles of $\pi/2$, π, $3\pi/2$, 2π, etc. Thus, the rotation angles are determined absolutely, as stressed above, and are actually independent of most non-linearities in emulsion response which would affect relative intensity determinations.

The weakness of this first method of analysis is illustrated in Fig 4: The points which satisfy the far-wing criteria best are those which give the broadest oscillations in Fig. 3 and are therefore the least accurately determined, while those which do not conform to the approximation give sharp structures which would be the most useful for an accurate analysis.

2. The second approach is to return to the theory and seek expressions for the transmitted intensity which involve none of the far-wing approximations. In practice, this means that both the contributions due to magnetic circular dichroism and magnetic circular birefringence must be included together. The easiest way to do this is through standard electromagnetic theory, by defining a complex magneto-optical angle (Buckingham 1969). Several authors (in particular Gawlik et al. 1979) have considered closely related situations which are actually special cases of the one considered here. In a forthcoming paper (Connerade 1982), the full expressions are derived, and the algebra will therefore not be repeated here. Rather, we shall concentrate on various numerical approaches we have devised to calculate the profiles and report on improvements which are still being studied.

To compute magneto-optical patterns, we start from an expression for the transmitted intensity:

$$I = \frac{I_o}{4}\frac{P}{100}\left[\left(e^{\frac{-a_+ z}{2}} - e^{\frac{-a_- z}{2}}\right) + 4\, e^{\frac{-(a_+ + a_-)z}{2}} \sin^2\varphi\right] + \frac{100-P}{100} I_o e^{-(a_+ + a_-)z} \qquad (1)$$

where I is the intensity of the incident plane wave, P is the polarisation efficiency of the grating, a+ and a- are the absorption coefficients for right and for left hand circularly polarised radiation, z is the length of the furnace and φ is the Faraday angle.

The quantities a+, a- and φ are clearly functions of the detuning $\nu-\nu_0$ and of the magnetic field strength B. We have tried different expressions for them. The simplest to use is the form given by standard dispersion theory, namely:

$$a_\pm = \frac{e^2 N f}{mc} \frac{(\Gamma/4\pi)}{(\nu_0 - \nu + \alpha)^2 + (\Gamma/4\pi)^2} \qquad (2)$$

for singlet terms, where $\alpha = eB/4\pi mc$ and all symbols are in the standard notation of Mitchell and Zemanski (1971). The advantage of this expression is that $n_\pm$ are then readily obtained as:

$$n_\pm - 1 = \frac{e^2 Nf}{4\pi m} \frac{1}{(\nu_o \pm \alpha)} \frac{\nu_o - \nu \pm \alpha}{(\nu_o - \nu \pm \alpha)^2 + (\Gamma/4\pi)^2} \qquad (3)$$

so that the rotation angle φ is readily calculated from:

$$\varphi = \frac{1}{2} \frac{\omega z}{c} (n+ - n-) \qquad (4)$$

However, it should be borne in mind that these expressions for a+ and n- are not strictly applicable. In fact, Doppler broadening dominates under the conditions of the experiment, and the analysis should be based on a Voigt profile. This procedure is more complicated and will be further discussed below.

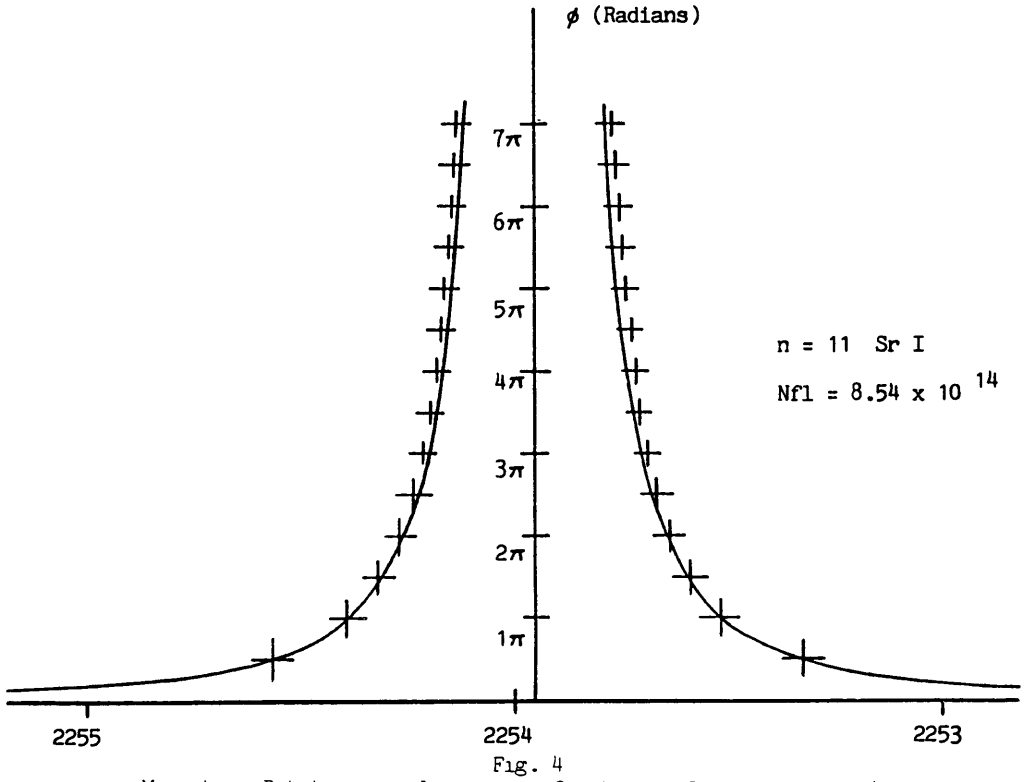

Fig. 4

Magnetic Rotation angle as a function of wavelength (in angstroms) for the far-wings of the pattern in Fig. 3. Notice how the points move off the theoretical curve as one approaches the centre of the pattern, where the sharpest oscillations occur. The accuracy of any analysis based on the far-wing formula is therefore limited.

In addition to the expressions (1-4) above, we need to perform an integration over the apparatus function. It is worth noting that this is not simply the instrumental function of the spectrograph, which could be determined, say, by analysing a zero-field profile: in the apparatus function, we must include fluctuations of either the magnetic field or the density of absorbers during the exposure. The simplest (and crudest) approach is to treat this unknown as a 'top hat' function, the width of which is then adjusted to reproduce observed magneto-optical patterns. A more realistic approach may be to use a Lorentzian of adjustable width. As we shall see, both give very good results.

We begin by considering the simplest approach, namely (1-4) together with 'top hat' smoothing. Fig. 5 gives two examples of magneto-optical patterns computed in this way.

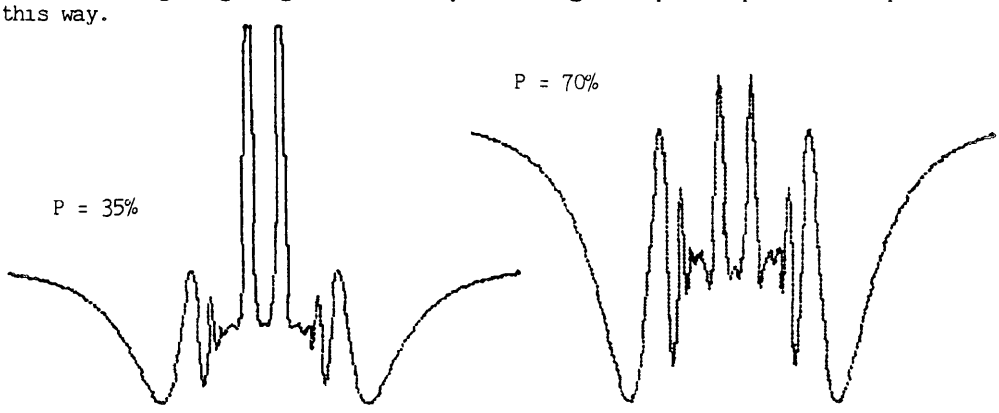

Fig. 5
Computed magneto-optical patterns for n=11 of Sr I, with Nf = 8.58x10 to the 14 and B = 4.2 Tesla, showing the effect of different polariser efficiencies.

Although not strictly relevant to the physics, it may be of interest to point out that the computations involved in obtaining Fig.5 were simple enough to be carried out on a CBM 4032 Microprocessor after some internal modification to provide a suitable fast graphics display. More elaborate calculations (which are described below) are definitely not in this class and require a large computer. The simpler theory can therefore be useful for a preliminary analysis of data.

As can be seen from Fig. 5, the profiles obtained are quite realistic and provide us with a basis to analyse the spectra. Indeed, we can now set up a scheme to compute all the profiles using (1-4), while varying the following parameters: P (to fit observed intensity ratios of the magneto-optical beats to the Lorentz components), the width of the apparatus function (to fit the observed fall in intensity of magneto-optical beats as their frequency increases) and NfzB (see below). If not measured directly, the magnetic field can be recovered from an analysis of the Zeeman structure (a highly accurate value of B is not required, since it will anyway factor out of the relative oscillator strength determinations). The dispersion width ($\Gamma/4\pi$) is taken as equal to the Doppler width.

Most of the parameters are held constant from one profile to the next for different profiles recorded on the same plate, since the experimental conditions are identical (We have, however, noticed a variation of the efficiency of the grating as a polariser over a range of about 400 angstroms). Thus, the problem reduces to a determination of NfzB for each profile. Attempts along these lines have led us to yet a third approach, which we regard as the most accurate to date.

3. The Magneto-Optical Vernier (MOV) Technique: The basis of this approach is a study of the behaviour of computed patterns as NfzB is varied. As it turns out, there are different rates of variation of the profiles over different parts of the rotation curve: in the far-wing, the pattern varies slowly, moving slightly out from the line centre as NfzB increases in accordance with the far-wing formula, while relative intensities remain substantially unchanged, provided the magneto-optical beats are well outside the width of the Lorentz components. Moving in towards the line centre, where the rotation angles become much larger, one finds that the relative intensities in the pattern fluctuate rapidly as a function of NfzB.

This behaviour is illustrated in Fig. 6, which shows just the central part of the computed patterns as a function of Nfz . In what follows, we refer to one period of the fluctuation as a magneto-optical cycle. The existence of the cycles was already demonstrated by Gawlik et al. (1979) for the special case of fixed energy photoexcitation at the zero-field resonance frequency, in which case the dichroism terms cancel, leaving only the fast-varying contribution due to birefringence: they were able, by studying the beats as a function of magnetic field strength, to obtain an accurate measurement of the relative f-values of the sodium D lines. By contrast, in the present method, the field B is held constant and the profile is scanned in frequency. This has a number of advantages. (a) We can use the outer part of the profiles to determine NfzB coarsely, say, to within one magneto-optical cycle, and then use the fast variation at the centre of the profile to determine NfzB accurately. This is the MOV method referred to above, and is capable of an optimum accuracy of +- 0.25%. (b) Holding the field constant allows us to work at very high fields and, by performing measurements at several different values of B, it should be possible to study the influence of the magnetic field strength itself on the relative oscillator strengths. (c) By working with high fields, one achieves a high sensitivity as well as a high accuracy, and relative oscillator strengths where one of the f-values is 10 to the minus 4 or less can be determined to an accuracy which is still of the order of +-10%.

As pointed out above, there remains some possibility of systematic errors in an analysis based on the MOV technique when the simple dispersion formulae (2-4) are used. Nevertheless, we have obtained results which, plotted on the 'renormalised' graphs of quantum defect theory (Starace 1976) are more consistent at high n than results obtained by the 'hook' technique (Parkinson Reeves and Tomkins 1976) and join more smoothly with the photoionisation cross section. This is illustrated in Fig.7.

In order to determine the significance of the systematic errors mentioned above and also to explore possible improvements in the details of the predicted patterns, we have also performed calculations using Voigt profiles, convolved with a Lorentzian instrument function. The computations were performed by using a simple algorithm (Hui Armstrong and Wray 1978) for the complex error function, the real and imaginary parts of which yield the absorption coefficients and refractive indices. Many more points were used (about 1000) in order to display well-resolved patterns. These calculations were carried out on the CDC 7600 computer at Imperial College. A typical profile is displayed in Fig.8.

As can be seen from Fig. 8, the new calculations using Voigt profiles and the more reasonable apparatus function are a significant improvement over earlier ones based on simple dispersion theory and a 'top hat' smoothing procedure: while the overall features are the same, the Lorentz components at the centre of the pattern are closer to the experimental lineshapes, and, with the finer mesh used in the more elaborate calculations, more detailed structure can be reproduced. Thus, the more elaborate scheme will, it is thought, provide a better framework for exploiting the MOV method. At time of writing, this aspect of the analysis is still being developed, which is why the results of Fig. 7 are based on simple dispersion theory. In particular, we are still exploring the most appropriate

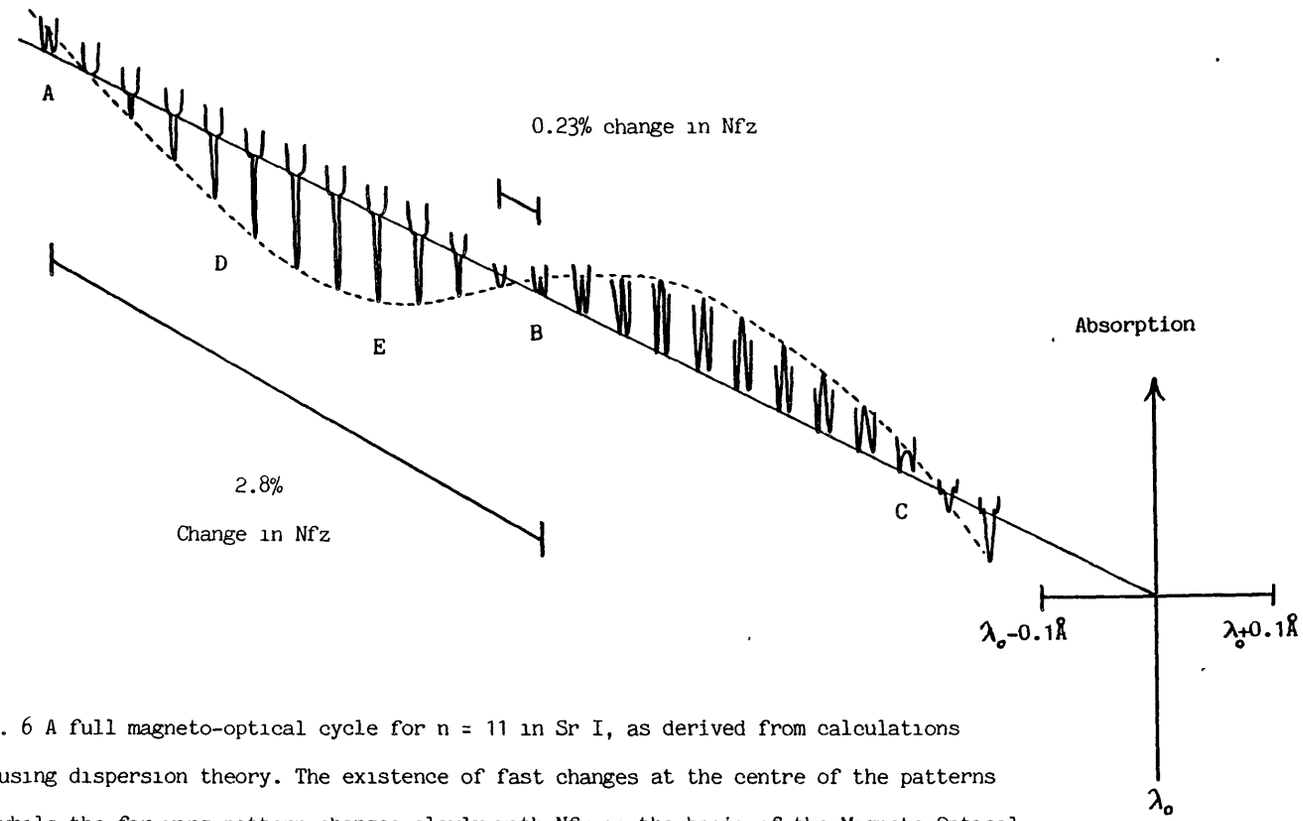

Fig. 6 A full magneto-optical cycle for n = 11 in Sr I, as derived from calculations using dispersion theory. The existence of fast changes at the centre of the patterns while the far-wing pattern changes slowly with Nfz is the basis of the Magneto-Optical Vernier (MOV) technique described in the text.

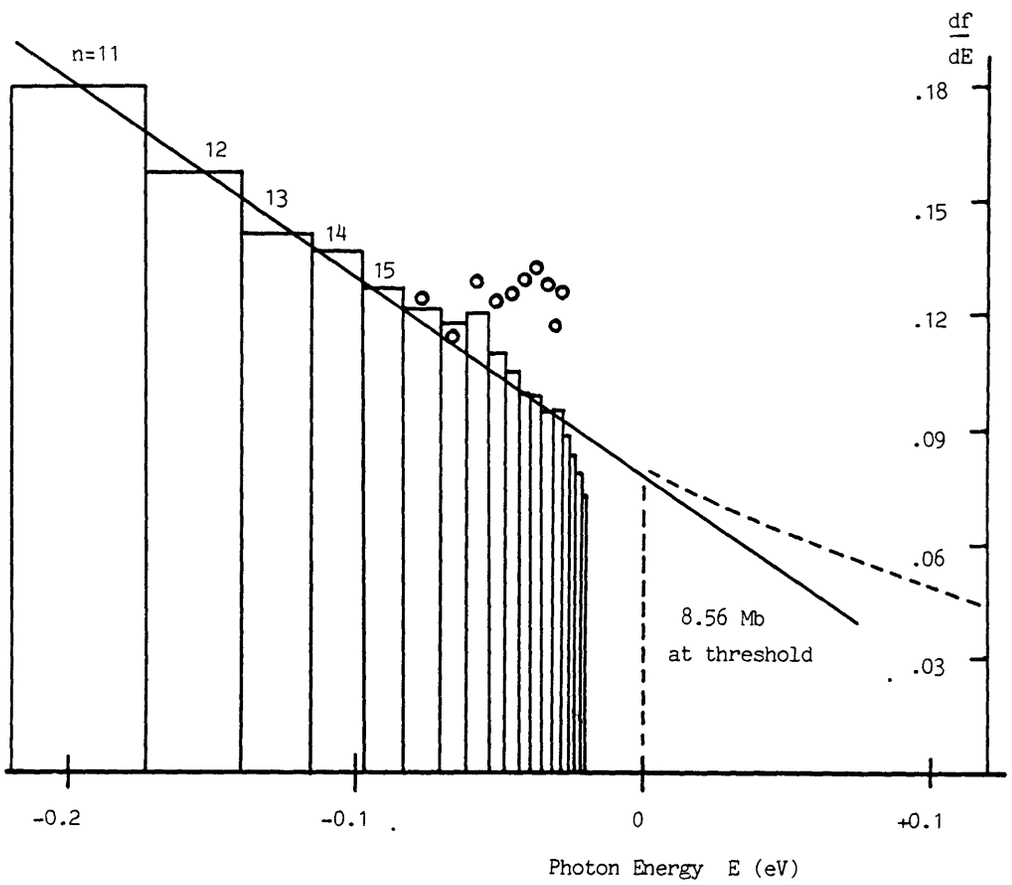

Fig. 7
Plot of renormalised oscillator strengths as a function of energy for the principal series of Sr I, showing the smooth join which is obtained between the present data (rectangles) and the photoionisation cross section of Sr I as measured by Hudson et al.(1969), scaled up by 1.5. This is compared with 'hook data' by Parkinson Reeves and Tomkins (1976-open circles), who suggest a scaling factor of 1.9 for the data of Hudson et al.(1969). A scaling factor of 1.7 was suggested by Lutjens(1972). The 'hook'values for n=11 to 15 are very close to the present values and are omitted for clarity. At high n, the present measurements still show some departures from a straight line and this is discussed in the text.

apparatus function to use. One might, for example, prefer a Gaussian shape, but the matter is not a simple one, because the width of the apparatus function is in fact dominated by fluctuations in furnace density and magnetic field strength, rather than just optical effects.

Thus, before deciding on the final method of interpretation, we wish to study the influence of various possible choices on the relative f-values obtained for a given set of data. This should also provide useful information on the accuracy of our technique.

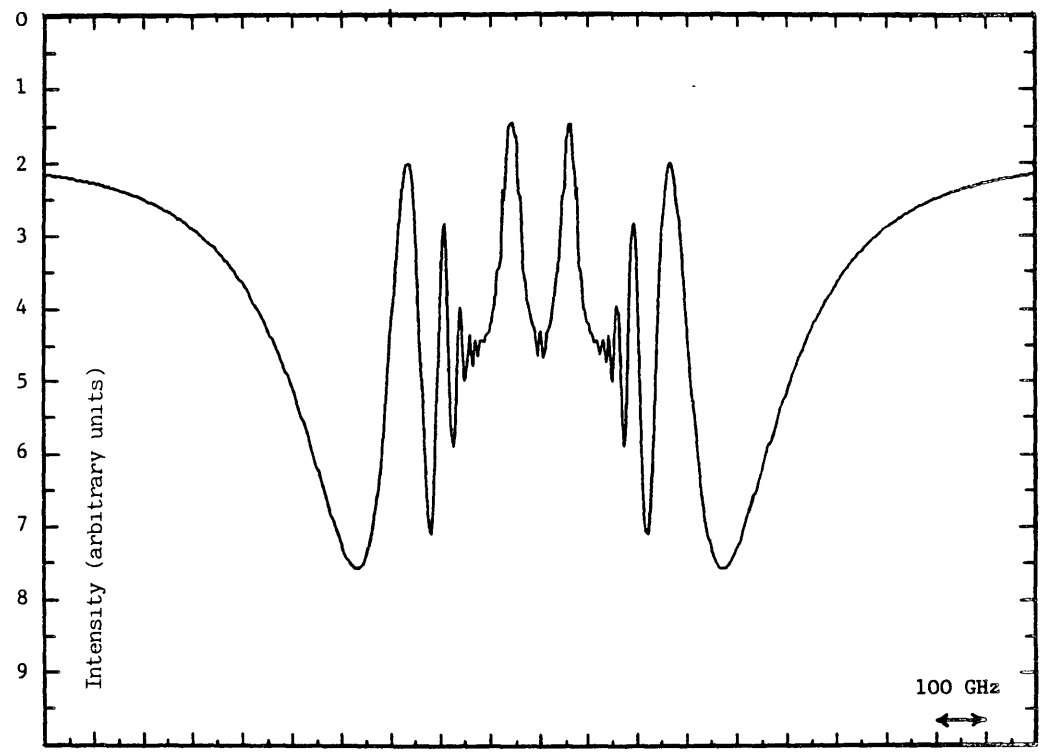

Fig. 8

Calculated magnetorotation pattern for n=11 in. Sr I. The parameters are Nfl = 8.38 x 10^{14}, H = 4.2 Tesla. A Voigt profile was assumed for the field-free absorption coefficient and the full expression including both circular birefungence and dichroism is then smoothed over a Lorentzian apparatus function.

Another aspect of the pattern in Fig.3 which has not been discussed so far is the asymmetry with respect to line centre which is apparent in the Zeeman components. A first temptation is to seek its cause in one of several processes which lead to antisymmetric Faraday effects (cf Fortson and Wilets 1980). These are, in order of significance as the magnetic field strength is increased, the Back-Goudsmit effect which breaks the coupling of J and I in hyperfine structure, and the Paschen-Back effect, which breaks LS coupling and thus mixes singlet and triplet states. In principle, if both the latter causes of asymmetry could be removed, eg by extrapolating to zero field strength, one would be left with the Weinberg-Salam effect for atoms, which, however, is much too small to be detected by our approach.

All the effects associated with antisymmetric rotation act simultaneously on the absorption coefficients and refractive indices, and therefore affect both the magneto-optical beats and the Lorentz components at the centre. Now, we find that the magneto-optical beats in well-resolved patterns such as the one in Fig.3 are in fact symmetrical about the centre of the patterns to within experimental error

(for partially resolved patterns, the situation is slightly different, as discussed below). Experimentally, the asymmetry only affects the intensity of the Zeeman components. This suggests that the cause, at least for Sr I at the field strengths we have studied, is not connected with any antisymmetry of the Faraday effect.

Another possibility is some ellipticity of the incident radiation. Synchrotron radiation is only plane-polarised in the orbital plane of the accelerator. As one increases the acceptance angle out of the plane of the orbit (or if, for some reason, the orbit of the electrons migrates slightly from the true plane) the radiation will, in fact, be elliptically polarised. In effect, we can represent this as a slight admixture of circularly polarised radiation in the incident beam. Now, such an admixture does not affect the rotation patterns at all, since there is no preferred plane in circularly polarised light. However, the Zeeman pattern is affected, because circularly polarised light of a given sense (say positive) will be absorbed by the Lorentz component on one side of the pattern, but not by the corresponding Lorentz component on the other side.

We have included this effect in our calculations, and we find that good results are indeed obtained for an admixture of circularly polarised light of a few percent in the incident beam. This is shown in Fig.9. The admixture of circularly polarised light for Fig.9 is perhaps a little higher than one would expect, but it could conceivably be due to optical imperfections, for example to a grazing incidence reflection on one side of the beam line tube.

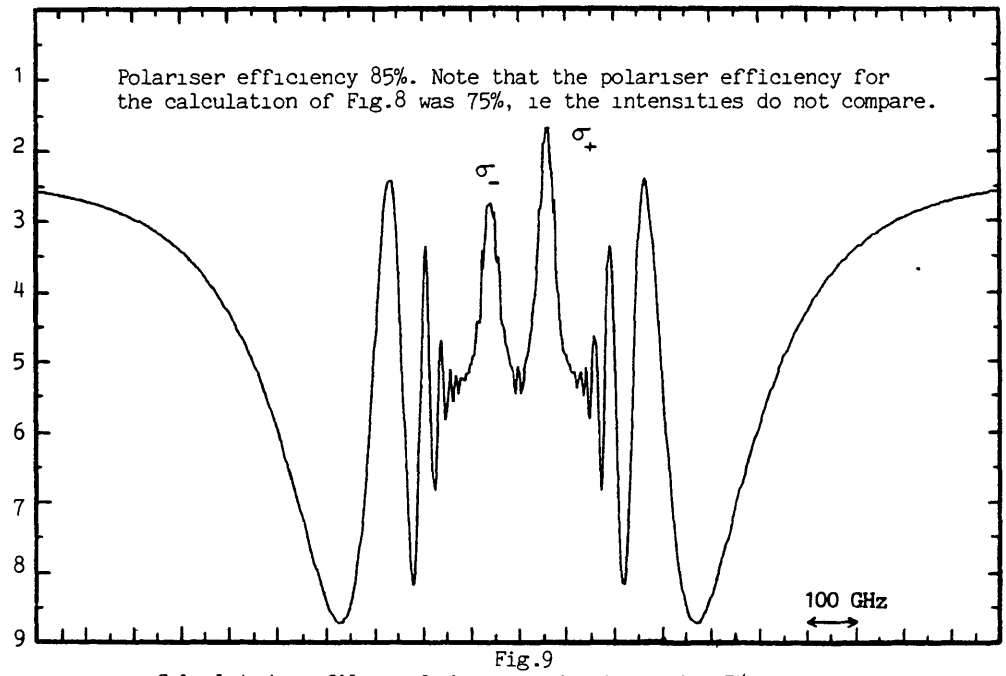

Fig.9
Calculated profile including an admixture of 15% right hand circularly polarised light, the net effect of which is to increase the intensity transmitted through the crossed polarisers at all wavelengths except in the σ_+ peak, at the centre of which right hand circularly polarised light is strongly absorbed. An asymmetry is thereby introduced in the pattern, but it will be noted that this does not extend to the magneto-optical beats. Also, the centre of the pattern has the same appearance as in the profile of Fig.8, which was calculated using otherwise identical parameters.

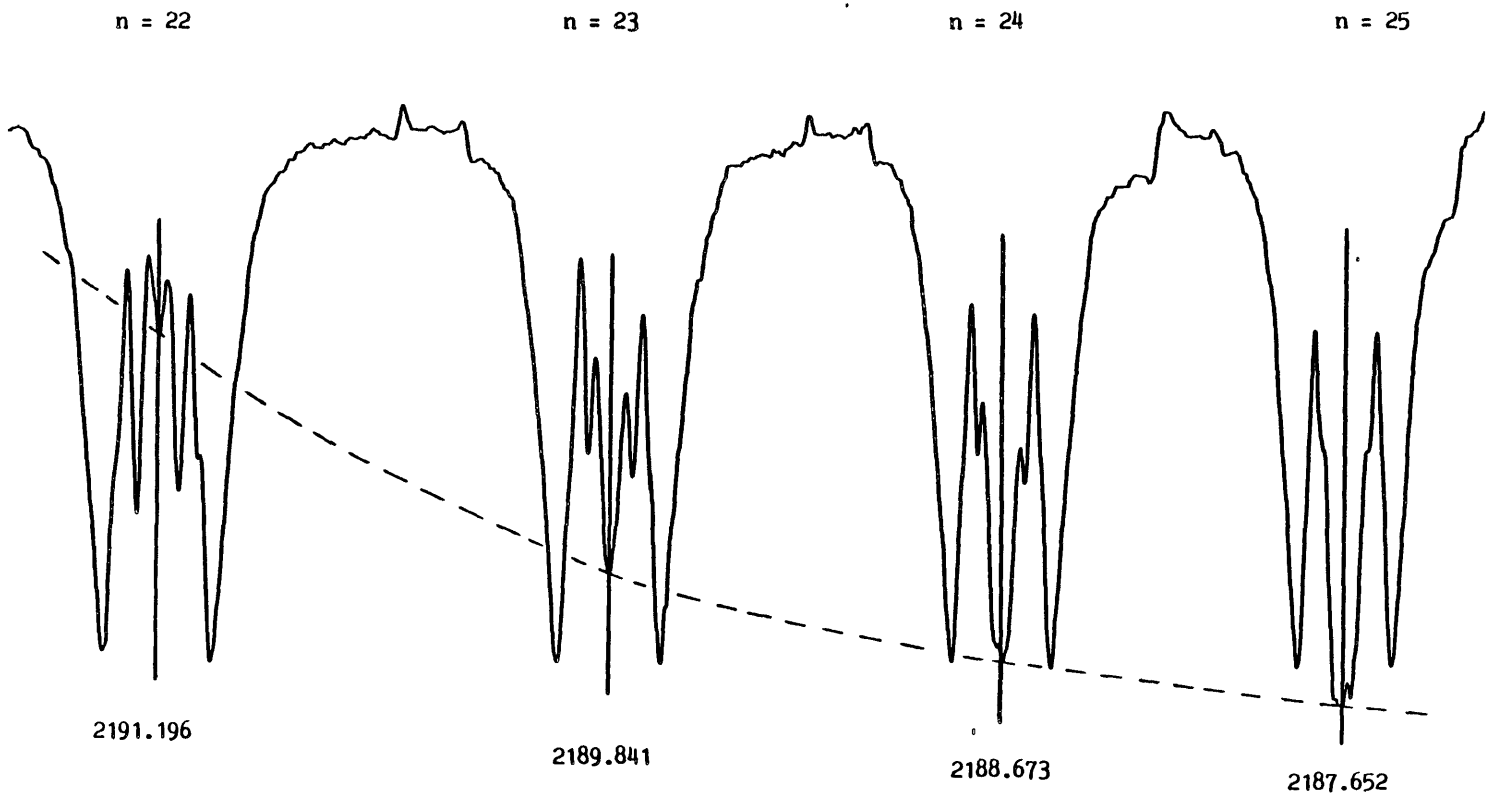

Fig.10 - Examples of experimentally recorded magneto-optical patterns under partially resolved conditions, for n = 22, 23, 24 & 25 in Sr I. Note the rapid variation in intensity at the centre of the patterns (dashed curve), which is the basis of the MOV method (see text).

So far, the discussion has centred on well resolved magneto-optical patterns, ie on patterns for which the magneto-optical beats stand well clear of the Zeeman structure. A proper understanding of these is clearly necessary to tackle the more complex situation where the structures overlap in energy, which we shall refer to as partially resolved patterns.

Partially resolved patterns are encountered as one progresses to higher n-values up a Rydberg series for a given magnetic field strength. With decreasing f-value, the available rotation decreases also, and eventually the magneto-optical beats move into the linewidth of the individual Lorentz components, so that it becomes difficult to attach precise labels to the peaks as was done in Fig.3.

Examples of partially resolved patterns are given in Fig.10. The first question one might ask is whether the MOV method is still applicable under such conditions. Fortunately, a clear answer is provided by the experiment itself: as can be seen in Fig.10, the outer regions of the patterns change slowly with increasing n-value, whereas the intensity at the centre (along the dashed curve in the figure) changes fast. This fact demonstrates that the MOV method continues to provide enhanced accuracy in the determination of f-values under partially resolved conditions.

In addition, the methods of profile computation described above also remain applicable under partially resolved conditions, which is another important advantage over the method of analysis based on the far-wing approximation. Examples of profiles computed under partially resolved conditions are presented in Fig. 11 and are seen to reproduce the observed patterns well.

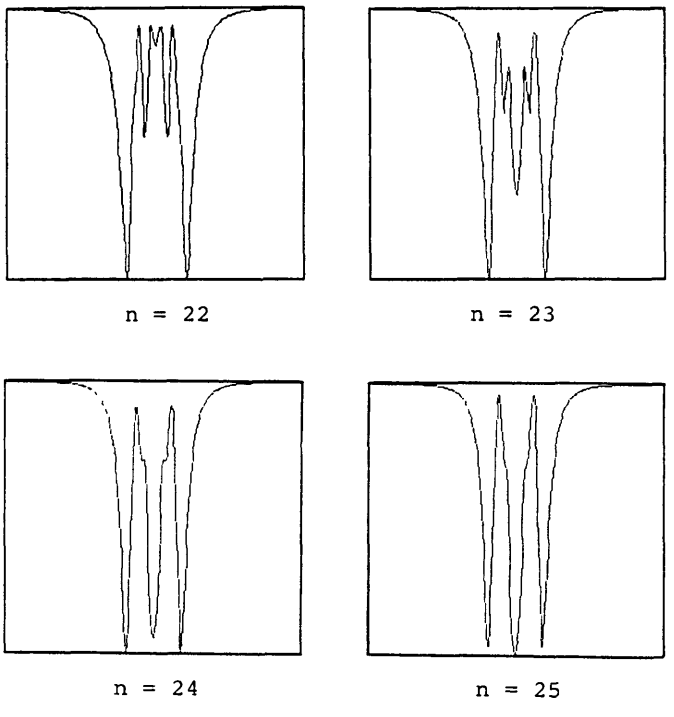

Fig11
Examples of computed profiles under partially resolved conditions.
The corresponding experimental profiles are shown in Fig.10.

The plot of oscillator strengths given in Fig. 7 was obtained by using dispersion theory and the simpler of the two computer codes described above. Although the trend of the data at high n is much more satisfactory than the one obtained from earlier measurements by the 'hook' technique (Parkinson Reeves and Tomkins (1976), there are still departures from the straight line in Fig. 7 which we do not understand, in particular (i) around n = 18 and (ii) for n = 25, 26, 27 and 28.

Considering (i) first, it is interesting that the 'hook' data (also shown in Fig. 7) exhibit a jump between n = 17 and n = 18 which is even more pronounced than in the present data. Our error estimate is +-1.8% at n = 18, and the departure from linearity in our data therefore seems significant. Esherick (1977 Fig. 3) has presented a quantum defect plot based on the earlier data by Garton and Codling (1968) which also shows a departure from linearity at n = 18, although there seems to be no perturber nearby. With this in mind, we have re-investigated the upper members of the principal series in Sr I up to n = 85 in zero field. Our new data (Fig. 12) show no sign of perturbations in the quantum defect, or of any transitions to triplet states. even at the highest values of n recorded.

We have therefore searched for a possible source of systematic error in the f-value measurements around n = 18. Between n = 17 and 18, there occurs an impurity line at 2201.42 Å which is due to $7p\,^1P_1$ in Ca I. In the presence of the field, this absorption line disappears and is replaced by a pair of magneto-optical intensity maxima, thus confiming that the impurity is only present within the absorption column inside the high-field region. From the known f-value of the Ca I transition (Parkinson Reeves and Tomkins 1976), we calculate a Ca/Sr ratio in the vapour of ~10-4. The additional rotation due to this line might conceivably be a source of error in our measurements, since its f-value is about 30 times greater than that of the n = 18 line in Sr I, but further work is needed to confirm this possibility.

In Fig. 13, we demonstrate that the departure from linearity at n = 18 is a real effect by giving both experimental and calculated profiles.

Turning now to (ii), it will be noticed that the values around n = 25, 26, 27 and 28 in Fig. 7 lie below the 'best' straight line through the data points, and that the discrepancy increases systematically with increasing n-value. Our estimates suggest that the errors are +-3.7%, 5.6%, 6.7% and 8.3% respectively for these transitions and that the departure from linearity is barely significant. Nevertheless, the systematic trend in Fig. 7 does suggest some underlying reason for it.

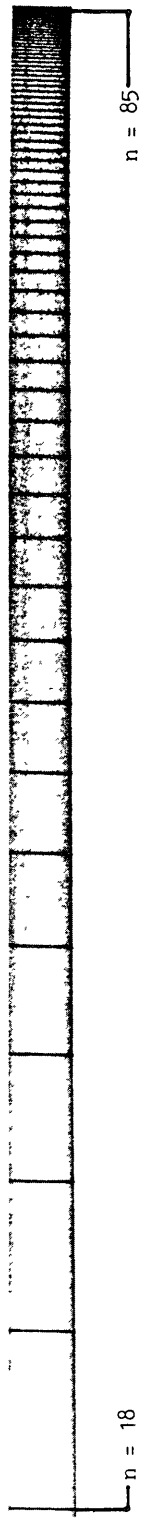

Fig. 12. Zero-field spectrum of Sr I. Note the absence of any transition to triplet states, even at the highest n-values.

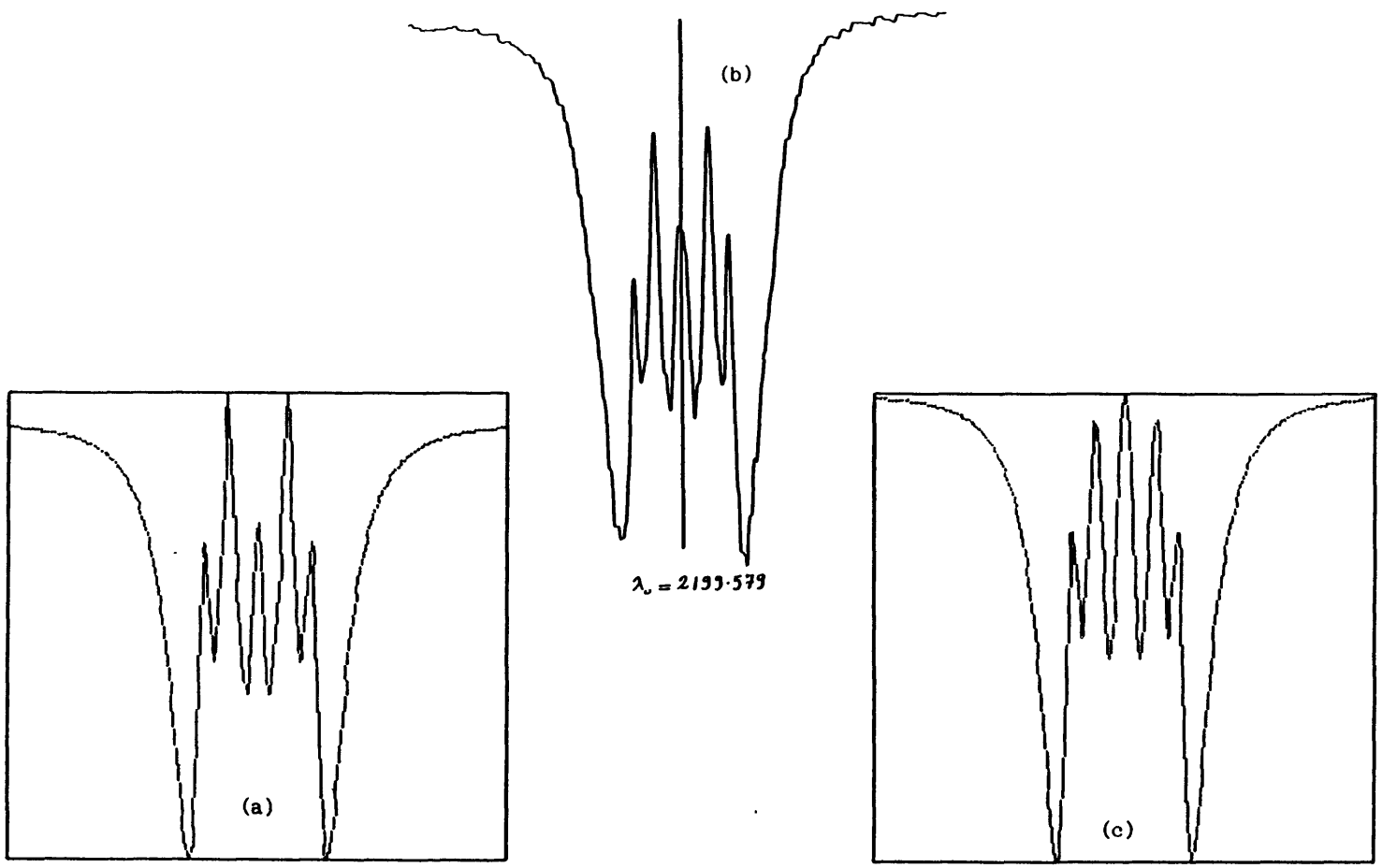

Fig. 13 - Experimental and calculated magneto-optical patterns for n = 18 in Sr I (a) closest calculated fit to the data (b) experimental profile and (c) calculated to agree with the straight line in Fig. 7 exactly (see text).

At time of writing, we can only speculate that this trend might be due to perturbations in the f-value produced by the applied magnetic field. It would seem quite reasonable that such perturbations should become important at n-values around 25: the data of Garton and Tomkins (1969) show that l-mixing satellites appear around n = 30 in fields of 40kG and, indeed, our own spectra show (Fig. 14) that the data become uninterpretable above n = 28 because of high field effects. It is an open question what further information could be derived from our data at high n-values. We are in possession of data recorded at several field strengths which would allow us in principle to search for systematic changes in f-value as a function of the applied magnetic field. Our analysis is still in progress, but first results indicate that it may be necessary to repeat our experiments at still higher fields to reveal the trend, and this will require an upgrade of our superconducting magnet.

One of the advantages of holding the magnetic field constant as we have done in our experiment is that high fields are readily obtained and effects due to the field are easily probed. This opens up exciting prospects for the application of the MOV technique to studies of high field effects.

Conclusion. - We have demonstrated a novel technique for the measurement of atomic oscillator strengths, which achieves a higher accuracy and sensitivity than other previously known methods. The new approach requires further development, both experimental and theoretical to be applied to full advantage. For example, in its present form, the theory has only been worked out in detail for singlet to singlet transitions. Also, it may be more appropriate to use a laser rather than a synchrotron radiation source, and sub-Doppler techniques could probably be applied with advantage. The new method holds great promise for the study of perturbations in f-value due to high external magnetic fields.

Acknowledgements. - The present work received financial support from the S.E.R.C. (UK) and the B.M.F.T. (West Germany). We are also grateful to the Argonne National Laboratory (Illinois, USA) for the loan of the superconducting magnet.

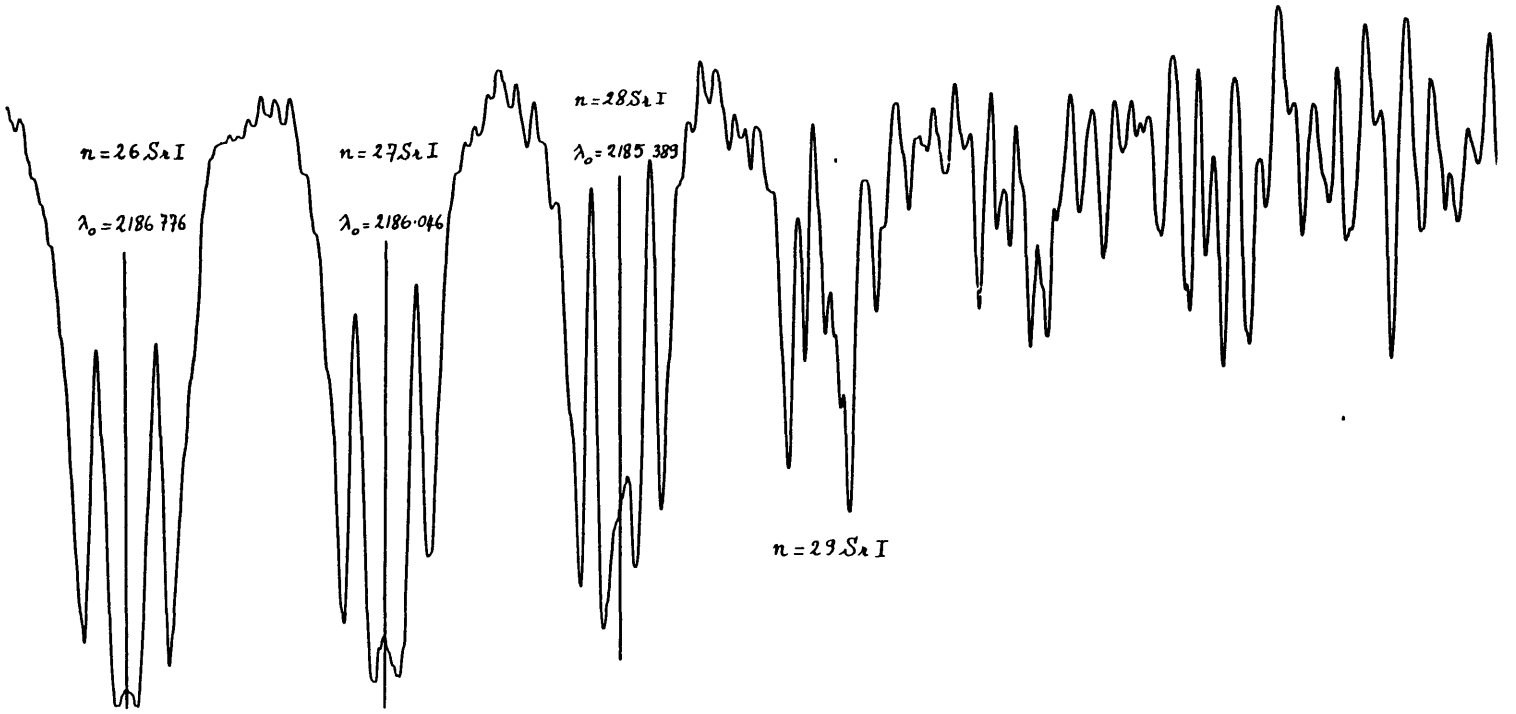

Fig. 14 - Showing the uppermost series members of Sr I in a field of 4.2 T. Note the increase in complexity of the spectrum above n = 28 which is attributed to l-mixing.

JOURNAL DE PHYSIQUE

Colloque C2, supplément au n°11, Tome 43, novembre 1982 *page* C2-317

MAGNETIC ROTATION SPECTROSCOPY WITH SYNCHROTRON RADIATION

J.P. Connerade*, W.R.S. Garton*, M.A. Baig, J. Hormes, T.A. Stavrakas * and B. Alexa

**Blackett Laboratory, Imperial College, London SW7 2AZ, U.K.*

Physikalisches Institut, Universitat Bonn, 53 Bonn, F.R.G.

Résumé: Nous décrivons des expériences récentes où la polarisation linéaire du rayonnement synchrotron dans le plan de l'orbite a été exploitée pour étudier les effets combinés de la biréfringence magnétique circulaire (effet Faraday) et du dichroisme magnétique circulaire (MCD) dans l'ultraviolet. A l'heure actuelle, nos études portent sur les séries principales des alcalino-terreux dans des champs magnétiques allant jusqu'à 4,6 Tesla. Nous avons pu observer des oscillations d'intensité dues à l'effet Faraday jusqu'à n=28 environ. Au-dessus de cette valeur, les structures supplémentaires dues au mélange de l en champ intense compliquent l'interprétation du phénomène. A partir de nos mesures, nous avons pu, par une méthode nouvelle, déduire les forces d'oscillateur relatives des transitions atomiques avec une précision qui va jusqu'a + - 0,25%, et qui dépasse donc largement celle des meilleures déterminations antérieures. Notre méthode offre aussi, du moins en principe, l'avantage de permettre l'étude des perturbations de la force d'oscillateur en présence d'un champ magnétique intense. Enfin, elle ne nécessite qu'une optique réfléchissante et peut donc être utilisée dans l'ultraviolet lointain.

Abstract: We describe recent experiments in which the linear polarisation of synchrotron radiation in the orbital plane has been exploited to study the combined effects of magnetic circular birefringence (Faraday rotation) and magnetic circular dichroism (MCD) in the ultraviolet. To date, our experiments have concentrated on the principal series of alkaline-earths in magnetic fields of up to 4.6 Tesla. We have observed intensity oscillations due to Faraday rotation up to about n=28. Above this value, additional structures due to l-mixing in high fields complicate the interpretation of the patterns. From our measurements, we have been able to deduce relative oscillator strengths of atomic transitions by a novel technique. The precision of these determinations can be as high as + - 0.25% in favourable cases, and is thus considerably higher than in earlier measurements using different techniques. Also, the present method has the advantage that, in principle, one could investigate perturbations of the f-value by intense magnetic fields. Finally, it requires only reflecting optics and can therefore be used in the vacuum ultraviolet.

Introduction. - The present paper is a report on experiments recently performed at the 500 MeV electron synchrotron of the Physikalisches Institut in Bonn, where a laboratory specialised in high resolution vacuum ultraviolet spectroscopy has been set up in collaboration with the Blackett Laboratory, Imperial College. An example of investigations carried out in Bonn using the same source and spectrographic apparatus as the present work is given by Connerade Baig Garton & McGlynn (1980).

In the experiment described below, the high degree of linear polarisation of synchrotron radiation in the orbital plane of the accelerator has been exploited to study the combined effects of magnetic circular birefringence (Faraday rotation) and magnetic circular dichroism from 2300 to about 1600 angstroms.

Nuclear Instruments and Methods 208 (1983) 841–843
North-Holland Publishing Company

MEASUREMENTS OF ATOMIC *f*-VALUES BY MAGNETO-ROTATION IN THE VUV

B. ALEXA, M.A. BAIG, J.P. CONNERADE, W.R.S. GARTON, J. HORMES and T.A. STAVRAKAS
Physikalisches Institut der Universitat Bonn, Germany, and Blackett Laboratory, Imperial College, London, England

We report a technique of exploiting plane polarized radiation from the Bonn 0.5 GeV synchrotron and the surprisingly high degree of polarization shown by a close-ruled holographic grating of 3 m radius, as a means of extracting atomic *f*-values from measurements of Faraday rotation in the neighbourhood of absorption lines of a gas in a magnetic field. The technique has novel and apparently promising features for work over most of the Schumann region. Since full descriptions are already in course of publication [1,2], only the essential outlines are given here.

The main objective of the experimental programme in Bonn, as regards Zeeman spectroscopy, has been towards study of diamagnetic shifts, splittings and configuration mixing effects in long Rydberg series. To our knowledge we have revealed the first resolved Zeeman patterns below 2000 Å to be recorded in the literature. Presumably previous lack of such observations has been due to a combination of scarcity of instruments of sufficient resolution and magnets of high enough field, problems associated with focussing and polarizing optical components in the VUV and of sources of polarized light, and of solving this group of problems in a single laboratory. Use of the plane polarized light from the synchrotron overcomes some of these problems, and we have also available modern holographically-produced close-ruled gratings and high-field superconducting magnets. The general layout of our apparatus is given in fig. 1.

Our first experiment showed well resolved structures in series lines of Mg I and Yb I, which will be the subject of other papers. In course of the experiments we discovered that the grating used (approx. 5000 lines/mm) showed strong polarizing properties over the range 1600–2500 Å, and possibly below 1600 Å. Specifically, the grating is several times more efficient for light with the electric vector parallel to the ruling, than traversely. As a result every absorption line has a Faraday rotation pattern-extending from the wings and through the core of the line. By using classical electromagnetic theory it is possible to derive *f*-values from measurement of the photometric traces like fig. 2. in effect we achieve the advantages of MOR measurements and those of MCD which, with the exception of recent work by Gawlik et al. [3], on the D-lines of Na I, have normally been the objectives of different experiments.

The method we have developed gives, we believe, values which are as good as or better than those of the other method of wide range for the determination of *f*-values, namely that of "Hooks". As illustration we compare in table 1 values of the Sr I *f*-values for the principal series (5s–*n*p) with previous values derived by the method. In this comparison we have to note, however, that recent improvements in the use of the "hook method" [4,5], might improve the values listed in the table by as much as a factor of 10 for this method.

We have now sufficient data and interpretation to

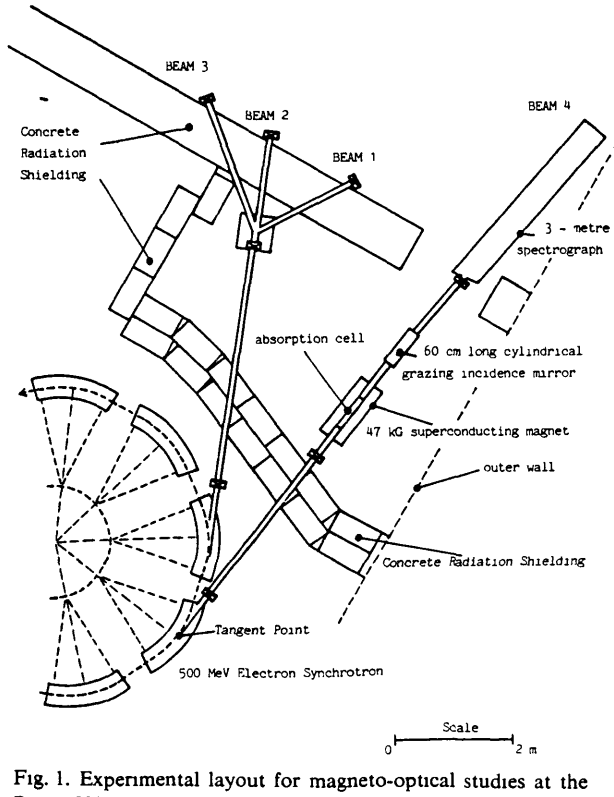

Fig. 1. Experimental layout for magneto-optical studies at the Bonn 500 MeV electron synchrotron. For clarity, the experiments on beam lines 1, 2 and 3 are not shown

0167-5087/83/0000–0000/$03.00

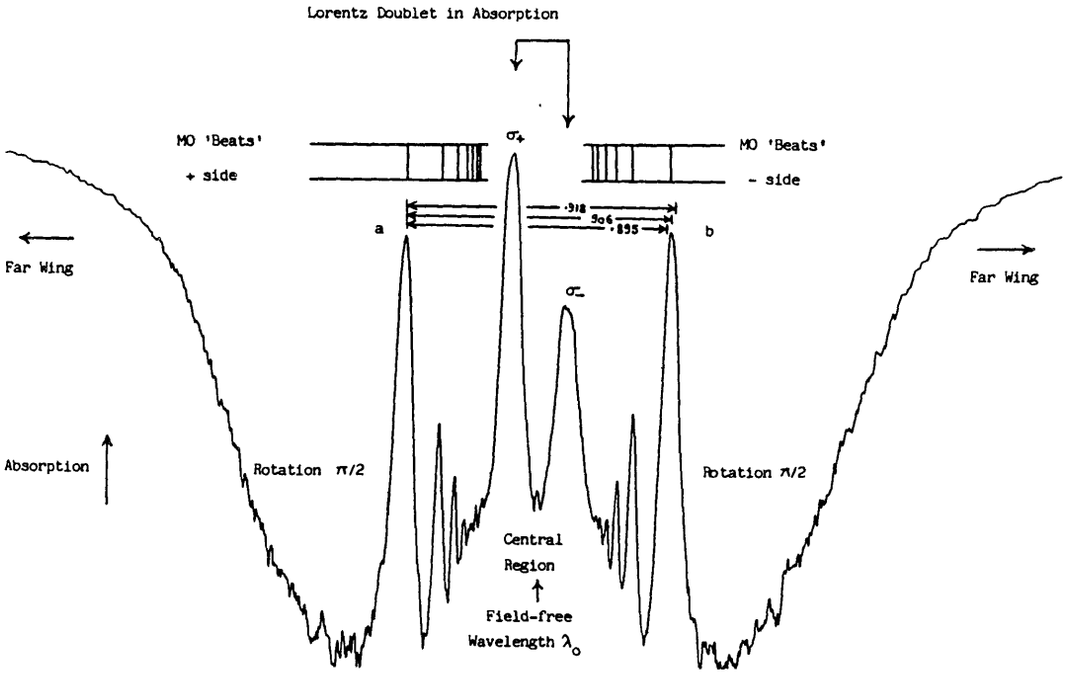

Fig. 2 A typical well-resolved magneto-optical pattern (for $n = 11$ in Sr I).

know that the existing system is good to at least 1600 Å. We expect the advantages of the method to enable us to work to shorter wavelengths, although we have as yet no knowledge of how well the degree of polarization of the grating behaves as the angle of incidence is diminished. If this falls off seriously we have the possibility of working in the second order, by which means we could then certainly be able to reach 1200 Å and below

Table 1
f-values for Sr I.

n	λ_0(Å)	n^*	f (present)	f (ref 7)	f (ref 6)
11	2253.954	8 372	0 00851 [a]	0 00891 ± 15%	0 00851 ± 12%
12	2238.350	9 346	0 00531 ± 0 6%	0 00525 ± 15%	0 00513 ± 12%
13	2226.997	10.330	0 00351 ± 0 7%	0 00372 ± 15%	0.00363 ± 12%
14	2218.507	11 319	0.00258 ± 0 8%	0 00257 ± 15%	0 00257 ± 12%
15	2211.999	12.311	0 00187 ± 1 3%	0 00209 ± 15%	0 00186 ± 12%
16	2206 927	13.302	0.00141 ± 1 5%	0 00148 ± 15%	0 00145 ± 15%
17	2202.863	14 302	0 00110 ± 1 7%	–	0 00107 ± 15%
18	2199.579	15 301	0 000924 ± 1 8%	–	0 00098 ± 15%
19	2196.900	16 294	0.000696 ± 1 9%	–	0 00078 ± 15%
20	2194 663	17 292	0 000555 ± 2 0%	–	0 00066 ± 15%
21	2192 788	18 290	0 000447 ± 2 2%	–	0 00058 ± 15%
22	2191.196	19 293	0 000378 ± 2 6%	–	0 00050 ± 20%
23	2189 841	20 288	0 000309 ± 3 2%	–	0.00042 ± 20%
24	2188 673	21.286	0 000268 ± 3 6%	–	0 00033 ± 20%
25	2187 652	22.288	0 000218 ± 3 7%	–	0 00031 ± 20%
26	2186 776	23 373	0 000179 ± 5 6%	–	0 00026 ± 20%
27	2186 046	24 281	0 000149 ± 6 7%	–	–
28	2185.389	25 273	0 000119 ± 8 3%	–	–

[a] All the present values are normalized onto the $n = 11$, f-value given by ref 6 which is regarded as exact when specifying the error bars in the column of present measuements

We are grateful to Argonne National Laboratory, acting through Dr. F.S. Tomkins for an extended loan of the superconducting solenoid used in this work at Bonn. The work has been supported by the Bundesministerium fur Forschung und Technologie, from funds for synchrotron radiation research, and by a grant from the Science & Engineering Research Council. On of us (J.H.) is grateful to the Deutsche Forschungsgemeinschaft for a research award.

References

[1] J.P Connerade, to be published.
[2] W R.S. Garton, J.P. Connerade, A Baig, J Hormes and B. Alexa, to be published.
[3] W Gawlik, J. Kowalski, R Neumann, H. Wiegeman and K. Winkler, J Phys B 15 (1979) L5
[4] M.C E. Huber and R.J. Sandeman, Phys Scr 22 (1980) 373
[5] R J. Sandeman, App Opt 18 (1979) 3873.
[6] W Parkinson, E.M Reeves and F S. Tomkins, J. Phys. B 9 (1976) 157.
[7] N.P. Penkin and L M Shabanova, Opt Spectrosc 12 (1962) 1.

In preparation

High Resolution Magneto-Optical Spectroscopy in the Ultraviolet

by

J.P. Connerade, T.A. Stavrakas and M.A. Baig

Blackett Laboratory, Imperial College, London SW7 2BZ

and

Physikalisches Institut der Universität Bonn, 53 Bonn, West Germany

Abstract

The Magneto-Optical method of measuring f-values is developed. First, the complex error function, the real part of which gives the absorption coefficient and the imaginary part, the refractive index, is shown to provide a better basis for the analysis of the data than earlier approximations. Secondly, the results are shown to be insensitive to various possible choices of apparatus function. Thirdly, the influence of overlapping patterns on the measurement of relative f-values is assessed and an experimental example of overlapping patterns from different species is calculated in full, the comparison being made over a wide range of parameters.

A criterion is given for a magneto-optical pattern to be considered as isolated, and an improved 'far-wing' approximation is derived from the analysis.

1. Introduction: Synchrotron Radiation and the MOV Method.

The properties of the electromagnetic field radiated by n equidistant electrons moving in a circle with uniform velocity were first studied by G.A. Schott (1912), whose work has been neglected for many years, probably because the reference is now difficult to find. It is very appropriate to remember him here because of the following statement, to be found on page 109 of his book, after a detailed calculation of the polarization properties of each of the harmonic vibrations into which synchrotron radiation can be decomposed:

"At the equator, where $\theta=\frac{\pi}{2}$, the polarization is linear, the electric force being along the equator and the magnetic force perpendicular to it. Near the axis, where θ is very small, the polarization is approximately circular, but the harmonic j=1 alone has appreciable value. The direction of rotation is that of the electron in its orbit. As θ increases in passing from the axis to the equator, the polarization becomes elliptic, the axes of the vibration ellipse being in and perpendicular to the meridian; and the perpendicular axis predominates more and more".

I believe this to be the first statement of the polarization properties of synchrotron radiation. However, as it predates not only Schwinger's (1949) work, but even the construction of the first cyclotron (Lawrence and Livingston, 1932), the work of Schott (1912) seemed only an exercise in applied mathematics at the time. Probably, the motivation for his work lay in Rutherford's speculation that the atom might consist of electrons orbiting around point nuclei. Since Schott's (1912) calculations showed that, classically, such a system would soon radiate all its energy, this approach was soon dismissed.

On the way, Schott (1912) also found that the Bessel function expansion he was using only converges if the velocity of the electrons is smaller than that of light, and he even considered the effect on his equations of a new and rather daring theory due to A. Einstein, which seemed to help if one could believe it.

The present paper is concerned with the exploitation of the polarization of synchrotron radiation in the equatorial plane, which (as remarked above) is linear with the electric vector in the plane of the orbit.

We have utilised this property for studies of Faraday Rotation in the vacuum ultraviolet, where an alternative continuum source would be difficult to find. Since quite detailed descriptions of our own method have been published (Connerade et al 1982; Garton et al 1983; Connerade 1983), We do not repeat them here, and give only the briefest of summaries before discussing a more recent elaboration of our theoretical work.

We have developed a magneto-optical vernier (MOV) technique for measuring atomic f-values which is, we believe, the first application of synchrotron radiation in the field of Faraday Rotation. The fundamental equations on which

the method is based are given below. In essence, the technique depends on the very slow variation against f of magneto-optical patterns in the far wing against the rapid variation experienced in the centre of patterns. It is thus possible to make coarse adjustments to fit one part of the pattern and a fine adjustment to fit the rapidly changing pattern at the centre. We have achieved accuracies of fractions of a percent in a preliminary analysis of our data and, before embarking on more difficult experiments, we have decided to consolidate our study by optimising the computational approach, and by studying interactions between overlapping patterns.

2. Brief summary of technique

The method we are using is essentially a standard layout for the observation of Faraday rotation, namely an absorption cell within a solenoid, placed between crossed polariser and analyser, to ensure that, for zero field, transmission is at a minimum. Thus, for ideal optics, signal would only be detected either (i) in the presence of magnetic circular birefringence, i.e. Faraday rotation of the plane of polarisation or (ii) in the presence of magnetic circular dichroism, i.e. selective absorption of one circularly polarised component in the Zeeman pattern.

The unconventional aspects of our setup are as follows. First, we use the synchrotron itself as the polariser. Second, the experiment is performed in a very high field (more than 40 k Gauss) with a long solenoid (70 cm) which therefore produces rotations through many turns in the core of absorption line. Third, the experiment is performed at rather high resolution (>300,000) in the ultraviolet, so that the stability of furnace and field strength during an exposure lasting a few minutes on Kodak SWR plates are, in fact, the limiting factors. Fourth, we use a high dispersion grating (5000 lines /mm) as the analyser, accepting that it does not behave as an ideal polariser (we make allowance for this fact in the analysis), which enables us to conduct the experiment with minimum loss of light. We have observed magneto-optical patterns down to about 1620Å using the Bonn 500 MeV electron synchrotron. A typical magneto-optical pattern is shown in Fig. 4 below.

3. Development of the MOV Method.

An introduction to the basic theory underlying the method is given by Buckingham (1969). The Magneto-Optical Vernier (MOV) method is a measurement technique described by Connerade (1983). The following discussion assumes familiarity with both papers.

For a Maxwellian distribution of velocities, the probability P(v) dv of finding an atom with velocity v in the range v, v+dv is

$$P(v)\,dv = \frac{1}{\sqrt{\pi}\,v_0}\, e^{-\left(\frac{v}{v_0}\right)^2} dv \quad ; \quad v_0 = \sqrt{\frac{2kT}{m}}$$

where the symbols have their usual meanings. The absorption coefficients $a_{\pm}^{V}$ and refractive indices $n_{\pm}^{V}$ are then found by convolving the Lorentzian natural line shape $a_{\pm}^{L}(\nu)$ and the corresponding refractive index $n_{\pm}^{L}(\nu)$ with the Gaussian distribution $P(v)$ thus:

$$a_{\pm}^{V}(\nu) = \int_{-\infty}^{\infty} a_{\pm}^{L}\left(\nu - \frac{v\nu}{c}\right) P(v)\, dv \tag{1}$$

where $a_{\pm}^{V}$ then has the form of a Voigt profile, and

$$n_{\pm}^{V}(\nu) = \int_{-\infty}^{\infty} n_{\pm}^{L}\left(\nu - \frac{v\nu}{c}\right) P(v)\, dv \tag{2}$$

The quantities $a_{\pm}^{L}$ and $n_{\pm}^{L}$ are then given by standard dispersion theory as

$$a_{\pm}^{L}(\nu) = \frac{e^2 N f}{mc} \frac{(\Gamma/4\pi)}{(\nu - \nu_0 \pm \alpha)^2 + (\Gamma/4\pi)^2} \tag{3}$$

and

$$n_{\pm}^{L}(\nu) - 1 = \frac{e^2 N f}{4\pi m} \frac{1}{(\nu_0 \pm \alpha)} \frac{\nu - \nu_0 \pm \alpha}{(\nu_0 - \nu \pm \alpha)^2 + (\Gamma/4\pi)^2} \tag{4}$$

in which $\alpha = e\beta/4\pi mc$ and $\Gamma/4\pi$ is the natural line width.

in an earlier paper (Connerade 1983), the complexities of the convolution (1) and (2) were circumvented by a somewhat crude approximation: $\Gamma/4\pi$ was taken as equal to the Doppler halfwidth and $a_{\pm}^{V}(\nu)$, $n_{\pm}^{V}(\nu)$ were taken to have the simple forms predicted by dispersion theory, before convolution with an apparatus function. Although excellent agreement with experiment was obtained, this might be considered artificial in that a number of parameters were adjusted for optimum fit to the data.

The present paper seeks to improve the theoretical basis for the MOV method by adopting a more rigorous approach. First, the correct form is taken for $a_{\pm}^{V}(\nu)$ and $n_{\pm}^{V}(\nu)$. Substituting (3) and (4) into (1) and (2) respectively, we have

$$a_{\pm}^{V}(\nu) = \frac{e^2 N f \gamma}{\sqrt{\pi}\,\Delta\nu_D\, mc} \int_{-\infty}^{\infty} \frac{e^{-y^2}\, dy}{[(\bar{\nu} \mp \bar{\alpha}) - y]^2 + \gamma^2} \tag{5}$$

and

$$n_{\pm}^{V}(\nu) - 1 = \frac{e^2 N f}{\pi^{3/2} \Delta\nu_D\, 4m} \frac{1}{\nu_0 \pm \alpha} \int_{-\infty}^{\infty} \frac{[(\bar{\nu} \mp \bar{\alpha}) - y]\, e^{-y^2} dy}{[(\bar{\nu} \mp \bar{\alpha}) - y]^2 + \gamma^2} \tag{6}$$

where $\gamma = \frac{\Gamma}{4\pi\Delta\nu_D}$, $y = \frac{\nu' - \nu_0}{\Delta\nu_D}$, $\bar{\alpha} = \frac{\alpha}{\Delta\nu_D}$ and $\bar{\nu} = \frac{\nu - \nu_0}{\Delta\nu_D}$ is the detuning expressed in Doppler widths $\Delta\nu_D = \nu_0 v/c$, and ν' is the variable of integration.

As suggested in the earlier paper (Connerade 1983), the algorithm of Hui et al (1978) has been applied for rapid computation of the complex error function. This leads directly to the integrals in both (5) and (6) by an argument which can be regarded as an expression of the Kramers-Kronig relations. The argument runs as follows: the complex error function is defined as

$$\psi(z) = e^{-z^2}\left[1 + \frac{2i}{\sqrt{\pi}} \int_0^z e^{-t^2} dt\right]$$

whence

$$\psi(z) = \begin{cases} P(z) & \text{for } Im(z) > 0 \\ P(z)\, 2e^{-z^2} & \text{for } Im(z) < 0 \end{cases}$$

where

$$P(z) = \frac{i}{\pi} \int_{-\infty}^{\infty} \frac{e^{-t^2} dt}{z - t} \tag{7}$$

By substituting t=y, $z=(\bar{\nu} \mp \bar{a}) - y + i\gamma$, we have from (7)

$$P(\bar{\nu}) = \frac{\gamma}{\pi} \int_{-\infty}^{\infty} \frac{e^{-y^2} dy}{[(\bar{\nu} \mp \bar{a}) - y]^2 + \gamma^2} + \frac{i}{\pi} \int_{-\infty}^{\infty} \frac{[(\bar{\nu} \mp \bar{a}) - y] e^{-y^2} dy}{[(\bar{\nu} \mp \bar{a}) - y]^2 + \gamma^2} \tag{8}$$

Thus, for Im(z)>0, the real part of p(z) above yields the form of the absorption coefficient (Voigt profile) while the imaginary part yields the corresponding refractive index. The condition Im(z)>0 is always satisfied here since γ, the linewidth expressed in Doppler widths, is positive definite.

Following Hui et al (1978) the complex error function was calculated as a quotient

$$P(z) \simeq \frac{\sum_{i=0}^{q} a_i z^i}{z^{q+1} + \sum_{i=0}^{q} b_i z^i} \tag{9}$$

where q= 6 and the coefficients a_i and b_i are tabulated (Hui et al.). The errors involved in using this approximation are less than one part in 10^6.

The results obtained in this way are then substituted in equation (9) of Connerade (1983) to calculate the intensity transmitted by the crossed polarisers as a function of frequency. Fig.1 shows the magneto-optical oscillations obtained in this way for a typical choice of parameters (for n=11 of Sr I).

Before a comparison with experiment can be made, the spectrum of Fig.1 must be convolved with an apparatus function. Unfortunately, the appropriate function cannot be determined from a separate experiment, because it involves the fluctuations in furnace conditions and magnetic field strength as well as spectrograph resolution. In all experiments performed to date, these fluctuations produced the largest broadening and also varied from one exposure to the next. Connerade (1983) therefore arbitrarily adopted a 'top hat' apparatus function which is easy to calculate and simply varied its width to obtain the optimum fit for a complete experimental spectrum.

Since Connerade's (1983) choice of apparatus function is arbitrary, it could lead to systematic errors in the interpretation of the data. We have investigated this source of error by performing the analysis with three different apparatus functions. Details of the procedure are as follows. The convolution integral was evaluated numerically over the finite range $\pm 2\,\Delta\nu_A$, where $\Delta\nu_A$ was the FWHM of the apparatus function and was treated as an adjustable parameter starting from the value given by Connerade (1983). A mesh of 100 points proved adequate for the integration. As $\Delta\nu_A$ was increased, the fine detail apparent in Fig.1 was lost, and the narrow oscillations became much weaker. It was found that

a 10% change in $\Delta\nu_A$ led to only a 0.1% error in the determination of the f-value - an indication of how insensitive the analysis is to the choice of apparatus function.

To explore this point further, we performed the convolution with the following three choices of instrumental function:

$$L^L(\nu,\nu') = \frac{\Delta\nu_L^A/2\pi}{(\nu-\nu')^2 + (\Delta\nu_L^A/2)^2}$$

$$L^G(\nu,\nu') = \frac{e^{-[(\nu-\nu')/\Delta\nu_G^A]}}{\sqrt{\pi}\ \Delta\nu_G^A} \qquad (10)$$

for $|\nu-\nu'| \leq \Delta_T^A$:

$= 0 \qquad L^T(\nu-\nu') = 0$

for $|\nu-\nu'| > \Delta\nu_T^A$:

$$L(\nu,\nu') = \frac{1-\left(\frac{\nu-\nu'}{\Delta\nu_T^A}\right)^2}{\Delta\nu_T^A}$$

all of which are normalised to unity, with widths $\Delta\nu_L^A$, $\Delta\nu_G^A$ and $\Delta\nu_T^A$ chosen to give the same FWHM in all three cases.

The effect of the different instrumental functions is as follows: the Gaussian, with its exponential decay in the far wings, selects more information from the immediate vicinity of the frequency ν while the Lorentzian takes more from the wings. The triangular function, like the 'top hat' function used by Connerade (1983) selects only a finite band of frequencies around ν. Nonetheless, Gaussian, Lorentzian or triangular functions all lead to closely similar results for the energies of the peaks and the overall appearance of the patterns (see Fig.2). The differences between the three are mainly in the level of transmitted intensity (which cannot anyway be determined accurately from a photographic record) and, (to a much lesser degree) in the sharpness of the oscillations (which can in practice be corrected for by a slight adjustment of the assumed half-width). All the calculations of Fig.2 were performed with identical half-widths for the apparatus function to bring out the differences more clearly.

The conclusion reached from this test was that the results are essentially independent of the choice of apparatus function. Convolving with a Lorenzian is a fairly realistic assumption and is more economical on computing time than convolving with a Gaussian, because there is no need to evaluate exponentials. It was therefore adopted as a convenient scheme for the convolution.

Next, we verified that the magneto-optical cycles, the properties of which

are fundamental to the accuracy of the MOV method, possess the same variation as in the earlier calculations based on approximated profiles. Samples of the cycle structure are shown in Fig.3. The accuracy of the MOV method depends on the rapid intensity variation with NfB on resonance as compared to the line wings, and the figure shows how this can fall off with increasing principal quantum number if a sequence of measurements is performed under identical experimental conditions.

The computations, carried out on a mesh of 1000 points, were too complex for a small computer and were therefore carried out on the CDC 7600 at Imperial College.

The improvement over the earlier approximate calculations is illustrated in Fig.4. Using our new code, we investigated the effect which substantial experimental errors in the determination of furnace temperature and applied magnetic field (much larger than the probable errors) would have on the accuracy. We found that a 40% error in measuring the temperature leads to a 0.1% error in the relative f-value determination, while 4.5% error in determining the magnetic field strength produces 0.3% error in the relative f-values.

4. Experimental Investigation of Overlapping Magneto-Optical Patterns

A basic difficulty in accurate methods of determining f-values from refractive index measurements, as pointed out in the Introduction, is the influence which the proximity of another transition (either from an impurity or from the same atom) can have on the experimental result. This problem arises in several ways. Thus, Garton et al. (1983) argue that the $n = 18$ f-value determination in Sr I is influenced by the proximity of a Ca I impurity line of much higher oscillator strength, so that a small impurity concentration of Ca in the sample can upset the measurements by both the hook (Parkinson et al 1976) and magneto-optical techniques. More generally, the problem arises among the uppermost members of a Rydberg series, which become so closely spaced in energy that there is no longer enough interval for a properly resolved magneto-optical pattern to develop without overlap. Before changes in f-value due to incipient l-mixing can be investigated, it is important to understand the effects of overlap between magneto-optical patterns.

This source of error does not appear to have been investigated systematically. We describe now the effect it has on measurements by the MOV method.

An experiment was performed with the same apparatus as used by Garton et al.(1983). The sample was Ba metal, containing <1% Sr metal as an impurity. Two transitions, one at 2427.41 Å (15p $^1P_1$ in Ba I) and the other at 2428.09 Å (4d5p $^1P_1$ in Sr I), which lie only 0.68 Å apart, were observed. Since barium and strontium have different vapour pressures, slight variations in temperature allow

large variations in relative concentration of the two elements. It was found by experiment that patterns of comparable scale could be obtained from both lines over a range of furnace temperature from 700 to 1000°C. It was also possible to vary the magnetic field strength, thereby altering the degree of overlap of the patterns over a wide range. A typical sequence of overlapping patterns is illustrated in Fig. 5.

The variation of the Faraday angle φ through two adjacent patterns can occur either (i) without any cancellation of rotation when the patterns are sufficiently well separated in energy to retain individual identities or (ii) with cancellation of the positive rotation due to one line by the negative rotation due to the other when the patterns penetrate each other sufficiently to coalesce. The transition from (i) to (ii) can be abrupt as the data show, and the question arises whether the theory can account for it correctly.

The code described in section 2 was set up for two adjacent lines, and the experimental variations were computed in detail. The calculated profiles are also shown in Fig. 5. Thus, the theory is able to account for the structure of the observed patterns over the full range from (i) to (ii).

The data of Fig.5, on the other hand, were obtained for large rotation angles, and yield accurate values for the ratio R of the intense $5d8p\ ^3P_1$ line at 2432.52 A to the $15p\ ^1P_1$ line in the presence of differing degrees of overlap with the SrI impurity. The ratio R is plotted against the spread in wavelength of the impurity pattern in Fig.6, from which we see that accurate f-values can be extracted from the data even in the presence of overlap, provided a detailed analysis of the structures is performed.

It is interesting to compare the value of R obtained from Fig.6 with values obtained by earlier authors using different techniques, with (it seems) no allowance for the effect of the impurity line. It is difficult to form a correct assessment of the errors in R from earlier work, because only estimates of the errors in absolute f-values are given, and these are dominated by uncertainties in vapour pressure determinations which affect all the lines. Thus, Penkin and Shabanova (1962) quote an absolute error of 8 - 15 % and state that relative f numbers were measured with 'great accuracy', but the latter is unspecified. Table 1 summarises the available data.

Assuming that the presence of the impurity line at 2428.33 Å is the major source of error in all the earlier work, and taking our value for R, one obtains corrected values of f_2 (Table 1) which, for each set of data, are smaller than the published values. Thus, we believe that an overlap with the Sr I impurity line (which is normally present with available grades of 'pure' barium metal) was responsible for systematic errors ranging from 11% (Penkin and Shabanova,1961; Miles and Wiese, 1969) to 6% (Parkinson Reeves and Tomkins 1976) in relative f-value determinations involving the $15p\ ^1P_1$ transition. The errors are within the

error bars in the absolute values quoted by these authors, but are larger than one might expect for relative measurements.

It is also necessary to give a rough criterion for conditions under which a suspected overlap may need to be considered. The Faraday angle $\varphi(\nu)$ is given by

$$\varphi(\nu) = \frac{\pi\nu}{c}(n_+ - n_-)\ell \qquad (11)$$

where is the length of the furnace, and (6) must be used to evaluate n+ and n-. The integration can be performed analytically if $(\bar{\nu} \mp \bar{\alpha}) >> \gamma$, and an explicit (approximate) form for $\varphi(\nu)$ can thus be extracted, which of course is only valid outside the line core:

$$\varphi(\nu) = -\frac{N f \ell B e^3}{8\pi m^2 c^2} \frac{\nu(\nu - 2\nu_0)}{(\nu_0^2 - \alpha^2)[(\nu-\nu_0)^2 - \alpha^2]} \qquad (12)$$

If (12) is used to calculate the rotation due to the impurity line at a frequency ν where a measurement is being carried out, and $\varphi(\nu) > 10^\circ$, then a full calculation including the profile of the impurity line will be required for an accurate result. Expression (12) is itself accurate to about 10% as compared to the full formula, within its range of validity. It is thus superior in practice to the far wing approximation given by Mitchell and Zemansky (1934), and may find wide application in calculations of rotation angles.

5. Conclusion

An important limitation of all the work in the present paper is that the structures all possess especially simple Zeeman patterns. In principle, it is known that the resonant Faraday Rotation signal exhibits rapid oscillations even for more complex patterns, and equations from which full profiles can be derived are given by Mitchell and Zemansky (1971). Thus, we hope to extend our work to more complex atomic transitions.

Even so, there is an important class of experiments to which our method can already be applied. The properties of atoms in strong fields (Connerade Gay and Liberman 1982) are a subject of great current interest. Experiments show (Garton and Tomkins 1969; Gay Delande and Biraben 1980) that atomic f-valves must be modified by strong magnetic fields. Recently, the first ab initio calculations (Kara and McDowell, 1980; McDowell 1982 and references therein) of changes in atomic photoabsorption cross-section induced by strong fields have been reported. Interest therefore attaches to any experimental method accurate enough to detect small changes in f-value among closely spaced upper Rydberg members, under externally applied intense magnetic fields. The MOV method, it seems is ideally suited for this purpose.

REFERENCES

BUCKINGHAM, A.D.
1969 Symposia of the Faraday Society no 3
"Magneto-Optical Effects", London
CONNERADE, J.P.
1983 J. Phys. B 16,399
CONNERADE, J.P., GAY, J.C. and LIBERMAN, S. (Eds.)
1982 "Atomic and Molecular Physics
Close to Ionization Thresholds in High Fields"
C.N.R.S. International Colloquium no 334
Journal de Physique 43, Colloque c2
GARTON, W.R.S., CONNERADE, J.P., BAIG, M.A., HORMES, J. and ALEXA, B.
1983 J. Phys. B 16,389
GARTON, W.R.S. and TOMKINS, F.S.
1969 Astrophys. J. 158, 839
GAY, J.C., DELANDE, D. and BIRABEN, F.
1980 J. Phys. B 13,1720
HUI, A.K., ARMSTRONG, B.H. and WRAY, A.A.
1978 J. Quant. Spectrosc. and Radiat. Transfer 19, 509
KARA, S.M. and McDOWELL, M.R.C.
1980 J.Phys. B 13,1337
LAWRENCE, E.O. and LIVINGSTON, M.S.
1932 Phys. Rev. 40, 19
McDOWELL, M.R.C.
1982 Journal de physique 43, C2-387
MILES, B.M. and WIESE, W.L.
1969 Atomic Data 1,1-17
MITCHELL, A.C.G. and ZEMANSKY, M.W.
1971 "Resonance Radiation and Excited Atoms"
Cambridge University Press, Cambridge.
PARKINSON, W.H. REEVES, E.M. and TOMKINS, F.S.
1976 J. Phys B 9,157
PENKIN, N.P. and SHABANOVA, L.N.
1962 Optics and Spectroscopy 12,1
SCHOTT, G.A.
1912 "Electromagnetic Radiation" Adams Prize Essay Cambridge.
University Press, Cambridge.
SCHWINGER, J.
1949 Phys. Rev. 75, 1912

Table 1

f-values of the Ba lines at 2432.52Å ($5d8p\,^3P_1$) and at 2428.15 Å ($15p\,^1P$ and their ratio R as obta ined by various authors.

	PS	MW	PRT	Present
f1 ($5d8p\,^3P_1$)	.0022	.00251	.00191	
f2 ($15p\,^1P_1$)	.0018	.00209	.00148	
R = f1/f2	1.22	1.201	1.291	1.366 +- 0.01
f2 (corr.)	.0016	.00184	.00139	

PS stands for Penkin and Shabanova (1962)
MW stands for Miles and Wiese (1969)
PRT stands for Parkinson Reeves and Tomkins (1976)

Figure Captions.

Fig.1: A magneto-optical pattern before allowance is made for the finite spectral resolution of the apparatus. A limited efficiency (85%) of the crossed polarisers is assumed, as well as a slight apparent asymmetry between k+ and k- (1:1.15) - both of which are of instrumental origin. The calculation is for n = 11 of Sr I, with Nfl = 9.68×10^{14} cm , T = 700°C and B = 4.2 Tesla.

Fig.2: The effect of convolving the pattern of Fig.1 with various choices of apparatus function, showing (a) the comparison of a Lorentzian (solid curve) with a Triangular function (dashed curve) and (b) the comparison between a Lorentzian (solid curve) and a Gaussian (dashed curve), the convolution being performed as described in the text. The half width of the apparatus functions was 8.5×10^{10} Hz in all cases.

Fig.3: The MOV cycle structure for a number of transitions in Sr I. The figures are produced by incrementing Nfl in small steps and using three-dimensional graphics to display the resulting families of magneto-optical profiles. The scale of the change in Nfl is given in units of 10^{12} cm^{-2} for (a) n = 11 (b) n = 16 (c) n = 18 and (d) n = 24 of Sr I. The sensitivity of the cycle structure to changes in Nfl decreases with increasing n (principal quantum number) under otherwise identical experimental conditions.

Fig.4: Comparison between (a) present calculations (b) an experimental magneto-optical pattern and (c) Connerade's (1983) calculation for the n = 11 transition of Sr I.

Fig.5: A sequence of experimental traces for the overlapping patterns of BaI and SrI with T = 775°C and (a) B = 2.0 Tesla (b) B = 2.5 Tesla and (c) B = 3.0 Tesla. Calculated patterns are shown for comparison.

Fig.6: The ratio R of f-values defined in the text and given in Table I plotted as a function of the wavelength interval spanned by the impurity line, showing that R is very nearly independent of the overlap. Extrapolation to zero field gives R = 1.366 +- 0.010. The correspondence with the patterns of Fig.5 and the magnetic field strength are also given.

Note: all intensity scales are in arbitrary units and refer to theory only.

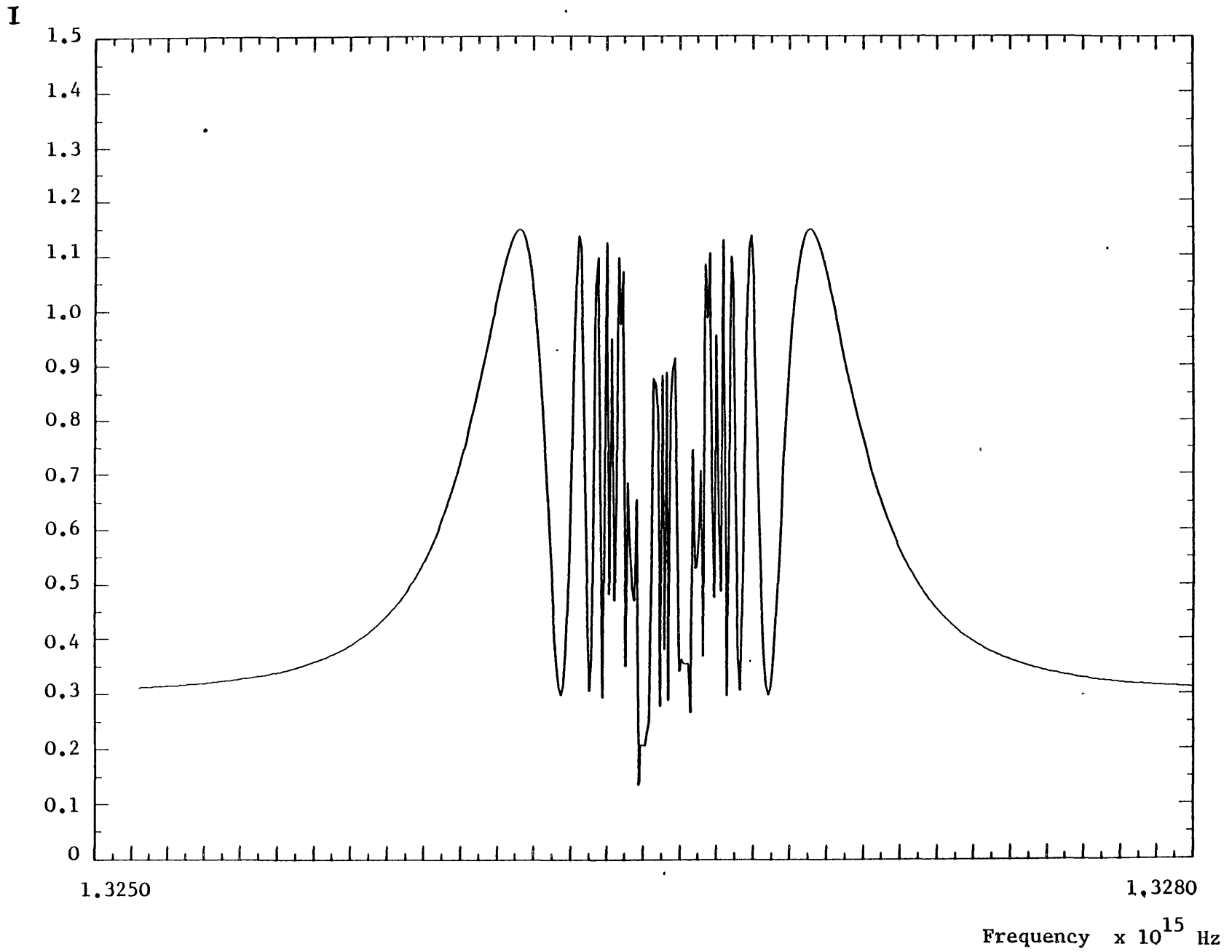
I
1.5
1.4
1.3
1.2
1.1
1.0
0.9
0.8
0.7
0.6
0.5
0.4
0.3
0.2
0.1
0
1.3250
1.3280
Frequency x 10^15 Hz

FIGURE 1

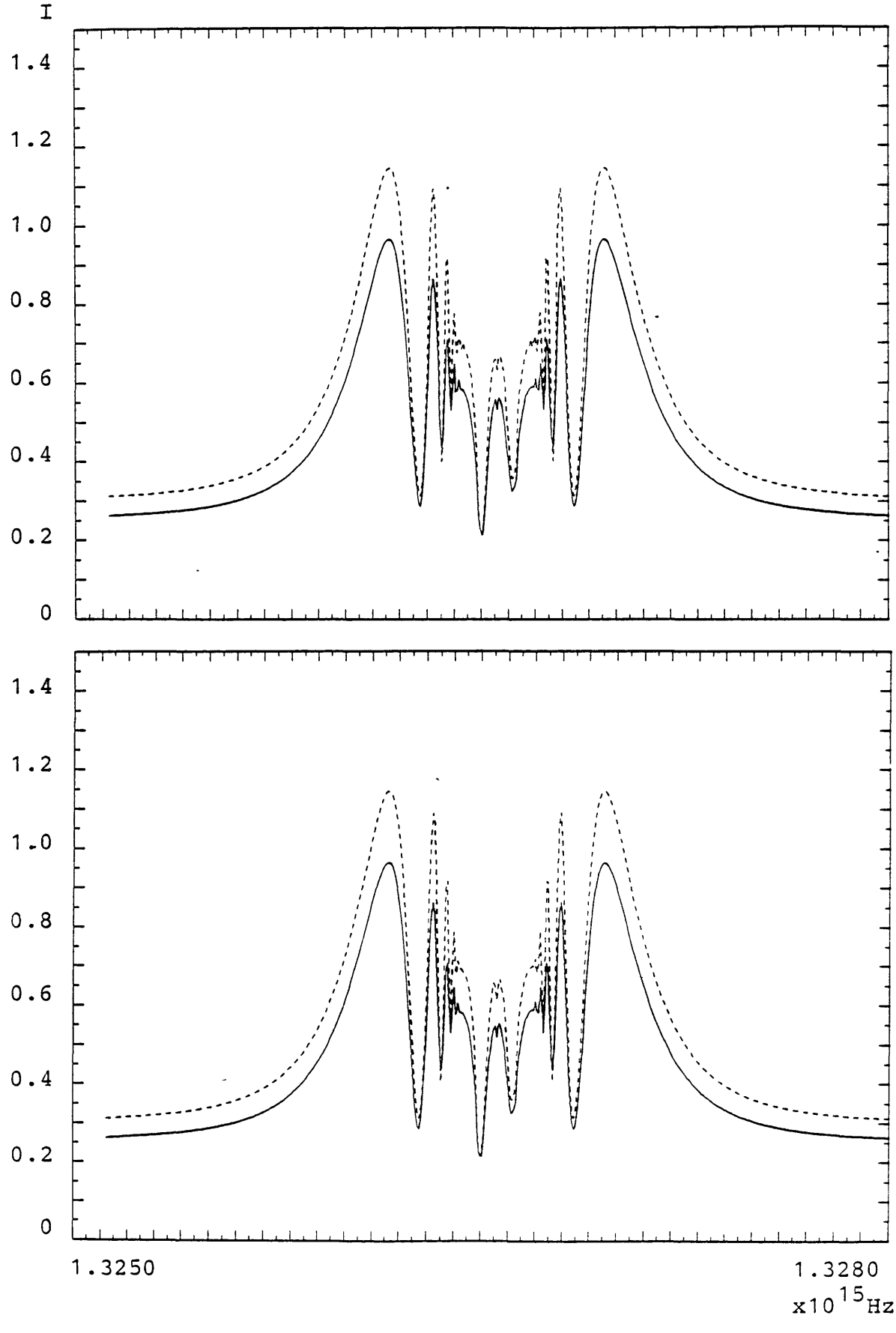

Fig. 2

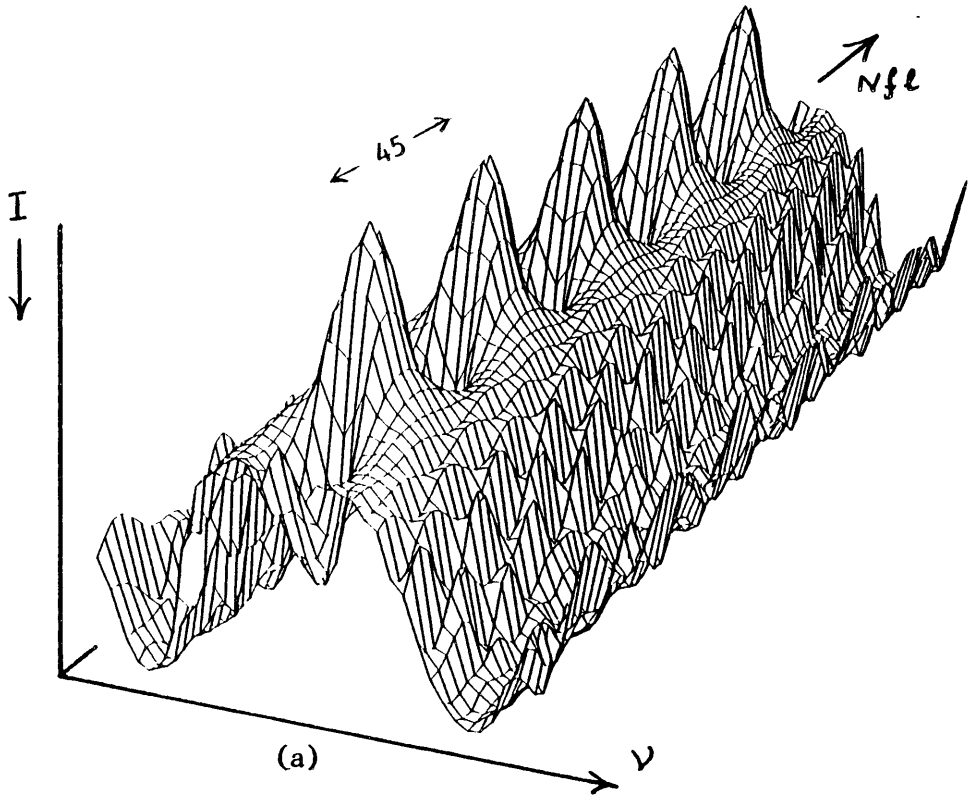

(a)

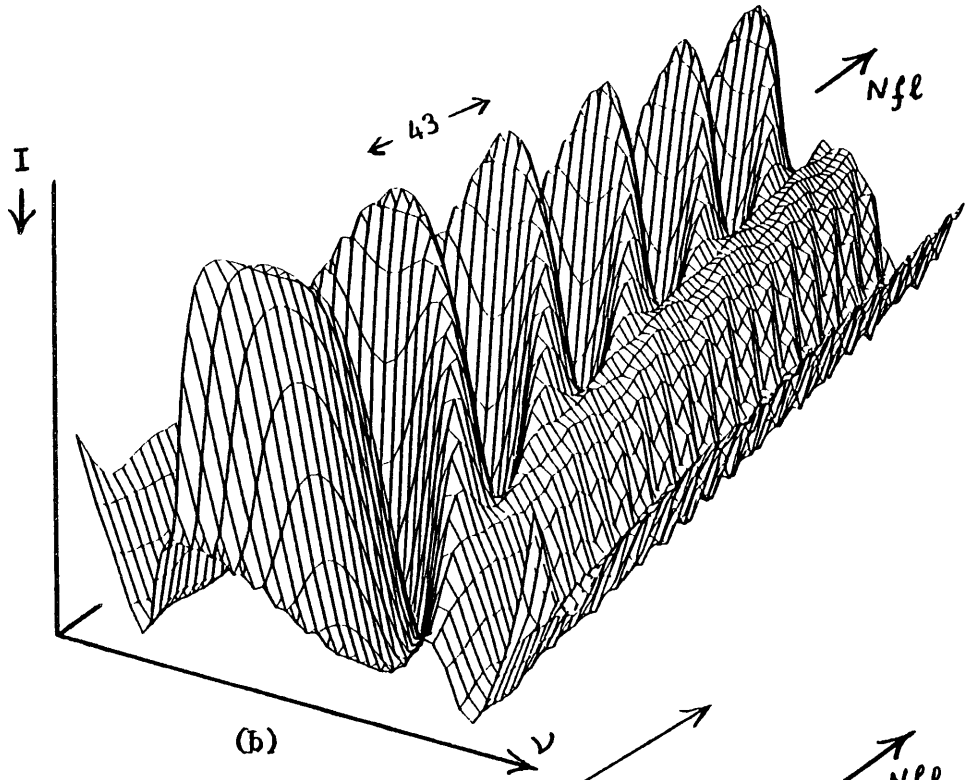

(b)

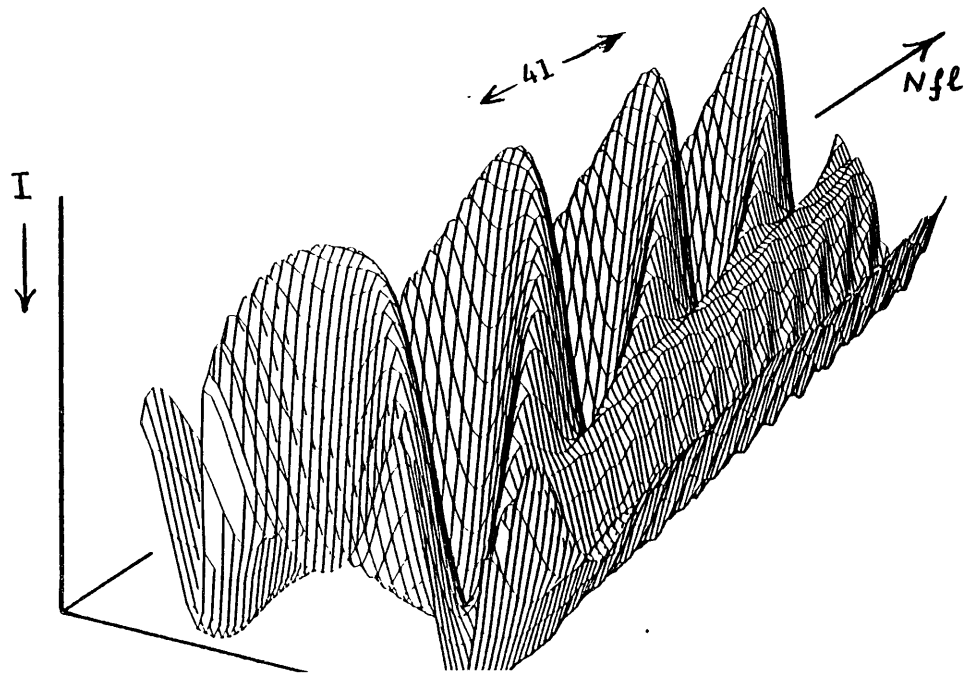

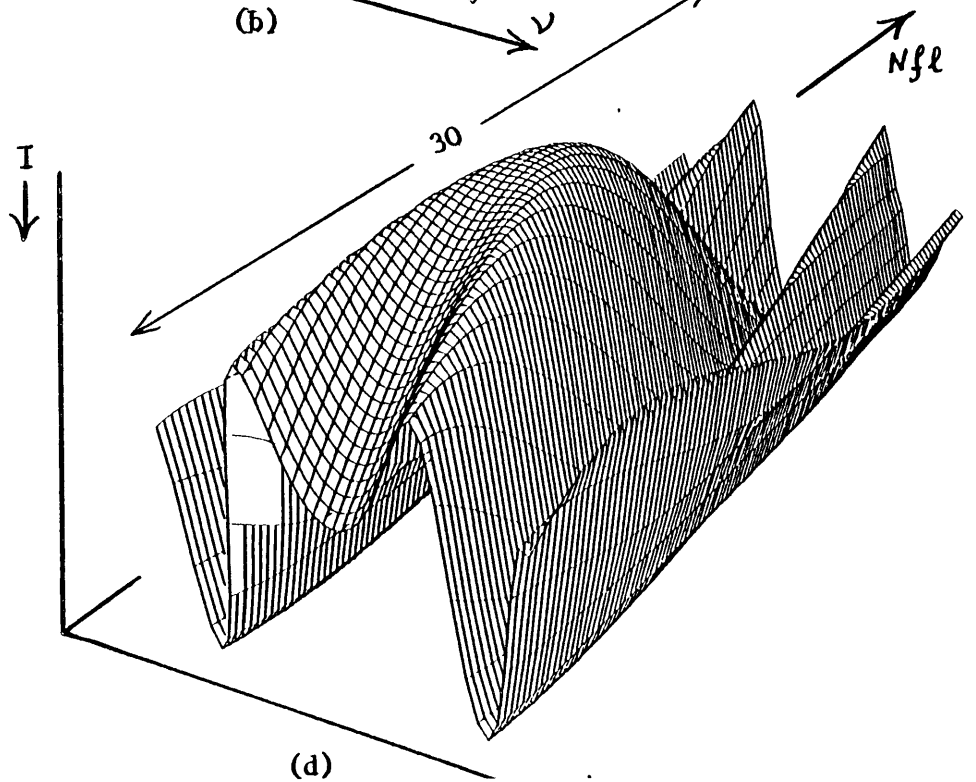

(d)

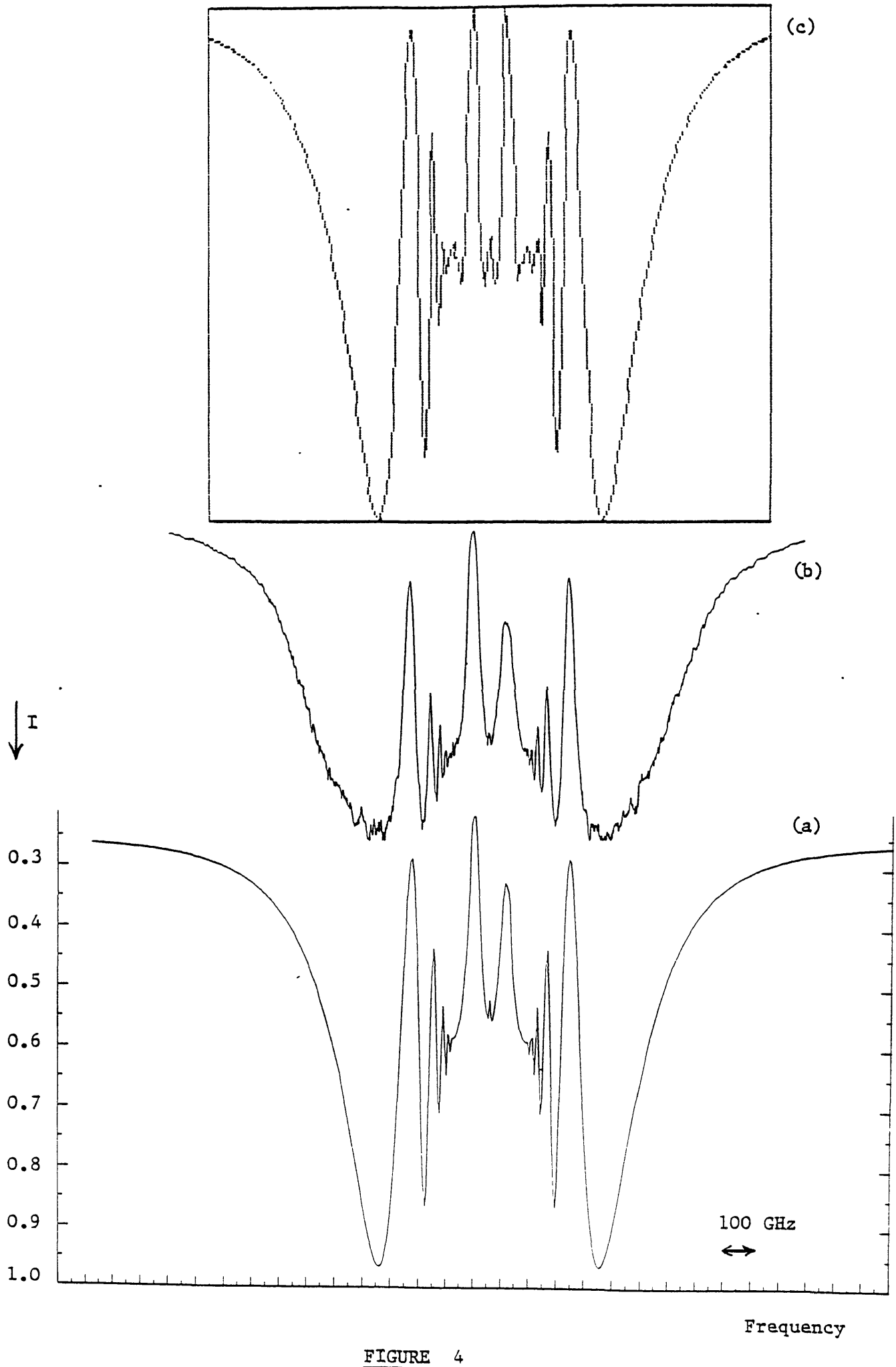

FIGURE 4

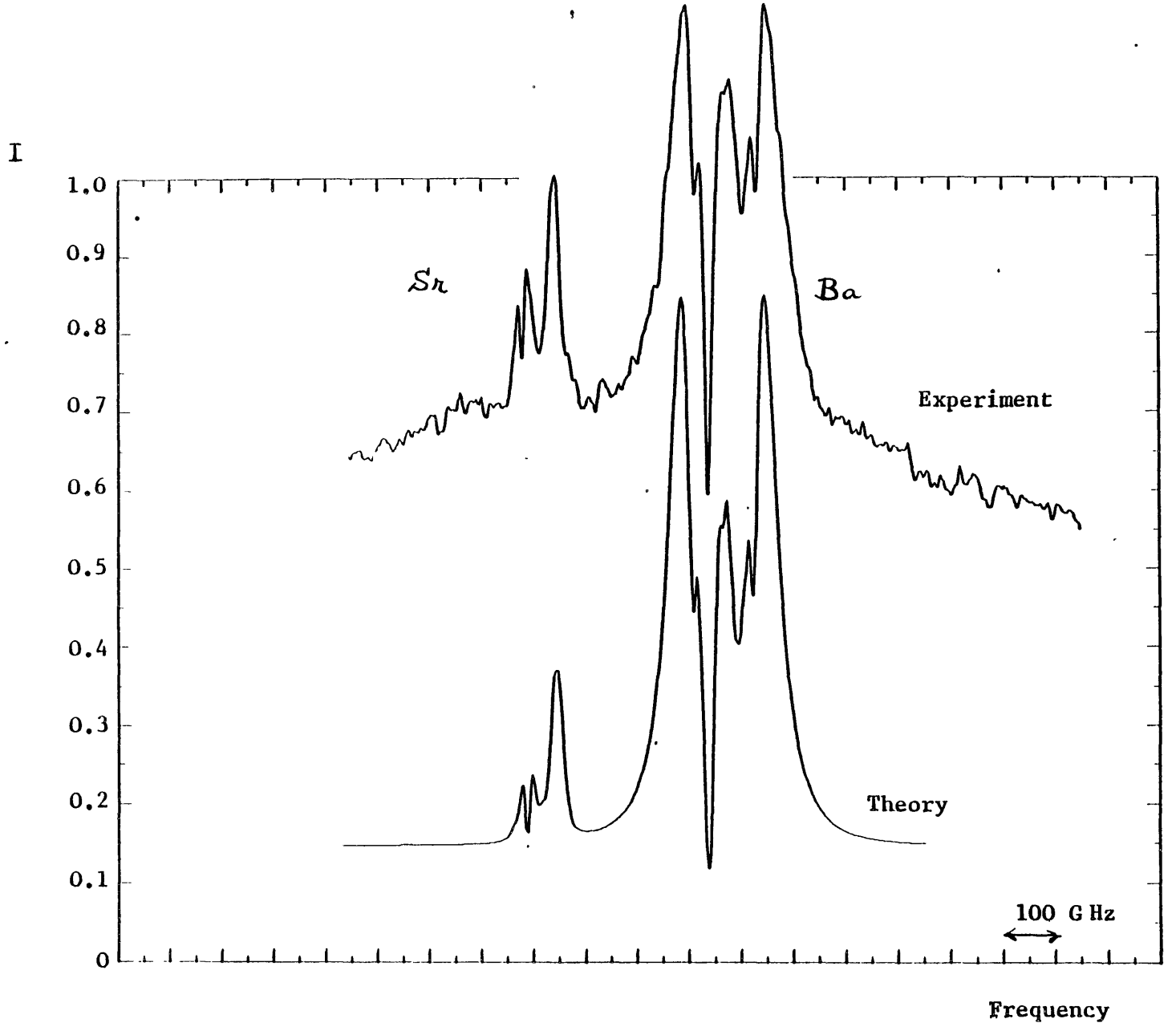
I
1.0
0.9
0.8
0.7
0.6
0.5
0.4
0.3
0.2
0.1
0
Sr
Ba
Experiment
Theory
100 G Hz
Frequency

FIGURE 5(a)

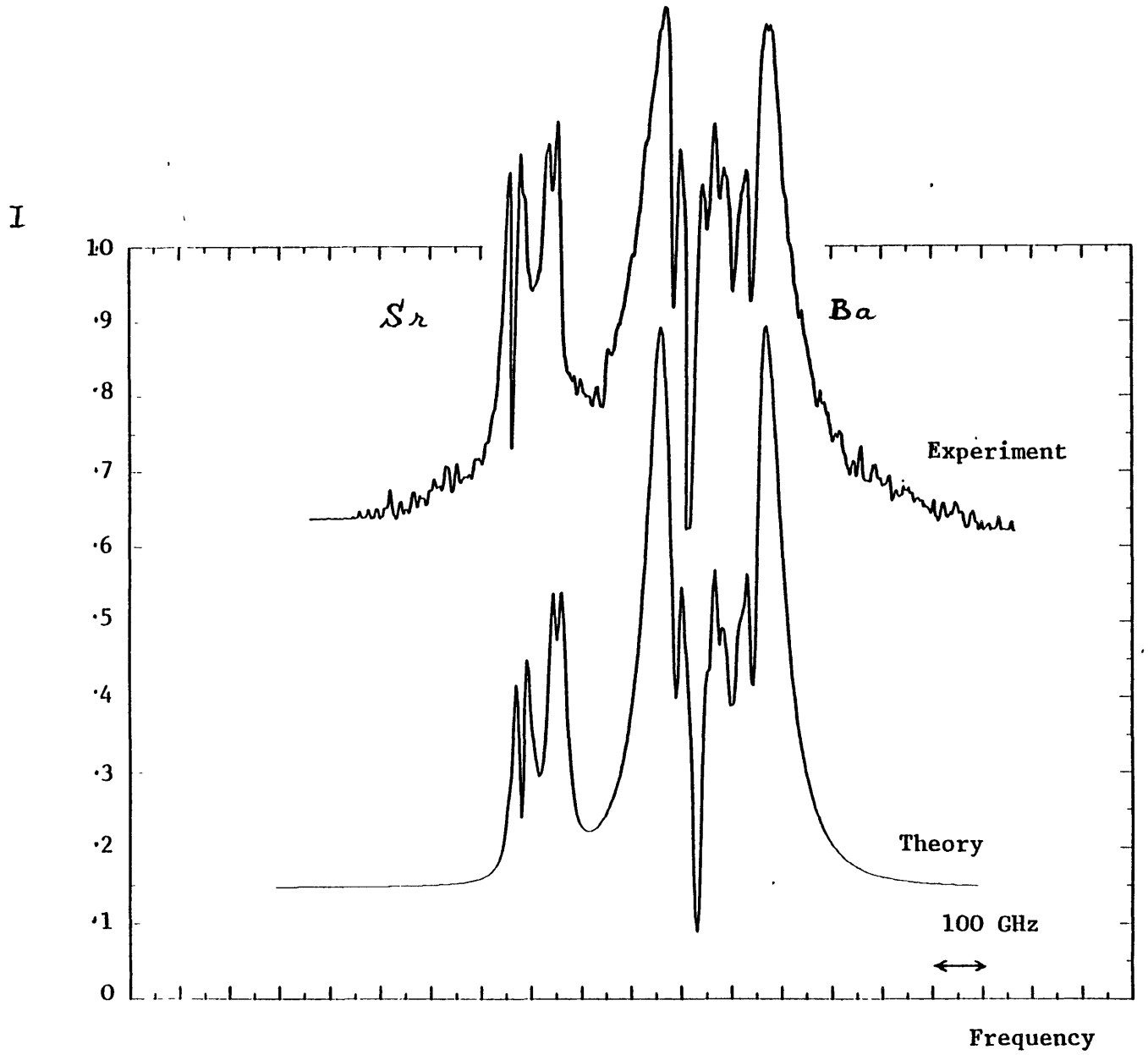

FIGURE 5(b)

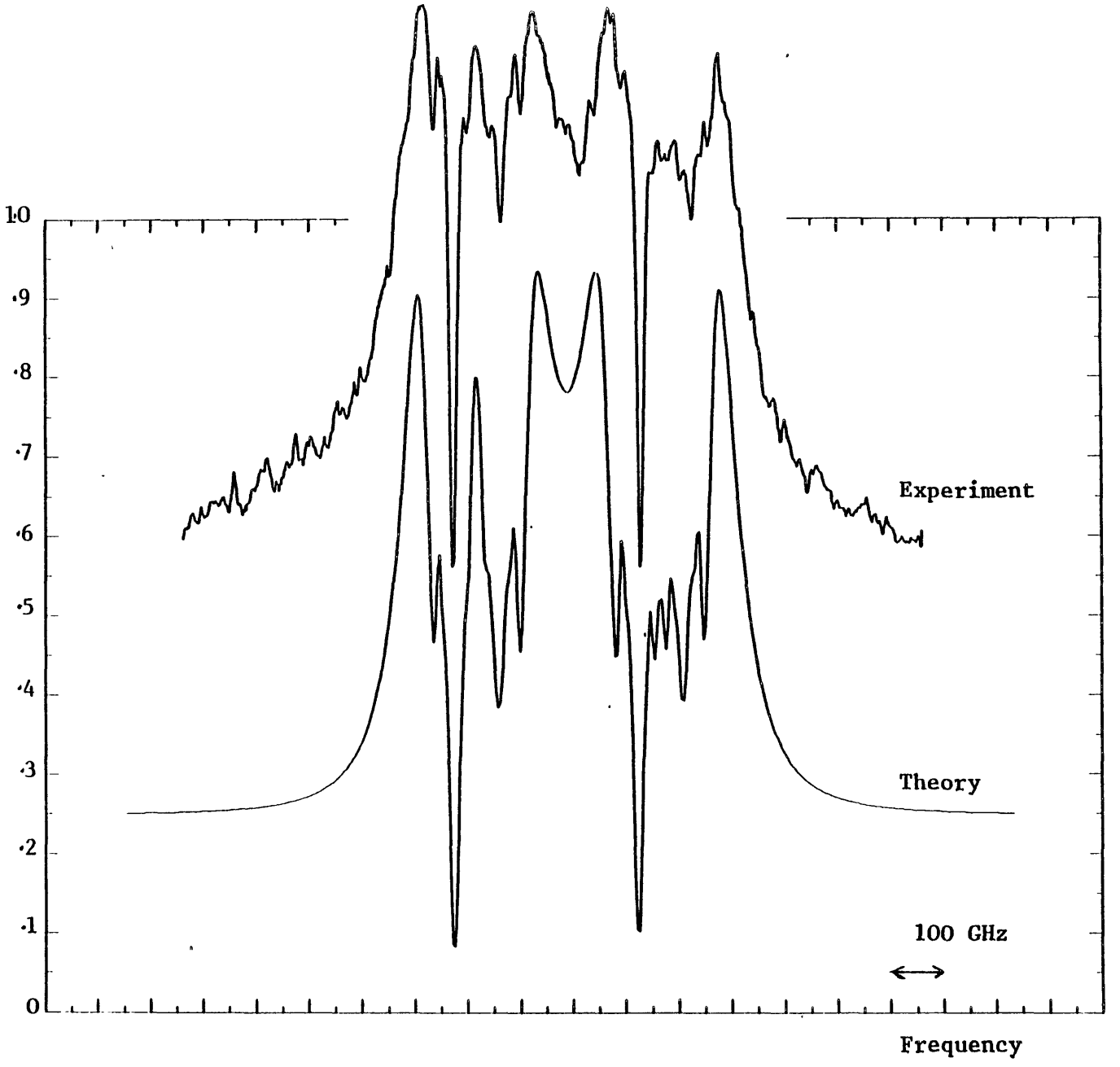

FIGURE 5(c)

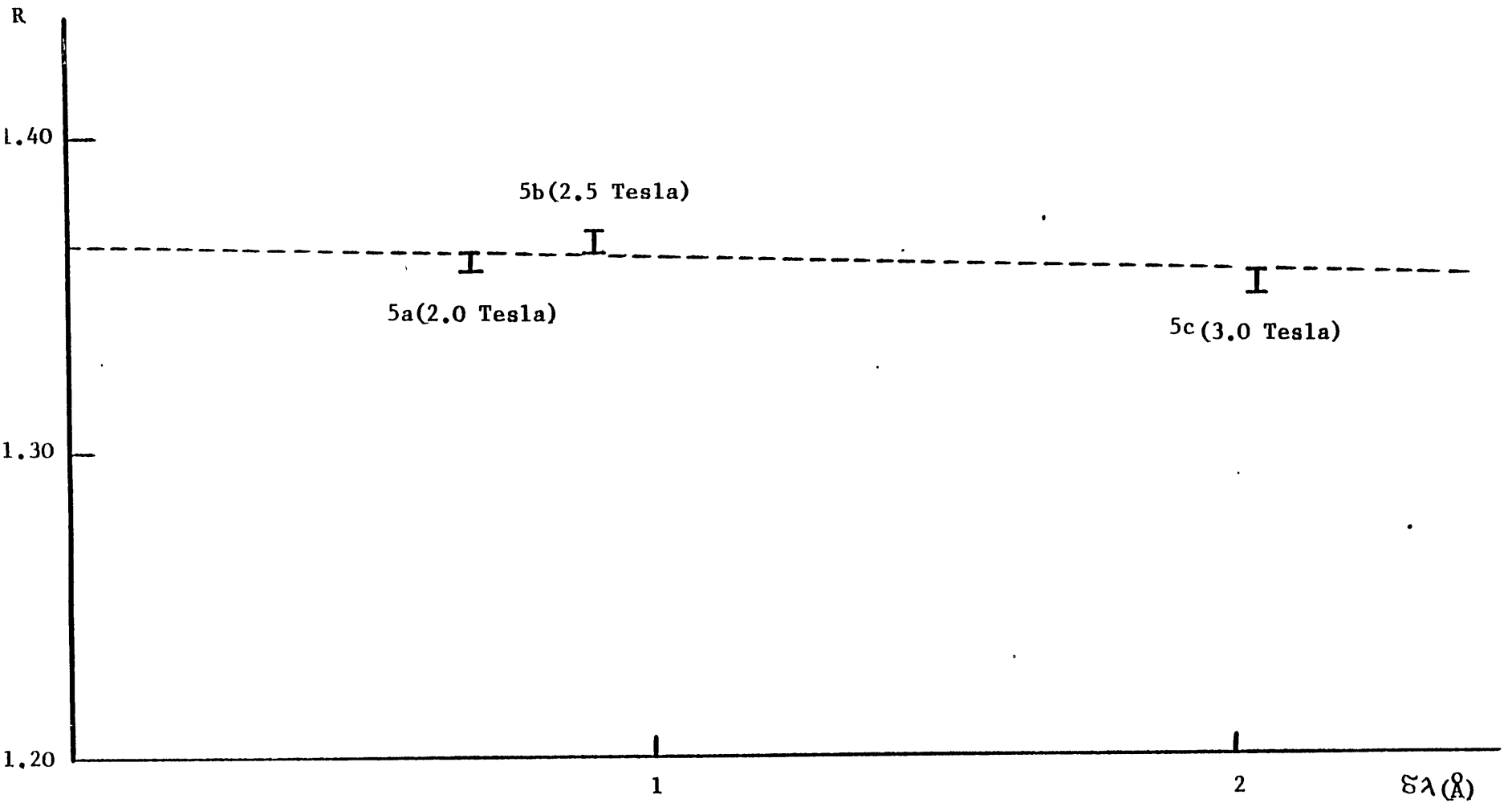

FIGURE 6

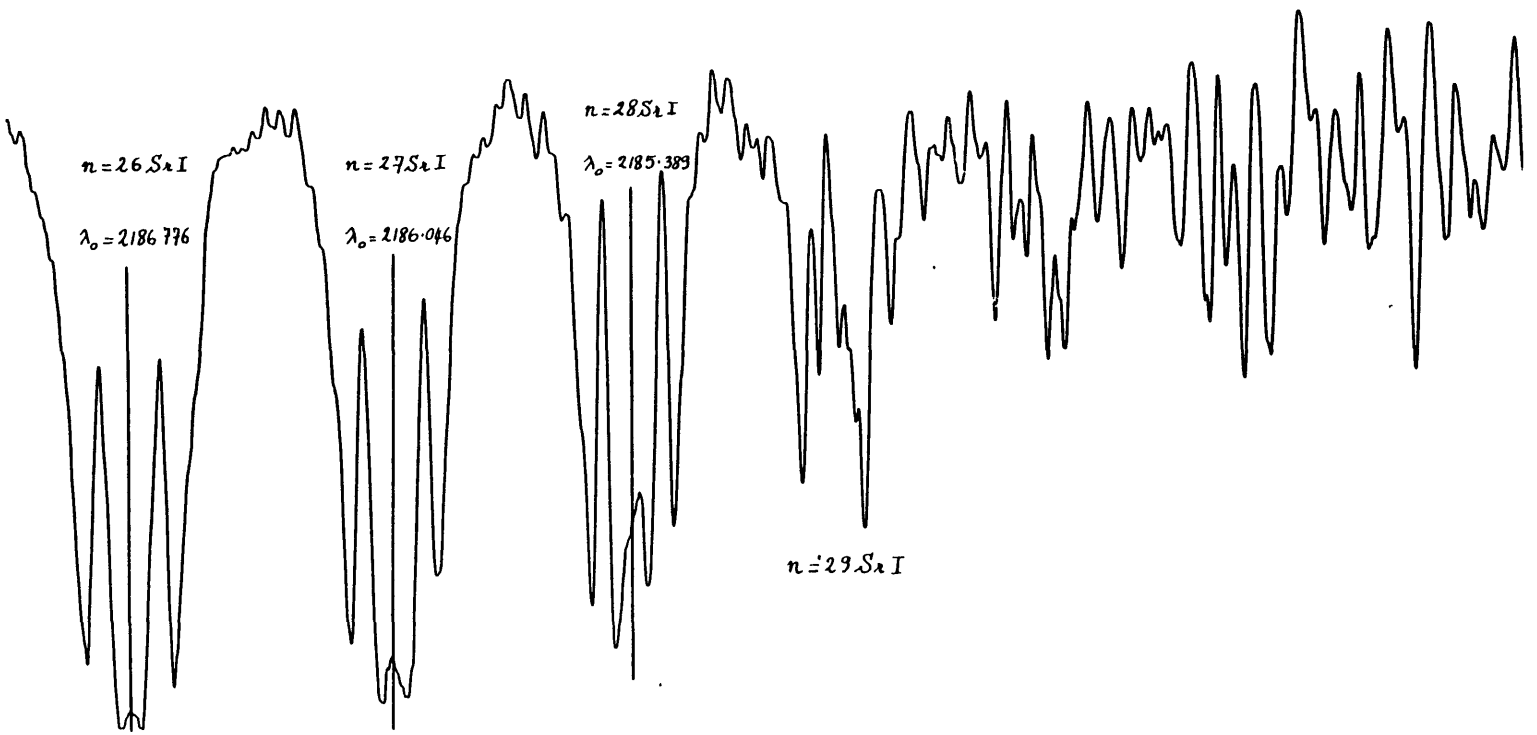

Fig. 14 - Showing the uppermost series members of Sr I in a field of 4.2 T. Note the increase in complexity of the spectrum above n = 28 which is attributed to l-mixing.

References.

BAIG, M.A. CONNERADE, J.P. & HORMES,J.
1982 J Phys B 15, L5

BUCKINGHAM, A.D.
1969 Symposia of the Faraday Society, London
no 3 "Magneto-Optical Effects"

CONNERADE, J.P.
1982 (to be published)

CONNERADE, J.P. BAIG, M.A. GARTON,W.R.S. & McGLYNN, S.P.
1980 J Phys B 13, 1705

ESHERICK, P.
1977 Phys Rev 15A, 1920

FORTSON, E.N. & WILETS, L.
1980 Advances in Atomic & Molecular Physics
Academic Press, New York, Vol 16, page 343

GARTON, W.R.S. & CODLING, K.
1968 J Phys B 1, 106

GAWLIK, W. KOWALSKI, J. NEUMANN, R WIEGEMANN, H & WINKLER, K
1979 J Phys B 12, 3873

HUDSON, R.D. CARTER, V.L. & YOUNG, P.A.
1969 Phys Rev 180, 77

HUI, A.K. ARMSTRONG, B.H. & WRAY, A.A.
1978 J Quant Spectrosc Radiat Transfer 19, 509

LEARNER, R.C.M.
1965 (Private Communication)

LUTJENS, P.
1972 Z Naturf 28a, 260

MITCHELL, A.C.G. & ZEMANSKI, M.W.
1971 "Resonance radiation and Excited Atoms"
Cambridge University Press, Cambridge.

PARKINSON, W.H. REEVES,E.M. & TOMKINS, F.S.
1976 J Phys B 9, 157

STARACE, A.F.
1976 "Photoionisation and Other Probes of Many-Electron Interactions"
page 395, Plenum Publishing Corporation, New York